Study of Mechanisms of Homologous Recombination in Mammalian Cells

Dissertation
zur
Erlangung der naturwissenschaftlichen Doktorwürde
(Dr. sc. nat.)
vorgelegt der
Mathematisch-naturwissenschaftlichen Fakultät
der
Universität Zürich
von

Andreas Sturzenegger

von
Wolfhalden AR

Promotionskomitee:

Prof. Dr. Petr Cejka (Vorsitz)
PD Dr. Pavel Janscak (Leitung der Dissertation)
Prof. Dr. Alessandro Sartori
Prof. Dr. Lumir Krejci

Zürich, 2016

- To my family -

Table of Contents

1. Zusammenfassung

Fast jede Zelle des menschlichen Körpers ist konstant DNS schädigenden Stoffen exogenen oder endogenen Ursprungs ausgesetzt, welche zu verschiedensten Genomschäden führen können. Diese DNS-Schäden sind potentiell mutagen und können zu einem instabilen Genom führen, einem der treibenden Faktoren für die Krebsentwicklung. Um solchen DNS-Veränderungen entgegenzuwirken, haben Zellen hochspezialisierte DNS-Reparatursysteme entwickelt. Zwei unterschiedliche Mechanismen, bekannt als nicht-homologes End-Joining (NHEJ) und homologe Rekombination (HR), sind für die Reparatur von DNS-Doppelstrangbrüchen zuständig, der gefährlichsten Form von DNS-Schäden. Die HR ist ein sehr genauer Reparaturmechanismus, allerdings ist sie beschränkt auf die S und G2-Phase des Zellzyklus. Dem gegenüber steht das NHEJ, welches während des gesamten Zellzyklus stattfinden kann, jedoch fehleranfällig ist. Um sie zu initiieren, benötigt die HR-Reaktion eine DNS-End-Resektion, die in 5' zu 3'-Richtung verläuft und einen 3'-Einzelstrang-DNS-Überhang generiert. In Hefezellen bilden die Exonuklease 1 und die Helikase/Nuklease Dna2 zusammen mit der RecQ-Typ Helikase Sgs1 zwei verschiedene Proteinmaschinerien, die zu einer extensiven DNS-End-Resektion führen können. In menschlichen Zellen sind jedoch fünf RecQ Homologe bekannt, nämlich RECQL1, BLM, WRN, RECQL4 und RECQL5. Es wurde schon bewiesen, dass das menschliche BLM Protein im Zusammenspiel mit DNA2 eine DNS-End-Resektion durchführen kann. Allerdings haben Daten aus einer Studie mit *Xenopus*-Eier Extrakten WRN als die wichtigste Helikase identifiziert, die in einem Komplex mit DNA2 zusammenarbeitet, um die DNS-End-Prozessierung auszuführen. Daher wollten wir untersuchen, ob WRN und DNA2 im Stande sind, zusammen die DNA-End-Resektion in menschlichen Zellen zu verrichten. In der vorliegenden Arbeit ist gezeigt, dass WRN in der Tat fähig ist, die DNA2-abhängige DNS-End-Resektion zu fördern, und dass diese Reaktion auf RPA und ATP angewiesen ist. Des Weiteren findet dieser Prozess in 5' zu 3'-Richtung statt und generiert damit den erwarteten 3'-Einzelstrang-DNS Überhang, der für die HR notwendig ist. Zusätzlich konnten wir zeigen, dass WRN und DNA2 *in vitro* und *in vivo* miteinander interagieren. Ausserdem haben wir herausgefunden, dass WRN und BLM in der Lage sind, die extensive DNS-End-Resektion, die durch DNA2 ausgeführt wird, *in vivo* zu stimulieren. Schlussendlich haben wir demonstriert, dass BLM als Bestandteil des BLM-TOPOIIIα-RMI1-RMI2 (BTRR) Komplexes an der DNS-End-Prozessierung beteiligt ist.

Zusammenfassend zeigen unsere Daten, dass DNA2 in Zusammenarbeit mit WRN oder dem BTRR Komplex die DNS-End-Resektion in menschlichen Zellen durchführt.

Die DNS-End-Resektion generiert einen 3’-Einzelstrang-DNS Überhang, der umgehend von RPA ummantelt wird und nicht nur als Substrat für die RAD51-Rekombinase dient, sondern auch als Plattform für die Aktivierung der ATR-Kinase, die durch ATRIP zur RPA-umhüllten Einzelstrang-DNS gebracht wird. Die aktivierte ATR-Kinase phosphoryliert CHK1 und induziert damit einen Kontrollmechanismus für DNS-Schäden, der umgehend den Zellzyklus stoppt. Obwohl vorangehende Studien demonstriert haben, dass MutSβ, ein heterodimerisches Mismatch-Reparatur-Protein, bestehend aus MSH2 und MSH3, im HR-Mechanismus involviert ist, ist seine genaue Funktion nach wie vor unklar. In dieser Arbeit wird gezeigt, dass MutSβ in menschlichen Zellen als Vermittler in der ATR-Aktivierung nach Formierung eines DNS-Doppelstranbruches dient. Wir beweisen ebenfalls die Proteinkomplexbildung von MSH2, MSH3 und ATR/ATRIP in menschlichen Zellen. Zusätzlich zeigen wir, dass die siRNS-gesteuerte Elimination von MSH2 oder MSH3 nach der Induktion eines Replikations-assoziierten DNS-Doppelstrangbruches die Phosphorylierung von ATR-Zielproteinen und die Bildung von ATRIP-Fokuspunkten verhindert. Des Weiteren haben Mutationen in dem Mismatch-bindenden Teil von MSH3 die Bindung von MutSβ zu bleibenden Haarnadel-Strukturen in der RPA-ummantelten DNS verunmöglicht und die ATR-Aktivierung *in vivo* eingeschränkt. Demzufolge zeigen unsere Resultate, dass MutSβ an beständige Haarnadel-Strukturen in RPA-umhüllter Einzelstrang-DNS bindet und die Rekrutierung und Aktivierung des ATR-ATRIP-Komplexes vermittelt.

Die HR hat das Potential eine Umgestaltung der chromosomalen Struktur durch die Formierung sogenannter Crossover auszulösen. Während diese Crossover in meiotischen Zellen für die Anordnung der einzelnen Chromosomen unerlässlich ist, durchläuft die HR in mitotischen Zellen vorzugsweise den synthese-abhängigen Stang-Anlagerungs (SDSA) Mechanismus, der immer zu nicht-crossover Reparaturprodukten führt. Daraus lässt sich schliessen, dass mitotische Zellen ein sehr strenges Kontrollsystem für die Auswahl der einzelnen HR-Subreaktionen besitzen. Allerdings ist über den molekularen Mechanismus, der diesem System zugrunde liegt, nicht sehr viel bekannt. Hier ist gezeigt, dass in menschlichen Zellen die siRNS-gesteuerte Elimination des RECQ5-Proteins die Reparatur von DNS-Doppelstrangbrüchen durch den SDSA-Weg vermindert. Die RAD52-vemittelte DNS-Einzelstrang-Anlagerung ist ein fundamentaler Schritt des SDSA-Mechanismus, und wir

konnten beweisen, dass RECQ5 dem inhibitorischen Effekt von RAD51 auf diesen Prozess entgegenwirkt. Abschliessend demonstrieren wir, dass RECQ5 den Austausch von Schwestrchromatid-Abschnitten verhindert und dadurch den BTRR Komplex ergänzt, welcher die Auflösung von HR-Zwischenprodukten katalysiert, um die Bildung von Crossovern zu vermindern. Unsere Resultate zeigen an, dass RECQ5 während der post-synaptischen Phase des SDSA-Mechanismus aktiv ist, um die Formierung von anomalen RAD51-Filamenten auf dem neu synthetisierten, invasiven DNS-Strang zu unterbinden und dadurch einschränkt, dass die Reparatur den riskanten Crossover-Mechanismus durchläuft.

Zusammengefasst identifizieren die Resultate der vorliegenden PhD-Arbeit neue Schlüsselfaktoren und deren genaue Wirkungsmechanismen in der zellulären Antwort auf DNS-Doppelstrangbrüche und stellen daher potentielle therapeutische Ziele für die Therapie von Krebsleiden dar.

2. Summary

Almost every cell of the human body is constantly exposed to DNA damaging agents of exogenous and endogenous origin, which can cause various lesions in the genome. These DNA damages can have mutagenic potential and lead to genomic instability that is one of the major drivers of carcinogenesis. To deal with DNA alterations, cells have developed highly specialized DNA repair pathways. Two distinct mechanisms, termed non-homologous end joining (NHEJ) and homologous recombination (HR), deal with repair of DNA double-strand breaks (DSBs), the most dangerous form of DNA damages. HR is an accurate repair mechanism, but it is restricted to S and G2 phases of the cell cycle. On the other hand, NHEJ can take place throughout the cell cycle and is error-prone. HR reaction relies on an initial 5' to 3' DNA end resection step generating 3' ssDNA overhangs. In yeast, the Exonuclease 1 and the helicase/nuclease Dna2 in conjunction with the RecQ-type helicase Sgs1 constitute two independent pathways for long-range DNA-end resection. In human cells, there are five RecQ homologs known, namely RECQL1, BLM, WRN, RECQL4 and RECQL5. It has already been demonstrated that human BLM can mediate DNA-end resection in conjunction with DNA2. However, data obtained from a study in *Xenopus* egg extracts identified WRN as the major helicase that works in complex with DNA2 to catalyse DNA-end resection. Therefore, we wanted to investigate whether WRN can mediate DNA-end resection in conjunction with DNA2 in human cells. Within this thesis work it is demonstrated that indeed WRN can promote DNA2-mediated DNA end processing and that this process is dependent on the presence of RPA and ATP. In addition, this reaction occurs in 5' to 3' direction generating the anticipated 3' ssDNA overhang required for HR repair. Further, we provide evidence for the physical interaction of WRN and DNA2 *in vitro* and *in vivo*. Moreover, we found that WRN and BLM stimulate extensive DNA end resection by DNA2 *in vivo*. Finally, we show that BLM mediates DNA-end resection as part of the BLM-TOPOIIIα-RMI1-RMI2 (BTRR) complex. Taken together our data provide evidence that in human cells, DNA2 resects broken DNA ends in conjunction with either WRN or BTRR complex.

The 3' ssDNA tail generated by DNA-end resection is subsequently coated with RPA and does not only serve as a substrate for the loading of RAD51 recombinase, but also provides a platform for the activation of ATR kinase that is recruited to RPA-coated ssDNA trough its interacting protein ATRIP. Activated ATR phosphorylates CHK1 thereby inducing the DNA damage checkpoint that leads to a cell cycle stop. Although previous studies show that MutSβ, a heterodimeric mismatch repair protein composed of MSH2 and MSH3, is involved in the HR process, its exact function is unclear. In this thesis work, it is demonstrated that MutSβ serves as a mediator in ATR activation upon DNA DSB induction in human cells. We provide evidence that MSH2, MSH3 and ATR/ATRIP form a complex in cells. In addition, we show that siRNA-mediated depletion of MSH2 or MSH3 impairs the phosphorylation of ATR targets and the formation of ATRIP foci in response to replication-associated DNA DSBs. Further, mutations in the mismatch-binding domain of MSH3 diminished the binding of MutSβ to persistent hairpin loops in RPA-coated ssDNA and compromised ATR activation *in vivo*. Thus, our results demonstrate that MutSβ binds to hairpin loop structures persisting in RPA-coated ssDNA at sites of DNA damage and mediates recruitment of the ATR-ATRIP complex for its activation.

HR has the potential to generate chromosomal rearrangements trough crossover formation. While crossovers are required in meiotic cells for proper chromosome segregation, in mitotic cells, HR predominantly proceeds via the synthesis-dependent strand annealing (SDSA) pathway that always leads to non-crossover products. This implies that mitotic cells possess a stringent control system for HR subpathway selection. However the underlying molecular mechanism is not well defined. Here, we present evidence that siRNA-mediated knockdown of RECQ5 impairs DNA DSB repair by SDSA in human cells. Further, we provide *in vivo* and *in vitro* data demonstrating that RECQ5 helicase counteracts the inhibitory effect of RAD51 on RAD52-mediated ssDNA annealing, a key step of SDSA. Finally, we show that RECQ5 suppresses sister chromatid exchanges in human cells in a complementary manner with the BTRR complex that mediates the dissolution of recombination intermediates to prevent crossovers. These results suggest that RECQ5 acts during the post-synaptic phase of SDSA to prevent formation of aberrant RAD51 filaments on the extended invading strand, thus limiting its channeling into potentially hazardous crossover pathway.

Taken together, the results of this thesis work identify new key players and their exact working mechanism in the cellular response to DNA DSBs and thus provide potential new therapeutic targets for cancer therapy.

3. Introduction

The adult human body is composed of approximately 10^{13} cells that can be divided into several different cell types forming highly structured tissues and organs [1]. Despite the fact that many cells are highly differentiated and fulfil distinct functions, they all contain the same genetic information and originate from one single progenitor cell. Cell division is not only a very important process during the development of a new individual, but it is also required in the adult organism. Cells with a short lifespan, for instance some particular white blood cells, need to be renewed in order to maintain proper body homeostasis [2]. To do so, cells undergo the so-called mitotic cell division, which is also required for wound closure in case of injuries. Further, meiosis, which is another type of cell division, is fundamental for the production of germ cells. Growth and division of cells within a tissue is mediated by a variety of complex mechanisms involving intra- and extracellular signal transduction pathways. Typically, a growth- and division-promoting ligand binds to a cell surface receptor, for instance receptor-tyrosin kinases, triggering an intracellular response that leads to an increase of the cell size and activates the cell division cycle [3]. In healthy tissues, these cell division-inducing signal molecules, also called mitogens, are highly regulated in their production and secretion [3]. Thus, cell division within healthy tissues is strictly controlled.

Cancer is a disease that is characterised by cells whose growth is out-of-control. More precisely, it is a group of diseases consisting of more than 100 different types of cancerous maladies that can in principle affect every organ in the human body. The single cancer types are unique with their own causes, symptoms and, if available, the methods of their treatment. The body is harmed when aberrant cells start to divide in an uncontrolled way and form tumours, which can grow and interfere with the normal function of organs. In some cases, they even release hormones that can alter the function of the whole body. Tumours should not be seen only as a clump of cells that is proliferating at very high rate. They form complex tissues in conjunction with different non-neoplastic cell types. In extreme cases, like the Hodgkin's lymphoma, these normal cells can make up to 99% of the tumour mass [4]. Trough heterotypic interactions, the neoplastic cells communicate with the tumour-associated stroma cells and *vice versa* enabling the tumour to also actively recruit certain cell types like tumour-associated macrophages. Thus, the normal cells of the tumour stroma are not only important for the survival of the neoplasia, but also actively participate in tumourigenesis [3]. While benign tumours are located to a defined place and their growth is usually limited, malignant cells start to invade the neighbouring healthy tissues. Under certain circumstances, cancer cells become able to move trough the blood and lymph system and form malignant tumours that spread from the primary tumour to other locations in the body to form metastases. These metastases are extremely dangerous and cause up to 90% of cancer deaths [5, 6]. Although these days the cardiovascular diseases are the leading causes of death, cancer might take over this position in the near future since cancer is an old-age disease and the expectancy of life is still increasing in industry nations [7, 8]. To understand the basic principles of tumour formation, it is important first to understand the ongoing processes in single cells that can lead to cancer development.

Hanahan and Weinberg have defined six hallmarks of cancer showing the different capabilities that cells may have to acquire during their evolution from normal to malignant tumour cells [9]. They also describe that development of cancerous lesions is a progressive process that passes trough several stages where these abilities are worked out [9]. As already mentioned above, cancer cells have the ability to proliferate continuously, which is probably the most fundamental hallmark in carcinogenesis (Figure 1). They can do so by several mechanisms. One possibility is that cells start to produce mitogens and subsequently release them to stimulate their own surface receptors resulting in increased cell-division rates [10]. Closely related to this action, the tumour-associated stroma cells can also be directly stimulated trough heterotypic interactions to release mitogens [11]. Further, cells could alter signal pathways by raising the expression of certain receptor proteins or simply by enabling receptor kinases to transduce signals even in the absence of the corresponding ligand [12]. Although cell proliferation induction and maintenance is crucial for a neoplasia to grow, there are tumour suppressor proteins working in anti-proliferative programs that have to be overcome (Figure 1). Such a protein is p53 that is a central effector and found frequently inactivated in many cancer types [13]. This protein gets input signals from intracellular stress- and damage response machineries and decides whether the progression of the cell cycle should be stopped to allow repair or whether apoptosis should be induced [14]. Apoptosis, the programmed cell death, is an important component of the cellular response to prevent carcinogenesis (Figure 1) [15, 16]. There are two major pathways known to induce apoptosis in a cell, an extrinsic and an intrinsic one [17]. The extrinsic program relies on an extracellular death-inducing signal by for instance Fas-ligand binding to its receptor activating an intracellular signal cascade [17]. On the other hand, the intrinsic apoptotic system is dependent on intracellular signals that are transduced by p53 for instance [18]. Both apoptosis pathways peak in the activation of the same effector caspases that lead to dismantling of the cell [17]. Cancer cells have established methods to avoid apoptosis by, among others, overexpressing anti-apoptotic factors of the Bcl-2 family or altering the structure of the aforementioned Fas-receptors in a way that its ligand is unable to bind [19, 20].

Having established ongoing proliferation in the progressive development of a cancer cell, it will encounter the issue that most cells can undergo only limited amount of growth and division cycles. This derives from the end-replication problem in which telomeres of the chromosomes in the cells get shorter during each division [21]. After certain numbers of cell-doublings, the telomeres get to short and the cell enters a phase, called senescence, where it is still viable but does not divide anymore. Those cells that are able to bypass this first barrier enter the crisis phase, a second arrest phase [22-24]. In this last phase usually all cells die due to recurrent chromosome bridge-breakage-fusion cycles leading to apoptosis [24]. Nevertheless under some circumstances, they are able to escape and get unlimited replicative capability (Figure 1) [3, 22, 23]. This immortalization can be achieved by re-expressing telomerase, an enzyme that is capable of re-extending the shortened telomeres [24]. In fact, this is the case in approximately 90% of malignant tumours [25].

As in the case of normal tissues, tumours require nutrition and oxygen supply. In addition, waste products accumulating during cell metabolism, like carbon dioxide, need to be taken away from the cells. Like cell division, angiogenesis is crucial during development and tightly regulated in the adult organism where it is only activated transiently for instance during wound healing [26]. If a tumour expanded up to a given size, hypoxia and nutrient starvation induce an angiogenic switch (Figure 1) [27]. This mechanism enables tumour cells to release factors like the vascular endothelial growth factor leading eventually to neovascularisation of the tumour tissue [28]. In contrast to the highly organised network of blood vessels in healthy tissues, tumour vasculature is unstructured, leaky and does not provide a continuous blood supply [29]. This derives from the fact that angiogenesis in a tumour is constantly active and does not allow stabilization of the newly formed vessels [29].

Probably the most devastating hallmark of cancer is the formation of metastases causing by far the most cancer-related deaths (Figure 1) [5, 6]. Metastasis formation of tumour cells is a multi-step process that in the case of carcinomas starts with the invasion of the tissue adjacent to the primary tumour [30]. Malignant cells then enter the vessels of the blood and lymphatic system by which they get transported throughout the body and at some point exit the vasculature trough a process called extravasion [30]. Next, a crucial step is the survival of the mobile cell in a new microenvironment at a distant location. Once adapted to the new conditions, the migrated cell eventually grows and divides, building a new colony of neoplastic cells [30]. To achieve this, cells need to undergo an epithelial-mesenchymal-transition by which they loose the cell-cell adhesion and become migratory [3, 30-32].

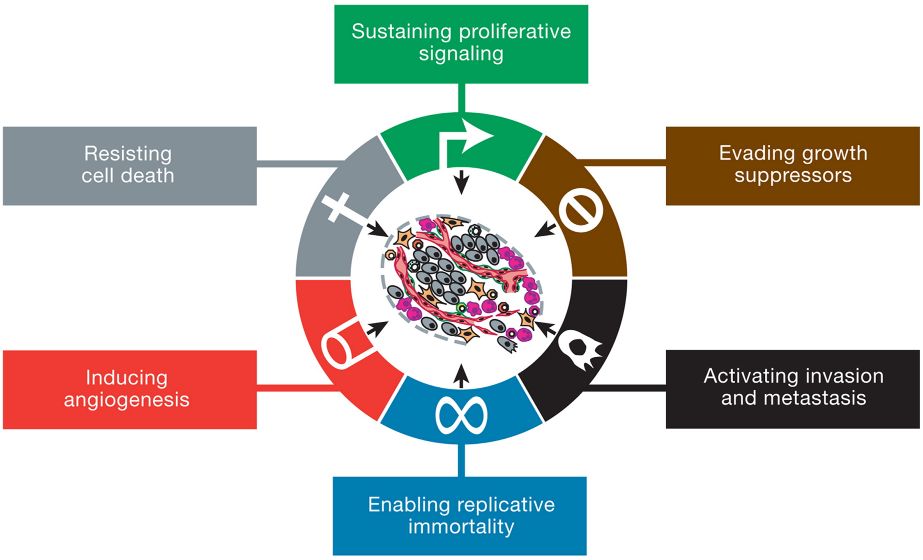

Figure 1: The six hallmarks of cancer. Depicted are the capabilities that cells have to acquire to become malignant. They have been defined by Hanahan and Weinberg in 2000 and refined in 2011. Adapted from [3].

The above-described hallmarks of cancer cells are caused by genome instability and tumour-promoting inflammation [3]. It is well known that macrophages infiltrate tumours where they rather induce further tumour progression than fight against the cancer cells [33, 34]. On the other hand, tumour formation and progression is also driven by specific mutations in two key gene types called proto-oncogenes and tumour suppressor genes. A gain-of-function mutation in proto-oncogenes turns them into oncogenes that enhance cell proliferation and inhibit differentiation and apoptosis [35]. Conversely, a loss-of-function mutation inactivates tumour suppressor genes that usually control the cell cycle and induce apoptotic pathways to prevent cancer formation [35]. Next to the mutations in these two kinds of genes that are crucial for the development of malignant cells an unstable genome also contributes to carcinogenesis. There are different types of genomic instability. Common among many cancers are altered number of chromosomes due to chromosome missegregation during mitosis [36-38]. Further, structural anomalies of the DNA can occur trough deletions, insertions or translocations of chromosome parts. In addition, single nucleotides can be changed, lost or inserted [39]. Thus, a very important objective for every cell is to propagate the genetic information to the next generation in an intact and unchanged form.

3.1. The genome maintenance network

Different sources of endogenous and exogenous origin can cause the above-mentioned types of genomic instability (Figure 2). In fact, a single human cell can receive several thousands of DNA lesions every day [40]. DNA damage can arise from physiological processes that take place during the cell cycle. Reactive oxygen species (ROS), formed by the respiratory chain of the cells, are such genotoxic chemicals that can harm the genetic information (Figure 2). ROS release by macrophages and neutrophils is part of the immune response to fight pathogens, demonstrating the toxic characteristics of these molecules [41, 42]. Further, polymerases can introduce mismatches while replicating the genome or DNA strand breaks can occur if DNA topoisomerase function is impaired (Figure 2) [43]. While the phosphodiester backbone of the DNA is chemically extremely stable under physiological conditions, hydrolytic reactions can lead to deamination of bases like cytosine or cleavage of the glycosidic bond under certain conditions resulting in DNA lesions [44-46].

The human skin is constantly exposed to ultraviolet (UV) light, an exogenous source of DNA damage (Figure 2). Although the earth is covered by the ozone layer, which absorbs a wide spectrum of the UV light, the UV-A and UV-B rays passing trough this protective shell contain still sufficient amounts of energy to induce around 10^5 DNA alterations in every exposed cell per hour [43]. Ionizing radiation (IR), including X-, ϒ-, α-, β- and cosmic-rays, also harbours mutation-inducing potential since it can lead to DNA lesions like DNA double-strand breaks (DSBs) (Figure 2) [47]. IR is generated for instance by the radioactive decay of radionuclides or is used in medical examinations while X-raying a patient. The danger to human health that emanates from excessive exposure to IR has been underlined after the detonations of the atomic bombs in Hiroshima and Nagasaki in 1945 and by the nuclear reactor disaster in Chernobyl on the 26 April 1986. Studies done with workers involved in the nuclear power plant accidents clean up in Chernobyl and Fukushima (11 March 2011) show that structural chromosomal anomalies were present in cells of these people and lasted there for several years [48, 49].

Exogenous DNA damaging agents like toxins from pathogens or heterocyclic amines are also present in our food. Some *Aspergillus* species like *A. flavus* produce extremely toxic secondary metabolites called aflatoxins. Once they are metabolised in the liver, these mycotoxines are counted to the most carcinogenic substances [50, 51]. Depending on how the molecules are processed, they form epoxide intermediates that are extremely reactive or are converted to aflatoxin M_1 that is less toxic [51]. Epoxides are able to form adducts on DNA bases and are thus mutagenic. Consistent with their characteristics, it has been demonstrated that these toxins can induce the formation of liver cancer [51-53].

Some aromatic chemicals like ethidium bromide, which are frequently used in research, intercalate into double-stranded (ds) DNA leading to a deformation of the two strands at certain spots. Such a distortion of the DNA integrity can affect DNA replication or transcription and is therefore thought to be mutagenic [54, 55]. Further, metals present in polluted drinking water like arsenic also have been shown to induce DNA damage and can lead to structural anomalies of chomosomes [56, 57].

Particular genotoxic agents can also induce the formation of DNA single-strand breaks (SSBs) (Figure 2). If this DNA lesion is left unrepaired, the replication machinery can collide with it resulting in the formation of DNA DSBs. Two SSBs that are located closely lead to the same effect. It is well known that DNA DSBs are highly cytotoxic and, if left unrepaired, can lead to chromosomal rearrangements or cell death [58, 59]. Nevertheless, DNA DSBs are also generated on purpose in V(D)J recombination of maturating B- and T-cells [60]. In addition, the Spo11 enzyme actively generates DNA DSBs during meiotic recombination [61].

To counteract DNA damage and the above-mentioned consequences that would come along with it, cells have evolved a multiplicity of mechanisms, collectively termed as the DNA damage response (DDR) that recognises a DNA lesion, signals its presence and initiates sophisticated pathways resulting in DNA repair (Figure 2) [43, 62]. Defects in the DDR machinery are usually linked to severe human diseases that are characterised by predisposition to cancer resulting from increased sensitivity to certain DNA damaging agents [43, 59, 63].

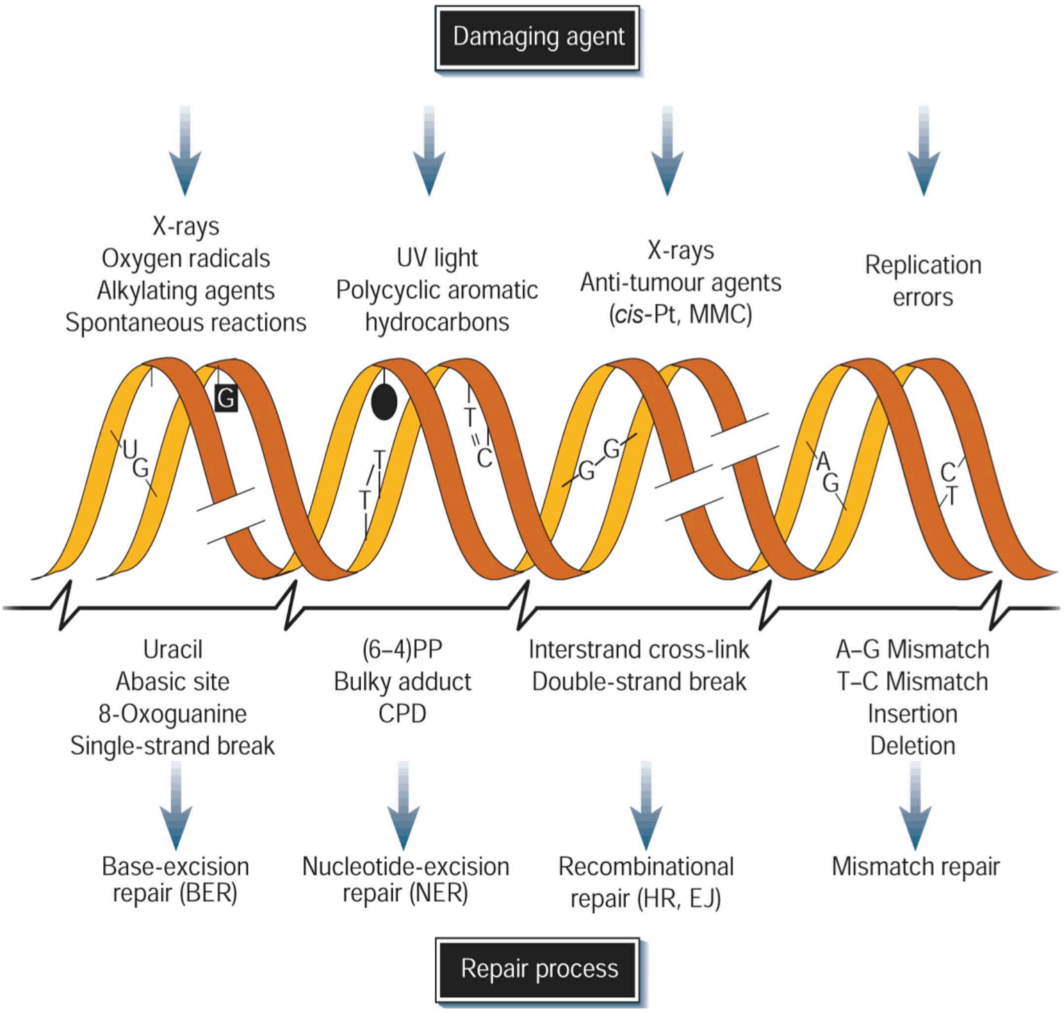

Figure 2: DNA damaging agents, types of DNA damage and corresponding repair pathways. Different agents cause distinct DNA lesions that have to be repaired by specialised DNA repair pathways to restore genomic integrity. Abbreviations: cis-Pt, cisplatin; MMC, mitomycin C; (6–4)PP, 6–4 photoproduct; CPD, cyclobutane pyrimidine dimer; HR, homologous recombination; EJ, end joining. Adapted and modified from [63].

3.2. DNA repair Pathways

In general, each type of damage is repaired by a specialised system that restores genomic integrity trough a sequence of events catalysed by different proteins [43, 63]. Mechanisms of the DNA repair pathways that deal with altered bases and damaged or mis-incorporated nucleotides as well as one of the repair systems that deals with DNA DSBs will be discussed in this chapter.

3.2.1. Nucleotide excision repair

DNA helix-distorting adducts, such as those generated by UV light (6-4 photoproducts and pyrimidine dimers), are eliminated by nucleotide excision repair (NER) that is split into two sub-pathways: transcription-coupled NER (TC-NER) and global genome NER (GG-NER) (Figure 3) [64]. Both pathways are mechanistically akin, however the way in which they recognise the DNA lesion is different. While the GG-NER acts genome wide and checks for DNA distortions, the TC-NER gets activated when RNA-Polymerase II is stuck during transcription because of the presence of DNA damage. In GG-NER, the helix distortion is sensed by XPC binding to the DNA [65, 66]. Since pyrimidine dimers cause only a limited destabilisation of the DNA, initiation of the pathway is assisted by XPE and DDB2 [67-70]. The following step is the verification of the damage that is conducted by XPC-mediated binding of the TFIIH complex to the DNA [71]. This transcription initiation and repair factor is composed of multiple subunits amongst others, the XPB and XPD helicases [72]. These proteins are able to unwind the DNA around the lesion and have opposite polarities. However it has been demonstrated that rather the ATPase than the helicase activity of XPB is required for opening the DNA [73]. The endonucleases XPF/ERCC1 and XPG then cleave the damaged strand 5' and 3' to the damage, respectively, removing a stretch of 22-30 nucleotides [74-76]. RPA binding to the undamaged strand is not only important to protect it from damaging effects, but it is also required for positioning of the aforementioned nucleases [77]. Restoration of DNA integrity is then carried out by combined action of a DNA polymerase, PCNA, RFC and a DNA Ligase whereas the identity of the proteins depends on the replicative state of the cell [75].

TC-NER mechanistically overlaps with GG-NER, however the initiation of the pathway is different (Figure 3) [75]. As mentioned above, if RNA Pol II gets stuck on a lesion during transcription, recruitment of the CSA and CSB proteins leads to initiation of TC-NER [78]. These proteins are crucial for the recruitment of other factors involved in TC-NER, the initiation of the repair reaction and potentially also for backtracking of the RNA Pol II that would otherwise block access to the DNA damage [78, 79]. After this step, TC-NER proceeds with the recruitment of the TFIIH complex and all the subsequent steps described above for GG-NER [75, 76].

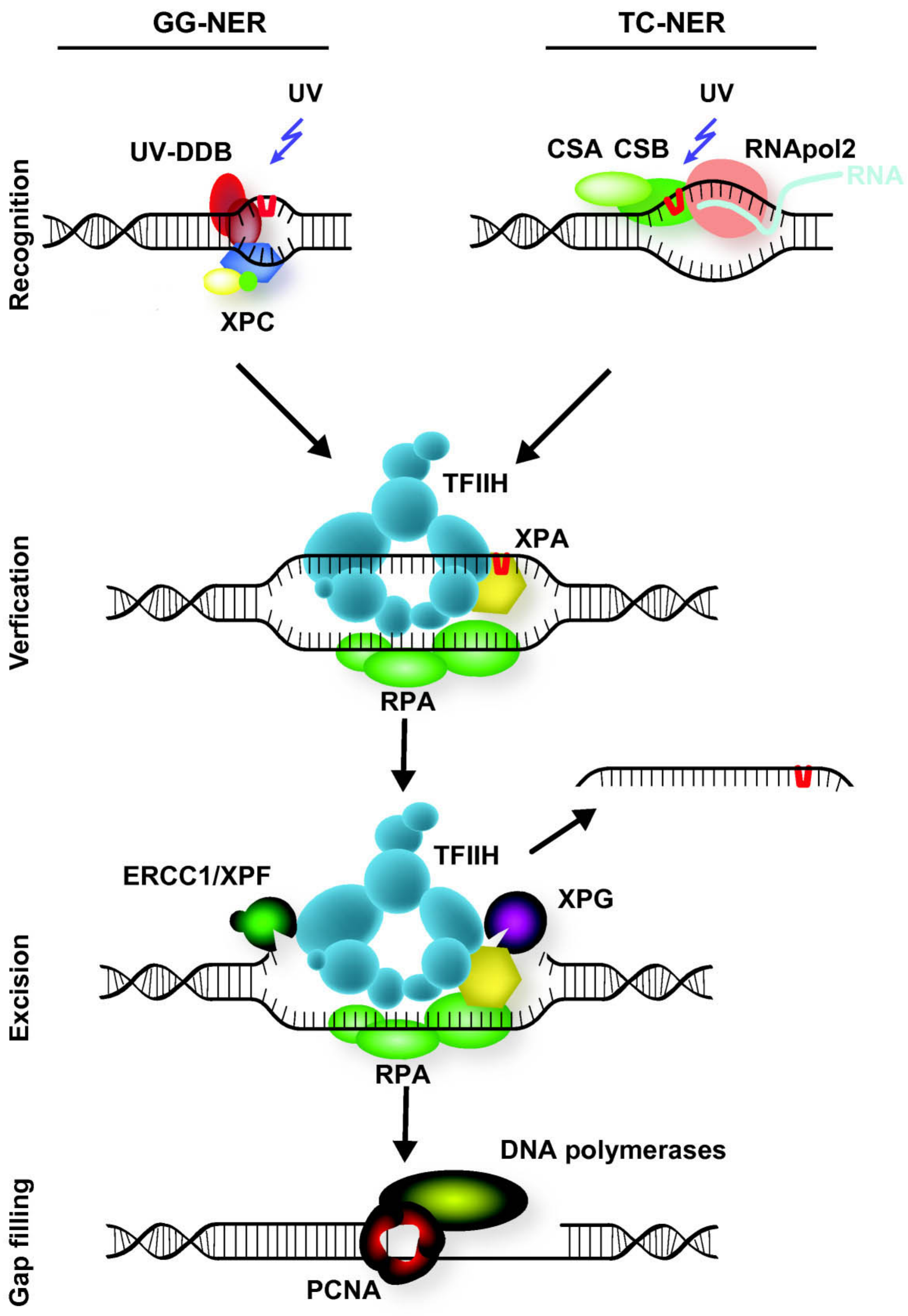

Figure 3: Nucleotide excision repair system. There are two nucleotide excision repair pathways known as transcription-coupled nucleotide excision repair (TC-NER) and global genome nucleotide excision repair (GG-NER). Although the recognition of the DNA lesion within the two sub-pathways is mediated by different factors, the downstream steps are identical. GG-NER is initiated by helix-distortions that are recognised by XPC. In case of a pyrimide dimer DNA lesion, the XPE and DDB2 proteins assist in this first step. On the other hand, TC-NER is started by a stalled RNA Pol II that recruits CSA and CSB. Verification of the damage is then conducted by the TFIIH complex, which is composed of several subunits. Unwinding of the DNA adjacent to the damage site is then conducted by XPD and XPB helicases, creating a substrate for endonucleolytic incision by XPF/ERCC1 and XPG that remove a 22-30nt oligonucleotide containing the lesion. The ssDNA generated during this process is protected by RPA binding. Eventually, a DNA polymerase, PCNA, RFC and a DNA ligase mediate resynthesis of the DNA to fill the ssDNA gap. Adapted and modified from [80].

3.2.2. Mismatch repair

During replication of the genome, errors can occur in the form of insertions, deletions or miss-incorporated nucleotides. Although the replicative polymerases δ and ε have proofreading function to check whether the inserted nucleotide is correct, it has been estimated that 1 in each 10^9 to 10^{10} base pairs is mutated per cell division [81, 82]. To detect and repair such mistakes, the mismatch repair (MMR) system continuously screens the newly synthesised strands [83]. In *E.coli,* distinction between the template and the newly synthesised strand occurs via DNA adenine methylation (Dam) at GATC sites [84]. Although the MMR mechanism seems to be evolutionarily conserved, it is currently unknown how the strand discrimination in eukaryotes takes place [85]. In addition, there are some other differences regarding the protein functions between bacteria and eukaryotes. MutS and MutL proteins, the core MMR factors, are present as homodimers in *E.coli* while in eukaryotic cells several heterodimeric complexes are formed by their homologues [85]. MutSα, composed of MSH2 and MSH6, binds to base-base mismatches and to small insertion-deletion loops (IDLs) of 1-2 nucleotides [86]. On the other hand, MutSβ, a heterodimer of MSH2 and MSH3, recognises IDLs of 1-14nt [87, 88]. Evidence suggests that MutSα as well as MutSβ are able to initiate repair of small IDLs [86]. In addition to their mismatch-binding domains, both protein complexes also display ATPase activity mediated by Walker-type ATPase domains that are present in both subunits of MutSα and MutSβ, respectively [89]. Among the other key players in the MMR reactions in eukaryotic cells, there are three heterodimers: MutLα (MLH1/PMS2), MutLβ (MLH1/PMS1) and MutLγ (MLH1/MLH3) [90]. Briefly, the model for eukaryotic MMR, especially in mammals, involves the recognition of a mismatch in the DNA by MutSα or MutSβ (Figure 4). After mismatch binding, MutSα (MutSβ) is converted into a DNA sliding clamp that comes along with an exchange of ADP to ATP in the ATP-binding pocket of the complex [91, 92]. Next, MutLα associates with the sliding clamp and mediates endonucleolytic incision of the error-containing DNA strand [93]. Complete removal of the damaged strand is then carried out by Exonuclease 1 (EXO1) [84]. Finally, the resulting single-stranded (ss) DNA gap is then filled-in by a DNA polymerase such as Pol δ and sealed by ligase I [83]. It has been shown in yeast that the incision in case of a mismatch in the leading strand can be mediated by RNaseH2 cleavage of mis-incorporated ribonucleotides, providing an entry side for EXO1-mediated strand degradation [89]. The lagging strand has the advantage that synthesis in okazaki fragments provides 5’ ends required for EXO1 function, as long as strand maturation is not completed and does therefore not necessarily need an incision for MMR to proceed [89]. In *E.coli,* the excision step is assisted by the UvrD helicase that unwinds the DNA until the mismatch is reached, the resulting ssDNA is then cleaved by an exonuclease (RecJ or Exo1)[94]. In human cells the identity of the helicase that mediates this step is unknown, but a recent study suggests that MCM9 performs the DNA unwinding reaction for subsequent degradation by EXO1 [95].

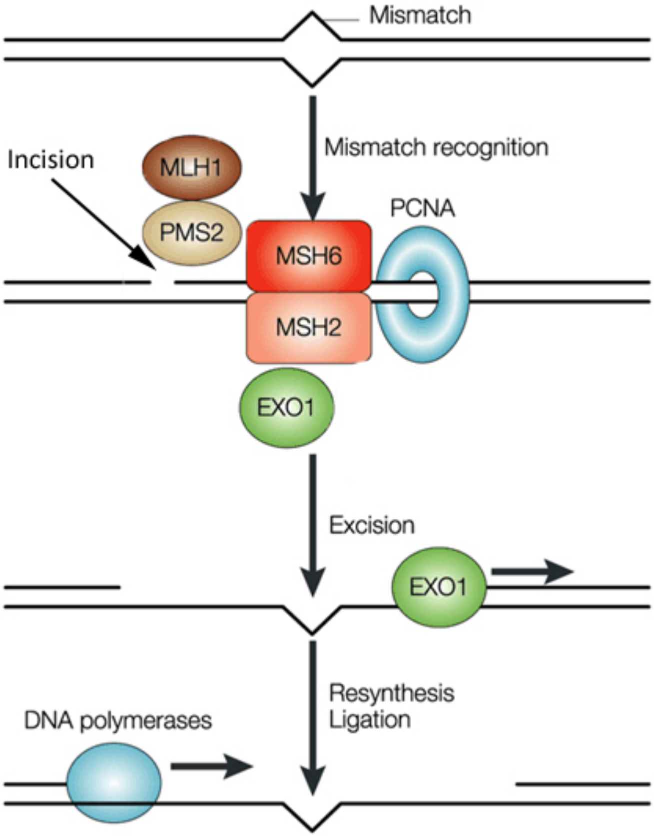

Figure 4: The mismatch repair system. Mismatch recognition in mammalian cells is mediated by either MutSα (composed of MSH2 and MSH6) or MutSβ (composed of MSH2 and MSH3). Depicted here is repair initiation trough MutSα that is converted into a sliding clamp upon binding to a mismatch. In the next step, MutLα gets recruited and performs incision of the error-containing strand providing an entry site for EXO1. After excision of the error-containing strand by EXO1, a DNA polymerase carries out DNA resynthesis. To complete the repair pathway, Ligase I restores continuity of the DNA strand. Adapted and modified from [96].

3.2.3. Base excision repair

If oxidative damage, alkylation agents, deamination or depurination/depyrimidation affects a single base, the base excision repair (BER) pathway is activated to replace the damaged base with an intact one (Figure 5) [44, 97-100]. About 10^4 bases in every cell per day are hit solely by spontaneous depurination making BER important to maintain genomic integrity, which is underlined by the fact that this repair system is highly conserved between *E. coli* and mammals [101, 102]. Todays mechanistic model of BER divides it into two distinct pathways, the short and the long-patch BER [103] (Figure 5). The first one results in the repair of a single nucleotide while the latter exchanges at least two nucleotides [97]. To initiate short-patch BER, a specific DNA glycosylase recognises a damaged base and removes it by cleaving the N-glycosidic bond leaving behind an apurinic or apyrimidinic site (AP site)[97, 104]. Subsequently, an AP endonuclease 1(APE1) cuts the DNA backbone 5' of the AP site [105]. Then the polymerase β fills in the corresponding nucleotide [106, 107]. Ultimately, the sealing of the remaining nick is carried out by DNA Ligase III/XRCC1. Long-patch BER has an identical initiation step like the short-patch repair, however after APE1 cleavage, Pol δ or ε, PCNA, FEN1 and ligase I are recruited to the damage site [97]. By using its strand displacement activity, the polymerase inserts new nucleotides and generates a 5' flap that requires FEN1 cleavage for proper repair [108, 109].

Extremely similar to BER is the pathway of DNA SSB repair, however the recognition of the lesion is mediated by enzymes of the Poly(ADP-ribose) polymerase (PARP) family, primarily PARP1 [110, 111].

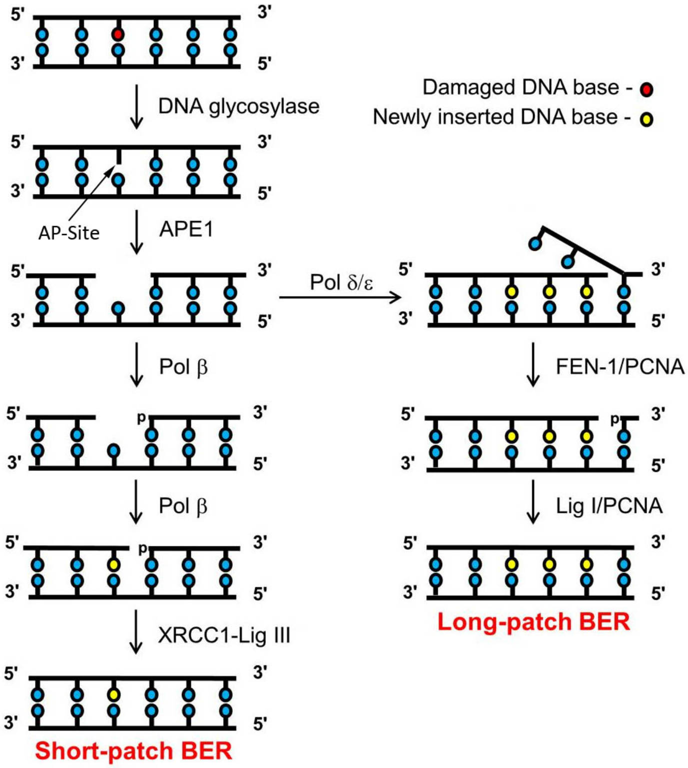

Figure 5: Mechanism of base excision repair. One of several specialised DNA glycosylases cleaves the N-glycosidic bond generating an AP-site. Subsequently, an AP endonuclease (APE1) cuts the DNA backbone 5' of the AP site. The resulting gap is then filled with a new nucleotide by polymerase β. In the final step the Ligase III/XRCC1 complex mediates religation of the DNA. Although the long-patch BER has an identical initiation step, different factors are recruited after APE1 cleavage to complete DNA repair. Trough its strand displacement activity Pol δ or ε resynthesizes the DNA producing a 5' flap that is cleaved by FEN1/PCNA and genomic integrity is restored by Ligase I/PCNA. Abbreviations: BER, Base excision repair. Adapted and modified from [112].

3.2.4. Non-homologous end joining

The presence of a DNA DSB in genomic DNA is a very dangerous situation for a cell. Therefore different mechanisms have evolved in eukaryotic cells to antagonize these lesions. Non-homologous end-joining (NHEJ), being one of these mechanisms, can rapidly repair DNA DSBs (Figure 6) [113]. This repair process is initiated by the Ku heterodimer, composed of Ku70 and Ku80, that binds to the DNA ends within seconds after DNA DSB formation [114]. The underlying mechanism for this is that Ku has a high affinity for DNA end, is present at high concentrations in every cell and further, its binding to DNA does not rely on any specific sequence [115]. One of the functions of the Ku heterodimer is protecting the DNA ends from being further processed. The protein forms a ring-shaped structure that can encircle the DNA ends and serves as a platform for recruitment of further core NHEJ factors that are required for DNA DSB repair, one of them being the DNA-dependent protein kinase (DNA-PK) [115, 116]. DNA-PKcs, which is the catalytic subunit of this serine/threonine kinase, gets activated upon interaction with DNA-bound Ku complex that itself slides a bit further on the dsDNA [117-119]. It has been suggested that Ku is important to bridge the two DNA ends and hold them in close proximity to each other [120]. This process potentially also involves other factors like DNA-PKcs [115]. Next, DNA end processing may be required since a DNA DSB induced by distinct DNA damaging agents can result in DNA ends that are not ligatable. Such end-blocking obstacles are for instance chemical adducts or the absence of 5’ phosphate or 3’ hydroxyl groups at the DNA termini. Therefore, various proteins may be required to make the ends permissive for repair. Not only nucleases like Artemis, WRN or APLF, but also polymerases have been shown to act during this step of NHEJ [121, 122]. Finally, the DNA Ligase IV/XRCC4/XLF complex seals together the DNA ends to restore genomic integrity. In this reaction, XRCC4 might also serve as a scaffold for the recruitment of additional NHEJ proteins, however it also stimulates the Ligase IV activity [115, 123]. In addition, studies have revealed that XLF not only has a stimulatory effect on the Ligase IV/XRCC4 complex, but it might also play a role in the regulation of NHEJ [124, 125]. Repair of a DNA DSB via the NHEJ pathway is not restricted to a particular cell cycle phase, however it is error-prone because of the end-processing step and contributes to genomic instability trough chromosomal translocations and deletions [126].

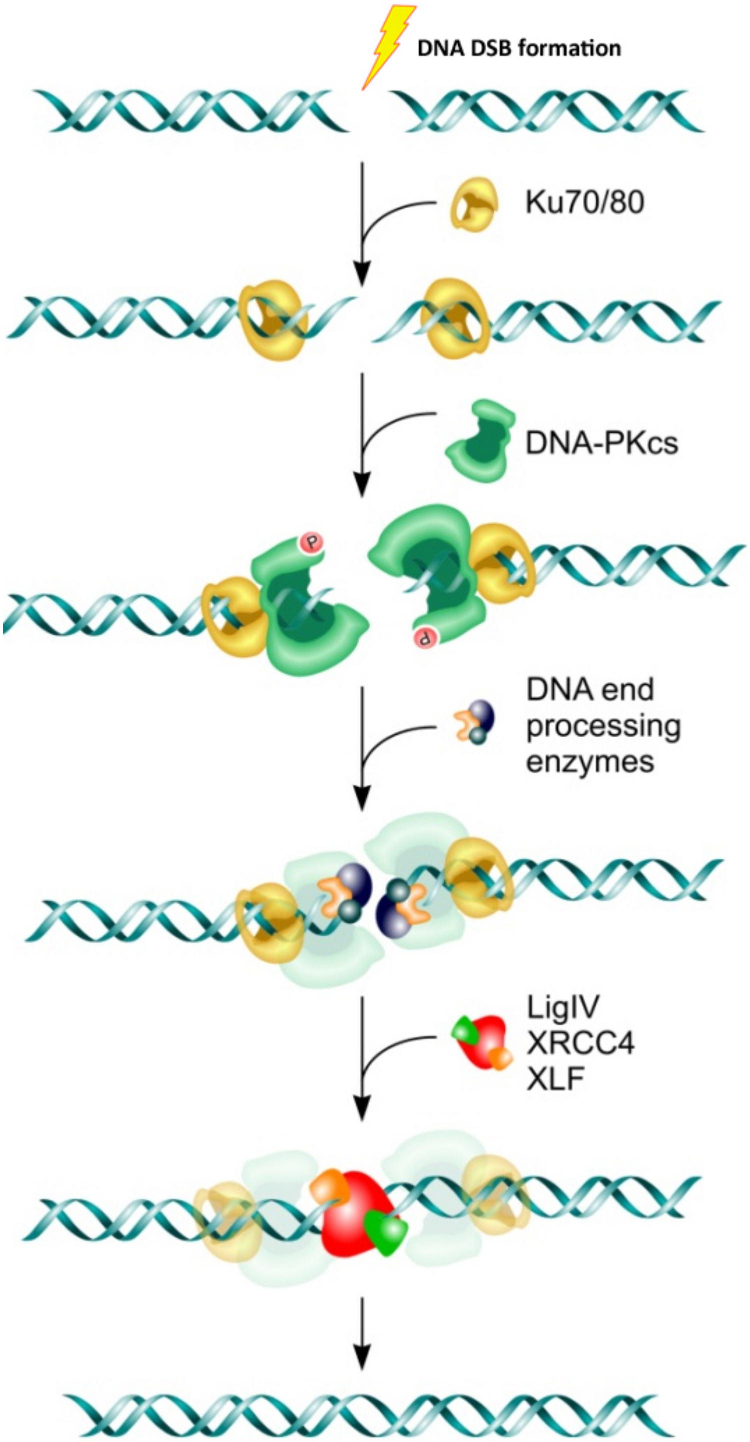

Figure 6: Repair of DNA double strand breaks by non-homologous end joining. Rapid binding of the Ku70/80 complex to DNA ends of a DNA DSB is followed by recruitment of the DNA-dependent protein kinase to the damage site. The next step includes processing of the DNA ends to make them compatible for further repair. Several nucleases and DNA polymerases have been shown to act at this step. The DNA Ligase IV/XRCC4/XLF complex then mediates religation of the broken DNA end. Abbreviations: DNA DSB, DNA double-strand break. Adapted and modified from [127].

There is another, but less well characterized, NHEJ pathway present in cells that is Ku-independent. This pathway is termed alternative end-joining or microhomology-mediated end-joining (MMEJ) and relies on the presence of 5-25nt long homologous sequences flanking the break site that are annealed to each other during the process, and therefore, it always results in a deletion [43, 128].

To maintain genomic stability, cells can counteract DNA DSBs via the homologous recombination pathway that provides faithful repair. This mechanism will be discussed in the next chapter.

3.3. Homologous recombination

Homologous recombination (HR) is a critical pathway to maintain genomic integrity and acts not only in mitotic cells, but also during meiosis where it mediates repair of DNA DSBs that are purposely generated by Spo11 [61, 126]. HR is therefore involved in the crossover formation during meiosis I that is important for alignment of the homologous chromosomes and their subsequent segregation [129]. In addition, this repair pathway is responsible to generate genetic diversity [130]. Furthermore, HR also plays roles in recovery of stalled and broken replication forks and, most importantly, in restoration of genomic integrity upon formation of DNA DSBs and interstrand crosslinks [131]. In contrast to end-joining pathways, HR provides a more accurate repair mechanism, however this goes at the cost of flexibility. The requirement of a homologous sequence present on the sister chromatid, restricts HR to S and G_2 phases of the cell cycle [43].

First knowledge of the mechanism of HR was gained from studies in yeast. Although there are fewer factors involved in yeast HR as compared to HR in higher eukaryotes, and the model has been updated during the past, the principle remains the same. Mechanistically, HR can be divided into several steps: (i) nucleolytic resection of the DNA DSB ends; (ii) formation of a nucleoprotein filament; (iii) homology search and strand invasion; (iv) DNA repair synthesis; and (v) resolution of recombination intermediates via different sub-pathways (Figure 7) [131, 132].

After initiation of HR by DNA damage like a DNA DSB, the DNA ends are first processed to generate 3’ ssDNA overhangs. From studies in yeast it is known that four nucleases participate in this first step: the Mre11-Rad50-Xrs2 (MRX) complex [Mre11-RAD50-NBS1 (MRN) in humans], Exonuclease 1 (Exo1) (EXO1 in humans), DNA replication helicase/nuclease 2 (Dna2) (DNA2 in humans) and Sae2 (CtIP in humans) (Figure 7). The ssDNA generated in the DNA-end resection process is covered by the ssDNA-binding replication protein A (RPA) [133, 134]. Binding of RPA to ssDNA prevents the formation of secondary structures, which is crucial for subsequent loading of the Rad51 recombinase that performs homology search and strand invasion [135]. Although RPA is extremely important for proper formation of Rad51 filaments, it presents a kinetic barrier to this process and has to be removed prior to Rad51 loading. Therefore, mediator proteins, divided into three different sub-classes, are assisting in this process to overcome this obstacle and assist in further downstream steps [130, 136]. The first class of these effectors in *S.cerevisiae* comprises of the Rad51 paralogs known as the Rad55-Rad57 complex and heterodimers of the Shu proteins (Shu1, Shu2, Psy3, and Csm2) [130, 137]. In mammalian cells, five RAD51 paralogues were identified so far, which form two distinct protein complexes (RAD51B-RAD51C-RAD51D-XRCC2 and RAD51C-XRCC3). Studies in yeast have shown that these proteins might be involved in the stabilisation of the nucleoprotein filament [138]. Moreover, studies done in *C. elegans* provided evidence that the Rad51 paralogs actively contribute to Rad51 filament remodelling, thereby promoting strand exchange and HR [139]. Rad52, represents the second class of mediators that interacts physically with Rad51 and RPA promoting the formation of a Rad51 nucleoprotein filament [137]. The third mediator class is composed of the human BRCA2 protein that is not present in yeast. BRCA2 interacts directly with RAD51 and recruits it to the RPA-coated ssDNA at the DNA DSB site [130, 140].

In the next step of HR, the Rad51-ssDNA-filament performs homology search on an appropriate DNA template like the sister chromatid. Subsequent strand invasion is then completed with the formation of a displacement loop (D-loop) (Figure 7). Afterwards distinct polymerases use the invading strand as a primer to start DNA synthesis. In humans it is known that also translesion polymerases can mediate this DNA extension step in addition to the replicative polymerase δ. A key player within this process is the Rad54 motor protein. It stabilises the Rad51 nucleoprotein filament and promotes D-loop formation. Eventually, Rad54 disrupts the Rad51 filament to allow initiation of DNA synthesis [130, 131, 141, 142].

To complete HR, one out of three possible sub-pathways can be followed (Figure 7). These are called: (i) break-induced replication (BIR); (ii) synthesis-dependent strand annealing (SDSA); and (iii) the classical DNA DSB repair (DSBR). The latter pathway involves the formation of a double Holliday junction structure (dHJ) [130]. BIR takes place when a DNA DSB has only one accessible end as in the case of collapsed replication forks or unprotected telomeres [143]. This repair pathway converts the D-loop into a replication fork-like structure and DNA synthesis is then carried out until the chromosome end is reached, leading to a restoration of the genomic integrity. However, loss-of-heterozygosity (LOH) and genomic duplications are potential outcomes of this reaction [143, 144]. If a second DNA end is present, somatic cells majorly follow the SDSA pathway [145]. In this reaction, the D-loop is dismantled after DNA synthesis and the newly formed DNA strand anneals back to the ssDNA-overhang of the second end [130]. The result of this process is a non-crossover product that limits the risk of genomic rearrangements [146]. A dHJ is created when the second end of the DNA DSB is captured to the D-loop (Figure 7). Depending on the proteins involved in its processing, the result is either a non-crossover or a crossover outcome. For the latter, it has been shown that in human cells the SLX1-SLX4 and MUS81-EME1 protein complexes and the Gen1 resolvase are involved that all display distinct endonuclease activities [147-149]. On the other hand, the Sgs1 (BLM in humans)-DNA Topoisomerase 3 (Top3)-Rmi1 (STR) complex mediates the dissolution of dHJ where non-crossovers are produced [130]. This mechanism involves the migration of the two junctions towards each other and a final cleavage by Top3 [130]. Another homology-dependent repair pathway that can take place if the break site is flanked by sequence repeats is called single-strand annealing (SSA) (Figure 7). In this process, the initial end resection step is followed by the annealing of the repeat sequences. Finally, structure specific nucleases cleave off the incompatible ssDNA flaps before a ligase restores DNA strand continuity. SSA always results in a deletion of one repeat and the sequence in between the repeats. Further, SSA does not require the presence of a template DNA to perform strand invasion to proceed with repair and is therefore not limited to distinct cell cycle phases. In addition, since Rad51 filament formation is not part of this mechanism it is Rad51 independent [132, 137].

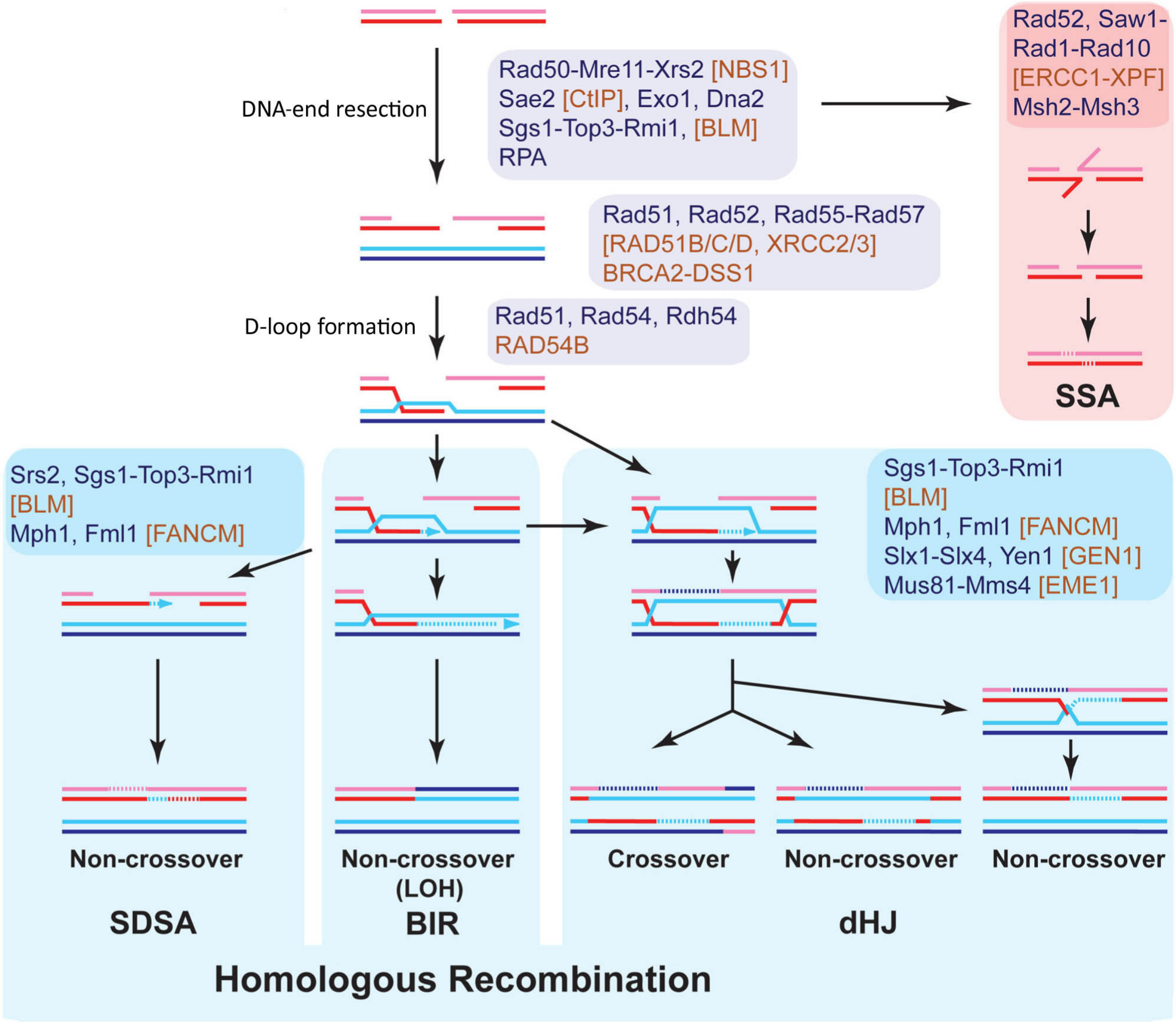

Figure 7: Repair of DNA double-strand break by homologous recombination. The first step of HR is called DNA-end resection and leads to the generation of 3’ ssDNA overhangs that are then coated by RPA. Four nucleases are known to be involved in this process: the Mre11-Rad50-Xrs2 complex, Exo1, Dna2 and Sae2. Mediator proteins like the Rad51 paralogs or BRCA2 then load the Rad51 recombinase on the RPA-coated ssDNA, thereby removing RPA from the DNA, and stabilise the nucleoprotein filament that subsequently performs homology search on the sister chromatid or homologous chromosome. This process ends up in the generation of a displacement loop, which represents a branching point between several possible downstream HR sub-pathways known as break-induced replication, synthesis-dependent strand annealing and the classical DNA DSB repair that proceeds via double Holliday junction formation. Every sub-pathway leads to a specific repair product with crossover or non-crossover outcome. The presence of repeats adjacent to the break site allows repair trough single-strand annealing pathway after extensive DNA-end resection. Proteins from *S.cerevisiae* and humans are written in blue and brown colour, respectively. Broken lines refer to newly synthesised DNA. Abbreviations: SSA, single-strand annealing; SDSA, synthesis-dependent strand annealing; BIR, break-induced replication; dHJ, double holliday junction; LOH, loss-of-heterozygosity. Adapted and modified from [130].

3.3.1. DNA-end resection in eukaryotes

Processing of DNA ends after DSB formation is essential for HR to proceed. The 5’ terminated strands undergo nucleolytic degradation to form 3’ ssDNA overhangs that are required for the formation of Rad51 nucleoprotein filaments. From studies in *S. cerevisiae*, it is known that two distinct pathways are capable of mediating rapid and extensive resection of DNA DSBs. One pathway is constituted by the 5′ to 3′ dsDNA exonuclease Exo1, while the other is composed of the nuclease/helicase Dna2 that works in conjunction with the 3′ to 5′ RecQ-type helicase Sgs1 [134, 150-156]. DNA-end resection is a two-step process where the ends are first processed by MRX in complex with Sae2 to generate a short ssDNA tail of about 50-100nt [134]. Next, one of the two above-mentioned pathways can take over to mediate long-range resection [134, 155, 156]. However, the initiation step mediated by MRX/Sae2 seems to be dispensable for extensive 5′ to 3′ strand degradation if the DSB ends are accessible for Exo1 or Dna2/Sgs1 [155]. In the presence of end-blocking obstacles, Sae2 has been shown to induce a latent endonuclease activity of MRX that specifically incises the 5′ terminated strand downstream of the DNA end, creating an entry site for Exo1 and/or Dna2/Sgs1 [157].

Several studies have shown that also RPA is crucial for DNA-end resection since it stimulates the unwinding activity of Sgs1 [158]. Further, RPA directs Dna2-mediated degradation of DNA towards the 5′ terminated strand and protects the 3′ strand since Dna2 is only able to displace RPA from the 5′ strand [158-160]. In addition, the Top3-Rmi1 complex that is involved in dHJ dissolution has been shown to have stimulatory effect on Sgs1/Dna2-mediated resection by enhancing the unwinding activity of Sgs1 [158]. Taken together, these data suggest that MRX/Sae2 display a first, limited end-processing activity and recruit further downstream factors including Sgs1, Dna2, RPA, Top3 and Rmi1 that further extend the 3′ ssDNA overhang.

Comparison of the resection machineries from yeast and *Xenopus* species shows that they are highly conserved. Consistent with this, work done in *Xenopus* egg extracts showed that xDNA2 is the major nuclease involved in DNA-end resection and depletion of xDNA2 impairs not only DNA end processing but also DNA DSB repair by SSA [161]. In addition, it has been demonstrated that the homologue of the human Werner syndrome (WS) protein in *Xenopus* (xWRN), which is also a RecQ-type helicase like the yeast Sgs1, acts in concert with xDNA2 to promote extensive DNA-end resection [162, 163]. Related to yeast RPA, xRPA interacts with xWRN directly and stimulates its helicase activity thereby enhancing the DNA end processing reaction mediated by xDNA2/xWRN [164]. Although the MRN complex was able to stimulate both long-range resection pathways, which is in line with the yeast data, depletion of Mre11 or CtIP (Sae2 in yeast) in *Xenopus* egg extracts abolished DNA-end resection almost completely [165]. Since the DNA end processing machineries in yeast and

Xenopus are extremely related, it is highly likely that this system is conserved trough evolution up to mammals.

In mammals, the RecQ helicase family consists of five members, called RECQL1, BLM, WRN, RECQL4 and RECQL5 [121]. Although it is well known that BLM participates in the dHj-dissolution pathway of HR and is able to unwind D-loops as well as G4-quandruplex structures, it has been observed that BLM displays a rapid localization to DNA-damage sites, implying that it plays an early role in DDR [166, 167]. In line with this observation, a recent study has shown that DNA2 and BLM form a complex and, in the presence of RPA, are able to mediate 5’ to 3’ DNA end processing, which is stimulated by addition of MRN to the reaction [168]. Interestingly, also nucleolytic degradation by EXO1 could be augmented by MRN, RPA and BLM [168]. Although also extensively studied, a role for the WRN helicase in DNA DSB-end processing has not been investigated so far. Data from work done in *Xenopus* egg extracts imply that WRN could also stimulate DNA2-mediated DNA-end resection in mammalian cells. Therefore, one of the goals of this PhD study is to test this hypothesis.

3.4. DNA-damage signalling

The distinct DNA damage repair pathways involve action of a huge variety of proteins whose activities have to be coordinated both spatially and temporally. Deregulated enzymatic activity within repair processes can have devastating outcome not only to the cell itself but also to the whole organism in case of cell transformation into a cancer cell. In the following section the signalling cascades of the DDR are discussed with a special focus on the processes arising upon DNA DSB induction in mammalian cells to promote repair trough the HR pathway.

Two key players of the DDR machinery are called ataxia telangiectasia mutated (ATM) and ataxia telangiectasia mutated and rad3-related (ATR). These two protein kinases, as well as DNA-PK, belong to the phosphatidylinositol 3-kinase like protein kinase (PIKK) family. In addition, the PARP proteins, of which 17 are known in humans, are also crucial for the DDR [169-171]. Upon DNA DSB formation, PARP1 and PARP2 get activated and start the formation of poly(ADP-ribose) (PAR) chains on target proteins. These PAR chains serve as a scaffold to recruit other factors to the DNA-damage site [172]. One of these proteins is the MRN complex, which is known to interact with PAR molecules via its Mre11 subunit [171]. Association of MRN with DNA DSBs leads to the recruitment and subsequent activation of

ATM (Figure 8) [173, 174]. The PIKK kinases, especially ATM in this case, then phosphorylate the histone variant H2AX at serine 139 forming γH2AX that is widely used in the DDR field as marker of DNA damage [171, 175]. MDC1 then binds γH2AX and mediates further recruitment of ATM resulting in an amplification of the γH2AX signal that can spread approximately 1-2 megabases from the DNA DSB site [171]. Activated MDC1 then mediates an exchange from a phosphorylation to an ubiquitination signal cascade by recruiting the ubiquitin ligases RNF8 and RNF168 [176]. Linking ubiquitin moieties to target proteins leads to the recruitment of RAP80 that interacts with BRCA1 [171]. Although the BRCA1 protein has been shown to be involved in promoting HR the underlying mechanisms remain elusive. It has been demonstrated, that BRCA1 can associate with CtIP in S and G2 phases of the cell cycle where it may play a role in activation of extensive resection that is required for HR [177]. However, HR can only repair DNA DSBs if a template sequence is present. It has been shown that 53BP1, which also gets recruited to these damage sites by the described signalling cascade, inhibits resection and promotes NHEJ under certain circumstances [178, 179].

In addition to its role in the recruitment of repair factors, ATM also induces the activation of a DNA damage checkpoint trough CHK2, a serine/threonine kinase that in turn phosphorylates p53 in response to DNA DSB formation (Figure 8) [180]. Activated p53 acts as a transcription factor and can lead to cell cycle halt to provide time for proper DNA repair or if this is not successful, it can induce senescence or apoptosis [181].

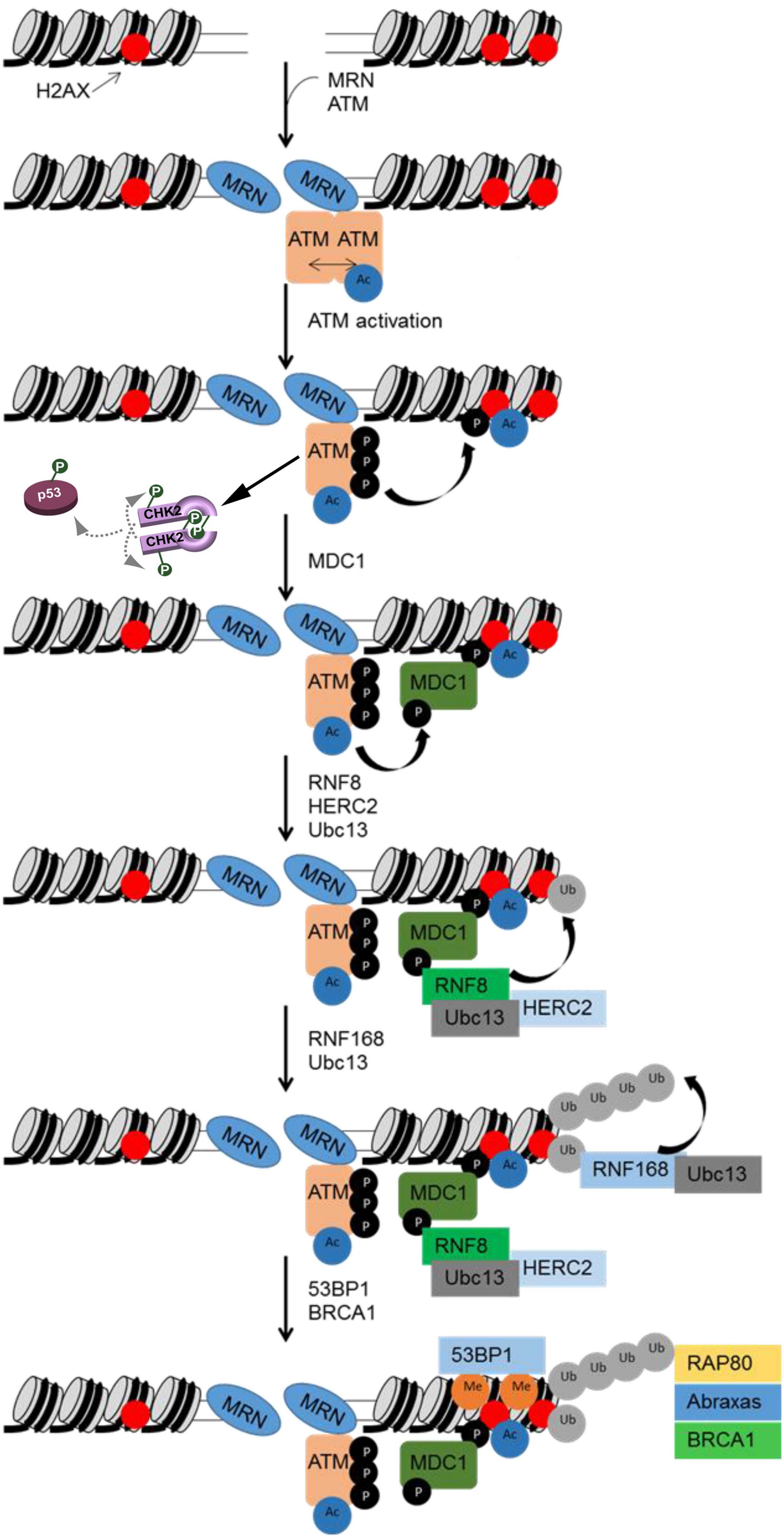

Figure 8: DNA double-strand break signalling cascade. PARP protein activation upon DNA DSB formation leads to association of repair proteins with the DNA DSB site. First proteins recruited to DNA DSB sites are the MRN complex and the ATM kinase. ATM phosphorylates the histone variant H2AX that is important for MDC1 recruitment. In addition, it also activates the checkpoint kinase CHK2, leading to a cell cycle stop to allow restoration of the DNA integrity or apoptosis trough p53. MDC1 then recruits the key ubiquitin ligases RNF8 and RNF168 that finally promote recruitment of factors that initiate homologous recombination or the non-homologous end joining pathway. Adapted and modified from [171, 182].

The activation of ATR is mediated by RPA-coated ssDNA that is generated by 5’-3’ DNA-end resection of broken DNA ends or is formed at stalled replication forks (Figure 9) [171]. ATR is recruited to RPA-ssDNA via its interacting partner ATRIP [183]. At the same time, TOPBP1 is recruited to the DNA-damage site by the RAD9-RAD1-HUS1 (9-1-1) complex that is loaded on dsDNA at the ssDNA/dsDNA junction by the RAD17-RFC clamp loader [184, 185]. TOPBP1 then activates ATR via direct interaction, which then leads to phosphorylation of the checkpoint kinase CHK1 [186-188]. Like in the case of ATM, also this signalling cascade can result in p53 activation and the consequences mentioned above [181]. In addition to CHK1, ATR phosphorylates a number of other targets including RPA itself, and this is required for proper DNA repair [189]. More recently, it has been published that ATR can be also activated in a manner dependent on the MRN complex without the use of the 9-1-1 complex. Especially the interaction between NBS1 and RPA seems to be crucial for this MRN-mediated ATR activation [190]. This suggests that there are several pathways involved in ATR activation once RPA-coated ssDNA has been formed.

DNA damage recognition and signalling is a very important process for cells and, in general, specialised proteins carry out this process. Interestingly, it has been demonstrated that some factors of the MMR system might also be involved in DNA DSB repair [191-194]. MSH2 has been shown to be important for efficient HR-mediated repair of DNA DSBs and checkpoint activation [195-197]. In addition, a recent study has shown that MutSβ seems to be important for DNA DSB repair, since cells defective for either subunit of this MMR protein display elevated levels of chromatid breaks [198]. However, the exact role of MutSβ in response to DNA DSB remains elusive. Therefore another aim of this thesis was to investigate the underlying mechanism of the action of MutSβ in DNA DSB repair.

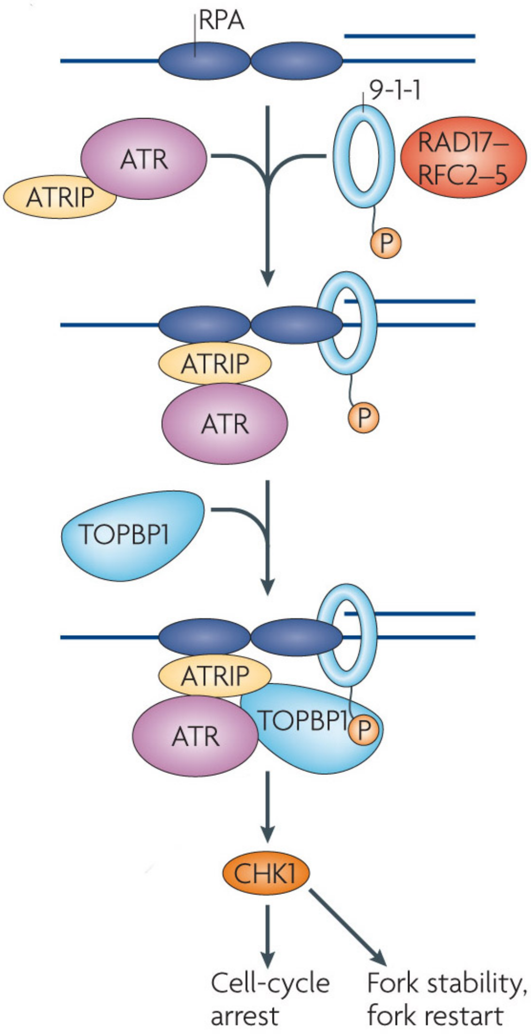

Figure 9: ATR activation in response to DNA damage. Association of ATR with RPA-coated ssDNA is mediated by ATRIP that directly interacts with RPA. In parallel, the RAD9-RAD1-HUS1 complex recruits TOPBP1 to the damage site that activates ATR. The checkpoint kinase CHK1, a downstream target of ATR, then induces cell cycle arrest. Adapted and modified from [199].

3.5. DNA double-strand break repair pathway choice

Cells have a huge arsenal of pathways that are specialized to repair certain DNA damage but not all of them might be suitable at a given scenario. Therefore, the selection of the most beneficial repair mechanism is crucial and depends on many different factors like the cell type, the cell cycle phase and the nature of DNA damage [130]. Although the presence of a homologous sequence during S and G2 phases of the cell cycle allows DNA DSB repair trough the more accurate HR pathway, it has been shown that during this cell cycle phases, NHEJ is still the predominant DNA DSBs repair pathway [200]. This might be due to the fact that HR is a relatively slow process that takes up to 7h to be completed, while genomic integrity can be restored by NHEJ in around 30 minutes [201]. In addition, HR relies on tightly controlled DNA-end resection, which is limited in G1 phase of the cell cycle [202]. The distinct DNA DSB repair pathways have their own consequences to the genomic integrity. The deleterious MMEJ and SSA mechanisms and BIR, possibly resulting in LOH, have mutagenic potential and are therefore likely to be suppressed if other systems can be applied. Therefore, in yeast and mammalian cells, it has been shown that HR mainly proceeds trough SDSA pathway in mitotic cells, since the formation of dHJs may end up in chromosomal rearrangements giving rise to genomic instability [203, 204]. *In vitro* studies demonstrated, that Rad51 actively inhibits the formation of dHJs and therefore favours repair trough SDSA, but the mechanisms underlying the regulation of HR pathway choice are still not very well defined [130, 205]. From studies in yeast, it is known that Mph1, a DNA helicase, counteracts formation of crossovers [206]. Further, another helicase called Srs2 is also able to suppress crossover products [207]. In mammalian cells, FBH1 displays the highest sequence homology to Srs2, however its role in SDSA remains elusive [208]. Other studies have demonstrated that RECQ5 is able to interact with RAD51 and, by translocating along the ssDNA, disrupts the RAD51-ssDNA filament [209-212]. Thus, one aim of this study was to define a potential role for RECQ5 in the regulation of HR sub-pathway choice.

4. Results

4.1. Summary of the results

To elucidate the role of WRN in DNA2-catalyzed DNA-end resection, we first expressed the recombinant human proteins in Sf-9 insect cells and purified them to apparent homogeneity. By using a biochemical assay based on a linearised pUC19 substrate, we found that WRN in conjunction with DNA2 can mediate 5'-3'-directed DNA-end resection in a reaction dependent on RPA and ATP. In addition, we found that WRN and DNA2 interact physically *in vitro* and *in vivo* and mapped the interaction site of DNA2 on WRN by using GST-tagged WRN fragments. We then sought to define the roles of these proteins in DNA-end resection *in vivo.* Through a chromosomally-based reporter assay for DNA DSB repair by SSA, we were able to show that WRN and BLM act epistatically with DNA2 to promote long-range resection of endonuclease-induced DNA DSBs in human cells. In addition, we obtained *in vitro* and i*n vivo* data suggesting that BLM promotes DNA-end resection as part of the BLM-TOPOIIIα-RMI1-RMI2 complex. Taken together we propose a model, where in DNA2/WRN, DNA2/BLM-TRR and EXO1 constitute the resection machineries responsible for extensive DNA-end resection (Sturzenegger *et al.,* JBC; see 2.2.1.).

Next, we identified the mismatch-binding protein MutSβ, a heterodimer of MSH2 and MSH3, as a mediator in the process of ATR activation. We showed that MSH2 and MSH3 form a complex with ATR and its regulatory partner ATRIP, and their depletion compromises the formation of ATRIP foci and phosphorylation of ATR substrates in cells responding to replication-associated DNA DSBs. By using purified MutSβ, we were able to show that it binds to hairpin loop structures persisting in RPA-ssDNA complexes and promotes ATRIP recruitment. Mutating the mismatch-binding domain of MSH3 abolished the binding of MutSβ to DNA hairpin loops and its ability to promote ATR activation by ssDNA. Interestingly, in the presence of ATP/Mg^{2+}, MutSβ dissociated from ssDNA and the ATR-ATRIP complex. These results suggest that hairpin loops form in ssDNA generated at sites of DNA damage and trigger ATR activation in a process mediated by MutSβ (Burdova et al., Mol. Cell; see 2.2.2.).

By using a chromosomally-based reporter assay, we demonstrate that RECQ5 is able to promote DNA DSB repair via SDSA pathway. Surprisingly we found that FBH1 rather seems to have an inhibitory effect on the SDSA pathway. Given the possibility that RECQ5 might disrupt abnormal RAD51 filaments that are formed after D-loop unwinding, we sought out to test this hypothesis. By using the above-mentioned SSA reporter assay, we could show that depletion of RAD51 or its loader BRCA2 lead to an increase in the efficiency of SSA-mediated DNA DSB repair, demonstrating that RAD51 filament formation suppresses SSA. In line with this observation, we showed that knockdown of RECQ5 resulted in a decrease in SSA efficiency. These results indicate that RECQ5 enhances SSA repair by removing RAD51 from ssDNA. Using purified recombinant human proteins in an *in vitro* RAD52-mediated DNA annealing assay, we were able to gain insight into the molecular mechanism of RAD51-ssDNA filament dynamics and could further strengthen our *in vivo* data. Next, we used chromatin immunoprecipitation (ChIP) to show that abundance of RAD51 near a given DNA DSB site is augmented in RECQ5-deficient cells, indicating involvement of RECQ5 in regulation of RAD51 filament formation at DNA DSBs. Furthermore, we found that RECQ5 depletion in cells lacking BLM leads to increased frequency of sister chromatid exchanges, further supporting our model that RECQ5 is involved in promoting SDSA (Paliwal *et al.*, NAR; See 2.2.3.).

In collaboration with the laboratory of Prof. Eli Rothenberg, we could demonstrate how BLM interacts with intra-strand G4 structures. By applying single-molecule FRET technique, we were able to show that the activity of BLM is substrate dependent, and highly regulated by the length of a short ssDNA piece that separates the G4 motif from double-stranded DNA. The RQC and HRDC domains of BLM cooperate during binding and unfolding of the G4 structure, where the RQC domain interaction with G4 is stabilized by HRDC binding to the short ssDNA strand. It is also demonstrated in this study that the G4 structure forms an obstacle that blocks unwinding of downstream dsDNA that could be resolved by addition of BLM and ATP, while the latter is only required for translocation of the helicase. From the results, we were able to present a model that proposes a unique role for G4 structures in modulating the activity of DNA processing enzymes (Chatterjee *et al.*, Nat Comm.; See 2.3.1)

4.2. Main results

4.2.1. DNA2 cooperates with the WRN and BLM RecQ helicases to mediate long-range DNA end resection in human cells

Andreas Sturzenegger, Kamila Burdova, Radhakrishnan Kanagaraj, Maryna Levikova, Cosimo Pinto, Petr Cejka and Pavel Janscak

This article was published in the Journal of Biological Chemistry in 2014.

In this work, I purified recombinant human wild-type WRN, helicase- and nuclease-dead WRN mutants, DNA2 and BLM from Sf-9 insect cells as well as RPA from *E. coli*. Next, I carried out all *in vitro* DNA-end resection and helicase assays. To demonstrate the interaction between WRN and DNA2, I performed binding assays with full-length proteins and GST-tagged WRN fragments. I would like to point out that a part of results shown in Figure 1 and 4 was obtained during my master thesis work.

DNA and Chromosomes:

DNA2 Cooperates with the WRN and BLM RecQ Helicases to Mediate Long-range DNA End Resection in Human Cells

Andreas Sturzenegger, Kamila Burdova, Radhakrishnan Kanagaraj, Maryna Levikova, Cosimo Pinto, Petr Cejka and Pavel Janscak

J. Biol. Chem. 2014, 289:27314-27326.
doi: 10.1074/jbc.M114.578823 originally published online August 13, 2014

THE JOURNAL OF BIOLOGICAL CHEMISTRY VOL. 289, NO. 39, pp. 27314–27326, September 26, 2014
© 2014 by The American Society for Biochemistry and Molecular Biology, Inc. Published in the U.S.A.

DNA2 Cooperates with the WRN and BLM RecQ Helicases to Mediate Long-range DNA End Resection in Human Cells*

Received for publication, May 3, 2014, and in revised form, August 12, 2014 Published, JBC Papers in Press, August 13, 2014, DOI 10.1074/jbc.M114.578823

Andreas Sturzenegger[‡1], **Kamila Burdova**[§1], **Radhakrishnan Kanagaraj**[‡2], **Maryna Levikova**[‡], **Cosimo Pinto**[‡], **Petr Cejka**[‡], **and Pavel Janscak**[‡§3]
From the [‡]*Institute of Molecular Cancer Research, University of Zurich, 8057 Zurich, Switzerland and the* [§]*Institute of Molecular Genetics, Academy of Sciences of the Czech Republic, 14300 Prague, Czech Republic*

Background: DNA end resection is a critical step in the homology-directed repair of DNA double strand breaks (DSBs).
Results: Human WRN helicase stimulates the DNA2-catalyzed resection of DNA ends and acts in concert with DNA2 to promote DSB repair by single strand annealing.
Conclusion: DNA2 cooperates with WRN or BLM to mediate the resection of DSBs in mammalian cells.
Significance: Defects in DNA end resection might, in part, account for the genomic instability phenotype of Werner syndrome.

The 5′-3′ resection of DNA ends is a prerequisite for the repair of DNA double strand breaks by homologous recombination, microhomology-mediated end joining, and single strand annealing. Recent studies in yeast have shown that, following initial DNA end processing by the Mre11-Rad50-Xrs2 complex and Sae2, the extension of resection tracts is mediated either by exonuclease 1 or by combined activities of the RecQ family DNA helicase Sgs1 and the helicase/endonuclease Dna2. Although human DNA2 has been shown to cooperate with the BLM helicase to catalyze the resection of DNA ends, it remains a matter of debate whether another human RecQ helicase, WRN, can substitute for BLM in DNA2-catalyzed resection. Here we present evidence that WRN and BLM act epistatically with DNA2 to promote the long-range resection of double strand break ends in human cells. Our biochemical experiments show that WRN and DNA2 interact physically and coordinate their enzymatic activities to mediate 5′-3′ DNA end resection in a reaction dependent on RPA. In addition, we present *in vitro* and *in vivo* data suggesting that BLM promotes DNA end resection as part of the BLM-TOPOIIIα-RMI1-RMI2 complex. Our study provides new mechanistic insights into the process of DNA end resection in mammalian cells.

DNA double strand breaks (DSBs)[4] are a very dangerous form of DNA damage because they can cause cell death or chromosomal rearrangements, a hallmark of cancer (1). DSBs can occur accidentally during normal cellular metabolism or upon exposure of cells to exogenous agents such as ionizing radiation and radiomimetic drugs (2). There are also programmed DSBs that drive recombination events essential for physiological processes, such as meiosis and lymphocyte development (3, 4). In eukaryotic cells, DSBs are repaired by one of two major pathways: non-homologous end joining (NHEJ) and homologous recombination (HR). NHEJ involves religation of the broken DNA ends and is frequently associated with a short deletion or insertion of DNA at the break site (5). In contrast, HR restores the DNA integrity accurately because it uses sister chromatids or homologous chromosomes as a template for repair (6, 7). HR is initiated by resection of the broken DNA ends to generate 3′ single-stranded (ss) DNA tails that are utilized by the RAD51 recombinase for a homology search on the donor DNA molecule (6, 7). Genetic and biochemical studies in budding yeast have shown that broken DNA ends are resected in a two-step process (8–10). DNA end resection in yeast is initiated by the Mre11-Rad50-Xrs2 complex in conjunction with Sae2 (8, 9, 11). These proteins may initiate resection of the 5′ strand of the broken DNA to remove a stretch of about 100–200 nucleotides from the DNA end (8, 9, 11). The Mre11-Rad50-Xrs2 complex also recruits the components of the long-range resection pathways Exo1 or Dna2-Sgs1 (8–10, 12, 13). Exo1 is a dsDNA-dependent 5′-3′ exonuclease that preferentially degrades DNA substrates with a 3′ ssDNA tail in a reaction stimulated by the ssDNA-binding protein RPA (13). Dna2 is a ssDNA-specific nuclease and a DNA helicase that functions in conjunction with the RecQ family DNA helicase Sgs1 and RPA to catalyze long-range DNA end resection (10, 14). In this reaction, RPA stimulates DNA unwinding by Sgs1 and promotes degradation of the 5′-terminated strand by Dna2 while protecting the growing 3′ ssDNA tail (10). DNA end resection is also the initial step in two other DSB repair pathways, single strand annealing (SSA) and microhomology-mediated end joining (8, 15).

The molecular machinery of DNA end resection appears to be largely conserved between yeast and man (15–19). However, it remains a matter of debate which DNA helicase mediates DNA2-catalyzed resection in mammalian cells. Mammals pos-

---

* This work was supported by Swiss National Science Foundation Grants 31003A-129747 and 31003A_146206, by Czech Science Foundation Grant GAP305/10/0281, and by the Stiftung zur Krebsbekämpfung. This work was also supported by Swiss National Science Foundation Grant PP00P3 133636 (to P.C.) and by Forschungskredit of the University of Zurich Grant FK-13-098 (to A. S.).

[1] Both authors contributed equally to this work.

[2] Present address: London Research Institute, Cancer Research UK, Clare Hall Laboratories, South Mimms, Herts, EN6 3LD, UK.

[3] To whom correspondence should be addressed: Institute of Molecular Cancer Research, University of Zurich, Winterthurerstr. 190, 8057 Zurich, Switzerland. Tel.: 41-44-6353470; Fax: 41-44-6353484; E-mail: pjanscak@imcr.uzh.ch.

[4] The abbreviations used are: DSB, double strand break; NHEJ, non-homologous end joining; HR, homologous recombination; ssDNA, single-stranded DNA; SSA, single strand annealing; BTRR, BLM-TOPOIIIα-RMI1-RMI2; nt, nucleotide(s); CPT, camptothecin.

sess five RecQ homologues: RECQ1, BLM, WRN, RECQ4, and RECQ5 (20). Biochemical studies have shown that human DNA2 can act in conjunction with the BLM helicase and RPA to mediate 5′-3′ resection of DNA ends *in vitro* (17). In agreement with these findings, it has been observed that cells depleted of both BLM and EXO1 show a reduction in the formation of RPA foci in response to DSBs and are defective in DSB repair by HR (16, 19). However, studies using *Xenopus* egg extracts and purified proteins have shown that Dna2 mediates DNA end resection together with WRN rather than BLM (21–23). This discrepancy prompted us to investigate the role of WRN in DNA end resection in human cells. Here we demonstrate that WRN helicase is capable of acting in concert with DNA2 and RPA to resect 5′-recessed DNA ends *in vitro* with a catalytic efficiency even higher than that of BLM. Moreover, our results show that human cells may employ either BLM or WRN to assist DNA2 in long-range DNA end resection. Finally, we present data suggesting that BLM acts in DNA end resection as part of the BLM-TOPOIIIα-RMI1-RMI2 (BTRR) complex.

EXPERIMENTAL PROCEDURES

Antibodies and siRNA—Primary antibodies used for immunoblotting were as follows: mouse monoclonal anti-WRN (BD Biosciences, catalog no. 611169), rabbit polyclonal anti-DNA2 (Abcam, catalog no. ab96488), rabbit polyclonal anti-BLM (Abcam, catalog no. ab476), rabbit polyclonal anti-TFIIH (Santa Cruz Biotechnology, catalog no. sc293), mouse monoclonal anti-FLAG (Sigma, catalog no. F1804), and rabbit polyclonal anti-RMI1 (Proteintech, catalog no. 14630-1-AP). Anti-FLAG M2 magnetic beads (Sigma) were used for immunoprecipitation. Primary antibodies used for immunofluorescence staining were as follows: mouse monoclonal anti-RPA2 (Abcam, catalog no. ab2175) and rabbit monoclonal anti-γ-H2AX (Cell Signaling Technology, catalog no. 9718S). Rabbit polyclonal anti-WRN antibody used for immunoprecipitation has been described previously (24).

All siRNA oligoduplexes used in this study were purchased from Microsynth. The sequences of the sense strands of these duplexes were as follows: siLuc, 5′-CGUACGCGGAAUACUUCGAdTdT-3′; siWRN, 5′-UAGAGGGAAACUUGGCAAAdTdT-3′; siBLM, 5′-CCGAAUCUCAAUGUACAUAGAdTdT-3′; siDNA2, 5′-UACCGCUUAAAUCUAAGUCAAdTdT-3′; siEXO1, 5′-CAGCCAUUCUUACUACGCUAAdTdT-3′; siMRE11, 5′-GAGCAUAACUCCAUAAGUAdTdT-3′ (25); siCtIP, 5′-UCCACAACAUAAUCCUAAUdTdT-3′ (26); and siRMI1, 5′-AGCCUUCACGAAUGUUGAUdTdT-3′ (27).

Plasmid Constructions—The human DNA2 (hDNA2) ORF was amplified by PCR without the initiation and stop codons to generate a fragment including ggatcc-hDNA2-ctcgag. After digestion with BamHI and XhoI, the hDNA2 fragment was cloned into pFLAG-CMV2 (Sigma) digested with BglII/SalI (pFLAG-CMV2-hDNA2). The human WRN (hWRN) ORF was inserted into pcDNA3.1/Hygro(−) (Invitrogen) via the NheI and DraI sites (pcDNA3.1-hWRN). The siRNA-resistant form of this construct was generated by changing four nucleotides in the siWRN-targeting region (T270C, A273G, G276C, and A279G) using the QuikChange site-directed mutagenesis kit (Stratagene).

Protein Purifications—Wild-type and mutant forms of WRN, BLM, EXO1, and RPA were produced and purified as described previously (28–31). The TOPOIIIα-RMI1-RMI2 (TRR) complex was a gift from Drs. Kata Sarlos and Ian Hickson (University of Copenhagen, Denmark). DNA2 was produced as a fusion with a His$_6$ tag (N terminus) and a FLAG tag (C terminus) in Sf9 cells using the Bac-to-Bac baculovirus expression system (Invitrogen). The transfer vector for bacmid preparation was a gift from Dr. Judith L. Campbell (32). The transfer vectors for nuclease-deficient (D227A) and helicase-deficient (K654R) mutants of DNA2 were generated using the QuikChange site-directed mutagenesis kit (Stratagene). Sf9 cells expressing DNA2 fusion proteins were harvested 52 h after infection (typically a 800-ml culture) and washed with PBS. All subsequent steps were carried out at 4 °C. Pelleted cells were resuspended in lysis buffer (25 mM Tris-HCl (pH 7.5), 2 mM β-mercaptoethanol, 1× complete EDTA-free protease inhibitor (Roche), 1 mM phenylmethylsulfonyl fluoride, 30 μg/ml leupeptin, and 15 mM imidazole) and incubated for 20 min under continuous stirring. Subsequently, glycerol and 5 M NaCl were added slowly to final concentrations of 15% (v/v) and 300 mM, respectively, while mixing the sample. The cell suspension was then incubated for an additional 30 min under continuous stirring. The cell lysate was centrifuged at 55,000 × *g* for 30 min to obtain soluble extract, which was then incubated with 5 ml of nickel-nitrilotriacetic acid-agarose beads (Qiagen) for 1 h batchwise. The resin was washed extensively with lysis buffer containing 10% (v/v) glycerol and 1 M NaCl. The protein was eluted with lysis buffer supplemented with 10% (v/v) glycerol, 100 mM NaCl, and 250 mM imidazole. Fractions containing detectable amounts of protein, as measured by Bradford assay, were pooled, diluted 1:1 with TBS buffer (50 mM Tris-HCl (pH 7.5) and 150 mM NaCl) and incubated batchwise with 1 ml of anti-FLAG M2 affinity resin (Sigma) for 30 min. The resin was then transferred to a gravity flow column and washed with TBS-PI buffer (TBS buffer containing 1 mM β-mercaptoethanol and 5 μg/ml leupeptin). Elution of the protein was achieved by adding TBS-PI buffer supplemented with 200 μg/ml 3× FLAG peptide (Sigma). Fractions containing DNA2 were pooled, diluted with 0.5 volumes of water and 1 volume of AQ buffer (25 mM Tris-HCl (pH 7.5), 100 mM NaCl, 10% (v/v) glycerol, and 5 mM β-mercaptoethanol) and loaded onto a 1-ml HiTrap Q column (GE Healthcare) pre-equilibrated with AQ buffer. The column was washed with AQ buffer and DNA2 was eluted by AQ buffer supplemented with 600 mM NaCl. Fractions containing DNA2 were identified by SDS-PAGE, pooled, and stored at −80 °C. The activity of purified recombinant DNA2 proteins was tested using a Y structure oligonucleotide duplex with single-stranded arms (10). In agreement with previous reports, wild-type DNA2 was found to be capable of degrading both ssDNA arms of this structure (data not shown) (10, 17). In the presence of RPA, the cleavage of the 3′ ssDNA arm by DNA2 was inhibited, and DNA2 degraded preferentially the 5′ ssDNA arm (data not shown) (10, 17). The DNA2-D227A mutant did not contain any nuclease activity, which indicated that the nuclease activity of our wild-type DNA2 preparation was inherent to DNA2 (data not shown).

Nuclease and Helicase Assays—To test the activity of purified DNA2, we used a 31-bp forked duplex with 19-nt ssDNA arms, as described previously (10). The helicase activity of WRN and BLM was tested using a 29-bp forked duplex generated by annealing of the following oligonucleotides: f-9 (5′-ACTATCATTC AGTCATGTAA CCTAGTCAAT CTGCGAGCTC GAATTCACTG GAGTGACCT-3′) and f-10 (5′-GAGGTCACTC CAGTGAATTC GAGCTCGCAG TCAATGTCGA CATACCTAGT ACTTTACTCC-3′). Both DNA substrates were radiolabeled at the end of the 5′ ssDNA arm.

Nuclease and helicase assays were performed in buffer containing 25 mM Tris acetate (pH 7.5), 2 mM magnesium acetate, 1 mM dithiothreitol, 0.1 mg/ml BSA, 10.7 mM phosphocreatine, and 0.02 mg/ml creatine phosphokinase. Reactions (15 μl) contained 1 nM ^{32}P-labeled forked DNA substrate and the indicated concentrations of DNA2 or WRN/BLM. Where indicated, RPA was present at a concentration of 6 nM. Reactions were assembled on ice and started by addition of ATP to a concentration of 1 mM. Reactions were incubated for 30 min at 37 °C. Termination of the reactions was achieved by adding 1/3 volume of stop solution (150 mM EDTA, 2% (w/v) SDS, 30% (v/v) glycerol, and 0.1% (w/v) bromphenol blue) and 1/15 volume of Proteinase K (10 mg/ml), followed by incubation at 37 °C for 15 min. The reaction products were separated by electrophoresis in a 10% Tris borate-EDTA polyacrylamide gel. Gels were dried on Whatman MM3 paper and analyzed by phosphorimaging using a Typhoon 9400 scanner (GE Healthcare). Images were quantified using ImageQuantTL software.

Construction of DNA Substrates for Resection Assays—The DNA substrates used in resection assays were derived from the plasmid pUC19 (2686 bp). The self-complementary oligonucleotide, 5′-AGCT GCTGAGG GCTGAGG GCTGAGG GCTGAGG AGGCCT CCTCAGC CCTCAGC CCTCAGC CCTCAGC-3′, was annealed to form a duplex that was cloned into the HindIII site of pUC19. This destroyed the HindIII site and inserted a single recognition sequence for StuI (AGGCCT) flanked on each side by four recognition sequences for the nickase Nt.BbvCI (CC*TCAGC; the cleavage position is indicated by the asterisk) that are oriented as an inverted repeat with respect to the StuI site. The resulting pOH-S plasmid allowed us to prepare a linear DNA substrate with 3′ overhangs of 26 nucleotides (nt) in length. A blunt-ended substrate was generated by digestion of pOH-S with StuI (New England Biolabs), followed by DNA purification using a Macherey Nagel NucleoSpin® gel and PCR cleanup kit. The substrate with 26-nt 3′ overhangs was generated as follows. After digestion of pOH-S with StuI and its heat inactivation, Nt.BbvCI (New England Biolabs) was added, and the reaction was incubated further for 2 h at 37 °C. Subsequently, the reaction mixture was diluted six times with water and incubated at 85 °C for 15 min. DNA purification was performed as described above. DNA concentration was determined using a NanoDrop ND-1000 spectrophotometer (Witec AG).

DNA End Resection Assays—DNA end resection reactions were carried out in a buffer containing 25 mM Tris acetate (pH 7.5), 2 mM magnesium acetate, 1 mM dithiothreitol, 0.1 mg/ml BSA, 10.7 mM phosphocreatine, 0.02 mg/ml creatine phosphokinase, and 1 mM ATP. Reactions contained 2 nM DNA substrate (molecules), 8 nM DNA2, 350 nM RPA (100% DNA strand coverage, assuming all DNA was single-stranded), and various concentrations of WRN or BLM as indicated. EXO1 was present at a concentration of 20 nM. The reactions were assembled on ice and initiated by the addition of ATP. Reaction mixtures (15 μl) were incubated at 37 °C for 60 min in the case of protein titration experiments. In time course experiments, 15-μl reaction aliquots were withdrawn at defined time points as indicated. Reactions were terminated as described for the helicase assays. The samples were subjected to electrophoresis in a 1% agarose gel run in 1× TAE buffer. Gels were post-stained with SYBR Gold (Invitrogen) and analyzed using MultiImage Light Cabinet (Alpha Innotech). To monitor resection by hybridization of radiolabeled oligonucleotide probes, terminated reactions (21 μl) were divided equally into two tubes. 5′ end-labeled oligonucleotide probes were then added to a final concentration of 5 nM. This mixture was heated in an oven to 75 °C for 5 min and then slowly cooled down to room temperature over 2.5 h. Reaction products were separated by electrophoresis in a 1% agarose gel. Gels were dried on DE81 anion exchange paper (Whatman) and subjected to phosphorimaging analysis using a Typhoon 9400 scanner (GE Healthcare). Images were quantified using ImageQuantTL software. The relative concentration of the resection products generated in WRN-DNA2 or BLM-DNA2 reactions was calculated as a percentage of the product generated in a reaction containing 20 nM EXO1 at the 2-min time point, which led to 100% resection within the region probed with radiolabeled oligonucleotides. Usually, the EXO1 reaction was loaded on each gel in triplicates. The following oligonucleotides were used for the preparation of the hybridization probes: oligo#224, 5′-GGCCGTCGTTTTACAACGTCGT-3′ (it anneals to the 3′-terminated strand; annealing position, 112–133 nt upstream of the StuI cleavage site; the complementary sequence is underlined); oligo#227, 5′-GGCATAGTTAAGCCAGCCCCGA-3′ (it anneals to the 3′-terminated strand; annealing position, 353–374 nt upstream of the StuI cleavage site); and oligo#237, 5′-GGTCGGGGCTGGCTTAACTATG-3′ (it anneals to the 5′-terminated strand; annealing position, 122–133 nt upstream of the StuI cleavage site). Oligonucleotides were 5′ end-labeled using [γ-^{32}P]ATP and T4 polynucleotide kinase (New England Biolabs). The two noncomplementary dG residues at the 5′ end of the oligonucleotides were added to ensure equal labeling efficiency.

Cell Culture and Transfection—U2OS and HEK293 cells were grown in DMEM (Sigma) supplemented with 10% fetal calf serum (Invitrogen) and streptomycin/penicillin (100 units/ml). Plasmid DNA was transfected using standard linear polyethyleneimine method. Lipofectamine RNAiMAX (Invitrogen) was used for siRNA transfection. To generate HEK293 clones stably expressing FLAG-DNA2, cells were cotransfected with pFLAG-CMV2-hDNA2 and pBABE-puro (Addgene) and subjected to puromycin 1 (μg/ml) selection. Puromycin-resistant clones were tested for expression of FLAG-DNA2 by Western blotting.

Immunoprecipitation—HEK293 cells were transfected with the pcDNA3.1-hWRN and/or pFLAG-CMV2-hDNA2 vectors. Cells were harvested to lysis buffer (50 mM Tris-HCl (pH 8.0), 120 mM NaCl, 20 mM NaF, 15 mM sodium pyrophosphate, and

0.5% (v/v) Nonidet P-40) supplemented before use with protease (Complete EDTA-free, Roche) and phosphatase (PhosSTOP, Roche) inhibitors, 2 mM $MgCl_2$ and benzonase (50 units/ml). Cells were sonicated briefly, and lysates were clarified by centrifugation at 16,000 × *g* for 30 min. Cell extracts (1 mg of protein) were subjected to immunoprecipitation using anti-FLAG M2 magnetic beads (10 μl) or Protein A/G Plus UltraLink Resin (10 μl, Thermo Scientific) coated with rabbit polyclonal anti-WRN antibody (10 μg), which was carried out overnight at 4 °C. Immunoprecipitates were washed four times with lysis buffer. Bound proteins were eluted by Laemmli sample buffer and analyzed by SDS-PAGE and Western blotting. To test the interaction between purified WRN and DNA2 proteins, 500 ng of each protein was mixed in 200 μl of NET-N100 buffer (10 mM Tris-HCl (pH 8.0), 1 mM EDTA, 100 mM NaCl, and 0.5% (v/v) Nonidet P-40) and incubated at 4 °C for 4 h. As a control, DNA2 was incubated in the absence of WRN. The protein mixtures were subsequently subjected to immunoprecipitation using anti-WRN antibody (4 μg), which was carried out at 4 °C for 2 h. Immunoprecipitates were washed four times with NET-N100 buffer. Bound proteins were eluted by Laemmli sample buffer and analyzed by SDS-PAGE and Western blotting.

GST Pulldown Assay—GST-tagged fragments of WRN were produced in the *Escherichia coli* BL21-CodonPlus(DE3)-RIL strain (Stratagene) and bound to GSH Sepharose 4B (GE Healthcare) as described previously (24). As a control, beads were coated with GST protein only. The beads were incubated with 500 ng of purified His_6-DNA2-FLAG protein in 400 μl of NET-N100 buffer at 4 °C for 2 h. After extensive washing with NET-N100 buffer, proteins bound to the beads were analyzed by Western blotting. Blots were first stained in Ponceau S solution (0.1% (w/v) Ponceau S and 5% (v/v) acetic acid) to visualize WRN fragments and subsequently probed with anti-FLAG antibody.

Reverse Transcription and Quantitative Real-time PCR—Total RNA was isolated from cells using the RNeasy mini kit (Qiagen). 200 ng of RNA was used for cDNA synthesis using a high-capacity cDNA reverse transcription kit (Applied Biosystems). The target gene expression level was determined by quantitative real-time PCR that was performed on a ABI Prism 7300 (Applied Biosystems) using SYBR Select Master Mix (Applied Biosystems). The following primer pairs were used to determine EXO1 mRNA levels: 5′-ACCTCTAAGG AACAAGGTTC-3′ (forward) and 5′-AGGAGGAAGC TTTTCAGAATC-3′ (reverse). The housekeeping gene RPLPO, used as a control, was amplified with the following primers: 5′-CCAGTCTGGA GAAACTGCTG-3′ (forward) and 5′-CAGCAGCTGG CACCTTATTGG-3′ (reverse). The Pfaffl equation was used for normalization and calculation of relative EXO1 expression levels in comparison with the control gene (33).

SA-GFP Reporter Assay—SA-GFP reporter assays were performed as described previously (34, 35). HEK293/SA-GFP cells were seeded in poly-L-lysine-coated 6-well plates at a density of 0.5 million cells/well. U2OS/SA-GFP cells were seeded in 6-well plates at a density of 0.25 million cells/well. The next day, cells were transfected with appropriate siRNA (40 nM) using Lipofectamine RNAiMAX (Invitrogen). After 24 h, siRNA-transfected cells were transferred into a 12-well plate, with 200,000 cells/well for HEK293/SA-GFP and 100,000 cells/well for U2OS/SA-GFP. 44 h after siRNA transfection, cells were transfected with 0.6 μg of the I-SceI expression vector pCBASce (36) using linear polyethyleneimine and, 6 h later, with appropriate siRNA (20 nM) using the standard calcium phosphate method. 52 h after I-SceI transfection, cells were harvested and subjected to flow cytometry analysis using LSRII (BD Biosciences) and FlowJo software to determine the percentage of GFP-positive cells. The mean values obtained with control siRNA (siLuc) samples were 0.9% for HEK293/SA-GFP cells and 2.0% for U2OS/SA-GFP cells. To test the effect of ectopic expression of WRN on SSA repair efficiency of WRN-depleted HEK293/SA-GFP cells, the mutant form of the pcDNA3.1-hWRN construct harboring silent mutations in the siWRN-targeting region (0.6 μg) was cotransfected with pCBASce (0.6 μg). The plasmid pcDNA3.1 was used as a control vector in these experiments. Cells were subjected to flow cytometry analysis at 52 h after plasmid transfection.

Immunofluorescence Assays—U2OS cells transfected with the indicated siRNAs were cultured on glass coverslips. 48 h after siRNA transfection, cells were treated with 1 μM camptothecin (CPT) for 1 h. After pre-extraction for 5 min on ice in 25 mM HEPES (pH 7.4) buffer containing 0.5% (v/v) Triton X-100, 50 mM NaCl, 1 mM EDTA, 3 mM $MgCl_2$ and 0.3 M sucrose, cells were fixed with 4% (v/v) formaldehyde for 15 min at room temperature. Subsequently, cells were permeabilized by soaking in 0.2% (v/v) Triton X-100 for 5 min at room temperature. After blocking in PBS containing 10 mg/ml BSA for 30 min at room temperature, fixed cells were incubated for 2 h at room temperature with the indicated primary antibodies. The slides were washed with PBS and incubated for 1 h at room temperature with secondary antibodies diluted in blocking solution (Alexa Fluor 568-conjugated goat anti-rabbit IgG and Alexa Fluor 488-conjugated goat anti-mouse IgG (Invitrogen)). After washing with PBS, coverslips were mounted using Vectashield containing DAPI (Vector Laboratories). Automated image acquisition was performed using an Olympus IX70 microscope equipped with the Scan^R imaging platform. A ×40/1.3 numerical aperture objective was used. 10 z stacks at a spacing of 0.3 μm were taken, and 100 images were acquired for each sample. Analysis was performed using Scan^R analysis software. Nuclei were identified on the basis of the DAPI signal, and RPA foci were identified on the basis of edge-based subobject counts. At least 1000 cells were analyzed for each condition.

RESULTS

DNA2 Can Mediate DNA End Resection in Conjunction with WRN Helicase—To test whether the human WRN helicase can mediate resection of broken DNA ends in concert with DNA2, we purified these proteins to homogeneity and analyzed their activities *in vitro* (Fig. 1*A*). WRN and BLM unwind DNA in the 3′-5′ direction and require a 3′ ssDNA tail for loading onto the DNA substrate (37, 38). Therefore, we generated a derivative of the pUC19 plasmid in which a StuI site was flanked on each side by four recognition sites for the nicking endonuclease Nt.BbvCI. Cleavage of this pUC19 derivative with StuI and Nt.BbvCI resulted in a 2.7-kb-long linear DNA molecule ending with 3′

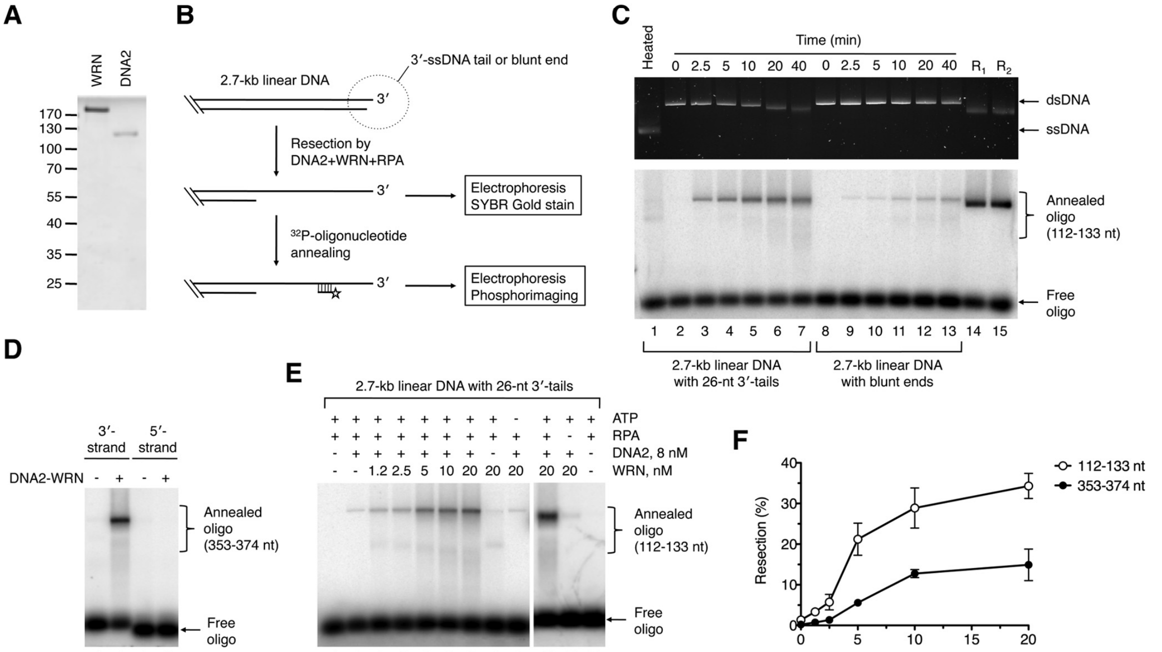

FIGURE 1. **DNA end resection by DNA2 and WRN.** *A*, SDS-PAGE analysis of purified WRN (0.7 μg) and DNA2 (0.4 μg) proteins. Gel was stained with Coomassie Brilliant Blue R-250. The molecular weights of protein standards are indicated on the *left*. *B*, schematic of the DNA end resection assay. The resection products were either left untreated or hybridized with synthetic ^{32}P-labeled oligonucleotides complementary to the 3′-terminated strand. DNA species were separated by electrophoresis in a 1% agarose gel and visualized by SYBR gold staining and phosphorimaging, respectively. Probes complementary to the regions spanning nt positions 112–133 and 353–374 (relative to the 3′ end) were used in this study. Only a part of the DNA substrate is shown. *C*, time course of resection of 3′-tailed (26 nt) and blunt-ended DNA substrates by DNA2 and WRN. Reactions were carried out at 37 °C and contained 2 nM DNA, 350 nM RPA, 10 nM WRN, and 8 nM DNA2. Reaction products at the indicated time points were analyzed as outlined in *B*. The 112- to 133-nt probe was used in this analysis. *Lane 1*, heat-denatured substrate; *lane 14*, 3′-tailed substrate incubated with 20 nM EXO1 and 350 nM RPA for 2 min (R1); *lane 15*, blunt-ended substrate incubated with 20 nM EXO1 and 350 nM RPA for 2 min (R2). *D*, directionality of DNA end resection by WRN-DNA2. Reactions were carried out at 37 °C for 60 min and contained 2 nM 3′-tailed DNA substrate, 350 nM RPA, 8 nM DNA2, and 10 nM WRN. Resection products were annealed with radiolabeled oligonucleotide probes complementary to either 3′-terminated (position 353–374 nt relative to the 3′ end) or 5′-terminated (position 353–374 nt relative to 3′ end) strand and analyzed as in *C*. *E*, 5′ end resection of 3′-tailed DNA substrate by WRN-DNA2 is dependent on WRN concentration and the presence of ATP and RPA. Reactions were carried out at 37 °C for 60 min and contained, as indicated, 2 nM DNA, 350 nM RPA, 1 mM ATP, 8 nM DNA2, and different WRN concentrations. Resection products were detected using the 112–133-nt probe. *F*, dependence of WRN-DNA2-catalyzed resection of 3′-tailed substrate on WRN concentration. Resection at the positions of 112–133 nt and 353–374 nt from the 3′ end of the DNA substrate was monitored. Reactions were carried out as in *E*. Relative concentration of the resection product generated by WRN-DNA2 at each WRN concentration was calculated as a percentage of the product generated by 20 nM EXO1 after 2 min. Data are mean ± S.D. ($n = 3$).

overhangs of 26 nt in length, whereas its cleavage by StuI alone gave rise to a linear DNA molecule with blunt ends. Processing of the DNA substrates was monitored by agarose gel electrophoresis followed by SYBR gold staining (Fig. 1*B*). In addition, ^{32}P-labeled synthetic oligonucleotides complementary to the 3′-terminated strand were used as hybridization probes to detect ssDNA generated by resection at specific positions (Fig. 1*B*) (10). We found that WRN, together with DNA2 and RPA, could catalyze efficient 5′ end resection on the 3′-tailed substrate but not the blunt-ended substrate (Fig. 1*C*). As expected, no reaction products were detected with an oligonucleotide probe complementary to the 5′-terminated strand, indicating that the observed DNA resection activity is limited to the 5′ strand (Fig. 1*D*). Of note, the end product of the resection reaction on the 3′-tailed DNA substrate appeared as a discrete band on SYBR gold-stained gel that was clearly shifted with respect to the unprocessed dsDNA substrate, indicating extensive resection (Fig. 1*C*, *top panel*, compare *lanes 2* and *7*). In contrast, no gradual shift in the electrophoretic mobility of the resection product was apparent after annealing of the radioactive probes. This is most likely due to the fact that DNA2 nuclease generates short oligonucleotides that can reanneal to the resected DNA along with the radioactive probe, leading to a DNA molecule with an electrophoretic mobility similar to that of the DNA substrate. Together, these results clearly demonstrate that DNA2, in conjunction with WRN and RPA, can catalyze extensive 5′ end resection, providing that the DNA substrate contains a 3′ ssDNA overhang.

To further characterize the DNA end resection reaction mediated by WRN-DNA2, reactions with the 3′-tailed substrate were carried out at various WRN concentrations, whereas DNA2 was kept at a concentration of 8 nM. We observed that the amount of resection product increased gradually with WRN concentration, reaching a plateau at about 10 nM (Fig. 1*E*, *lanes 2–7*, and Fig. 1*F*). Quantitative analysis of gel images revealed that about 35% of the DNA substrate was resected to the position of 133 nt from the 3′ end and that about 15% of the DNA substrate was resected to the position of 374 nt

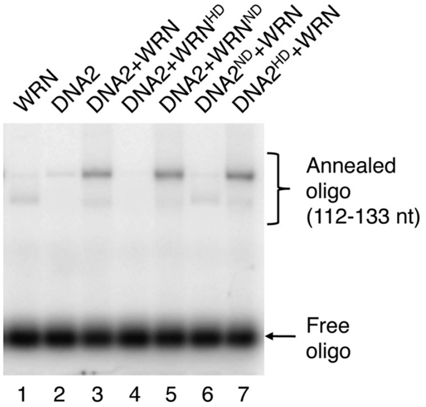

FIGURE 2. **5′ end resection of 3′-tailed DNA substrate by WRN-DNA2 depends on the helicase activity of WRN and the nuclease activity of DNA2.** Reactions were carried out at 37 °C for 60 min and contained 2 nM DNA, 350 nM RPA, 1 mM ATP, 8 nM DNA2, and 10 nM WRN. Resection products were detected using the 112–133 nt probe. WRN^{HD}, helicase-deficient mutant of WRN (K567M); WRN^{ND}, nuclease-deficient mutant of WRN (E84A); $DNA2^{HD}$, helicase-deficient mutant of DNA2 (K654R); $DNA2^{ND}$, nuclease-deficient mutant of DNA2 (D277A).

within 1 h of incubation (Fig. 1*F*). Interestingly, a small amount of resected product (1–2%) could also be detected in the absence of WRN, suggesting that DNA2 itself could slowly resect dsDNA ends, likely following RPA-mediated stabilization of ssDNA ends generated by thermal fraying (Fig. 1*E*, *lane 2*). In the absence of DNA2, WRN was only capable of DNA unwinding, as evident from the appearance of a fast-migrating band (Fig. 1*E*, *lane 8*). The resection process catalyzed by WRN and DNA2 was found to be dependent on the presence of ATP and RPA, as expected for a helicase-driven reaction (Fig. 1*E*, compare *lanes 9–12*).

WRN acts not only as a 3′-5′ DNA helicase, but it also possesses a dsDNA-dependent 3′-5′ exonuclease activity residing in a separate domain located in the N-terminal portion of the protein (39, 40). DNA2 functions as a 5′-3′ helicase and a ssDNA-specific endonuclease (32, 41). To define the functions of the enzymatic activities of WRN and DNA2 in DNA end resection, we carried out a set of resection reactions with the 3′-tailed pUC19 substrate where either WRN or DNA2 were substituted with catalytically inactive mutants. We found that the helicase-deficient mutant of WRN (K567M) failed to stimulate DNA resection by DNA2, whereas the nuclease-deficient mutant of WRN (E84A) behaved similarly as the wild-type WRN in this reaction (Fig. 2, *lanes 2–4*). Substitution of DNA2 with its nuclease-deficient mutant (D277A) completely abolished resection and stimulated unwinding of the plasmid substrate (Fig. 2, *lane 6*). In contrast, the helicase-deficient mutant of DNA2 (K654E) could resect the DNA substrate to the same degree as the wild-type protein (Fig. 2, compare *lanes 3* and *7*). These results indicate that DNA end resection mediated by DNA2, WRN, and RPA is dependent on the helicase activity of WRN and the endonuclease activity of DNA2.

DNA2 and WRN Interact Physically—Yeast Dna2 has been shown to interact physically with Sgs1 (10). Likewise, BLM forms a complex with human DNA2 (17). Therefore, we investigated whether human DNA2 interacts physically with WRN. To this end, HEK293 cells were transfected with plasmids expressing WRN and FLAG-tagged DNA2, respectively, and complex formation between these proteins was tested by immunoprecipitation using beads conjugated with anti-FLAG M2 antibody. We found that WRN coimmunoprecipitated with FLAG-DNA2, indicating that these proteins form a complex *in vivo* (Fig. 3*A*, *lane 3*). This interaction was specific because anti-FLAG beads did not immunoprecipitate WRN from an extract lacking FLAG-DNA2 (Fig. 3*A*, *lane 1*). To further investigate complex formation between WRN and DNA2, we generated a stable HEK293 cell line expressing FLAG-DNA2. By immunoprecipitation using anti-FLAG M2 beads or anti-WRN antibody, we found that FLAG-DNA2 formed a complex with endogenous WRN in these cells (Fig. 3, *B* and *C*). Western blot analysis indicated that the level of FLAG-DNA2 in these cells was only slightly higher than that of endogenous DNA2, suggesting that WRN and DNA2 form a complex under physiological conditions (Fig. 3*B*, *top panel*). Interaction between FLAG-DNA2 and endogenous BLM was also detected as expected (Fig. 3*B*) (17). The cellular concentration of these protein complexes was not altered when cells were subjected to treatment with CPT, which causes breakage of DNA replication forks (Fig. 3*B*, *lanes 2–5*) (42). This suggests that the interaction of DNA2 with WRN and BLM in the cell is not dependent on DNA damage.

To test whether WRN and DNA2 interact directly, purified proteins were mixed and incubated at 4 °C for 4 h. Complex formation between WRN and DNA2 was tested by immunoprecipitation using anti-WRN antibody. We found that DNA2 coimmunoprecipitated with WRN. DNA2 was not present in the immunoprecipitated material whether WRN was omitted, confirming a direct protein-protein interaction (Fig. 3*D*). To map the interaction site of DNA2 on WRN, we tested binding of purified His_6-DNA2-FLAG protein to various WRN fragments covering the entire WRN polypeptide (Fig. 3*E*). The WRN fragments were produced in *E. coli* as fusions with a GST tag and isolated on GSH-Sepharose beads. Using a GST pulldown assay, we found that DNA2 bound specifically to a WRN fragment including the core helicase domain (helicase/Zn^{2+}-binding domains) and the winged helix domain (Fig. 3*F*, compare *lanes 1* and *4*) a binding site of a number of other proteins shown to interact with WRN (43, 44). DNA2 was also bound to a fragment containing only the helicase core or to the C-terminal portion of WRN starting at the beginning of the winged helix domain (Fig. 3*F*, compare *lanes 1*, *3*, *4*, and *5*). In contrast, DNA2 did not bind the N-terminal portion of WRN containing the exonuclease domain (Fig. 3*F*, *lane 2*). Collectively, these results suggest that there are at least two DNA2-interaction sites on WRN: one located in the central helicase domain and the other in the C-terminal region of WRN.

WRN-DNA2 Resects DNA Ends More Efficiently Than BLM-DNA2—Next, we set out to compare WRN and BLM with respect to their abilities to resect DNA ends in concert with DNA2 and RPA *in vitro*. Using a Y structure oligonucleotide duplex (29 bp) with single-stranded arms (30 nt each), we found that our preparations of WRN and BLM exhibited similar levels of specific helicase activity (Fig. 4*A*). For resection reactions, we used the 3′-tailed DNA substrate that was readily processed by

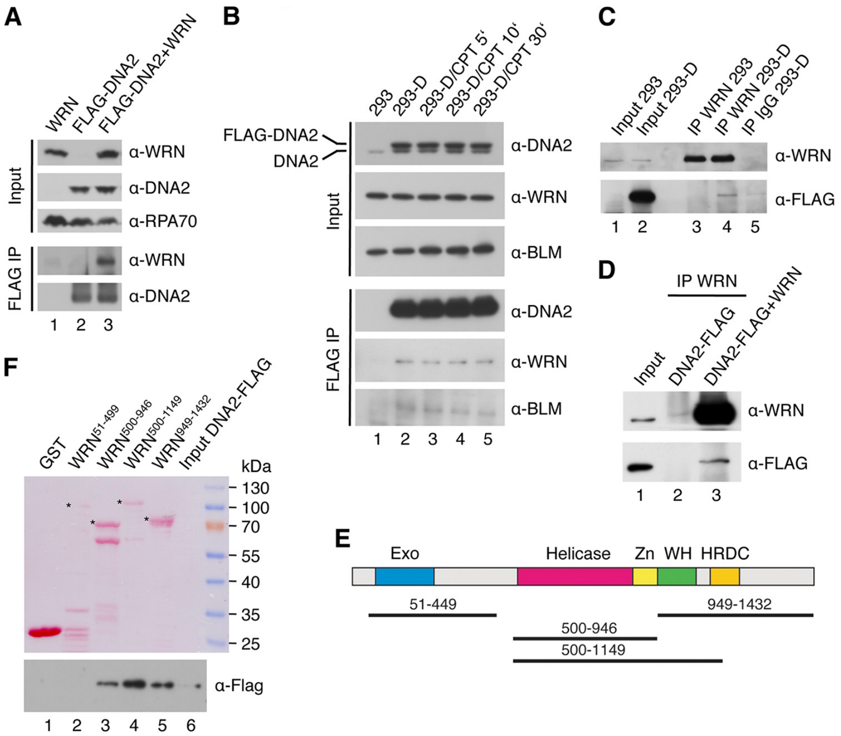

FIGURE 3. **Physical interaction between DNA2 and WRN *in vitro* and *in vivo*.** *A*, coimmunoprecipitation of WRN with DNA2 from human cells. HEK293 cells were transfected with vectors expressing FLAG-DNA2 and WRN as indicated. Cell extracts were immunoprecipitated (*IP*) with anti-FLAG antibody as described under "Experimental Procedures." Blots were probed with the indicated antibodies. 5% of input material was loaded. *B*, effect of DNA damage on the formation of DNA2-WRN and DNA2-BLM complexes in human cells. HEK293 cells stably transfected with the FLAG-DNA2 construct (*HEK293-D*) were treated with 1 μM CPT. At the indicated time points, complex formation between FLAG-DNA2 and endogenous WRN and BLM, respectively, was tested by immunoprecipitation using anti-FLAG antibody. *C*, coimmunoprecipitation of DNA2 with WRN from human cells. Extracts from HEK293-D cells were subjected to immunoprecipitation with anti-WRN antibody or control IgG. The immunoprecipitates were tested for the presence of FLAG-DNA2 and WRN by Western blotting. As a control, a WRN immunoprecipitate from HEK293 cells was also analyzed (*lane 3*). *D*, coimmunoprecipitation of DNA2 with WRN from a mixture of purified proteins. DNA2 (500 ng) was incubated with or without WRN (500 ng) at 4 °C for 4 h. The mixtures were subjected to immunoprecipitation with anti-WRN antibody. *E*, domain organization of WRN. *Exo*, exonuclease domain; *Zn*, zinc-binding domain; *WH*, winged-helix domain; *HRDC*, helicase and RNaseD C-terminal domain. *Black lines* indicate WRN fragments used for mapping the DNA2-interaction site on WRN. *F*, GST pulldown assay. Glutathione beads coated with the indicated GST-tagged fragments of WRN were incubated with purified His$_6$-DNA2-FLAG protein at 4 °C for 2 h, and bound proteins were analyzed by Western blotting as described under "Experimental Procedures." 1% of input was loaded in *B* and *C*, whereas 10% of input was loaded in *D* and *F*.

WRN-DNA2 in the presence of RPA (Fig. 1*C*). The extent of DNA resection at various reaction time points was monitored by annealing of radiolabeled oligonucleotide probes. These experiments clearly showed that WRN-DNA2 resected the DNA substrate at a much higher rate compared with BLM-DNA2 (Fig. 4, *B* and *C*). Notably, WRN-DNA2-catalyzed resection to the position of 374 nt away from the 3′ end was faster than BLM-DNA2-catalyzed resection to the position of 133 nt (Fig. 4, *B* and *C*). We also compared the activities of WRN-DNA2 and BLM-DNA2 on blunt-ended DNA substrate in the presence of RPA. We found that this DNA substrate was largely refractory not only to processing by WRN-DNA2 but also to processing by BLM-DNA2 (Fig. 4*D*, compare *lanes 4* and *5* to *lanes 10* and *11*). Taken together, we show that WRN-DNA2 resects DNA ends more efficiently than BLM-DNA2 *in vitro*.

Dissection of Pathways Involved in DNA End Resection in Human Cells—To assess whether WRN is involved in DNA end resection *in vivo*, we investigated the effect of its depletion on the efficiency of SSA-mediated repair of endonuclease-induced DSBs in cells that were either proficient or deficient for EXO1 and DNA2, respectively. For this epistasis analysis, we initially used the human embryonic kidney cell line HEK293 stably transfected with the SA-GFP reporter cassette consisting of two truncated *GFP* gene alleles (*5′GFP* and *Sce3′GFP*) that form a direct sequence repeat (280 bp) separated by a region of about 2.4 kb (Fig. 5*A*) (34, 45). SSA-mediated recombination between these homologous sequences triggered by a DSB generated in the distal GFP allele by the I-SceI endonuclease results in the formation of a functional *GFP* gene (Fig. 5*A*). This requires extensive DNA end resection to expose the complementary ssDNA regions for annealing. The proteins of interest were depleted from HEK293/SA-GFP cells by RNA interference. Cells were subsequently transfected with an I-SceI expression vector to create a DSB in the reporter cassette, and the percentage of GFP positive cells arising upon SSA-mediated repair was determined by flow cytometry 2 days after plasmid transfection. We found that cells depleted of either EXO1, WRN, or DNA2 exhibited a marked reduction in the frequency of SSA repair events (55, 65, and 75%, respectively) compared with mock-depleted cells (Fig. 5, *B* and *C*). In contrast, knockdown of

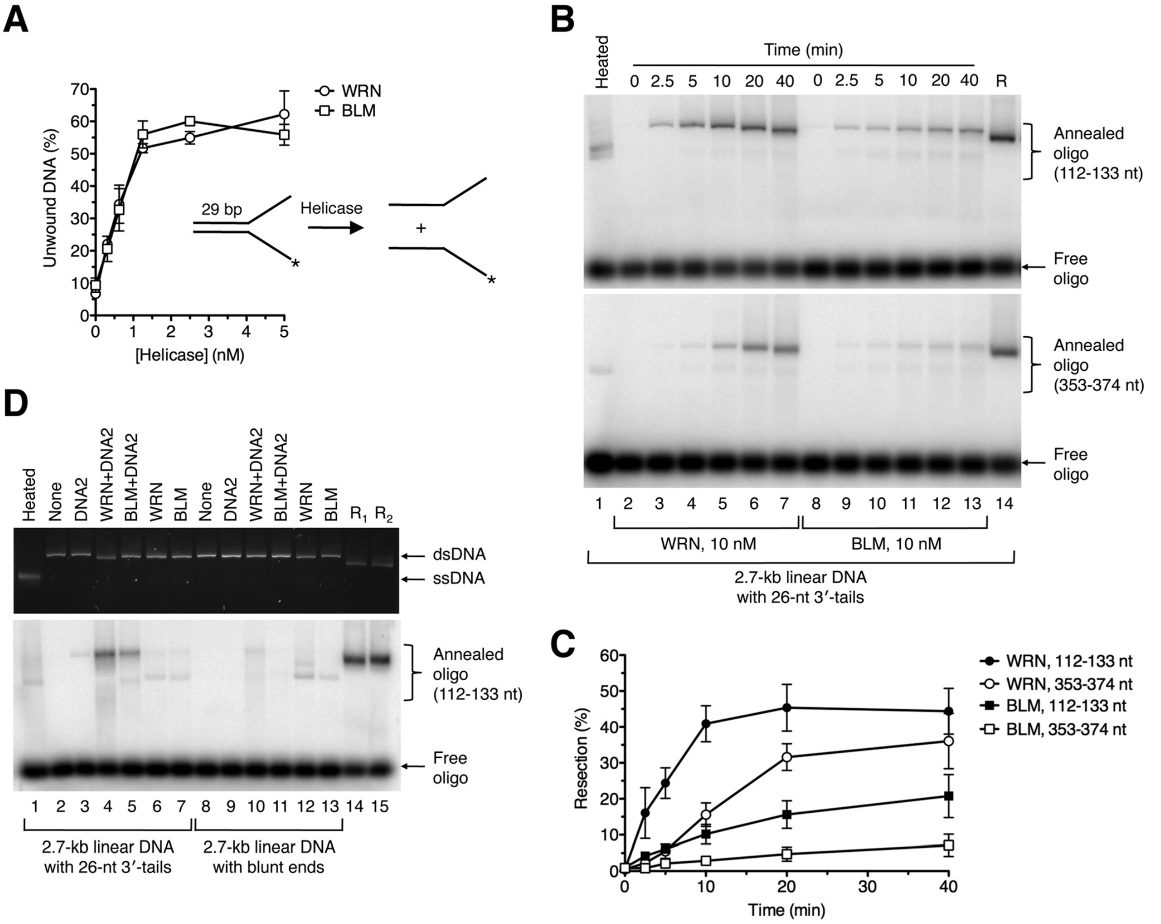

FIGURE 4. **Comparison of DNA end resection activities of WRN-DNA2 and BLM-DNA2.** *A*, comparison of helicase activities of WRN and BLM. Reactions contained 1 nM ^{32}P-labeled forked DNA duplex (*inset*) and different concentrations of WRN or BLM. Reactions were incubated at 37 °C for 30 min, and reaction products were quantified as described under "Experimental Procedures." Data are mean ± S.D. ($n = 3$). *B*, time course of resection of 3′-tailed DNA substrate catalyzed by WRN-DNA2 and BLM-DNA2, respectively. Reactions contained 2 nM DNA, 350 nM RPA, 8 nM DNA2, and 10 nM WRN/BLM. Reaction aliquots withdrawn at the indicated time points were subjected to electrophoresis on a 1% agarose gel after hybridization of radiolabeled probes complementary to 3′-terminated strand at the indicated positions. Radiolabeled DNA species were visualized by phosphorimaging. *C*, quantification of the reactions in *B*. Relative concentration of resection products generated at each time point was calculated as a percentage of the product generated by 20 nM EXO1 after 2 min. Data are mean ± S.D. ($n = 3$). *D*, processing of 3′-tailed (26 nt) and blunt-ended DNA substrates in reactions with indicated composition. Reactions were carried out at 37 °C for 60 min and contained 2 nM DNA, 350 nM RPA, and, where indicated, 8 nM DNA2, 20 nM WRN, and 20 nM BLM. Reaction products were analyzed as in Fig. 1*C*. *Lane 1*, heat-denatured substrate; *lane 14*, 3′-tailed substrate incubated with 20 nM EXO1 for 2 min (R1); *lane 15*, blunt-ended substrate incubated with 20 nM EXO1 for 2 min (R2).

BLM was found to be associated with a significant increase in SSA repair efficiency (140%) compared with control cells (Fig. 5, *B* and *C*). Of note, the SSA repair defect of WRN-depleted cells could be rescued by ectopic expression of the siRNA-resistant form of WRN, excluding an off-target effect of the WRN siRNA used in this study (Fig. 5*D*). Combined depletion of EXO1 and WRN or EXO1 and DNA2 further decreased the repair efficiency compared with the respective single depletions, whereas codepletion of DNA2 and WRN did not (Fig. 5, *B* and *C*). In addition, combined depletion of EXO1 and BLM had nearly the same effect on the SSA repair efficiency as EXO1 depletion (Fig. 5, *B* and *C*). Therefore, these findings suggest that HEK293 cells have at least two pathways for long-range resection of DSB ends: one mediated by EXO1 and the other dependent upon DNA2 and WRN.

To substantiate these findings, we performed a similar set of experiments using U2OS/SA-GFP cells (35). This analysis indicated that combined depletion of EXO1 and DNA2 almost completely abolished (reduced by 91%) SSA-mediated DSB repair in U2OS/SA-GFP cells, as did depletion of MRE11 (by 89%) or CtIP (by 82%), suggesting that long-range DNA end resection in U2OS cells is largely dependent on EXO1 and DNA2 (Fig. 5, *E*–*G*). However, in contrast to the results obtained with HEK293/SA-GFP cells, we observed a significant reduction in SSA repair efficiency not only after depletion of WRN (by 57%) but also after depletion of BLM (by 59%) (Fig. 5, *E* and *F*). Codepletion of BLM and WRN further decreased the repair efficiency to a level comparable with that in DNA2-depleted (by 73%) cells (Fig. 5, *E* and *F*). Moreover, combined depletion of DNA2 with either BLM or WRN had nearly the

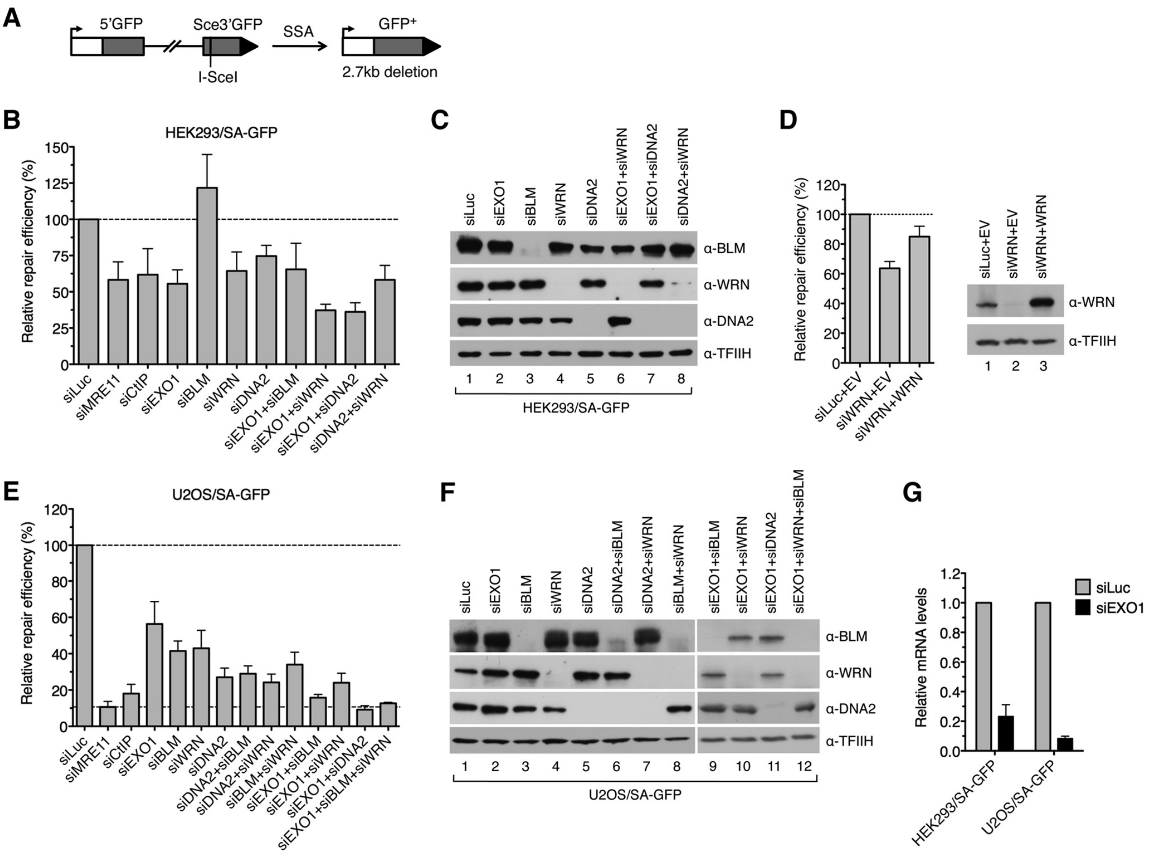

FIGURE 5. **WRN and BLM interact epistatically with DNA2 to promote DSB repair by SSA in human cells.** *A*, schematic of the SA-GFP reporter cassette. SSA-mediated repair of a DSB at the I-SceI-cutting site results in the formation of a functional GFP allele. *B*, efficiency of SSA-mediated repair of I-SceI-induced DSB in HEK293/SA-GFP cells treated with the indicated siRNAs. Cells were transfected with the appropriate siRNAs (40 nM) 2 days prior to transfection of the I-SceI-expressing plasmid. The percentage of GFP-positive cells in each sample was measured by flow cytometry 2 days after I-SceI plasmid transfection and taken as a measure of DSB repair efficiency. The plotted values represent the relative repair efficiency calculated as a percentage of repair efficiency measured in cells transfected with control siRNA (*siLuc*, 100%). Data are mean ± S.D. (n ≥ 3). *C*, Western blot analysis of extracts from HEK293/SA-GFP cells transfected with indicated siRNAs under the same conditions as for SA-GFP reporter assays. Blots were probed with the indicated antibodies. *D*, rescue of the SSA-repair defect of WRN-depleted HEK293/SA-GFP cells by expression of the siRNA-resistant variant of WRN. An SA-GFP reporter assay was performed as in *B*. The WRN plasmid (*WRN*) or empty vector (*EV*) were cotransfected with the I-SceI plasmid. *E*, efficiency of SSA-mediated repair of I-SceI-induced DSB in U2OS/SA-GFP cells treated with the indicated siRNAs. Experiments were performed as in *B*. *F*, Western blot analysis of extracts from U2OS/SA-GFP cells transfected with the indicated siRNAs. Blots were probed with the indicated antibodies. *G*, quantitative real-time PCR showing that EXO1 mRNA levels are down-regulated by specific siRNA. Data are mean ± S.D. (*n* = 3).

same inhibitory effect on SSA repair as DNA2 depletion (Fig. 5, *E* and *F*). On the contrary, codepletion of EXO1 with either WRN or BLM caused a much higher reduction in repair efficiency than depletion of DNA2 alone, and triple depletion of EXO1, BLM, and WRN brought repair efficiency down to the level measured in cells depleted of EXO1 and DNA2 (Fig. 5, *E* and *F*). Collectively, these data suggest that, in U2OS cells, both WRN and BLM assist DNA2 to mediate long-range resection of broken DNA ends.

To bolster our conclusion that DNA2, WRN, and BLM have an epistatic relationship in DSB end resection, we extended our analysis to measurement of RPA focus formation in U2OS cells treated with CPT. As expected, 1 h after addition of CPT, RPA formed numerous foci in γ-H2AX-positive cells, which were dependent on the presence of CtIP (Fig. 6). Depletion of DNA2 resulted in a marked reduction in the number of RPA foci per cell compared with mock-depleted cells (Fig. 6). Cells depleted of BLM or WRN displayed a mild decrease in RPA focus frequency compared with mock-depleted cells (Fig. 6). In contrast, combined depletion of BLM and WRN caused approximately the same reduction in RPA focus frequency as depletion of DNA2 alone. Moreover, cells depleted of DNA2 and BLM or DNA2 and WRN displayed an RPA foci frequency comparable with that of DNA2-depleted cells (Fig. 6). These data further support the conclusion that DNA2, WRN, and BLM operate in the same DNA end resection pathway.

Role of the BLM-TOPOIIIα-RMI1-RMI2 Complex in DNA End Resection—In human cells, BLM exists in a complex with TOPOIIIα, RMI1, and RMI2, which is known to catalyze double Holliday junction dissolution during HR (46–49). Studies in yeast have shown that Top3α and Rmi1 are also required for DNA-end resection *in vivo* and stimulate DNA end resection by

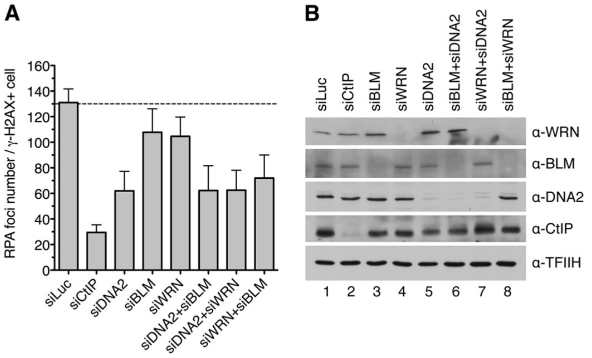

FIGURE 6. **DNA2, WRN, and BLM act in the same pathway of DSB end resection.** *A*, frequency of camptothecin-induced RPA foci in nuclei of U2OS cells depleted of the indicated proteins. Cells were transfected with appropriate siRNAs and, 48 h later, treated with 1 μM camptothecin for 1 h. Cells were then detergent-extracted and fixed with formaldehyde. RPA and γ-H2AX (a marker of DNA damage) were visualized by indirect immunofluorescence. DAPI was used to stain nuclei. The average number of RPA foci per γ-H2AX-positive cell was determined for each sample using an Olympus Scan^R screening station. The data points are mean ± S.D. ($n = 3$). *B*, Western blot analysis of extracts from U2OS cells transfected with indicated siRNAs. Blots were probed with the antibodies indicated on the *right*.

Sgs1-Dna2 *in vitro* by promoting the helicase activity of Sgs1 (9, 10, 14). Our study revealed that BLM-DNA2 resects DNA ends less efficiently than WRN-DNA2 *in vitro*, whereas *in vivo*, at least in U2OS cells, BLM and WRN appeared to contribute equally to promote DNA end resection (Fig. 5*E*). Therefore, we investigated whether BLM requires TOPOIIIα, RMI1, and RMI2 (TRR) to efficiently support DNA end resection by DNA2. To this end, we first investigated the effect of a purified TRR complex on DNA end resection by BLM-DNA2 *in vitro* (Fig. 7*A*). We found that TRR enhanced resection of the 3′-tailed pUC19 substrate by BLM-DNA2 (Fig. 7, *B* and *C, lanes 3–6*). On the contrary, the TRR complex had no effect on DNA end resection by WRN-DNA2 (data not shown). Moreover, it could not enhance DNA end resection by DNA2 in the absence of BLM (Fig. 7, *B* and *C*, compare *lanes 2* and *7*).

Next we tested the effect of depletion of RMI1 on the efficiency of SSA-mediated repair of I-SceI-induced DSBs in U2OS/SA-GFP cells. We found that RMI1 depletion reduced the repair efficiency to the level displayed by BLM- or DNA2-depleted cells (Fig. 7, *D* and *E*). Importantly, codepletion of RMI1 with BLM or DNA2 did not further reduce the repair efficiency compared with single depletions of these proteins, suggesting that RMI1, BLM, and DNA2 act in the same pathway (Fig. 7, *D* and *E*). Collectively, these results suggest that, in human cells, BLM promotes long-range DNA end resection as part of the BTRR complex.

DISCUSSION

Here we present evidence suggesting that human DNA2 acts in conjunction with either WRN or BLM to mediate long-range resection of broken DNA ends *in vivo*. Moreover, we show that WRN helicase can cooperate with DNA2 and RPA to catalyze resection of DNA ends *in vitro*, generating long 3′-terminated ssDNA tails. Our study also reveals that both WRN-DNA2 and BLM-DNA2 require a 3′ ssDNA overhang to efficiently initiate DNA end resection *in vitro*, which is in agreement with the "two-step" resection model in which the initial 5′ end trimming is carried out by the MRE11-RAD50-NBS1/Xrs2 complex in conjunction with CtIP/Sae2 (8, 9, 11, 19). In addition, we present evidence that BLM and DNA2 interact epistatically with RMI1 to mediate DNA end resection *in vivo*. Moreover, we show that the TRR complex stimulates DNA end resection by BLM-DNA2 *in vitro*. These data suggest that, in cells, BLM mediates DNA end resection as part of the BTRR complex.

Our discovery of the involvement of WRN in DNA end resection is consistent with the findings that WRN interacts physically with the MRN complex and accumulates at sites of DSBs in human cells (50, 51). Moreover, it has been demonstrated that WRN depletion leads to a marked reduction in the frequency of RPA and BrdU/ssDNA foci formed in response to ionizing radiation, indicative of a resection defect (52). A similar phenotype has been observed in DNA2-depleted cells (18). Although the previous studies did not address the relationship between WRN and DNA2, they demonstrated that these enzymes act synergistically with EXO1 to promote DNA end resection in human cells (18, 52). A role for WRN as a critical DNA end resection factor is also consistent with the cellular phenotype of Werner syndrome, a severe premature aging disorder caused by inherited mutations in the *WRN* gene (53). Cells derived from Werner syndrome patients are characterized by non-homologous chromosome exchanges, termed variegated translocation mosaicism, and large chromosomal deletions that may result from aberrant DSB repair by NHEJ as a consequence of a defect in DNA end resection (54–56). Indeed, it is becoming clear that NHEJ accounts for most chromosomal translocations in humans (57). Moreover, a role for DNA end resection as the critical determinant of DSB repair pathway choice is well established (58). Accumulating evidence suggests that defects in homology-directed repair pathways, which are dependent on DNA end resection, result in overuse of NHEJ for repair, leading to accumulation of chromosomal rearrangements (57). However, it should be noted that WRN is also known to promote DSB repair by the classical Ku-dependent NHEJ (C-NHEJ) pathway to suppress microhomology-mediated end joining (59, 60). This alternative end joining pathway is capable of producing chromosomal translocations, particularly when Ku-dependent NHEJ is deficient (57). Moreover, WRN has been shown to be involved in the resolution HR intermediates (61, 62). Therefore, it seems that the genomic instability in Werner syndrome is a consequence of multiple defects in DNA repair pathways.

Our finding that the TRR complex stimulates DNA end resection by BLM-DNA2 *in vitro* is consistent with previous reports showing that the association of BLM with TOPOIIIα and RMI1 enhances its DNA unwinding activity, which drives the BLM-DNA2-catalyzed resection reaction (17, 63). Similarly, RMI1 and RMI2 have been shown to enhance the efficiency of the BLM-TOPOIIIα-mediated double Holliday junction dissolution reaction (48, 49, 64). It has also been shown that RMI1 forms a complex with RPA and that this interaction is essential for the stimulatory effect of RPA on double Holliday junction dissolution by the BTRR complex (65). Therefore, it is possible that a physical interaction between RMI1 and RPA

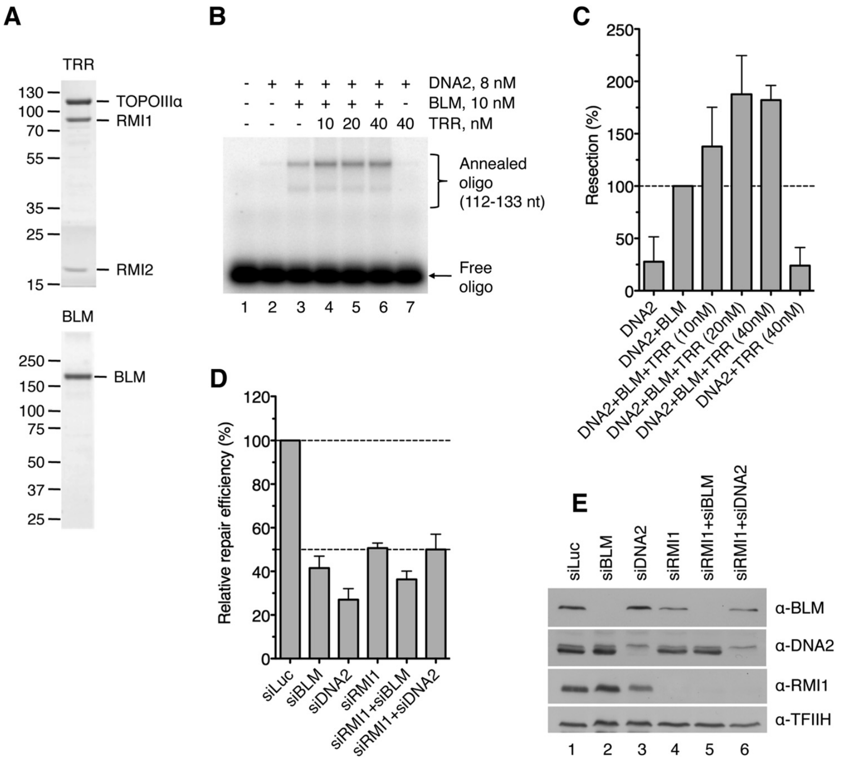

FIGURE 7. **Involvement of TOPOIIIα, RMI1, and RMI2 in DNA end resection.** *A*, SDS-PAGE analysis of purified TRR complex (1.5 μg) and BLM (0.5 μg). The gel was stained with Coomassie Brilliant Blue R-250. The molecular weights of protein standards are indicated on the *left*. *B*, stimulation of BLM-DNA2-catalyzed DNA end resection by the TRR complex. Reactions contained 2 nM 3′-tailed pUC19 substrate, 8 nM DNA2, 10 nM BLM, 350 nM RPA, and varying concentrations of TRR. BLM and TRR were preincubated for 5 min on ice prior to addition to the reaction. Reaction products were analyzed as in Fig. 1*C* using the 112–133-nt probe. *C*, quantification of the product of reactions in *B*. Data are mean ± S.D. ($n = 3$). The data are normalized to the amount of product in the reaction containing only BLM and DNA2 (100%). *D*, RMI1 acts epistatically with BLM and DNA2 to promote DSB repair by SSA in human cells. Efficiency of SSA-mediated repair of I-SceI-induced DSB in U2OS/SA-GFP cells transfected with indicated siRNAs was measured as in Fig. 5*E*. *E*, Western blot analysis of extracts from U2OS/SA-GFP cells transfected with indicated siRNAs under the same conditions as for SA-GFP reporter assays. Blots were probed with the indicated antibodies.

loaded on the 3′-terminated DNA strand during DNA2-catalyzed resection might enhance the DNA unwinding processivity of the BTRR complex and, hence, increase the efficiency of the resection reaction. However, it should be noted that the stimulatory effect of the TRR complex on DNA end resection by BLM-DNA2 *in vitro* was rather modest under our experimental conditions. On the contrary, RMI1 depletion in U2OS/SA-GFP cells reduced the efficiency of SSA-mediated DSB repair to levels displayed by BLM- or DNA2-deficient cells, suggesting that BLM requires RMI1 to promote DNA end resection *in vivo*. Of note, it has been shown that silencing of RMI1 or RMI2 expression by RNA interference destabilizes both BLM and TOPOIIIα (47, 49). Therefore, it is evident that, in addition to being important for the functional attributes of the BTRR complex, RMI1 and RMI2 are indispensable for the structural integrity of its components *in vivo*.

Although BLM depletion compromised SSA-mediated DSB repair in U2OS/SA-GFP cells, it had an opposite effect on SSA in HEK293/SA-GFP cells. Similarly, the efficiency of SSA-mediated DSB repair in HEK293/SA-GFP cells was elevated significantly upon depletion of RMI1 (data not shown). These findings suggest that, in HEK293 cells, the BTRR complex might act as an SSA suppressor, most likely through unwinding of the annealed intermediate formed following DNA end resection. Strikingly, we found that BLM concentration in HEK293 cells was much higher than in U2OS cells (data not shown). Therefore, it appears that the BTRR complex exerts an inhibitory effect on SSA when its concentration in the cell exceeds certain threshold.

Acknowledgments—We thank Kata Sarlos and Ian D. Hickson for the purified TRR complex, Judith L. Campbell for the transfer vector for preparation of the bacmid expressing His$_6$-hDNA2-FLAG, Jeremy M. Stark for the HEK293/SA-GFP and U2OS/SA-GFP cell lines, Stefano Ferrari and Stephanie Bregenhorn for help with protein purification, and Christiane Koenig for technical assistance.

REFERENCES

1. Jackson, S. P., and Bartek, J. (2009) The DNA-damage response in human biology and disease. *Nature* **461,** 1071–1078
2. Khanna, K. K., and Jackson, S. P. (2001) DNA double-strand breaks: signaling, repair and the cancer connection. *Nat. Genet.* **27,** 247–254
3. Longhese, M. P., Bonetti, D., Guerini, I., Manfrini, N., and Clerici, M. (2009) DNA double-strand breaks in meiosis: checking their formation,

processing and repair. *DNA Repair* **8,** 1127–1138

4. Soulas-Sprauel, P., Rivera-Munoz, P., Malivert, L., Le Guyader, G., Abramowski, V., Revy, P., and de Villartay, J. P. (2007) V(D)J and immunoglobulin class switch recombinations: a paradigm to study the regulation of DNA end-joining. *Oncogene* **26,** 7780–7791
5. Lieber, M. R. (2010) The mechanism of double-strand DNA break repair by the nonhomologous DNA end-joining pathway. *Annu. Rev. Biochem.* **79,** 181–211
6. San Filippo, J., Sung, P., and Klein, H. (2008) Mechanism of eukaryotic homologous recombination. *Annu. Rev. Biochem.* **77,** 229–257
7. Heyer, W. D., Ehmsen, K. T., and Liu, J. (2010) Regulation of homologous recombination in eukaryotes. *Annu. Rev. Genet.* **44,** 113–139
8. Mimitou, E. P., and Symington, L. S. (2008) Sae2, Exo1 and Sgs1 collaborate in DNA double-strand break processing. *Nature* **455,** 770–774
9. Zhu, Z., Chung, W. H., Shim, E. Y., Lee, S. E., and Ira, G. (2008) Sgs1 helicase and two nucleases Dna2 and Exo1 resect DNA double-strand break ends. *Cell* **134,** 981–994
10. Cejka, P., Cannavo, E., Polaczek, P., Masuda-Sasa, T., Pokharel, S., Campbell, J. L., and Kowalczykowski, S. C. (2010) DNA end resection by Dna2-Sgs1-RPA and its stimulation by Top3-Rmi1 and Mre11-Rad50-Xrs2. *Nature* **467,** 112–116
11. Nicolette, M. L., Lee, K., Guo, Z., Rani, M., Chow, J. M., Lee, S. E., and Paull, T. T. (2010) Mre11-Rad50-Xrs2 and Sae2 promote 5′ strand resection of DNA double-strand breaks. *Nat. Struct. Mol. Biol.* **17,** 1478–1485
12. Shim, E. Y., Chung, W. H., Nicolette, M. L., Zhang, Y., Davis, M., Zhu, Z., Paull, T. T., Ira, G., and Lee, S. E. (2010) *Saccharomyces cerevisiae* Mre11/Rad50/Xrs2 and Ku proteins regulate association of Exo1 and Dna2 with DNA breaks. *EMBO J.* **29,** 3370–3380
13. Cannavo, E., Cejka, P., and Kowalczykowski, S. C. (2013) Relationship of DNA degradation by *Saccharomyces cerevisiae* exonuclease 1 and its stimulation by RPA and Mre11-Rad50-Xrs2 to DNA end resection. *Proc. Natl. Acad. Sci. U.S.A.* **110,** E1661–E1668
14. Niu, H., Chung, W. H., Zhu, Z., Kwon, Y., Zhao, W., Chi, P., Prakash, R., Seong, C., Liu, D., Lu, L., Ira, G., and Sung, P. (2010) Mechanism of the ATP-dependent DNA end-resection machinery from *Saccharomyces cerevisiae*. *Nature* **467,** 108–111
15. Truong, L. N., Li, Y., Shi, L. Z., Hwang, P. Y., He, J., Wang, H., Razavian, N., Berns, M. W., and Wu, X. (2013) Microhomology-mediated end joining and homologous recombination share the initial end resection step to repair DNA double-strand breaks in mammalian cells. *Proc. Natl. Acad. Sci. U.S.A.* **110,** 7720–7725
16. Gravel, S., Chapman, J. R., Magill, C., and Jackson, S. P. (2008) DNA helicases Sgs1 and BLM promote DNA double-strand break resection. *Genes Dev.* **22,** 2767–2772
17. Nimonkar, A. V., Genschel, J., Kinoshita, E., Polaczek, P., Campbell, J. L., Wyman, C., Modrich, P., and Kowalczykowski, S. C. (2011) BLM-DNA2-RPA-MRN and EXO1-BLM-RPA-MRN constitute two DNA end resection machineries for human DNA break repair. *Genes Dev.* **25,** 350–362
18. Karanja, K. K., Cox, S. W., Duxin, J. P., Stewart, S. A., and Campbell, J. L. (2012) DNA2 and EXO1 in replication-coupled, homology-directed repair and in the interplay between HDR and the FA/BRCA network. *Cell Cycle* **11,** 3983–3996
19. Shibata, A., Moiani, D., Arvai, A. S., Perry, J., Harding, S. M., Genois, M. M., Maity, R., van Rossum-Fikkert, S., Kertokalio, A., Romoli, F., Ismail, A., Ismalaj, E., Petricci, E., Neale, M. J., Bristow, R. G., Masson, J. Y., Wyman, C., Jeggo, P. A., and Tainer, J. A. (2014) DNA double-strand break repair pathway choice is directed by distinct MRE11 nuclease activities. *Mol. Cell* **53,** 7–18
20. Bernstein, K. A., Gangloff, S., and Rothstein, R. (2010) The RecQ DNA helicases in DNA repair. *Annu. Rev. Genet.* **44,** 393–417
21. Yan, H., McCane, J., Toczylowski, T., and Chen, C. (2005) Analysis of the *Xenopus* Werner syndrome protein in DNA double-strand break repair. *J. Cell Biol.* **171,** 217–227
22. Liao, S., Toczylowski, T., and Yan, H. (2008) Identification of the Xenopus DNA2 protein as a major nuclease for the 5′→3′ strand-specific processing of DNA ends. *Nucleic Acids Res.* **36,** 6091–6100
23. Liao, S., Guay, C., Toczylowski, T., and Yan, H. (2012) Analysis of MRE11's function in the 5′→3′ processing of DNA double-strand breaks. *Nucleic Acids Res.* **40,** 4496–4506
24. Saydam, N., Kanagaraj, R., Dietschy, T., Garcia, P. L., Peña-Diaz, J., Shevelev, I., Stagljar, I., and Janscak, P. (2007) Physical and functional interactions between Werner syndrome helicase and mismatch-repair initiation factors. *Nucleic Acids Res.* **35,** 5706–5716
25. Adams, K. E., Medhurst, A. L., Dart, D. A., and Lakin, N. D. (2006) Recruitment of ATR to sites of ionising radiation-induced DNA damage requires ATM and components of the MRN protein complex. *Oncogene* **25,** 3894–3904
26. Sartori, A. A., Lukas, C., Coates, J., Mistrik, M., Fu, S., Bartek, J., Baer, R., Lukas, J., and Jackson, S. P. (2007) Human CtIP promotes DNA end resection. *Nature* **450,** 509–514
27. Yang, J., O'Donnell, L., Durocher, D., and Brown, G. W. (2012) RMI1 promotes DNA replication fork progression and recovery from replication fork stress. *Mol. Cell Biol.* **32,** 3054–3064
28. Orren, D. K., Brosh, R. M., Jr., Nehlin, J. O., Machwe, A., Gray, M. D., and Bohr, V. A. (1999) Enzymatic and DNA binding properties of purified WRN protein: high affinity binding to single-stranded DNA but not to DNA damage induced by 4NQO. *Nucleic Acids Res.* **27,** 3557–3566
29. Kanagaraj, R., Saydam, N., Garcia, P. L., Zheng, L., and Janscak, P. (2006) Human RECQ5β helicase promotes strand exchange on synthetic DNA structures resembling a stalled replication fork. *Nucleic Acids Res.* **34,** 5217–5231
30. El-Shemerly, M., Janscak, P., Hess, D., Jiricny, J., and Ferrari, S. (2005) Degradation of human exonuclease 1b upon DNA synthesis inhibition. *Cancer Res.* **65,** 3604–3609
31. Henricksen, L. A., Umbricht, C. B., and Wold, M. S. (1994) Recombinant replication protein A: expression, complex formation, and functional characterization. *J. Biol. Chem.* **269,** 11121–11132
32. Masuda-Sasa, T., Imamura, O., and Campbell, J. L. (2006) Biochemical analysis of human Dna2. *Nucleic Acids Res.* **34,** 1865–1875
33. Pfaffl, M. W. (2001) A new mathematical model for relative quantification in real-time RT-PCR. *Nucleic Acids Res.* **29,** e45
34. Bennardo, N., Cheng, A., Huang, N., and Stark, J. M. (2008) Alternative-NHEJ is a mechanistically distinct pathway of mammalian chromosome break repair. *PLoS Genet.* **4,** e1000110
35. Gunn, A., and Stark, J. M. (2012) I-SceI-based assays to examine distinct repair outcomes of mammalian chromosomal double strand breaks. *Methods Mol. Biol.* **920,** 379–391
36. Richardson, C., Moynahan, M. E., and Jasin, M. (1998) Double-strand break repair by interchromosomal recombination: suppression of chromosomal translocations. *Genes Dev.* **12,** 3831–3842
37. Karow, J. K., Chakraverty, R. K., and Hickson, I. D. (1997) The Bloom's syndrome gene product is a 3′-5′ DNA helicase. *J. Biol. Chem.* **272,** 30611–30614
38. Brosh, R. M., Jr., Waheed, J., and Sommers, J. A. (2002) Biochemical characterization of the DNA substrate specificity of Werner syndrome helicase. *J. Biol. Chem.* **277,** 23236–23245
39. Shen, J. C., Gray, M. D., Oshima, J., Kamath-Loeb, A. S., Fry, M., and Loeb, L. A. (1998) Werner syndrome protein: I: DNA helicase and DNA exonuclease reside on the same polypeptide. *J. Biol. Chem.* **273,** 34139–34144
40. Kamath-Loeb, A. S., Shen, J. C., Loeb, L. A., and Fry, M. (1998) Werner syndrome protein: II: characterization of the integral 3′ → 5′ DNA exonuclease. *J. Biol. Chem.* **273,** 34145–34150
41. Kim, J. H., Kim, H. D., Ryu, G. H., Kim, D. H., Hurwitz, J., and Seo, Y. S. (2006) Isolation of human DNA2 endonuclease and characterization of its enzymatic properties. *Nucleic Acids Res.* **34,** 1854–1864
42. Avemann, K., Knippers, R., Koller, T., and Sogo, J. M. (1988) Camptothecin, a specific inhibitor of type I DNA topoisomerase, induces DNA breakage at replication forks. *Mol. Cell Biol.* **8,** 3026–3034
43. Lee, J. W., Harrigan, J., Opresko, P. L., and Bohr, V. A. (2005) Pathways and functions of the Werner syndrome protein. *Mech. Ageing Dev.* **126,** 79–86
44. Kanagaraj, R., Parasuraman, P., Mihaljevic, B., van Loon, B., Burdova, K., König, C., Furrer, A., Bohr, V. A., Hübscher, U., and Janscak, P. (2012) Involvement of Werner syndrome protein in MUTYH-mediated repair of oxidative DNA damage. *Nucleic Acids Res.* **40,** 8449–8459
45. Stark, J. M., Pierce, A. J., Oh, J., Pastink, A., and Jasin, M. (2004) Genetic steps of mammalian homologous repair with distinct mutagenic conse-

quences. *Mol. Cell Biol.* **24,** 9305–9316

46. Wu, L., and Hickson, I. D. (2003) The Bloom's syndrome helicase suppresses crossing over during homologous recombination. *Nature* **426,** 870–874
47. Yin, J., Sobeck, A., Xu, C., Meetei, A. R., Hoatlin, M., Li, L., and Wang, W. (2005) BLAP75, an essential component of Bloom's syndrome protein complexes that maintain genome integrity. *EMBO J.* **24,** 1465–1476
48. Wu, L., Bachrati, C. Z., Ou, J., Xu, C., Yin, J., Chang, M., Wang, W., Li, L., Brown, G. W., and Hickson, I. D. (2006) BLAP75/RMI1 promotes the BLM-dependent dissolution of homologous recombination intermediates. *Proc. Natl. Acad. Sci. U.S.A.* **103,** 4068–4073
49. Xu, D., Guo, R., Sobeck, A., Bachrati, C. Z., Yang, J., Enomoto, T., Brown, G. W., Hoatlin, M. E., Hickson, I. D., and Wang, W. (2008) RMI, a new OB-fold complex essential for Bloom syndrome protein to maintain genome stability. *Genes Dev.* **22,** 2843–2855
50. Cheng, W. H., von Kobbe, C., Opresko, P. L., Arthur, L. M., Komatsu, K., Seidman, M. M., Carney, J. P., and Bohr, V. A. (2004) Linkage between Werner syndrome protein and the Mre11 complex via Nbs1. *J. Biol. Chem.* **279,** 21169–21176
51. Lan, L., Nakajima, S., Komatsu, K., Nussenzweig, A., Shimamoto, A., Oshima, J., and Yasui, A. (2005) Accumulation of Werner protein at DNA double-strand breaks in human cells. *J. Cell Sci.* **118,** 4153–4162
52. Tomimatsu, N., Mukherjee, B., Deland, K., Kurimasa, A., Bolderson, E., Khanna, K. K., and Burma, S. (2012) Exo1 plays a major role in DNA end resection in humans and influences double-strand break repair and damage signaling decisions. *DNA Repair* **11,** 441–448
53. Yu, C. E., Oshima, J., Fu, Y. H., Wijsman, E. M., Hisama, F., Alisch, R., Matthews, S., Nakura, J., Miki, T., Ouais, S., Martin, G. M., Mulligan, J., and Schellenberg, G. D. (1996) Positional cloning of the Werner's syndrome gene. *Science* **272,** 258–262
54. Salk, D., Au, K., Hoehn, H., and Martin, G. M. (1981) Cytogenetics of Werner's syndrome cultured skin fibroblasts: variegated translocation mosaicism. *Cytogenet. Cell Genet.* **30,** 92–107
55. Fukuchi, K., Martin, G. M., and Monnat, R. J., Jr. (1989) Mutator phenotype of Werner syndrome is characterized by extensive deletions. *Proc. Natl. Acad. Sci. U.S.A.* **86,** 5893–5897
56. Melcher, R., von Golitschek, R., Steinlein, C., Schindler, D., Neitzel, H., Kainer, K., Schmid, M., and Hoehn, H. (2000) Spectral karyotyping of Werner syndrome fibroblast cultures. *Cytogenet. Cell Genet.* **91,** 180–185
57. Bunting, S. F., and Nussenzweig, A. (2013) End-joining, translocations and cancer. *Nat. Rev. Cancer* **13,** 443–454
58. Symington, L. S., and Gautier, J. (2011) Double-strand break end resection and repair pathway choice. *Annu. Rev. Genet.* **45,** 247–271
59. Chen, L., Huang, S., Lee, L., Davalos, A., Schiestl, R. H., Campisi, J., and Oshima, J. (2003) WRN, the protein deficient in Werner syndrome, plays a critical structural role in optimizing DNA repair. *Aging Cell* **2,** 191–199
60. Perry, J. J., Yannone, S. M., Holden, L. G., Hitomi, C., Asaithamby, A., Han, S., Cooper, P. K., Chen, D. J., and Tainer, J. A. (2006) WRN exonuclease structure and molecular mechanism imply an editing role in DNA end processing. *Nat. Struct. Mol. Biol.* **13,** 414–422
61. Saintigny, Y., Makienko, K., Swanson, C., Emond, M. J., and Monnat, R. J., Jr. (2002) Homologous recombination resolution defect in Werner syndrome. *Mol. Cell Biol.* **22,** 6971–6978
62. Swanson, C., Saintigny, Y., Emond, M. J., and Monnat, R. J., Jr. (2004) The Werner syndrome protein has separable recombination and survival functions. *DNA Repair* **3,** 475–482
63. Bussen, W., Raynard, S., Busygina, V., Singh, A. K., and Sung, P. (2007) Holliday junction processing activity of the BLM-Topo IIIα-BLAP75 complex. *J. Biol. Chem.* **282,** 31484–31492
64. Raynard, S., Bussen, W., and Sung, P. (2006) A double Holliday junction dissolvasome comprising BLM, topoisomerase IIIα, and BLAP75. *J. Biol. Chem.* **281,** 13861–13864
65. Xue, X., Raynard, S., Busygina, V., Singh, A. K., and Sung, P. (2013) Role of replication protein A in double Holliday junction dissolution mediated by the BLM-Topo IIIα-RMI1-RMI2 protein complex. *J. Biol. Chem.* **288,** 14221–14227

4.2.2. The Mismatch-Binding Factor MutSß Can Mediate ATR Activation in Response to DNA Double-Strand Breaks

Kamila Burdova, Boris Mihaljevic, **Andreas Sturzenegger**, Naga Raja Chappidi and Pavel Janscak

This work was published in Molecular Cell in 2015.

Here, I first constructed different plasmids for expression of MSH3 in human cells (pcDNA3.1- and pEGFP-c1-vector) and for generation of bacmids (pFastBac1-vector). In addition, I also generated various MSH3 mutant constructs, where the loop-binding motif of MSH3 has been mutated (MSH3-Y245S, MSH3-K246E and MSH3-Y245S/K246E). Next, I purified recombinant MSH2/MSH3-Y245S/K246E herodimer after expression in Sf-9 insect cells. Moreover, I performed all DNase I footprinting experiments.

Molecular Cell

Article

The Mismatch-Binding Factor MutSβ Can Mediate ATR Activation in Response to DNA Double-Strand Breaks

Graphical Abstract

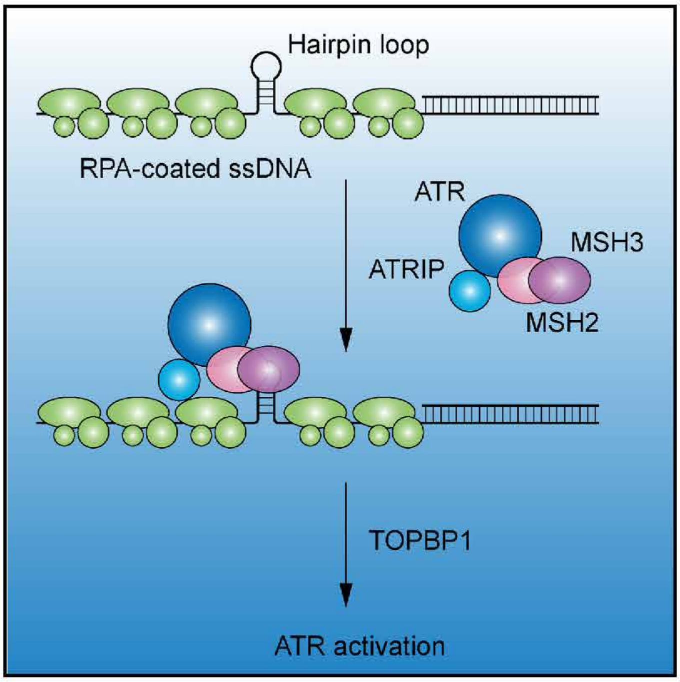

Authors

Kamila Burdova, Boris Mihaljevic, Andreas Sturzenegger, Nagaraja Chappidi, Pavel Janscak

Correspondence

pjanscak@imcr.uzh.ch

In Brief

ATRIP mediates binding of the ATR kinase to RPA-coated ssDNA at sites of DNA damage, which leads to ATR activation. Burdova et al. show that MutSβ binds to hairpin loops in RPA-ssDNA and mediates ATR-ATRIP recruitment to promote ATR activation.

Highlights

- MutSβ promotes ATR activation in response to DNA double-strand breaks (DSBs)
- MutSβ interacts with ATR-ATRIP and promotes ATRIP recruitment to DSB sites
- MutSβ binds to hairpin loops in RPA-ssDNA and facilitates ATRIP recruitment
- ATR activation by ssDNA depends on the hairpin loop-binding activity of MutSβ

Burdova et al., 2015, Molecular Cell *59*, 603–614
August 20, 2015 ©2015 Elsevier Inc.
http://dx.doi.org/10.1016/j.molcel.2015.06.026

CellPress

Molecular Cell
Article

The Mismatch-Binding Factor MutSβ Can Mediate ATR Activation in Response to DNA Double-Strand Breaks

Kamila Burdova,[1,3] Boris Mihaljevic,[2,3,4] Andreas Sturzenegger,[2] Nagaraja Chappidi,[2] and Pavel Janscak[1,2,*]
[1]Institute of Molecular Genetics, Academy of Sciences of the Czech Republic, 142 20 Prague 4, Czech Republic
[2]Institute of Molecular Cancer Research, University of Zurich, 8057 Zurich, Switzerland
[3]Co-first author
[4]Present address: Department of Immunology and Medical Genetics, School of Medicine, University of Split, 21000 Split, Croatia
*Correspondence: pjanscak@imcr.uzh.ch
http://dx.doi.org/10.1016/j.molcel.2015.06.026

SUMMARY

Ataxia telangiectasia-mutated and Rad3-related (ATR) protein kinase, a master regulator of DNA-damage response, is activated by RPA-coated single-stranded DNA (ssDNA) generated at stalled replication forks or DNA double-strand breaks (DSBs). Here, we identify the mismatch-binding protein MutSβ, a heterodimer of MSH2 and MSH3, as a key player in this process. MSH2 and MSH3 form a complex with ATR and its regulatory partner ATRIP, and their depletion compromises the formation of ATRIP foci and phosphorylation of ATR substrates in cells responding to replication-associated DSBs. Purified MutSβ binds to hairpin loop structures that persist in RPA-ssDNA complexes and promotes ATRIP recruitment. Mutations in the mismatch-binding domain of MSH3 abolish the binding of MutSβ to DNA hairpin loops and its ability to promote ATR activation by ssDNA. These results suggest that hairpin loops might form in ssDNA generated at sites of DNA damage and trigger ATR activation in a process mediated by MutSβ.

INTRODUCTION

Cells are constantly challenged by various types of DNA damage that can induce genomic instability, a hallmark of tumorigenesis and cancer progression (Ciccia and Elledge, 2010; Jackson and Bartek, 2009). The most dangerous DNA lesion in the cell is the DNA double-strand break (DSB), because it can give rise to chromosomal rearrangements (Jackson and Bartek, 2009). DSBs can be generated by agents such as ionizing radiation and radiomimetic drugs, or they can result as a consequence of replication fork collapse (Jackson and Bartek, 2009). Eukaryotic cells respond to DSBs by activating a complex network of pathways that lead to cell-cycle arrest, to DNA repair, and, in the case of excessive damage, to apoptosis or senescence (Ciccia and Elledge, 2010; Jackson and Bartek, 2009). Cells evolved two mechanistically distinct pathways to repair DSBs: non-homologous end joining (NHEJ) and homologous recombination (HR). NHEJ involves religation of the broken DNA ends and is frequently associated with a short deletion or insertion of DNA at the break site (van Gent and van der Burg, 2007). On the contrary, HR provides an accurate means of DSB repair because it is directed by an intact homologous DNA sequence (San Filippo et al., 2008). This process is largely restricted to the S/G2 phases of the cell cycle to ensure that the undamaged sister chromatid is used as a repair template, a mechanism preventing chromosomal rearrangements (San Filippo et al., 2008; Symington and Gautier, 2011).

The HR process is initiated by nuclease-mediated resection of broken DNA ends to generate 3′ single-stranded (ss) DNA tails that are coated by the heterotrimeric ssDNA-binding protein RPA (Symington and Gautier, 2011). This nucleoprotein structure serves as a platform for the recruitment and activation of the *Ataxia telangiectasia*-mutated (ATM)- and Rad3-related (ATR) kinase, a master DNA damage response regulator that phosphorylates the checkpoint kinase 1 (CHK1) and other proteins such as SMC1 and RPA to promote cell-cycle arrest and DNA repair (Cimprich and Cortez, 2008). ATR is targeted to RPA-coated ssDNA via its interacting partner ATRIP (Zou and Elledge, 2003). Activation of the ATR kinase depends on its interaction with TOPBP1 that is recruited to the DNA damage site and associates with the RAD9-RAD1-HUS1 (9-1-1) complex loaded on double-stranded DNA (dsDNA) at the ssDNA/dsDNA junction by the RAD17-RFC clamp loader (Delacroix et al., 2007; Kumagai et al., 2006; Lee et al., 2007; Mordes et al., 2008; Zou et al., 2002). ATR can be also activated in a 9-1-1/RAD17-independent manner through targeting of TOPBP1 to RPA-coated ssDNA via the MRE11-RAD50-NBS1 (MRN) complex (Shiotani et al., 2013).

The mismatch repair (MMR) system corrects DNA mismatches arising during DNA replication and genetic recombination (Jiricny, 2006; Kunkel and Erie, 2005). Germline mutations in the genes responsible for MMR are the major cause of hereditary non-polyposis colon cancer, a dominantly inherited disorder with high penetrance (Peltomäki, 2001). The key proteins involved in the initiation of MMR reaction are highly conserved in evolution. In eukaryotic cells, mispaired bases are recognized by two heterodimeric complexes, MSH2-MSH6 (MutSα) and

MSH2-MSH3 (MutSβ), which have different but overlapping DNA substrate specificity. MutSα recognizes base-base mismatches and single- and double-base insertions, while MutSβ binds to loops of 1–14 extrahelical nucleotides (Habraken et al., 1996; Palombo et al., 1996). In addition to mismatch-binding functionality, both MutSα and MutSβ contain two Walker-type ATP-binding sites, one in each subunit, and display ATPase activity, which is essential for the MMR reaction (Kunkel and Erie, 2005). Binding of MutSα or MutSβ to a mismatch brings about an exchange of ADP for ATP in the ATP-binding sites of the enzyme and converts it into a sliding DNA clamp that, in a complex with MutLα (heterodimer of MLH1 and PMS2), triggers EXO1-mediated excision of the error-containing strand followed by DNA resynthesis (Gradia et al., 1999; Jiricny, 2006; Wilson et al., 1999).

Interestingly, a number of studies have demonstrated that the proteins required for the initiation of MMR are also involved in the cellular response to DSBs. It has been shown that the human MMR proteins MSH2, MSH3, MSH6, and MLH1 accumulate rapidly at sites of DSBs generated by laser microirradiation (Hong et al., 2008). Studies in mouse cells have revealed that Msh2 is required for efficient repair of DSBs by HR and confers resistance to DSB-inducing agents (Bennardo et al., 2009; Franchitto et al., 2003; Pichierri et al., 2001). In response to ionizing radiation, G2/M checkpoint activation in Msh2$^{-/-}$ cells is inefficient, such that the cells arrest only transiently before progressing into mitosis (Franchitto et al., 2003). More recently, it has been shown that Msh2$^{-/-}$ and Msh3$^{-/-}$, but not Msh6$^{-/-}$, mouse embryonic fibroblasts display a significant increase in chromatid breaks compared to wild-type cells, indicating a defect in DSB repair due to loss of MutSβ function (van Oers et al., 2014). However, the role of MutSβ in the cellular response to DSBs remains largely uncharacterized. Here, we present several lines of evidence suggesting that MutSβ mediates ATR-ATRIP recruitment to RPA-coated ssDNA at sites of replication-associated DSBs to promote ATR activation.

RESULTS

MSH2 and MSH3, but Not MSH6, Are Required for Efficient Repair of DSBs by HR

In agreement with previously published data, we observed a rapid accumulation of the human MMR proteins MSH2, MSH3, and MSH6 at nuclear volumes irradiated by UVA laser if cells were pretreated with bromodeoxyuridine (BrdU), indicating that these proteins act at sites of DSBs (Figures S1A and S1B) (Hong et al., 2008). Interestingly, the MMR proteins accumulated at laser stripes in both cyclin A-positive (S/G2) and cyclin A-negative (G1) cells, indicating that they operate at DSBs throughout interphase (Figures S1C and S1D). A study using mouse embryonic stem cells has shown that MSH2 is required for efficient repair of DSBs via HR, whereas it is dispensable for DSB repair via NHEJ and single-strand annealing (Bennardo et al., 2009). In order to determine which of the two heterodimeric complexes of MSH2 (MutSα and MutSβ) is involved in HR-mediated DSB repair, we tested the effect of small interfering RNA (siRNA)-mediated depletion of MSH2, MSH3, and MSH6 on the HR repair activity of the established reporter cell lines HEK293/DR-GFP and U2OS/DR-GFP (Bennardo et al., 2009; Gunn and Stark, 2012). In these cells, a single HR event triggered by a DSB created by the I-SceI endonuclease gives rise to a functional GFP allele, which can be scored by flow cytometry (Bennardo et al., 2009; Gunn and Stark, 2012). We found that cells depleted of MSH2 or MSH3 showed a markedly reduced frequency of I-SceI-induced HR repair events as compared to mock-depleted cells (Figure 1A; Figure S1E). In contrast, lack of MSH6 did not significantly affect HR repair efficiency in either reporter cell line (Figure 1A). To substantiate these findings, we investigated the role of MMR proteins in the repair of replication-associated DSBs induced by the topoisomerase I inhibitor camptothecin (CPT) (Avemann et al., 1988). Using pulsed-field gel electrophoresis, we found that, upon treatment with CPT, MSH2- and MSH3-depleted cells displayed much higher levels of chromosome fragmentation compared to mock-depleted cells, suggesting a DNA repair defect (Figures 1B–1D). On the contrary, the level of DNA breakage in MSH6-depleted cells was comparable to that of mock-depleted cells (Figures 1B–1D). These results provide strong evidence that MSH2 promotes HR-mediated DSB repair as part of the MutSβ heterodimer. Of note, depletion of MSH6 dramatically decreased the level of MSH2 (Figure 1D; Figure S1E). This is consistent with the observation that the majority of MSH2 molecules in the cell exist in complex with MSH6 (Chang et al., 2000). The level of expression of MSH3 mRNA in human cells is much lower compared to the expression levels of MSH2 and MSH6 (Chang et al., 2000). Therefore, upon acute depletion of MSH6, there is not enough MSH3 available to substitute for MSH6 in binding and stabilization of MSH2.

MSH2 Accumulates at DSB Sites during the Presynaptic Phase of HR

To gain insight into the role of human MutSβ in DSB repair by HR, we asked which HR factors are required for the recruitment of MSH2 to sites of laser-induced DSBs in U2OS cells. We found that MSH2 recruitment to DSB sites, revealed by staining for the phosphorylated form of histone H2AX (γ-H2AX), was not significantly affected upon depletion of RAD51 recombinase, suggesting that, during DSB repair by HR, MSH2 is recruited prior to the formation of joint DNA molecules (Figures 1E and 1F; Figure S1F). On the contrary, depletion of CtIP, which acts in conjunction with the MRN complex to initiate DSB-end resection, significantly abrogated the recruitment of MSH2 to laser-induced DSBs both in G1 and S/G2 cells (Figures 1E and 1F; Figure S1G) (Sartori et al., 2007). In addition, using the ATLD1 cell line carrying a hypomorphic mutation in the *MRE11* gene and its derivative harboring a retrovirus expressing wild-type MRE11 cDNA, we found that the trafficking of MSH2 to DSB sites was dependent on the presence of MRN complex (Figures 1G and 1H). Together, these results suggest that MutSβ and MutSα are recruited to sites of DSBs during the presynaptic phase of HR.

MutSβ Promotes ATR Activation in Response to DSBs

Having obtained evidence that MMR proteins operate at sites of DSBs prior to the formation of recombination intermediates, we sought to assess whether they have a role in DNA-end resection. To this end, we tested the effect of depletion of these proteins on

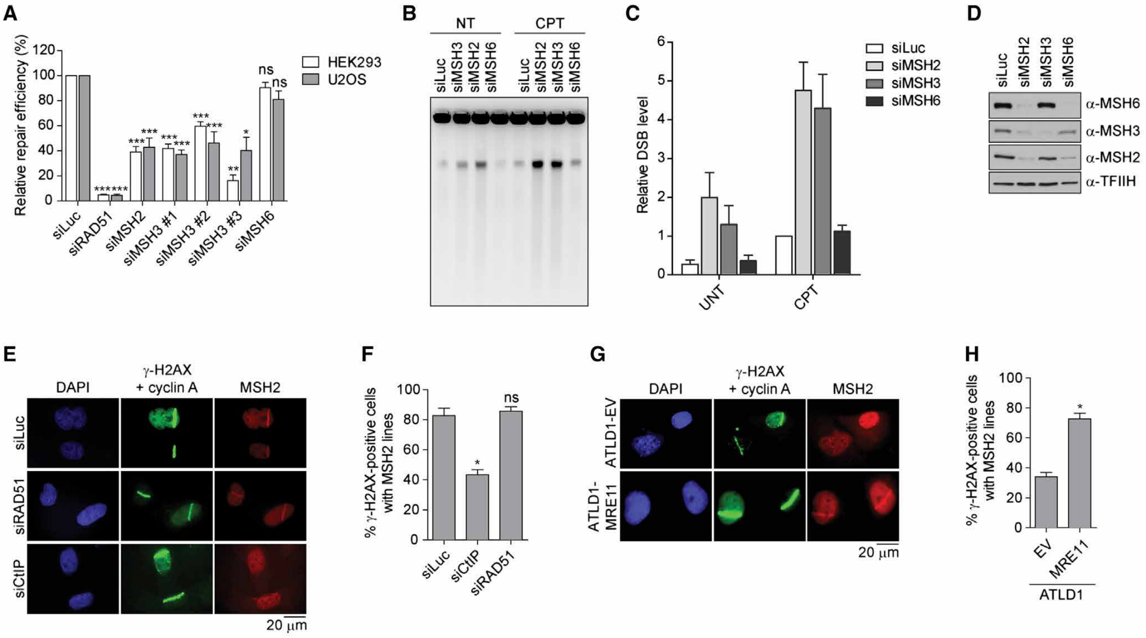

Figure 1. Involvement of MSH2 and MSH3 in HR-Mediated DSB Repair

(A) Efficiency of HR-mediated repair of I-SceI-induced DSBs in HEK293/DR-GFP and U2OS/DR-GFP cells transfected with indicated siRNAs. Data are normalized to the value measured for mock-depleted cells (siLuc).

(B) Effect of depletion of MMR proteins on the extent of DNA breakage in U2OS cells treated with 1 μM CPT for 2 hr. Genomic DNA was analyzed by PFGE.

(C) Quantification of chromosomal breakage by PFGE in cells treated as in (B). DNA bands were quantified using ImageJ software. Data are normalized to the value estimated for CPT-treated cells transfected with siLuc. UNT, untreated.

(D) Western blot analysis of extracts from U2OS cells transfected with indicated siRNAs.

(E) Indirect immunofluorescence imaging of MSH2, γ-H2AX, and cyclin A in mock-, CtIP-, and RAD51-depleted U2OS cells at 30 min after microirradiation with UVA laser. Cells positive for cyclin A (dispersed nuclear staining) are in S/G2, whereas cells lacking cyclin A are in G1.

(F) Quantitative analysis of immunofluorescence micrographs represented in (E).

(G) Indirect immunofluorescence imaging of MSH2, γ-H2AX, and cyclin A in ATLD1-EV and ATLD1-MRE11 cells exposed to laser microirradiation. EV, empty vector.

(H) Quantitative analysis of images represented in (G).

For (A), (C), (F), and (H), the data are represented as mean ± SEM. $^{*}p < 0.05$; $^{**}p < 0.005$; $^{***}p < 0.0005$; ns, not significant.

See also Figure S1.

the formation of RPA foci in response to replication-associated DSBs induced by CPT. We found that siRNA-mediated depletion of MSH2, MSH3, MSH6, or MLH1 had no significant effect on the formation of RPA foci in CPT-treated U2OS cells (Figure 2A; Figures S2A and S2B). In contrast, the formation of CPT-induced RPA foci was severely compromised by depletion of CtIP (Figure 2A; Figures S2A and S2B).

In response to CPT, the N-terminal domain of the middle subunit of RPA, RPA2, is sequentially phosphorylated on multiple residues, a process required for DSB repair (Anantha et al., 2007; Sartori et al., 2007; Shiotani et al., 2013). Therefore, we asked whether MMR proteins play a role in CPT-induced phosphorylation of RPA in U2OS cells. Using phospho-specific antibodies, we found that depletion of MSH2 or MSH3, but not MSH6 or MLH1, abrogated RPA2 phosphorylation at Ser4/8 (Figures 2B–2D; Figures S2C and S2D), which is mediated by DNA-dependent protein kinase (DNA-PK) or ATM following RPA2 Ser33 phosphorylation by ATR (Anantha et al., 2007; Shiotani et al., 2013). We also found that depletion of MSH2 or MSH3 significantly reduced the phosphorylation of RPA2 Ser33 as compared to mock-depleted cells (Figure S2E). Notably, the fold of reduction of RPA2 Ser33 phosphorylation caused by lack of the MutSβ subunits was comparable to that observed upon depletion of CtIP (Figure S2E). The defect in CPT-induced RPA phosphorylation of cells lacking MSH2 or MSH3 was also apparent from disappearance of the RPA2 band with a reduced electrophoretic mobility, which corresponds to hyper-phosphorylated form of RPA2 (Figure 2B; Figure S2E). Depletion of MMR proteins did not cause a reduction in BrdU incorporation in U2OS cells, excluding the possibility that the observed impairment of CPT-induced phosphorylation of RPA2 in MSH2- and MSH3-depleted cells was due to a defect in DNA replication that is required for the induction of DSBs by CPT (Figure S2F). Moreover, depletion of MMR proteins had no effect on p53

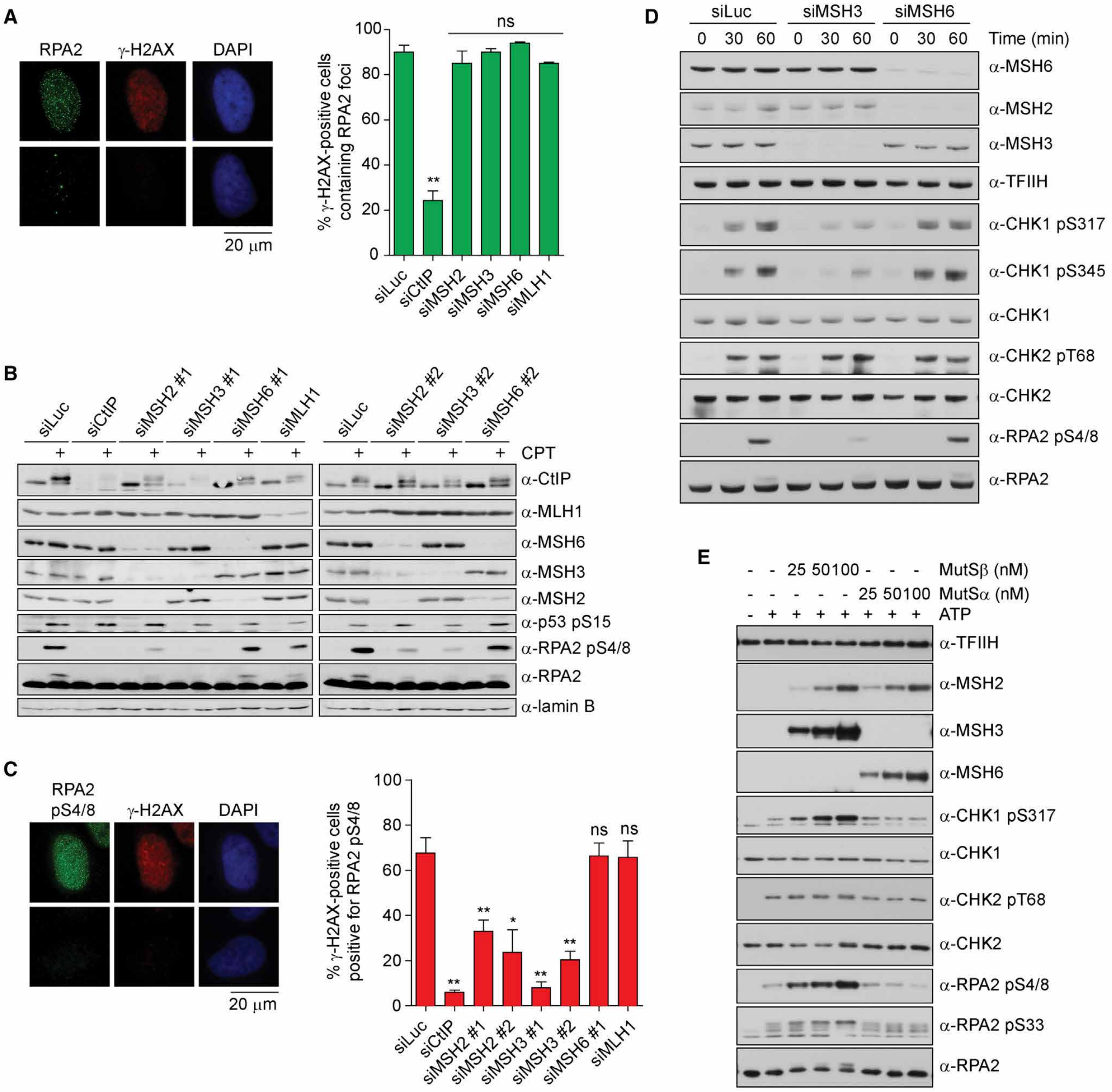

Figure 2. Lack of MutSβ Impairs ATR-Dependent Phosphorylation of RPA and CHK1 in Response to Replication-Associated DSBs

(A) Formation of RPA2 foci in mock-, CtIP-, MSH2-, MSH3-, and MSH6-depleted U2OS cells treated with 1 μM CPT for 1 hr. Left: representative images of mock-depleted (siLuc) cells positive (top) or negative (bottom) for γ-H2AX staining. Right: a graph showing percentage of γ-H2AX-positive cells with RPA foci determined for each sample using the Olympus Scan^R screening station.

(B) Western blot analysis of extracts of U2OS cells depleted of indicated proteins. Cells were either treated with 1 μM CPT for 1 hr (lane marked by +) or left untreated.

(C) Formation of Ser4/8-phophorylated form of RPA2 in mock-, CtIP-, MSH2-, MSH3-, and MSH6-depleted U2OS cells after treatment with 1 μM CPT for 1 hr. Left: representative images of mock-depleted cells positive (top) or negative (bottom) for γ-H2AX staining. Right: a graph showing percentage of γ-H2AX-positive cells containing Ser4/8-phosphorylated RPA2 determined for each condition using the Olympus Scan^R screening station.

(D) Kinetics of CPT-induced phosphorylation of CHK1 in mock-, MSH3-, and MSH6-depleted U2OS cells. Cells were treated with 1 μM CPT for indicated times. Whole-cell extracts were analyzed by western blotting.

(E) Effect of recombinant MutSα or MutSβ on ssDNA-induced phosphorylation of RPA and CHK1 in nuclear extracts of HCT116 cells. MutSα and MutSβ were present at indicated concentrations.

For (A) and (C), the data are represented as mean ± SEM. $^*p < 0.05$; $^{**}p < 0.005$; ns, not significant.

See also Figures S2 and S3.

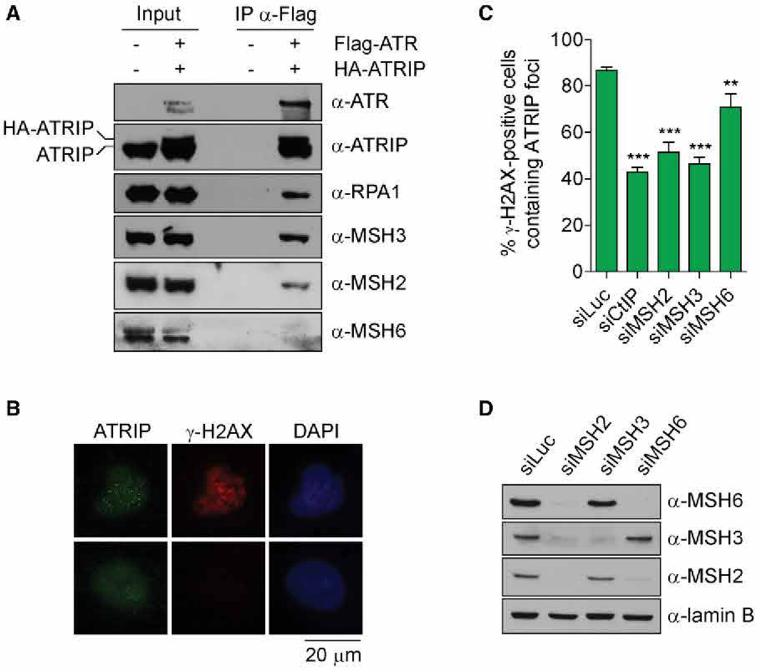

Figure 3. MSH2 and MSH3 Form a Complex with ATR and ATRIP and Promote ATRIP Recruitment to Sites of DSBs in Human Cells

(A) Co-immunoprecipitation assay. HEK293 cells were transfected with plasmids expressing Flag-tagged ATR and HA-tagged ATRIP. Whole-cell extracts from transfected and non-transfected cells were subjected to immunoprecipitation with anti-Flag M2 beads (α-Flag). Immunoprecipitates (IPs) were analyzed by western blotting. Bands corresponding to HA-ATRIP and endogenous ATRIP are indicated.

(B) Formation of ATRIP foci in U2OS cells treated with 1 μM CPT for 1 hr. Representative images of cells that are positive (top) or negative (bottom) for γ-H2AX staining are shown.

(C) Frequency of the formation of CPT-induced ATRIP foci in mock-, MSH2-, MSH3-, MSH6-, and CtIP-depleted U2OS cells. Percentage of γ-H2AX-positive cells containing ATRIP foci was determined for each condition using the Olympus Scan^R screening station. The data are represented as mean ± SEM. $^{**}p < 0.005$; $^{***}p < 0.0005$.

(D) Western blot analysis of extracts from U2OS cells transfected with indicated siRNAs.

See also Figure S4.

phosphorylation at Ser15 or the formation of γ-H2AX after CPT treatment, further confirming that CPT-induced DSBs arise normally in these cells (Figure 2B; data not shown).

Phosphorylation of RPA2 on Ser33 is characteristic of ATR activation (Shiotani et al., 2013). Thus, the finding that MSH2- and MSH3-deficient cells have a defect in RPA2 Ser33 phosphorylation in response to CPT treatment prompted us to further explore a possible role of MutSβ in the activation of ATR by DSBs. In response to CPT, ATR rapidly phosphorylates the checkpoint effector kinase CHK1 at several sites, including Ser317 and Ser345 (Shiotani et al., 2013) (Figure S3A). Hence, we asked whether depletion of MutSβ affected this critical event in the ATR-mediated DNA damage checkpoint pathway (Bartek and Lukas, 2003). We found that depletion of MSH3, but not MSH6, largely abolished CHK1 Ser317 and Ser345 phosphorylation in U2OS cells treated with CPT, suggesting that MutSβ indeed promotes ATR activation (Figure 2D; Figure S2D). On the contrary, the CPT-induced CHK2 phosphorylation at Thr68 was not affected in cells lacking MSH3, indicating that MutSβ has no role in the activation of ATM (Figure 2D) (Bartek and Lukas, 2003).

ATR-dependent phosphorylation of RPA2 can be induced in HeLa cell nuclear extracts by the addition of ssDNA (Shiotani et al., 2013). In order to substantiate the aforementioned findings, we measured the levels of RPA2 phospho-Ser4/8, RPA2 phospho-Ser33, and CHK1 phospho-Ser317 in nuclear extracts of the MSH3-deficient colorectal cancer cell line HCT116 that were supplemented with increasing concentrations of purified MutSβ (or MutSα) protein together with a 90-mer ssDNA oligonucleotide. We found that MutSβ, but not MutSα, stimulated phosphorylation of both RPA2 and CHK1 in a dose-dependent manner, whereas it had no effect on CHK2 phosphorylation at Thr68 under these conditions (Figure 2E). Similar results were obtained with HeLa cell nuclear extracts (Figure S2G). Moreover, we found that MutLα, added alone or in combination with either MutSα or MutSβ, had no effect on ssDNA-induced phosphorylation of RPA and CHK1 in HCT116 extracts (Figure S2H).

Together, these results provide strong evidence that MutSβ promotes ATR activation in response to DSBs in a manner independent of MutSα and MutLα.

MutSβ Forms a Complex with ATR and ATRIP and Mediates ATRIP Recruitment to Sites of DSBs in Human Cells

MSH2 has been shown to form a complex with ATR and ATRIP in human cells (Wang and Qin, 2003). This suggests that MutSβ might mediate ATR activation by recruiting ATR-ATRIP to resected DNA ends. To explore this possibility, we first investigated whether the cellular complex formed between MSH2, ATR, and ATRIP contains MSH3. To this end, HEK293 cells were transfected with vectors expressing Flag-ATR and HA-ATRIP, respectively, and complex formation between the aforementioned proteins was investigated by immunoprecipitation using beads conjugated with an anti-Flag antibody. We found that the Flag-ATR immunoprecipitate from these cells contained ATRIP, RPA1, MSH2, and MSH3, but not MSH6 (Figure 3A). None of those proteins was present in a control immunoprecipitate from cells transfected with the empty vector (Figure 3A). Thus, these data demonstrate that, in human cells, MSH2 interacts with the ATR-ATRIP complex as part of the MutSβ heterodimer.

To determine whether MutSβ promotes the recruitment of ATR-ATRIP to sites of DSBs, we evaluated the effect of depletion of MSH2 or MSH3 on the formation of ATRIP foci in U2OS cells treated with CPT. We found that, 1 hr after addition of CPT, nearly 90% of γ-H2AX-positive cells contained ATRIP foci (Figures 3B and 3C). However, if cells were depleted of MSH2 or MSH3, the formation of ATRIP foci in response to CPT was markedly attenuated, with only 45% of γ-H2AX-positive cells displaying ATRIP foci under these conditions (Figures 3C and 3D; Figure S4). A comparable reduction in the frequency of ATRIP foci was observed with cells depleted of CtIP (Figures 3C and 3D; Figure S4). Thus, these data provide strong evidence for a role of MutSβ in the recruitment of ATR-ATRIP complex to sites of DSBs. Of note, MSH6 depletion also impaired the formation of ATRIP foci in response to CPT treatment, but to a lesser degree than depletion of MSH2 or MSH3 (Figure 3C).

MutSβ Binds to Hairpin Loop Structures Persisting in RPA-Coated ssDNA

Next, we asked how MutSβ might mediate ATRIP recruitment to sites of DNA damage. The ATR-ATRIP complex is recruited to DNA damage sites by RPA-coated ssDNA (Zou and Elledge, 2003). Therefore, we tested whether MutSβ binds to RPA, both free and in complex with ssDNA. In these experiments, we used a recombinant MutSβ heterodimer carrying a His_6-tag on the MSH3 subunit and a 90-mer oligonucleotide biotinylated at the 5′ end (b90). Where necessary, the ssDNA substrate (20 nM) was preincubated with over-stoichiometric amounts of RPA (100 nM) to ensure full DNA coverage. A 90-mer oligonucleotide is expected to accommodate three RPA molecules, assuming that the RPA trimer occupies a region spanning about 30 nucleotides (Fan and Pavletich, 2012). By a pull-down assay with nickel-nitrilotriacetic acid (Ni-NTA) agarose beads, we found that MutSβ was bound to RPA-ssDNA complexes, whereas it did not show any detectable binding to free RPA (Figure 4A). MutSα (His_6-tag on MSH6) that was also included in this analysis failed to bind both free RPA and RPA-ssDNA (Figure 4A). By pull-down assays with streptavidin-coated magnetic beads, we then compared binding of MutSα and MutSβ to free and RPA-coated ssDNA. We found that, although both proteins were bound to free ssDNA, RPA-ssDNA associated efficiently only with MutSβ (Figure 4B). Interestingly, binding of MutSβ to RPA-ssDNA was completely inhibited by ATP (Figure 4C). Full inhibition of MutSβ binding to RPA-ssDNA was also observed upon addition of the poorly hydrolyzable ATP analog ATP-γ-S, but not upon addition of ADP, suggesting that ATP binding by MutSβ triggers its dissociation from RPA-ssDNA (Figures 4C and S5A). This is further supported by the observation that ATP-induced dissociation of MutSβ from RPA-ssDNA was blocked by EDTA, which sequesters the ATPase cofactor Mg^{2+}, which is required for both ATP binding and hydrolysis (Figure S5B). Of note, in the presence of ATP or ATP-γ-S, MutSβ also failed to stably bind free ssDNA (Figure 4C).

As MutSβ was not bound to free RPA, it is possible that its interaction with RPA-coated ssDNA is mediated by hairpin loop structures that persist in ssDNA in the presence of RPA. In fact, the 90-mer oligonucleotide b90 used in our study can form several hairpin loops (Figure S6A). Therefore, we repeated our experiments using a 90-mer oligonucleotide containing only dT residues (b90T), which cannot form secondary structures. We found that MutSβ failed to bind b90T oligonucleotide if it was precoated with RPA (Figure 4D). In the absence of RPA, MutSβ was bound to b90T, but less efficiently compared to its binding to b90 (Figure S6B). Moreover, in HCT116 nuclear extract supplemented with MutSβ, b90T stimulated ATR activation less efficiently than b90 (Figure S6C). To substantiate these findings, we tested binding of MutSβ to five other oligonucleotides that can form hairpin loops (Figure S6A). We found that MutSβ was bound efficiently to all these oligonucleotides regardless of the presence of RPA (Figures 4D and S6B). Moreover, we found that MutSβ failed to bind RPA-ssDNA complexes at RPA concentrations exceeding 200% coverage of putative RPA-binding sites (Figure 4E).

To obtain further evidence that MutSβ binds to hairpin loop structures in the presence of RPA, we performed DNase I footprinting experiments with a non-biotinylated version of the b90 oligomer, which was radioactively labeled at the 5′ end. We found that, at a 6-fold molar excess of RPA over DNA (200% coverage of putative RPA-binding sites), the oligonucleotide was protected from DNase I cleavage, except for a region of about 30 nt at its 3′ end that can form two strong hairpin loops (Figure 4F; Figure S6A). It is important that, upon addition of MutSβ, this region was resistant to DNase I cleavage, suggesting that it indeed forms the predicted hairpin loops to which MutSβ binds (Figure 4G; Figure S6D). MutSβ failed to protect the oligonucleotide from DNase I cleavage if ATP was added to the reaction, which is consistent with our earlier finding that ATP binding to MutSβ triggers its dissociation from free or RPA-coated ssDNA (Figures 4C and 4G). In addition, in agreement with the results of our biotin pull-down experiments, we found that RPA could protect the entire oligonucleotide if present at concentrations exceeding 200% coverage of RPA-binding sites (Figures 4E and 4F).

Taken together, these data suggest that MutSβ binds to RPA-coated ssDNA through persistent DNA secondary structures.

Mutations in the Mismatch-Binding Domain of MSH3 Compromise Binding of MutSβ to RPA-ssDNA and Its Ability to Promote ATR Activation

Recent crystal structures of complexes of human MutSβ with DNA substrates containing insertion/deletion loops (IDLs) of different lengths have revealed the amino acid residues of MSH3 that are involved in IDL recognition, with tyrosine 245 interacting with the base pair immediately upstream of IDL and lysine 246 making contacts with the phosphodiester backbone of IDL (Gupta et al., 2012). Consistently, mutations of the tyrosine-lysine pair equivalent in the mismatch-binding domain (MBD) of *Saccharomyces cerevisiae* Msh3 (Y157S and K158E) have been found to cause a mutator phenotype (Dowen et al., 2010). To prove that MutSβ binds to RPA-coated ssDNA through persistent hairpin loops, we constructed and purified a mutant form of MutSβ carrying Y245S and K246E substitutions in the MSH3 subunit (Figure 5A). By both biotin pull-down assay and DNase I footprinting, we found that the MutSβ mutant could not bind to RPA-coated ssDNA, even if present in a large molar excess over the DNA substrate (Figures 5B

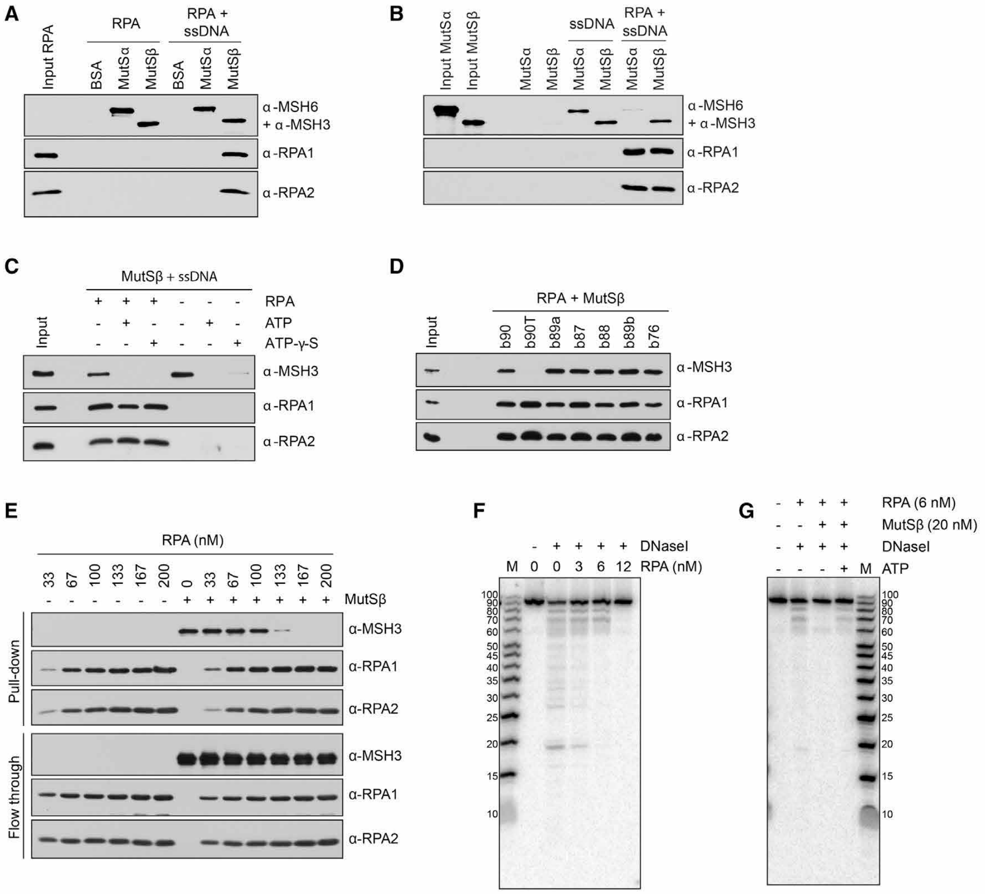

Figure 4. Binding of MutSβ to Hairpin Loop Structures Persisting in RPA-ssDNA Complexes

(A) Binding of RPA (100 nM) to His-tagged MutSα or MutSβ (50 nM each) in the absence and the presence of 90-mer ssDNA (b90, 20 nM). RPA was preincubated with ssDNA before addition of MutS proteins. MutSα or MutSβ was captured with Ni-NTA beads, and bound proteins were detected by western blotting.

(B) Binding of MutSα or MutSβ (50 nM each) to biotinylated 90-mer ssDNA (b90, 20 nM) in the absence or the presence of RPA (100 nM). The oligonucleotide was precoated with RPA before addition of MutS proteins. After incubation, ssDNA was captured with streptavidin beads and bound proteins were detected by western blotting.

(C) Effect of ATP on binding of MutSβ to RPA-coated ssDNA. Binding reactions were assembled and analyzed as in (B). ATP was present at a concentration of 2 mM.

(D) MutSβ (50 nM) binding to indicated biotinylated oligonucleotides (20 nM) precoated with RPA. Binding reactions were carried out and analyzed as in (B).

(E) Dependence of MutSβ binding to RPA-ssDNA on RPA concentration. Reactions were carried out as in (B).

(F) Binding of RPA to 5′-[^{32}P]-labeled 90-mer oligonucleotide (equivalent of b90) monitored by DNase I footprinting. 1 nM DNA substrate was incubated with indicated RPA concentrations. Lane 1, DNA size marker (M).

(G) Binding of MutSβ to RPA-ssDNA as detected by DNase I footprinting assay. 1 nM 90-mer DNA substrate was preincubated with 6 nM RPA before the addition of 20 nM MutSβ. Where indicated, 2 mM ATP was added prior to the addition of DNase I.

See also Figures S5 and S6.

and 5C). Moreover, in contrast to wild-type MutSβ, this mutant could not stimulate ATR activation by ssDNA in nuclear extracts of HCT116 cells (Figure 5D). To examine whether the MBD of MSH3 plays a role in ATR activation in vivo, we tested the effect of ectopic expression of wild-type and mutant (Y245S/K246E) forms of GFP-tagged MSH3 (GFP-MSH3) on CPT-induced phosphorylation of RPA2 Ser4/8 in HCT116 cells. We found that, at 60 min after the addition of CPT, cells expressing wild-type MSH3, but not those expressing the Y245S/K246E mutant, showed significantly higher levels of RPA phosphorylation as compared to cells expressing GFP alone (Figures 5E and 5F). GFP-MSH3 expression did not affect the level of chromatin-bound RPA in CPT-treated HCT116 cells (Figure S7). Collectively, these findings imply that MutSβ

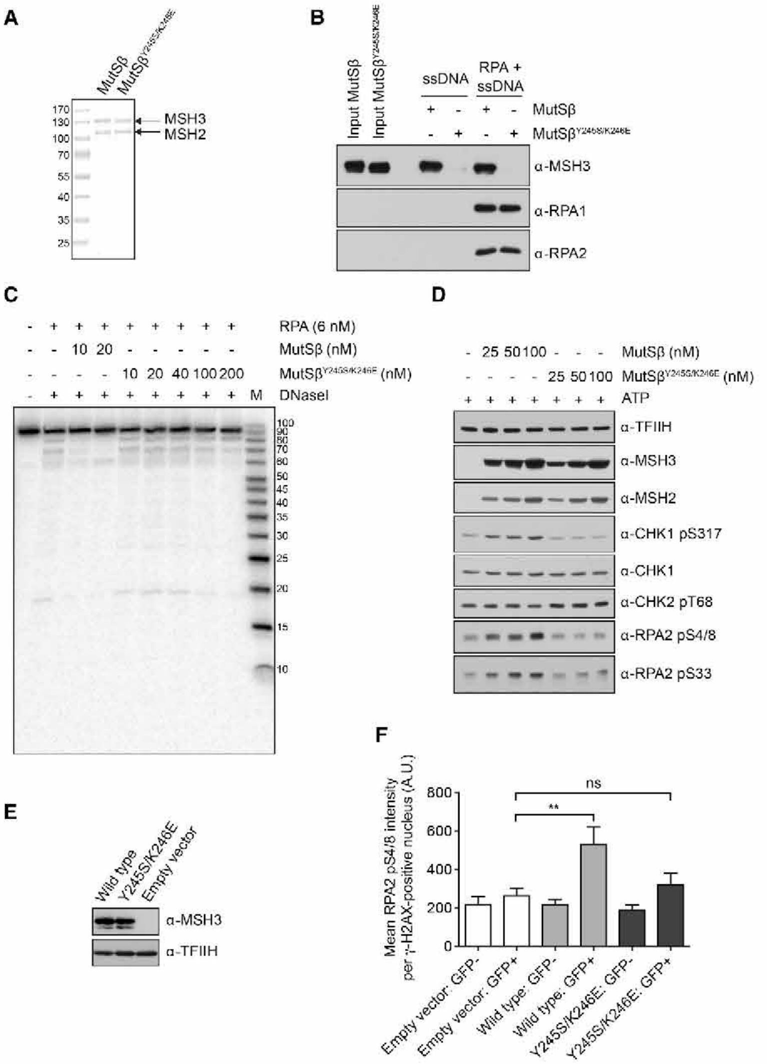

Figure 5. Effect of Y245S/K246E Substitutions in the Mismatch-Binding Domain of MSH3 on the Binding of MutSβ to RPA-ssDNA and Its Ability to Promote ATR Activation

(A) SDS-PAGE analysis showing the purity of wild-type and mutant forms of MutSβ used in this study.

(B) Binding of wild-type and mutant forms of MutSβ to RPA-ssDNA as revealed by biotin pull-down assay. Reactions were carried out as in Figure 4B.

(C) Binding of wild-type and mutant forms of MutSβ to RPA-ssDNA as revealed by DNase I footprinting assay. Reactions were carried out as in Figure 4G.

(D) Effect of wild-type and mutant forms of MutSβ on ssDNA-induced phosphorylation of RPA and CHK1 in nuclear extracts of HCT116 cells.

(E) Western blot analysis of extracts of HCT116 cells transiently transfected with vectors encoding for GFP-MSH3 (wild-type), GFP-MSH3$^{Y245S/K246E}$ (Y245S/K246E), or GFP alone (empty vector).

(F) Effect of ectopic expression of wild-type and mutant forms of GFP-tagged MSH3 on phosphorylation of RPA2 Ser4/8 in HCT116 cells treated with 1 μM CPT. Cells were fixed at 60 min after addition of CPT and subjected to immunofluorescence staining for RPA2 pS4/8 and γ-H2AX. The RPA2 pS4/8 intensity in γ-H2AX-positive nuclei was measured using the Olympus Scan^R screening station for both GFP^{+} and GFP^{-} cells. The data are represented as mean ± SEM; n = 5. **p < 0.005; ns, not significant. A.U., arbitrary units.

See also Figure S7.

promotes ATR activation through its binding to hairpin loop structures persisting in RPA-coated ssDNA.

MutSβ Promotes Binding of ATRIP to RPA-ssDNA

Finally, we tested whether MutSβ enhances binding of ATRIP to RPA-ssDNA complexes in vitro. To this end, the b90 oligonucleotide coated with RPA was preincubated with or without purified MutSβ protein, followed by addition of an extract of HEK293 cells over-producing HA-tagged ATRIP. At different time points after addition of the cell extract, protein-DNA complexes were isolated using streptavidin magnetic beads and analyzed by western blotting. We found that, in the presence of MutSβ, HA-ATRIP was bound to RPA-ssDNA more efficiently than in its absence (Figure 6). Of note, MutSβ gradually dissociated from RPA-ssDNA after addition of the cell extract, which is most likely caused by ATP from the extract. In support of this notion, MutSβ dissociation was inhibited if the extract was supplemented with EDTA (Figure S5C). Conversely, dissociation of MutSβ from RPA-ssDNA was dramatically accelerated if the extract was supplemented with an ATP-regenerating system (Figure S5D). These results suggest that MutSβ targets ATR-ATRIP complexes to RPA-coated ssDNA.

DISCUSSION

The MSH2-MSH3 heterodimer, termed MutSβ, binds to IDLs generated by DNA polymerase slippage during DNA replication and activates the MMR machinery (Habraken et al., 1996; Jiricny, 2006; Kunkel and Erie, 2005; Palombo et al., 1996). Recent studies have shown that, in addition to its role in MMR, MutSβ promotes repair of DNA DSBs, which might, in part, underlie its tumor suppression effect in p53$^{-/-}$ mice (van Oers et al., 2014). However, the molecular basis of this genome maintenance function of MutSβ has not been elucidated. Here, we

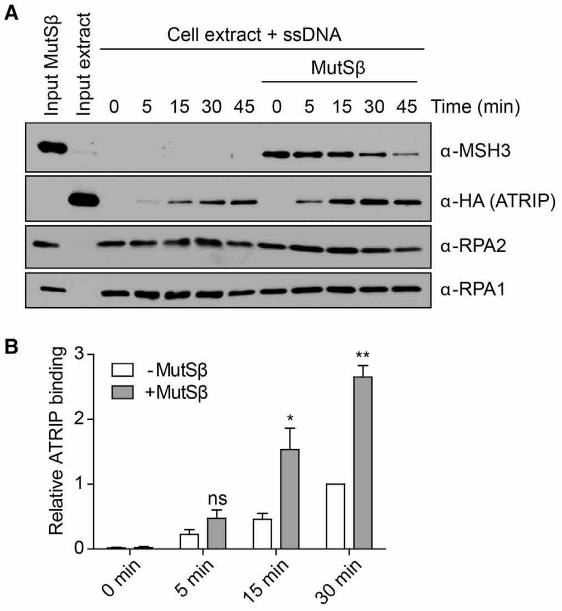

Figure 6. Effect of MutSβ on Binding of ATRIP to RPA-Coated ssDNA

(A) Biotinylated 90-mer ssDNA (b90, 20 nM) precoated with RPA (100 nM) was incubated with extract of HEK293 cells expressing HA-tagged ATRIP. Where indicated, MutSβ (25 nM) was added to RPA-ssDNA 30 min before the addition of the cell extract. At indicated time points, protein-DNA complexes were isolated using streptavidin magnetic beads and analyzed by western blotting.

(B) Graph showing data from quantitative analysis of ATRIP blots in (A) performed using ImageJ software. The values were normalized to the value obtained for the 30-min time point of binding reaction without MutSβ. The data are represented as mean ± SEM. $^*p < 0.05$; $^{**}p < 0.005$; ns, not significant.

See also Figure S5.

provide several lines of evidence suggesting that MutSβ promotes HR-mediated DSB repair by acting as a mediator in the process of ATR activation, which is essential for the execution of HR (Wang et al., 2004) (Figure S3B). First, we demonstrate that depletion of MutSβ subunits compromises phosphorylation of the ATR targets CHK1 and RPA in response to replication-associated DSBs, which are preferentially repaired by HR (Britton et al., 2013). Second, we show that MSH2 accumulates at DSBs prior to the formation of RAD51 filaments in a manner dependent on DNA-end resection. Third, we demonstrate that MutSβ binds to hairpin loop structures persisting in RPA-ssDNA complexes and promotes ATRIP recruitment in vitro. Fourth, we show that MutSβ exists in a complex with ATR and ATRIP in human cells and is required for the formation of ATRIP foci in response to replication-associated DSBs. Finally, we show that mutations in the MBD of MSH3 abolish the binding of MutSβ to RPA-ssDNA and its ability to promote ATR activation in vitro and in vivo. Based on these findings, we propose that MutSβ mediates ATR-ATRIP recruitment to ssDNA generated by resection of broken chromosome ends and, hence, promotes ATR activation and homology-directed repair. It is likely that MutSβ also promotes ATR activation by ssDNA generated upon replication arrest or by processing of other types of DNA damage (Cimprich and Cortez, 2008). In support of this notion, it has been demonstrated that MSH2 is required for the formation of ATR/ATRIP foci in response to cisplatin that induces replisome stalling by forming intra- and inter-strand DNA crosslinks (Pabla et al., 2011). This study has also revealed that MSH2-deficient cells are resistant to cisplatin-induced apoptosis, which indicates a defect in ATR-mediated checkpoint signaling (Pabla et al., 2011).

Based on our findings, we propose a model for ATR activation wherein MutSβ recruits the ATR-ATRIP complex to hairpin loop structures formed in RPA-coated ssDNA at sites of DNA damage (Figure 7). This facilitates the direct binding of ATR-ATRIP to RPA-ssDNA, leading to ATR activation by TOPBP1 (Figure 7) (Kumagai et al., 2006; Zou and Elledge, 2003). Interestingly, we found that ATP binding by MutSβ caused its dissociation from RPA-ssDNA, reminiscent of the ATP-driven dissociation of MutSβ from the mismatch site, which is triggered by conformational changes in MutSβ subunits induced by ATP binding (Figures 4C and 4G) (Wilson et al., 1999). Thus, it is possible that, upon the switch to direct binding of ATR-ATRIP to RPA-ssDNA, MutSβ binds ATP and dissociates from the DNA damage site (Figure 7). ATP-driven dissociation of MutSβ from RPA-ssDNA would ensure that MutSβ, bound to ssDNA, does not block the downstream steps of HR, such as RAD51 filament assembly.

However, the question arises as to whether hairpin loop structures can form efficiently in RPA-coated ssDNA in the cell? Interestingly, hairpin loops were detected at persistent DSB ends in rad52Δ yeast cells, suggesting that these structures might form at a high load of DNA damage in the cell, which would reduce the concentration of free RPA (Lao et al., 2008). We note that ATR-CHK1 signaling ensures the maintenance of RPA surplus over ssDNA after replication stress (Toledo et al., 2013). In the absence of ATR, stalled replication forks undergo nucleus-wide breakage after unscheduled origin firing that generates an excess of ssDNA that exhausts the nuclear pool of RPA (Toledo et al., 2013). It is, therefore, possible that formation of hairpin loops in ssDNA generated at DNA DSBs or stalled replication forks could signal lack of free RPA in the cell and serve as a trigger for ATR activation in a process mediated by MutSβ. This will prevent RPA depletion by newly initiated replication forks and ensure that there is sufficient amount of RPA for DNA repair.

Interestingly, a recent study has shown that the ATR-CHK1 pathway is also activated by DSBs generated in G1 cells (Gamper et al., 2013). Similarly, DNA-resection-dependent G1 checkpoint activation was observed in budding yeast in response to ionizing radiation (Balogun et al., 2013; Barlow et al., 2008). These findings might explain our observation that MSH2 and MSH3 were recruited to sites of laser-induced DSBs not only in S/G2 cells but also in G1 cells (Figure 1E; Figures S1C and S1D).

It should be noted that the S_N1-type alkylating agents producing O^6-methyl-G DNA adducts induce ATR-mediated checkpoint response in a manner requiring the MMR proteins MutSα and MutLα (Wang and Qin, 2003; Yoshioka et al., 2006). Interestingly, studies addressing the underlying mechanism provided evidence for a mode of ATR activation that does not include DNA processing to form RPA-coated ssDNA (Yoshioka et al.,

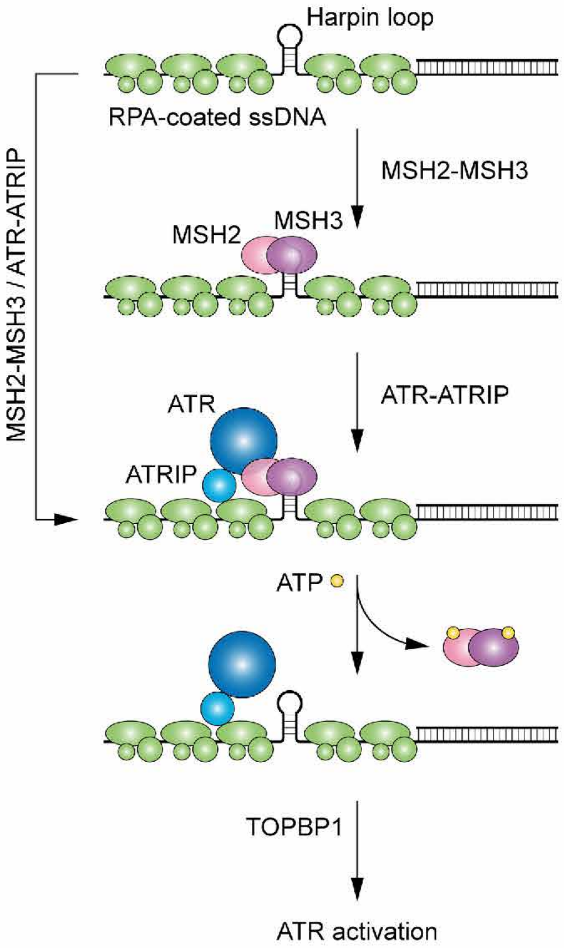

Figure 7. Model for the Role of MutSβ in ATR Activation
MutSβ (MSH2–MSH3) binds to hairpin loop structures formed in RPA-coated ssDNA at sites of DNA damage and recruits the ATR-ATRIP complex. Alternatively, MutSβ binds to DNA hairpin loops in complex with ATR-ATRIP. Subsequently, ATR-ATRIP binds directly to RPA-ssDNA leading to ATR activation by TOPBP1. ATP binding by MutSβ triggers its dissociation from ssDNA and the ATR-ATRIP complex.

2006). It has been shown that MutSα, along with MutLα, bind to O^6-methyl-G/T mismatches generated by replication O^6-methyl-G-containing DNA and serve as a scaffold for the recruitment of ATR-ATRIP and TOPBP1 to trigger ATR activation (Liu et al., 2010; Yoshioka et al., 2006). These findings, along with our data, highlight a role for the MMR proteins in ATR targeting to sites of DNA damage via recognition of DNA structures that are similar to those these proteins recognize in the canonical MMR reaction. One key mechanistic difference between the ATR activation processes mediated by MutSα and MutSβ, respectively, is that the latter is independent of MutLα (Figures 3B and 3C; Figure S2H). In the process of ATR activation by O^6-methyl-G/T mismatches, MutLα is likely to mediate the recruitment of TOPBP1 (Liu et al., 2010). Obviously, this activity is not needed in case of ATR activation on RPA-coated ssDNA, where TOPBP1 can be loaded by the 9-1-1 or MRN complexes (Delacroix et al., 2007; Lee et al., 2007; Shiotani et al., 2013).

In conclusion, our study identifies the MMR factor MutSβ as a critical component of the ATR signaling cascade and provides insights into the molecular mechanism underlying ATR activation by RPA-coated ssDNA. The recent discovery of synthetic lethal interaction between ATR and the ATM-p53 tumor suppressor pathway in cells exposed to DNA-damaging agents or replicative stress-generating conditions establishes ATR as a potential target for cancer therapy (Reaper et al., 2011; Toledo et al., 2011). There is no doubt that detailed knowledge of the molecular mechanism of ATR activation is a key for development of highly selective ATR inhibitors that can be used in combination with ionizing radiation and genotoxic drugs for treatment of p53-deficient tumors (Reaper et al., 2011; Toledo et al., 2011). In addition, it can be inferred from the aforementioned findings that the use of specific inhibitors of the ATM kinase could improve the efficacy and specificity of radio- and chemotherapy regimens for colorectal cancers associated with loss of MutSβ function (Peltomäki, 2001; Plaschke et al., 2004).

EXPERIMENTAL PROCEDURES

Antibodies, Purified Proteins, Cell Lines, DNA Oligonucleotides, and siRNAs

This information is provided in the Supplemental Experimental Procedures.

DR-GFP Assays

DR-GFP reporter assays using HEK293/DR-GFP or U2OS/DR-GFP cells were performed as previously described (Gunn and Stark, 2012).

Pulsed-Field Gel Electrophoresis

Pulsed-field gel electrophoresis was performed as reported previously (Neelsen et al., 2013).

Laser Microirradiation

In order to generate DSBs in defined nuclear compartments, an MMI CELLCUT system containing a 355-nm UVA laser (Molecular Machines & Industries) was used. Laser speed, focus, and intensity were all set to 50%. Prior to laser microirradiation, cells were grown for 24 hr on 12-mm glass microscope coverslips (OmniLab) in a medium containing 10 μM BrdU (Sigma-Aldrich). The coverslips were transferred to microirradiation chambers (Lab-Tek) containing complete growth medium. After irradiation, cells were incubated at 37°C for 30 min, fixed, and immunostained as described later.

Immunofluorescence Assays

Cells cultured on glass coverslips were fixed with 4% (v/v) formaldehyde for 15 min at room temperature (RT) and subsequently permeabilized by soaking in 0.2% (v/v) Triton X-100 for 5 min at RT, followed by a 30 min incubation in ice-cold methanol (only for laser-irradiated cells). Where required, before fixation, cells were pre-extracted for 5 min on ice in 25 mM HEPES-KOH (pH 7.4) containing 0.5% (v/v) Triton X-100, 50 mM NaCl, 1 mM EDTA, 3 mM $MgCl_2$, and 0.3 M sucrose. Immunofluorescence staining and analysis were carried out as described in the Supplemental Experimental Procedures.

In Vitro Kinase Assays

Nuclear extracts were prepared as described in the Supplemental Experimental Procedures. Reactions (15 μl) contained 10 μg of nuclear extract, 25–100 nM MutSβ or MutSα, and 1 pmol of ssDNA (b90) and were started by the addition of ATP to a final concentration of 1 mM. After incubation for 30 min at 37°C, reactions were stopped by the addition of SDS-PAGE loading buffer and analyzed by western blotting.

Immunoprecipitation Assays

HEK293 cells were transfected with pcDNA3.1-Flag-ATR (Tibbetts et al., 2000) and, 24 hr later, with pLPCX-HA-ATRIP (Ball et al., 2005) using linear polyethylenimine solution (Sigma). Cells were harvested 48 hr after the first transfection and suspended in lysis buffer (50 mM Tris-HCl [pH 7.5], 150 mM NaCl, 10 mM β-glycerophosphate, 10% [v/v] glycerol, 1% [v/v] Tween 20, 0.1% [v/v] Nonidet P-40, 2 mM MgCl$_2$) supplemented with protease and phosphatase inhibitors (Roche) and benzonase (50 U/ml; Merck). Aliquots of cell extracts containing 1 mg of protein were subjected to immunoprecipitation using anti-Flag M2 magnetic beads (10 μl; Sigma-Aldrich). Immunoprecipitates were analyzed by western blotting.

Affinity Pull-Down Assays

Binding reactions (50 μl) were carried out in a buffer containing 50 mM Tris-HCl (pH 7.5), 120 mM NaCl, and 0.1% (v/v) Triton X-100. To form RPA-ssDNA complexes, 1 pmol of appropriate 5′-end-biotinylated oligonucleotide was incubated with 5 pmol of RPA for 30 min at RT. Reactions were then supplemented with indicated amounts of MutSα or MutSβ and incubated for 1 hr at 4°C. Finally Ni-NTA agarose beads (5 μl; QIAGEN) or streptavidin-coupled M280 Dynabeads (5 μl; Life Technologies) were added, and incubation was continued for 30 min at 4°C. Bound proteins were analyzed by western blotting. Where indicated, ATP (2 mM), ATP-γ-S (2 mM), or ADP (2 mM) was added along with MgCl$_2$ (2 mM) at 60 min after MutSβ addition, and incubations were continued for 30 min at 4°C. In control reactions, BSA was substituted for MutSα/β. For measurements of ATRIP binding to RPA-ssDNA, an extract of pLPCX-HA-ATRIP-transfected HEK293 cells was prepared as described for immunoprecipitation assay, except that MgCl$_2$ and benzonase were omitted in the lysis buffer. To form RPA-ssDNA complexes, Dynabeads (2.5 μl) precoated with 1 pmol of b90 oligonucleotide were incubated with 5 pmol RPA for 30 min at RT. Where indicated, MutSβ was added, and mixtures were incubated for additional 30 min at 4°C. Finally, the binding reactions were supplemented with HA-ATRIP-containing cell extract (250 μg of protein). After incubation at 4°C for 30 min, beads were washed, and bound proteins were analyzed by western blotting.

DNA Footprinting

DNase I footprinting assays were carried out as described in the Supplemental Experimental Procedures.

SUPPLEMENTAL INFORMATION

Supplemental Information includes Supplemental Experimental Procedures and seven figures and can be found with this article online at http://dx.doi.org/10.1016/j.molcel.2015.06.026.

AUTHOR CONTRIBUTIONS

K.B. and B.M. performed most of the experiments. A.S. and N.C. performed DNase I footprinting and pulsed-field gel electrophoresis (PFGE) experiments, respectively. P.J. and K.B. designed the study and wrote the manuscript.

ACKNOWLEDGMENTS

We thank Josef Jiricny, Jiri Bartek, Alessandro Sartori, Jana Dobrovolna, and Javier Pena Diaz for stimulating discussions and comments on the manuscript; David Cortez for pLPCX-HA-ATRIP construct; Randy Tibbetts for pcDNA3.1-Flag-ATR construct; and Jeremy Stark for HEK293/DR-GFP and U2OS/DR-GFP cell lines. This work was supported by the Czech Science Foundation (P305-10-0281 and 14-05743S), Oncosuisse (KLS-02344-02-2009), Swiss National Science Foundation (31003A_146206), Novartis Foundation for Medical and Biological Research (11A16), and the Cancer League of the Canton Zurich and Stiftung zur Krebsbekämpfung.

Received: August 30, 2014
Revised: May 1, 2015
Accepted: June 19, 2015
Published: July 23, 2015

REFERENCES

Anantha, R.W., Vassin, V.M., and Borowiec, J.A. (2007). Sequential and synergistic modification of human RPA stimulates chromosomal DNA repair. J. Biol. Chem. *282*, 35910–35923.

Avemann, K., Knippers, R., Koller, T., and Sogo, J.M. (1988). Camptothecin, a specific inhibitor of type I DNA topoisomerase, induces DNA breakage at replication forks. Mol. Cell. Biol. *8*, 3026–3034.

Ball, H.L., Myers, J.S., and Cortez, D. (2005). ATRIP binding to replication protein A-single-stranded DNA promotes ATR-ATRIP localization but is dispensable for Chk1 phosphorylation. Mol. Biol. Cell *16*, 2372–2381.

Balogun, F.O., Truman, A.W., and Kron, S.J. (2013). DNA resection proteins Sgs1 and Exo1 are required for G1 checkpoint activation in budding yeast. DNA Repair (Amst.) *12*, 751–760.

Barlow, J.H., Lisby, M., and Rothstein, R. (2008). Differential regulation of the cellular response to DNA double-strand breaks in G1. Mol. Cell *30*, 73–85.

Bartek, J., and Lukas, J. (2003). Chk1 and Chk2 kinases in checkpoint control and cancer. Cancer Cell *3*, 421–429.

Bennardo, N., Gunn, A., Cheng, A., Hasty, P., and Stark, J.M. (2009). Limiting the persistence of a chromosome break diminishes its mutagenic potential. PLoS Genet. *5*, e1000683.

Britton, S., Coates, J., and Jackson, S.P. (2013). A new method for high-resolution imaging of Ku foci to decipher mechanisms of DNA double-strand break repair. J. Cell Biol. *202*, 579–595.

Chang, D.K., Ricciardiello, L., Goel, A., Chang, C.L., and Boland, C.R. (2000). Steady-state regulation of the human DNA mismatch repair system. J. Biol. Chem. *275*, 18424–18431.

Ciccia, A., and Elledge, S.J. (2010). The DNA damage response: making it safe to play with knives. Mol. Cell *40*, 179–204.

Cimprich, K.A., and Cortez, D. (2008). ATR: an essential regulator of genome integrity. Nat. Rev. Mol. Cell Biol. *9*, 616–627.

Delacroix, S., Wagner, J.M., Kobayashi, M., Yamamoto, K., and Karnitz, L.M. (2007). The Rad9-Hus1-Rad1 (9-1-1) clamp activates checkpoint signaling via TopBP1. Genes Dev. *21*, 1472–1477.

Dowen, J.M., Putnam, C.D., and Kolodner, R.D. (2010). Functional studies and homology modeling of Msh2-Msh3 predict that mispair recognition involves DNA bending and strand separation. Mol. Cell. Biol. *30*, 3321–3328.

Fan, J., and Pavletich, N.P. (2012). Structure and conformational change of a replication protein A heterotrimer bound to ssDNA. Genes Dev. *26*, 2337–2347.

Franchitto, A., Pichierri, P., Piergentili, R., Crescenzi, M., Bignami, M., and Palitti, F. (2003). The mammalian mismatch repair protein MSH2 is required for correct MRE11 and RAD51 relocalization and for efficient cell cycle arrest induced by ionizing radiation in G2 phase. Oncogene *22*, 2110–2120.

Gamper, A.M., Rofougaran, R., Watkins, S.C., Greenberger, J.S., Beumer, J.H., and Bakkenist, C.J. (2013). ATR kinase activation in G1 phase facilitates the repair of ionizing radiation-induced DNA damage. Nucleic Acids Res. *41*, 10334–10344.

Gradia, S., Subramanian, D., Wilson, T., Acharya, S., Makhov, A., Griffith, J., and Fishel, R. (1999). hMSH2-hMSH6 forms a hydrolysis-independent sliding clamp on mismatched DNA. Mol. Cell *3*, 255–261.

Gunn, A., and Stark, J.M. (2012). I-SceI-based assays to examine distinct repair outcomes of mammalian chromosomal double strand breaks. Methods Mol. Biol. *920*, 379–391.

Gupta, S., Gellert, M., and Yang, W. (2012). Mechanism of mismatch recognition revealed by human MutSβ bound to unpaired DNA loops. Nat. Struct. Mol. Biol. *19*, 72–78.

Habraken, Y., Sung, P., Prakash, L., and Prakash, S. (1996). Binding of insertion/deletion DNA mismatches by the heterodimer of yeast mismatch repair proteins MSH2 and MSH3. Curr. Biol. *6*, 1185–1187.

Hong, Z., Jiang, J., Hashiguchi, K., Hoshi, M., Lan, L., and Yasui, A. (2008). Recruitment of mismatch repair proteins to the site of DNA damage in human cells. J. Cell Sci. *121*, 3146–3154.

Jackson, S.P., and Bartek, J. (2009). The DNA-damage response in human biology and disease. Nature *461*, 1071–1078.

Jiricny, J. (2006). The multifaceted mismatch-repair system. Nat. Rev. Mol. Cell Biol. *7*, 335–346.

Kumagai, A., Lee, J., Yoo, H.Y., and Dunphy, W.G. (2006). TopBP1 activates the ATR-ATRIP complex. Cell *124*, 943–955.

Kunkel, T.A., and Erie, D.A. (2005). DNA mismatch repair. Annu. Rev. Biochem. *74*, 681–710.

Lao, J.P., Oh, S.D., Shinohara, M., Shinohara, A., and Hunter, N. (2008). Rad52 promotes postinvasion steps of meiotic double-strand-break repair. Mol. Cell *29*, 517–524.

Lee, J., Kumagai, A., and Dunphy, W.G. (2007). The Rad9-Hus1-Rad1 checkpoint clamp regulates interaction of TopBP1 with ATR. J. Biol. Chem. *282*, 28036–28044.

Liu, Y., Fang, Y., Shao, H., Lindsey-Boltz, L., Sancar, A., and Modrich, P. (2010). Interactions of human mismatch repair proteins MutSalpha and MutLalpha with proteins of the ATR-Chk1 pathway. J. Biol. Chem. *285*, 5974–5982.

Mordes, D.A., Glick, G.G., Zhao, R., and Cortez, D. (2008). TopBP1 activates ATR through ATRIP and a PIKK regulatory domain. Genes Dev. *22*, 1478–1489.

Neelsen, K.J., Zanini, I.M., Herrador, R., and Lopes, M. (2013). Oncogenes induce genotoxic stress by mitotic processing of unusual replication intermediates. J. Cell Biol. *200*, 699–708.

Pabla, N., Ma, Z., McIlhatton, M.A., Fishel, R., and Dong, Z. (2011). hMSH2 recruits ATR to DNA damage sites for activation during DNA damage-induced apoptosis. J. Biol. Chem. *286*, 10411–10418.

Palombo, F., Iaccarino, I., Nakajima, E., Ikejima, M., Shimada, T., and Jiricny, J. (1996). hMutSbeta, a heterodimer of hMSH2 and hMSH3, binds to insertion/deletion loops in DNA. Curr. Biol. *6*, 1181–1184.

Peltomäki, P. (2001). DNA mismatch repair and cancer. Mutat. Res. *488*, 77–85.

Pichierri, P., Franchitto, A., Piergentili, R., Colussi, C., and Palitti, F. (2001). Hypersensitivity to camptothecin in MSH2 deficient cells is correlated with a role for MSH2 protein in recombinational repair. Carcinogenesis *22*, 1781–1787.

Plaschke, J., Krüger, S., Jeske, B., Theissig, F., Kreuz, F.R., Pistorius, S., Saeger, H.D., Iaccarino, I., Marra, G., and Schackert, H.K. (2004). Loss of MSH3 protein expression is frequent in MLH1-deficient colorectal cancer and is associated with disease progression. Cancer Res. *64*, 864–870.

Reaper, P.M., Griffiths, M.R., Long, J.M., Charrier, J.D., Maccormick, S., Charlton, P.A., Golec, J.M., and Pollard, J.R. (2011). Selective killing of ATM- or p53-deficient cancer cells through inhibition of ATR. Nat. Chem. Biol. *7*, 428–430.

San Filippo, J., Sung, P., and Klein, H. (2008). Mechanism of eukaryotic homologous recombination. Annu. Rev. Biochem. *77*, 229–257.

Sartori, A.A., Lukas, C., Coates, J., Mistrik, M., Fu, S., Bartek, J., Baer, R., Lukas, J., and Jackson, S.P. (2007). Human CtIP promotes DNA end resection. Nature *450*, 509–514.

Shiotani, B., Nguyen, H.D., Håkansson, P., Maréchal, A., Tse, A., Tahara, H., and Zou, L. (2013). Two distinct modes of ATR activation orchestrated by Rad17 and Nbs1. Cell Rep. *3*, 1651–1662.

Symington, L.S., and Gautier, J. (2011). Double-strand break end resection and repair pathway choice. Annu. Rev. Genet. *45*, 247–271.

Tibbetts, R.S., Cortez, D., Brumbaugh, K.M., Scully, R., Livingston, D., Elledge, S.J., and Abraham, R.T. (2000). Functional interactions between BRCA1 and the checkpoint kinase ATR during genotoxic stress. Genes Dev. *14*, 2989–3002.

Toledo, L.I., Murga, M., Zur, R., Soria, R., Rodriguez, A., Martinez, S., Oyarzabal, J., Pastor, J., Bischoff, J.R., and Fernandez-Capetillo, O. (2011). A cell-based screen identifies ATR inhibitors with synthetic lethal properties for cancer-associated mutations. Nat. Struct. Mol. Biol. *18*, 721–727.

Toledo, L.I., Altmeyer, M., Rask, M.B., Lukas, C., Larsen, D.H., Povlsen, L.K., Bekker-Jensen, S., Mailand, N., Bartek, J., and Lukas, J. (2013). ATR prohibits replication catastrophe by preventing global exhaustion of RPA. Cell *155*, 1088–1103.

van Gent, D.C., and van der Burg, M. (2007). Non-homologous end-joining, a sticky affair. Oncogene *26*, 7731–7740.

van Oers, J.M., Edwards, Y., Chahwan, R., Zhang, W., Smith, C., Pechuan, X., Schaetzlein, S., Jin, B., Wang, Y., Bergman, A., et al. (2014). The MutSβ complex is a modulator of p53-driven tumorigenesis through its functions in both DNA double-strand break repair and mismatch repair. Oncogene *33*, 3939–3946.

Wang, Y., and Qin, J. (2003). MSH2 and ATR form a signaling module and regulate two branches of the damage response to DNA methylation. Proc. Natl. Acad. Sci. USA *100*, 15387–15392.

Wang, H., Wang, H., Powell, S.N., Iliakis, G., and Wang, Y. (2004). ATR affecting cell radiosensitivity is dependent on homologous recombination repair but independent of nonhomologous end joining. Cancer Res. *64*, 7139–7143.

Wilson, T., Guerrette, S., and Fishel, R. (1999). Dissociation of mismatch recognition and ATPase activity by hMSH2-hMSH3. J. Biol. Chem. *274*, 21659–21664.

Yoshioka, K., Yoshioka, Y., and Hsieh, P. (2006). ATR kinase activation mediated by MutSalpha and MutLalpha in response to cytotoxic O6-methylguanine adducts. Mol. Cell *22*, 501–510.

Zou, L., and Elledge, S.J. (2003). Sensing DNA damage through ATRIP recognition of RPA-ssDNA complexes. Science *300*, 1542–1548.

Zou, L., Cortez, D., and Elledge, S.J. (2002). Regulation of ATR substrate selection by Rad17-dependent loading of Rad9 complexes onto chromatin. Genes Dev. *16*, 198–208.

Molecular Cell, Volume *59*

Supplemental Information

The Mismatch-Binding Factor MutSβ Can Mediate ATR Activation in Response to DNA Double-Strand Breaks

Kamila Burdova, Boris Mihaljevic, Andreas Sturzenegger, Nagaraja Chappidi, and Pavel Janscak

Burdova *et al.*, Figure S1

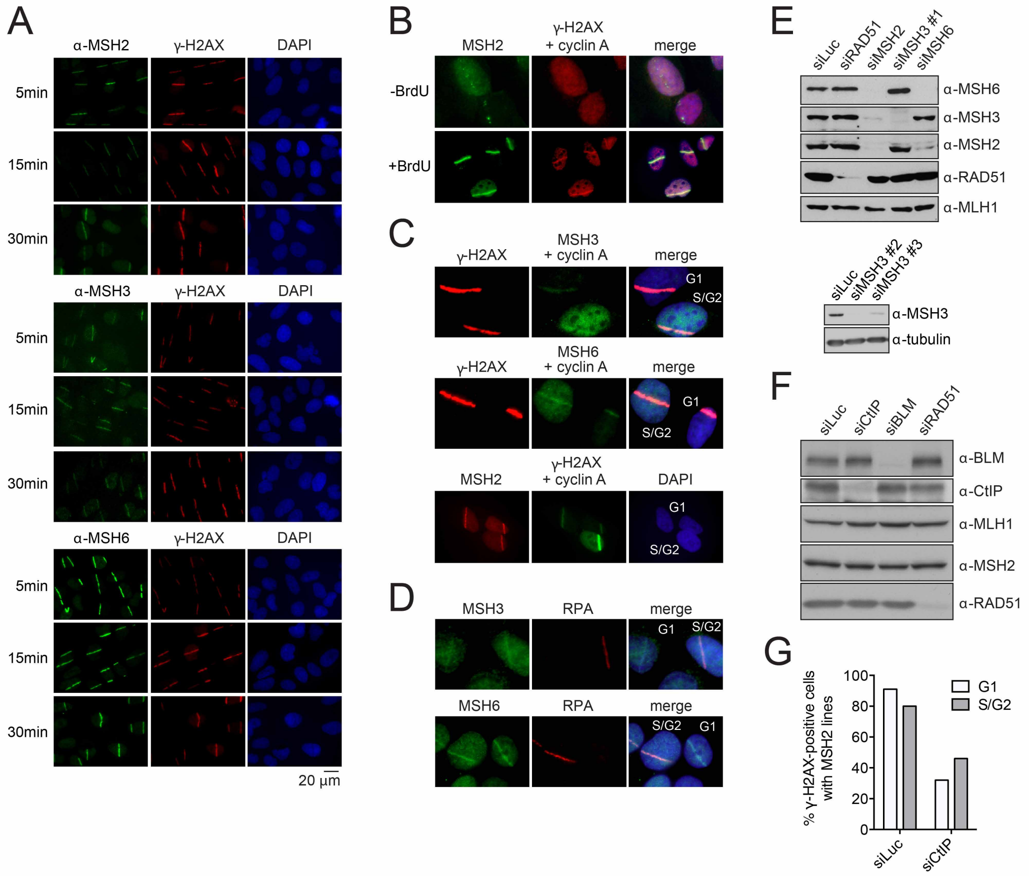

Burdova *et al.*, Figure S2

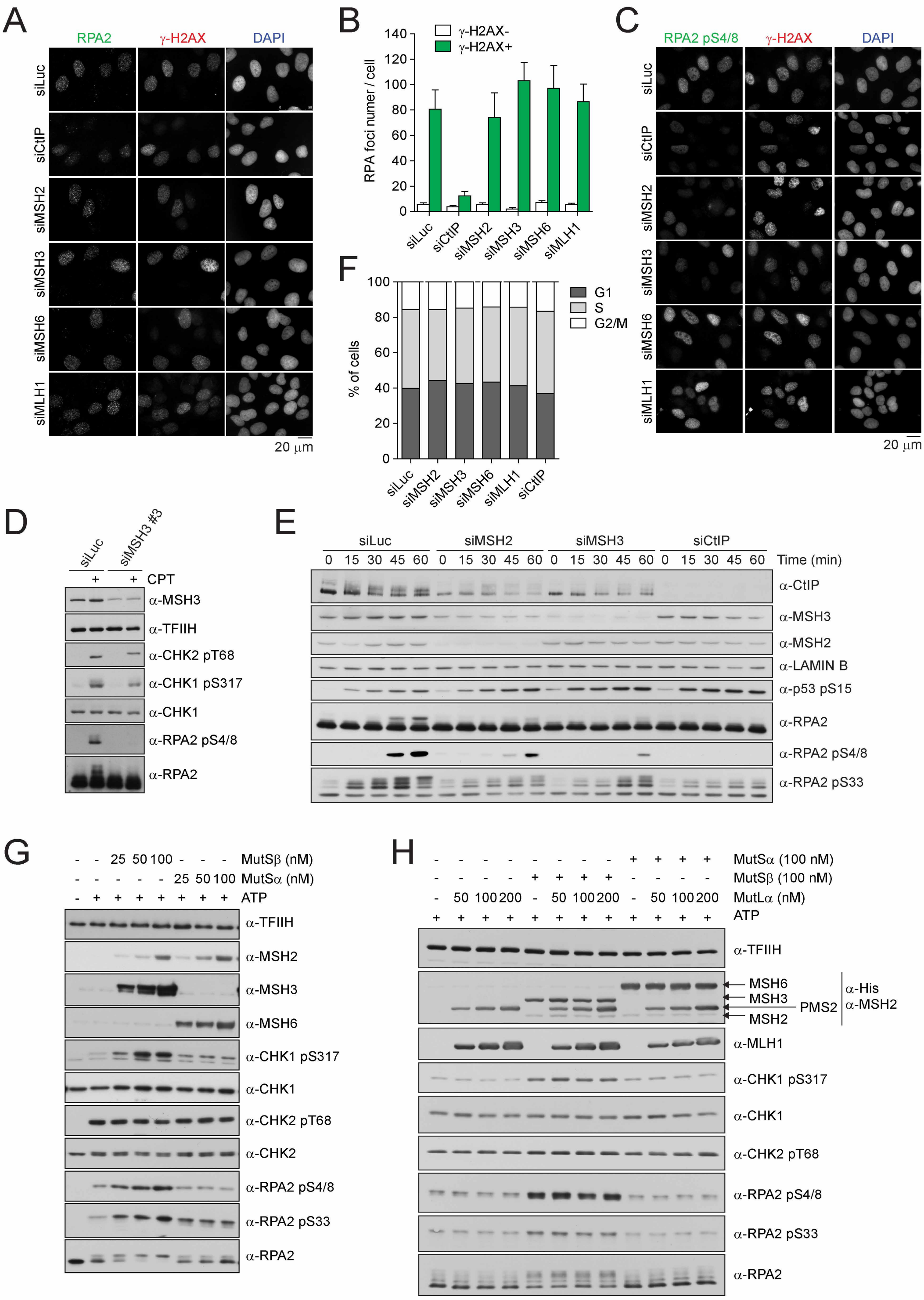

Burdova *et al.*, Figure S3

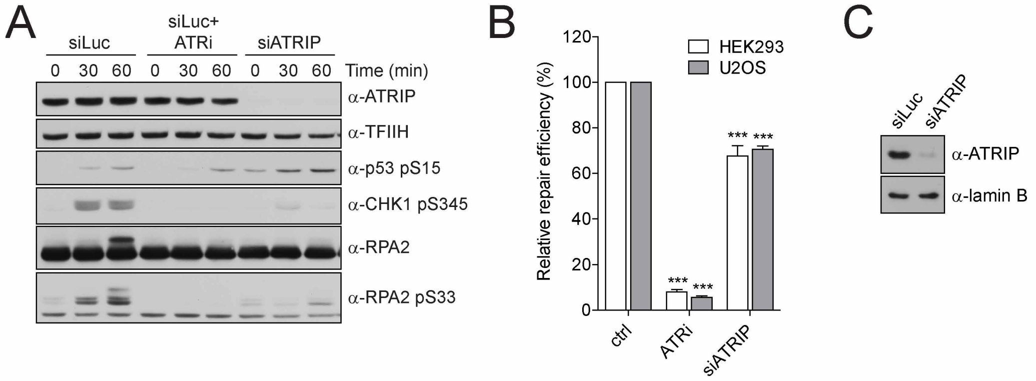

Burdova *et al.*, Figure S4

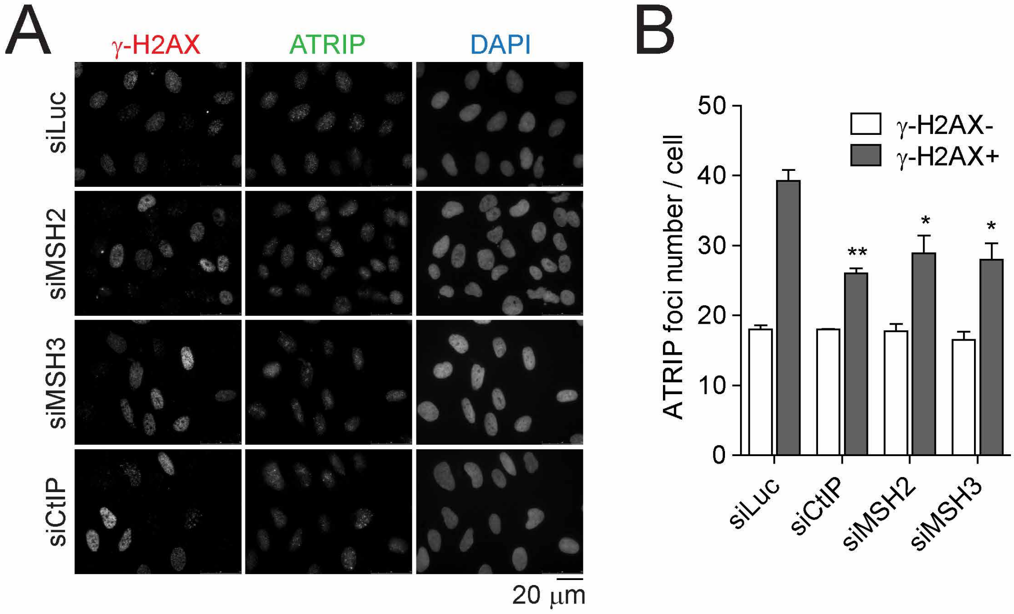

Burdova *et al.*, Figure S5

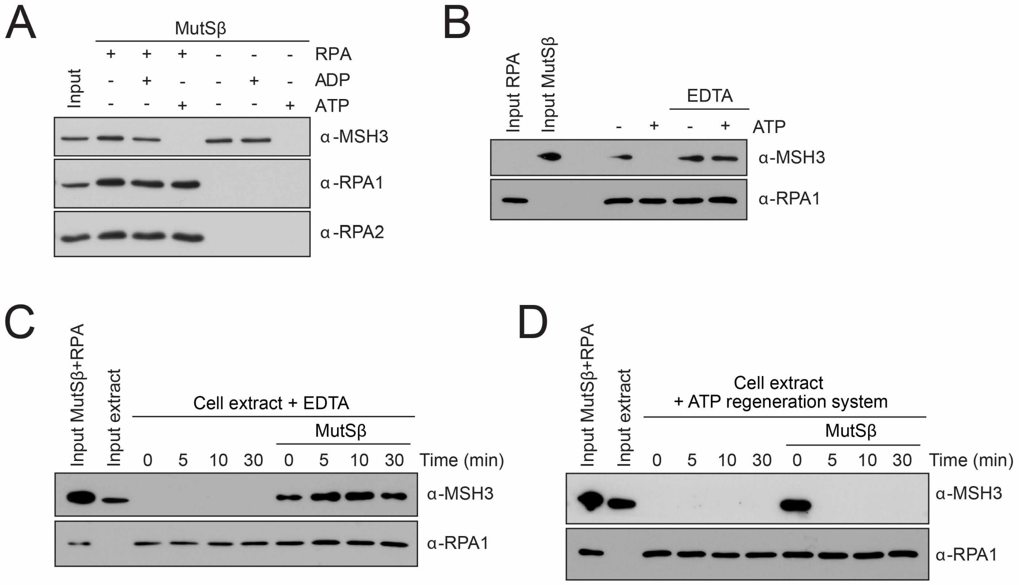

Burdova *et al.*, Figure S6

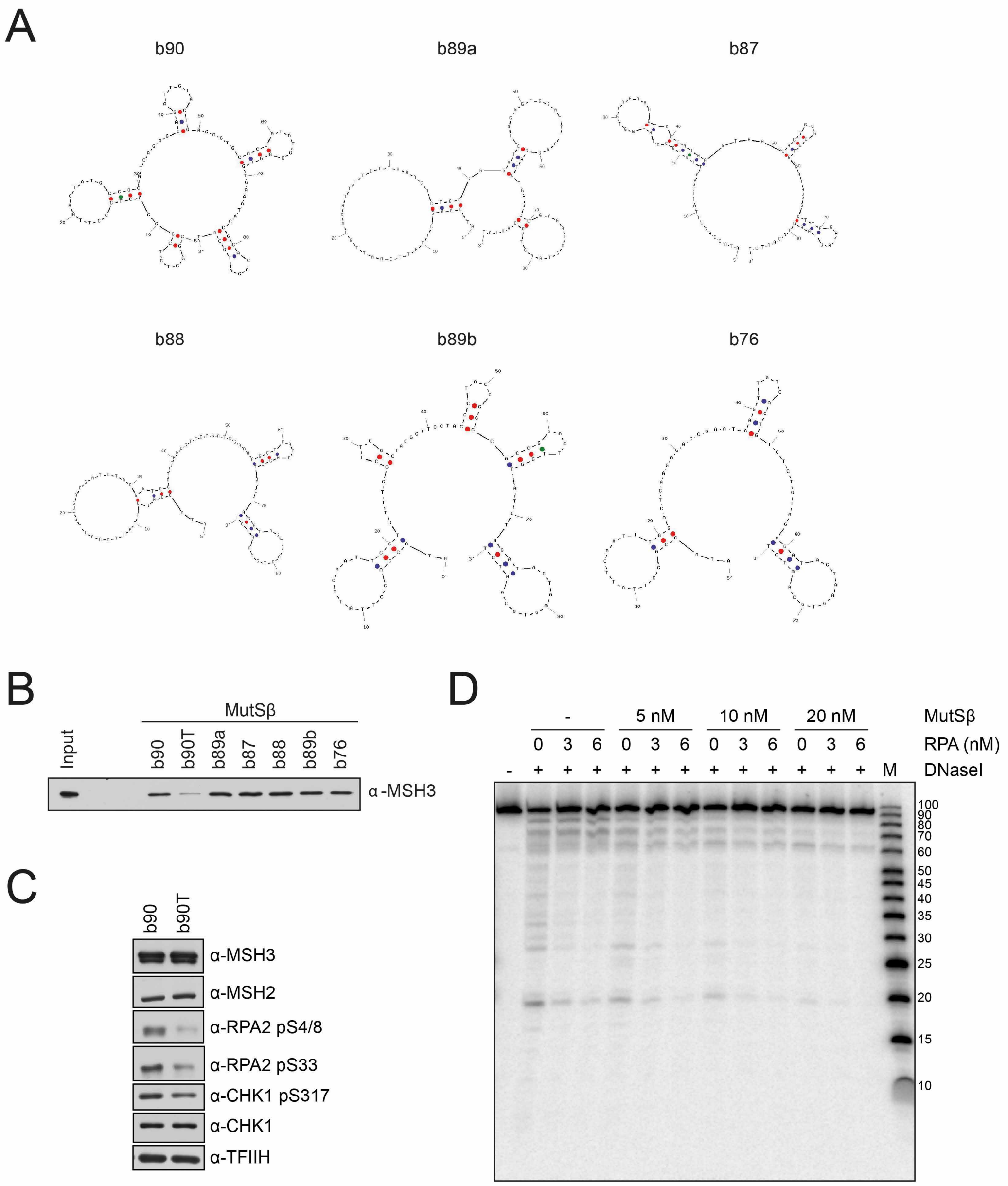

Burdova *et al.*, Figure S7

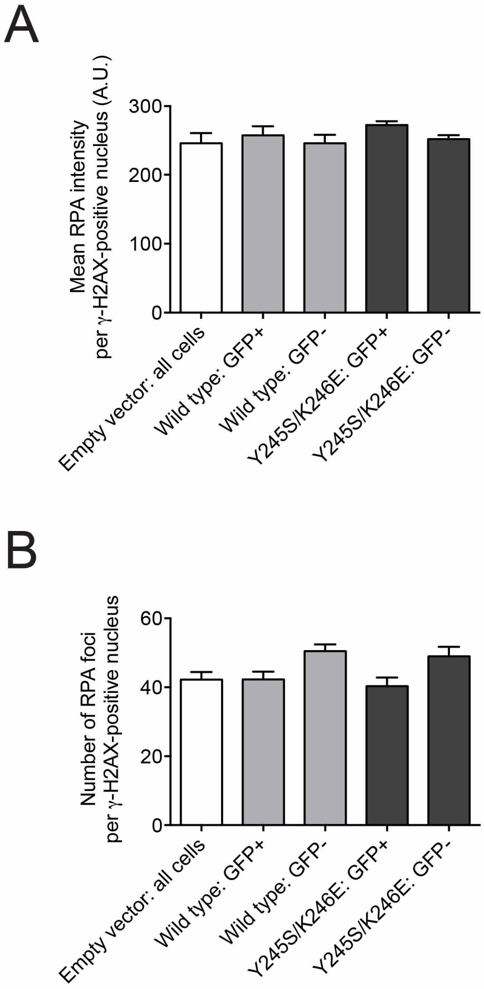

SUPPLEMENTAL FIGURE LEGENDS

Figure S1. Recruitment of mismatch repair proteins to sites of DNA double-strand breaks, related to Figure 1. **(A)** Rapid accumulation of MSH2, MSH3 and MSH6 in nuclear volumes exposed to laser microirradiation. U2OS cells were grown in the presence of 10 µM BrdU for 24 h prior to irradiation. At indicated time points post-irradiation, cells were fixed with formaldehyde and co-immunostained with antibodies against γ-H2AX (red) and one of the indicated MMR proteins (green). DAPI was used to stain nuclei. **(B)** MSH2 accumulates at sites of laser microirradiation only if cells are pretreated with BrdU. U2OS cells were either mock-treated or pretreated with 10 µM BrdU for 24 h prior to irradiation. Following incubation period of 30 min after irradiation, cells were fixed and stained with antibodies against cyclin A, γ-H2AX and MSH2. **(C)** Indirect immunofluorescence imaging of MMR proteins (MSH2, MSH3 and MSH6, respectively), γ-H2AX and cyclin A in U2OS cells subjected to laser microirradiation. Cells were grown in the presence of 10 µM BrdU for 24 h prior to laser microirradiation. Cells positive for cyclin A (dispersed nuclear staining) are in S/G2, whereas cells lacking cyclin A are in G1 as indicated. **(D)** Indirect immunofluorescence imaging of MSH3, MSH6 and RPA in U2OS cells subjected to laser microirradiation. Irradiated cells negative for RPA lines are in G1 and cells positive for RPA lines are in S/G2. **(E)** Western blot analysis of extracts from HEK293/DR-GFP cells transfected with indicated siRNAs. The blots show protein levels at the time of harvesting cells for FACS analysis. **(F)** Western blot analysis of extracts from U2OS cells transfected with indicated siRNAs. **(G)** Effect of CtIP depletion on the recruitment of MSH2 to laser lines in G1 and S/G2 cells.

Figure S2. MutSβ promotes ATR activation, related to Figure 2. **(A)** Representative immunofluorescence images of mock-, CtIP-, MSH2-, MSH3- and MSH6-depleted U2OS cells stained for RPA and γ-H2AX after treatment with 1 μM CPT for 1 h. **(B)** Quantitative analysis of RPA foci in cells represented in (A). The number of RPA foci in γ-H2AX-negative and γ-H2AX-positive cells was determined using Olympus Scan^R screening station. The data are represented as mean ± SEM. **(C)** Representative immunofluorescence images of mock-, CtIP-, MSH2-, MSH3- and MSH6-depleted U2OS cells stained for pRPA Ser4/8 and γ-H2AX after treatment with 1 μM CPT for 1 h. A plot of data from quantitative analysis of these images is shown in Figure 2C. **(D)** Western blot analysis of extracts of U2OS cells depleted for MSH3 using siMSH3 #3. Cells were either treated with 1 μM CPT for 1 hour (lane marked by "+") or left untreated. Whole cell extracts were prepared and analyzed by western blotting using indicated antibodies. **(E)** Kinetics of CPT-induced phosphorylation of RPA in U2OS cells following siRNA-mediated depletion of MSH2, MSH3 or CtIP. Whole cell extracts were prepared and analyzed by western blotting using indicated antibodies. **(F)** Flow cytometry analysis of BrdU incorporation in U2OS cells transfected with indicated siRNAs. 10 μM BrdU was added 2 days after siRNA transfection for 30 min before cell fixation. BrdU incorporation was plotted against DNA content (propidium iodide) and cell cycle analysis was performed. The percentage of S-phase (BrdU positive), G1-phase (BrdU negative, 2n) and G2/M-phase (BrdU negative, 4n) cells is indicated. **(G)** Effect of recombinant MutSα (25-100 nM) or MutSβ (25-100 nM) on ssDNA-induced phosphorylation of RPA and CHK1 in nuclear extract of HeLa cells. *In vitro* kinase assay was performed as described under Experimental Procedures. Phosphorylation status of RPA, CHK1 and CHK2 was analyzed by western blotting using phosphospecific antibodies. **(H)** Effect of recombinant MutLα (50-200 nM) on ssDNA-induced phosphorylation of RPA and CHK1 in nuclear extracts of HCT116 cells supplemented with recombinant MutSα (100 nM) or MutSβ (100 nM).

Figure S3. Loss of ATR function impairs checkpoint activation and HR-mediated DSB repair, related to Figure 2. **(A)** Effects of ATR inhibition and ATRIP depletion on CPT-induced phosphorylation of RPA and CHK1. U2OS cells were transfected either with control siRNA (siLuc) or with ATRIP siRNA (siATRIP) as described under Supplemental Experimental Procedures. Two days after second siRNA transfection, cells were treated with 1 μM CPT for 1 h. Where indicated, ATR inhibitor VE-821 (10 μM) was added 15 min prior to CPT. Total cell extracts were prepared and analyzed by western blotting using indicated antibodies. **(B)** Effect of ATR inhibition and ATRIP depletion on DSB repair by HR as determined by DR-GFP reporter assay. ATR inhibitor (10 μM) was added 15 min before transfection of I-SceI-expressing plasmid and present in the medium until harvest of cells. The data are represented as mean ± SEM. **(C)** Western blot analysis of extracts from U2OS/DR-GFP cells transfected with indicated siRNAs. NT, non-treated; ATRi, ATR inhibitor; CPT, camptothecin.

Figure S4. MutSβ promotes ATRIP recruitment to sites of DSBs in human cells, related to Figure 3. **(A)** Representative immunofluorescence images of mock-, MSH2-, MSH3-, CtIP-depleted U2OS cells stained for ATRIP and γ-H2AX after treatment with 1 μM CPT for 1 h. DAPI was used to stain nuclei. **(B)** Quantitative analysis of ATRIP foci in cells represented in (A). Number of ATRIP foci in nuclei of γ-H2AX-negative and γ-H2AX-positive cells was determined using Olympus Scan^R screening station. The data are represented as mean ± SEM.

Figure S5. MutSβ dissociation from RPA-coated ssDNA in the presence of ATP, related to Figure 4 and 6. **(A)** Effect of ATP and ADP on binding of MutSβ to RPA-coated ssDNA. Binding reactions were assembled and analyzed as in Figure 4C. ATP and ADP were present at a concentration of 2 mM. **(B)** ATP-induced dissociation of MutSβ from RPA-coated ssDNA is inhibited by EDTA. Biotinylated 90-mer oligonucleotide (b90, 20 nM) was precoated with RPA (100 nM) before addition of MutSβ complex. ssDNA was captured with streptavidin beads and supplemented or not with 10 mM EDTA before addition of 2 mM ATP. **(C)** MutSβ binding to RPA-coated ssDNA in cell extracts is stabilized by EDTA. Biotinylated 90-mer oligonucleotide (b90, 20 nM) was precoated with RPA (100 nM) and incubated alone or with MutSβ (25 nM) before addition of extract from HEK293 cells supplemented with 10 mM EDTA. At indicated time points, protein-DNA complexes were isolated using streptavidin magnetic beads and analyzed by western blotting for the presence of MSH3 and RPA. **(D)** MutSβ dissociates from RPA-coated ssDNA if ATP regeneration system is added to cell extract. Reactions were carried out and analyzed as in (A) except that cell extract was supplemented with 12 mM creatine phosphate, 10 U/ml creatine phosphokinase, 2 mM $MgCl_2$.

Figure S6. MutSβ binds preferentially to ssDNA forming secondary structures, related to Figure 4. **(A)** Schematic representation of the most probable hairpin structures formed by the oligonucleotides used in this study. DNA sequences were analyzed at http://eu.idtdna.com/analyzer/Applications/OligoAnalyzer/. **(B)** Binding of MutSβ (50 nM) to indicated biotinylated oligonucleotides (20 nM). Reactions were carried out as described in Experimental Procedures. Bound proteins were detected by western blotting. **(C)** Effect of b90 and b90T oligonucleotides on phosphorylation of RPA and CHK1 in nuclear extracts of HCT116 cells supplemented with MutSβ (100 nM). **(D)** Binding of MutSβ to 5’-[^{32}P]-labeled

90-mer oligonucleotide monitored by DNase I footprinting. 1 nM DNA substrate was preincubated with the indicated concentrations of RPA prior to the addition of increasing concentrations of MutSβ.

Figure S7. Effect of ectopic expression of wild-type and mutant forms of GFP-tagged MSH3 on RPA loading on chromatin in HCT116 cells treated with CPT, related to Figure 5. Cells were preextracted and fixed at 60 min after addition of 1 μM CPT and subjected to immunofluorescence staining for RPA2 and γ-H2AX. The mean RPA2 intensity **(A)** and the number of RPA2 foci **(B)** in γ-H2AX-positive nuclei were measured using Olympus Scan^R screening station for both GFP$^+$- and GFP$^-$-cells. The data are represented as mean ± SEM, n=3. A.U., arbitrary units. Note that cells transfected with empty vector lost GFP after preextraction.

SUPPLEMENTAL EXPERIMENTAL PROCEDURES

Antibodies

Primary antibodies used for immunoblotting are as follows: mouse monoclonal anti-MSH2 (NA27, Oncogene); rabbit polyclonal anti-MSH3 (provided by Dr. Giancarlo Marra); mouse monoclonal anti-MSH6 (610919, BD Transduction Laboratories); mouse monoclonal anti-MLH1 (554073, BD Pharmingen); mouse monoclonal anti-CtIP (sc-271339, Santa Cruz Biotechnology); rabbit polyclonal anti-CtIP (A300-488A, Bethyl Laboratories); rabbit polyclonal anti-RAD51 (sc-8349, Santa Cruz Biotechnology); rabbit polyclonal anti-RPA1 (A300-241A, Bethyl Laboratories); mouse monoclonal anti-RPA2 (NA19, Calbiochem); rabbit polyclonal anti-p53 pSer15 (#9284, Cell Signaling); rabbit polyclonal anti-RPA2 pSer4/8 (A300-245A, Bethyl Laboratories); rabbit polyclonal anti-RPA2 pSer33 (NB100-544, Novus); rabbit polyclonal anti-CHK1 pSer317 (#2344, Cell Signaling); rabbit polyclonal anti-CHK1 pSer345 (#2341, Cell Signaling); mouse monoclonal anti-CHK1 (sc-8408, Santa Cruz); rabbit polyclonal anti-CHK2 pThr68 (#2661, Cell Signaling); mouse monoclonal anti-CHK2 (sc-17748, Santa Cruz); rabbit polyclonal anti-TFIIH (sc-293, Santa Cruz Biotechnology); mouse monoclonal anti-lamin B (NA12, Calbiochem); rabbit polyclonal anti-ATRIP (07-625, Millipore); mouse monoclonal anti-HA (mms-101R, Covance); mouse monoclonal anti-His (A00186, Genscript). Primary and secondary antibodies used for immunofluorescence staining are listed at the end of this section.

Plasmid constructions

The human MSH3 and MSH6 ORFs, respectively, were cloned as N-terminal fusions with a hexahistidine tag in pFastBac1 between XhoI and HindIII sites (pFastBac1-His-hMSH3, pFastBac1-His-hMSH6). The vector expressing human MSH3 as an N-terminal fusion with green fluorescence protein (GFP) was constructed by sub-cloning the XhoI/HindIII fragment of pFastBac1-hMSH3 (Palombo et al., 1996) into pEGFP-c1 (pEGFP-c1-hMSH3). Point mutations in MSH3 were made using QuikChange Site-Directed Mutagenesis Kit (Stratagene).

Oligonucleotides

The 5'-end-biotinylated oligonucleotides used in this study were synthesized and PAGE-purified at Microsynth AG or Sigma. The sequences of these oligonucleotides are shown in the following table:

Name	Length (nt)	Sequence (5' - 3')
b90	90	CGGGTGTCGGGGCTGGCTTAACTATGCGGCATCAGAGCAGAT TGTACTGAGAGTGCACCATATGCGGTGTGAAATACCGCA CAGATGCGT
b90T	90	TTTTTTTTTTTTTTTTTTTTTTTTTTTTTTTTTTTTTTTTTTTTTTT TTTTTTTTTTTTTTTTTTTTTTTTTTTTTTTTTTTTTTTTTTT
b87	87	ATACCAGCTTATTCAATTGTGCCTACGGTGTAAAAAGTCGCA TAAGTAACACGGGGCGTGGATAGGCTTAGATAGTAAGTGCAA TCT
b88	88	ATACCAGCTTATTCAATTGCGAGGATCTAGGGTGGATTCAGG GTCGAGATGGAAAAGCTCAACAGCTACTAGATAGTAAGTGCA ATCT
b89a	89	ATACCAGCTTATTCAATTGCAGATTTTCTTAAACACTGGGGGA TCTGGGGTGGATTTAGGGATCTGTGGCGAGATAGTAAGTGCA ATCT
b89b	89	ATACCAGCTTATTCAATTGGTGTTTGGCTTGGCTACGCTTCCT ACCCTACGGGGCACCGGAATTGGTATCTAGATAGTAAGTGCA ATCT
b87	87	ATACCAGCTTATTCAATTACTACGGGGGCTTGCGGCTGCGCC GGGACTATCGCAAATAGTTGGGCGGGAAGATAGTAAGTGCA ATCT
b76	76	ATACCAGCTTATTCAATTTGGACTGAAGAGACCGAATCAGTT GTCACTGTGTCTGTAGAGATAGTAAGTGCAATCT

Non-biotinylated form of b90 used in DNase I footprinting experiments was also purchased from Microsynth.

Purified proteins

RPA was produced in bacteria and purified as described (Henricksen et al., 1994). MutSα and MutSβ heterodimers carrying a hexahistidine tag on MSH6 and MSH3, respectively, were produced in Sf9 insect cells by means of baculovirus system. Harvested cells were disrupted by Dounce homogenization in buffer A [50 mM Tris-HCl (pH 7.5), 0.25 M NaCl, 0.1 % (v/v) Nonidet P-40, 10 % (v/v) glycerol] supplemented with 20 mM imidazole and protease inhibitors (cOmplete, Roche). MutSα and MutSβ were isolated from cell extracts using Ni-NTA beads (Qiagen). Bound proteins were eluted with 250 mM imidazole in buffer A and dialyzed against buffer B [50 mM Tris-HCl (pH 7.5), 0.2 M NaCl, 1 mM DTT, 0.1 mM EDTA, 25 % (v/v) glycerol]. The pFastBac1-based transfer vectors for generation of MSH3 and MSH6 baculoviruses are described above. The plasmid pFastBac1-hMSH2 was described previously (Iaccarino et al., 1998). MutLα was produced and purified as previously described (Raschle et al., 2002).

DNase I footprinting

1 nM 90-mer oligonucleotide, radioactively labeled at 5'-end, was preincubated for 30 min on ice with or without indicated concentrations of RPA (3-12 nM) in buffer containing 10 mM Tris-HCl (pH 7.5), 100 mM NaCl, 0.5 mg/ml BSA. Reactions (typically 20 µl) were supplemented with indicated concentrations of MutSβ (1 µl) and incubation was continued for additional 60 min on ice. Subsequently, reactions were supplemented with 2 µl of 10x DNase I reaction buffer [100 mM Tris-HCl (pH 7.6), 25 mM $MgCl_2$, 5 mM $CaCl_2$] and 1 µl of DNase I dilution (0.07 U) (New England Biolabs) and incubated at 37°C for 5 min. Where indicated, ATP was added to a concentration of 2 mM before addition of DNase I. Reactions were stopped by adding 10 µl of 3x Formamide Dye Mix [98 % (v/v) formamide, 10 mM EDTA and 0.3 % (w/v) bromphenol blue] followed by incubation at 95°C for 5 min. Samples

(10 µl) were subjected to electrophoresis in a 15 % polyacrylamide denaturing gel containing 6 M urea. Gels were run in 1x TBE buffer at 800V. After soaking in fixing solution [40 % (v/v) methanol, 10% (v/v) acetic acid, 5% (v/v) glycerol] for 30 min under continuous shaking, gels were dried on Whatman MM3 paper and subjected to phosphorimaging on a Typhoon FLA 9500 (GE Healthcare).

Cell culture

U2OS, HeLa, HCT116 and HEK293 cells were grown in Dulbecco modified Eagle's medium (DMEM, Sigma Aldrich) supplemented with 10 % fetal calf serum (FCS, Life Technologies or Gibco) and streptomycin/penicillin (100 U/ml, Sigma Aldrich). Immortalized ATLD1 cells harboring retrovirus expressing wild-type MRE11 cDNA (ATLD1-MRE11) or corresponding empty vector (ATLD1-EV) were grown in DMEM supplemented with 20 % FCS, streptomycin/penicillin antibiotics (100 U/ml) and 1 µg/ml puromycin (Sigma Aldrich) (Carson et al., 2003). HCT116 cells carry homozygous frameshift mutations of the $[A]_8$ repeat in the exon 7 of the *MSH3* gene (Haugen et al., 2008).

siRNA and transfections

All small-interfering RNA (siRNA) oligoduplexes used in this study were purchased from Microsynth. The sequences of the sense strands of these siRNAs are shown below:

siCtrl: 5'-CGUACGCGGAAUACUUCGAdTdT-3'

siCtIP: 5'-UCCACAACAUAAUCCUAAUdTdT-3'

siRAD51: 5'-AAGGGAAUUAGUGAAGCCAAAdTdT-3'

siMSH2 #1: 5'-AAUCUGCAGAGUGUUGUGCUUdTdT-3'

siMSH2 #2: 5'-UCCAGGCAUGCUUGUGUUGAAdTdT-3'

siMSH3 #1: 5'-UCGAGUCGAAAGGAUGGAUAAdTdT-3' siMSH3 #2: 5'-CAGCAAGGAGUUAUGGAUUAAdTdT-3'

siMSH3 #3: 5'-TGCAACCAGTTTATCCACCAAdTdT-3'

siMSH6 #1: 5'-AUCGCCAUUGUUCGAGAUUUAdTdT-3'

siMSH6 #2: 5'-CAGCAGGGCUAUAAUGUAUGAdTdT-3'

siMLH1: 5'-GUGGCUCAUGUUACUAUUACAdTdT-3'

siATRIP: 5'-AAGGUCCACAGAUUAUUAGAUdTdT-3'

Transfection of siRNA oligonucleotides (40 nM) was carried out using Lipofectamine RNAiMAX (Invitrogen) according to manufacturer's instructions. Cells were analyzed 48-72 h after siRNA transfection. For siATRIP, cells were re-transfected with 20 nM siRNA at 44 h after first transfection to enhance protein depletion efficiency. In the figures where the numbers of MSH2 and MSH3 siRNAs are not indicated, data for siMSH2 #1 and siMSH3 #2 are shown.

Plasmid DNA transfections

The vectors encoding for GFP-MSH3 and GFP-MSH3$^{Y245S/K246E}$, respectively, were transfected to HCT116 cells using linear polyethyleneimine method. Cells were subjected to CPT treatment at 24 hours after plasmid transfection.

Immunofluorescence staining and analysis

Cells cultured on glass coverslips were fixed with 4 % (v/v) formaldehyde for 15 min at room temperature (RT) and subsequently permeabilized by soaking in 0.2 % (v/v) Triton X-100 for 5 min at RT, followed by a 30-min incubation in ice-cold methanol (only for laser-irradiated cells). Where required, before fixation, cells were pre-extracted for 5 min on ice in 25 mM HEPES (pH 7.4) containing 0.5 % (v/v) Triton X-100, 50 mM NaCl, 1 mM EDTA, 3 mM $MgCl_2$ and 0.3 M sucrose. After blocking in PBS containing 10 mg/ml BSA for 30 min at

RT, coverslips were incubated overnight at 4°C (laser-irradiated cells) or 2 h at RT (CPT-treated cells) with appropriate primary antibodies. Incubations with secondary antibodies were carried out for 1-2 h at RT. Coverslips were mounted using Vectashield containing DAPI (Vector Laboratories) and images were captured on an Olympus IX81 fluorescence microscope (laser-irradiated cells) or Leica DM6000 fluorescence microscope (CPT-treated cells).

Scan^R analysis

Automated image acquisition was performed using an Olympus IX70 microscope equipped with Scan^R imaging platform. 40×/1.3 NA objective was used. For analysis of RPA2 pSer4/8 intensity in U2OS cells, 225 images were acquired per sample, while for analysis of RPA2 pSer4/8 intensity in HCT116 cells, 100 images were acquired per sample. For RPA2 and ATRIP foci analysis, 10 z-stacks at a spacing of 0.3 μm were taken and 100 images were acquired for each sample. Analysis was performed using Scan^R analysis software based on signal intensity for RPA2 pSer4/8 or edge based sub-object counts for RPA2 and ATRIP foci. Nuclei were identified based on the DAPI signal. At least 1000 cells were analyzed for each condition.

Preparation of nuclear extracts

Nuclear extracts were prepared as previously described (Vidal-Eychenie et al., 2013). Briefly, HCT116 or HeLa cells were grown to near confluency and harvested by scraping to PBS. Cells were collected by centrifugation, resuspended in 5 volumes of hypotonic buffer A [10 mM HEPES-KOH (pH 7.9), 10 mM KCl, 1.5 mM $MgCl_2$, 0.5 mM DTT] supplemented with protease and phosphatase inhibitors (Roche) and incubated on ice for 5 min. Cells were spun down, resuspended in 2 volumes of buffer A and lysed by Dounce homogenization using a tightly fitting pestle. Nuclei were collected by centrifugation at 4’000 g for 5 min at 4°C, resuspended in 1 volume of buffer B [20 mM HEPES-KOH (pH 7.9), 600 mM KCl, 1.5 mM $MgCl_2$, 0.2 mM EDTA, 25 % (v/v) glycerol, 0.5 mM DTT], supplemented with protease and phosphatase inhibitors (Roche) and kept at 4°C with over-head rotation for 30 min. After centrifugation (16’000 g for 15 min at 4 °C), supernatant was diluted using buffer C [20 mM HEPES-KOH (pH 7.9), 1.5 mM $MgCl_2$, 0.2 mM EDTA, 0.5 mM DTT] supplemented with protease and phosphatase inhibitors to a final KCl concentration of 100 mM. Extracts were incubated at 4°C for 30 min and cleared by centrifugation at 16’000 g for 30 min at 4 °C. Resulting nuclear fraction was aliquoted, snap frozen in liquid nitrogen and kept at -80 °C before use.

DR-GFP assays

HEK293/DR-GFP or U2OS/DR-GFP cells (Bennardo et al., 2008; Gunn and Stark, 2012) were transfected with 40 nM siRNA using Lipofectamine RNAiMAX. After 24 h, siRNA-transfected cells were transferred into a 12-well plate, with 200’000 cells per well for HEK293/DR-GFP cell line and 150’000 cells per well for U2OS/DR-GFP cell line, respectively. At 44 h after siRNA transfection, cells were transfected with 0.6 μg of the I-SceI expression vector pCBASce (Richardson et al., 1998) using linear polyethyleneimine solution (1 mg/ml), and 6 h later with appropriate siRNA at a final concentration of 20 nM using standard calcium phosphate method. At 52 h after I-SceI transfection, cells were harvested and subjected to FACS analysis using LSRII (BD Biosciences) and FlowJo software (Tree Star) to determine the percentage of GFP-positive cells, which was taken as measure of repair efficiency.

BrdU incorporation analysis

BrdU was added to media to a final concentration of 10 µM for 30 min before harvesting the cells. Staining with FITC-conjugated α-BrdU antibody (347583, BD Biosciences) was done according to manufacturer's protocol. Flow cytometry analysis was performed using LSRII (BD Biosciences) and FlowJo software (Tree Star). BrdU incorporation was plotted against DNA content (propidium iodide) and the percentage of S phase (BrdU positive), G1 phase (BrdU negative, 2n) and G2-M phase (BrdU negative, 4n) cells was analyzed.

Statistical analysis

Data were analyzed in GraphPad Prism by two-tailed paired t-test with confidence interval of 95%. P-values smaller than 0.05 were marked *, p-values smaller than 0.005 were marked ** and p-values smaller than 0.0005 were marked ***.

List of antibodies used for immunofluorescence staining

Primary antibodies	**Secondary antibodies**	**Note**
Camptothecin-treated cells		
Mouse monoclonal anti-RPA2 (NA19, Calbiochem) Rabbit monoclonal anti-γ-H2AX (#9718, Cell Signaling)	Alexa Fluor 488-conjugated goat anti-mouse IgG (A11029, Life Technologies) Texas Red-conjugated sheep anti-rabbit IgG (ab6793, Abcam)	Fig. 2A Fig. S2A and B
Rabbit polyclonal anti-RPA2 pSer4/8 (A300-245A, Bethyl Laboratories) Mouse monoclonal anti-γ-H2AX (05-636, Millipore)	Alexa Fluor 488-conjugated goat polyclonal anti-rabbit (A11034, Life Technologies) Texas Red-conjugated sheep anti-mouse IgG (ab6806, Abcam)	Fig. 2C Fig. S2C
Rabbit polyclonal anti-ATRIP	Alexa Fluor 488-conjugated goat polyclonal	Fig. 3B

(07-625, Millipore) Mouse monoclonal anti-γ-H2AX (05-636, Millipore)	anti-rabbit (A11034, Life Technologies) Alexa Fluor 568-conjugated goat polyclonal anti-mouse (A11031, Life Technologies)	and C Fig. S4
Laser-microirradiated cells		
Rabbit polyclonal anti-MSH3 (provided by Dr. Giancarlo Marra) Rabbit monoclonal anti-γ-H2AX (#9718, Cell Signaling)	Alexa Fluor 488-conjugated goat polyclonal anti-rabbit (A11034, Life Technologies) Alexa Fluor 568-conjugated goat polyclonal anti-mouse (A11031, Life Technologies)	Fig. S1A
Mouse monoclonal anti-MSH2 (NA27, Oncogene) or mouse monoclonal anti-MSH6 (610919, BD Transduction Laboratories) Rabbit monoclonal anti-γ-H2AX (#9718, Cell Signaling)	Alexa Fluor 488-conjugated goat anti-mouse IgG (A11029, Life Technologies) Alexa Fluor 568-conjugated goat polyclonal anti-rabbit (A11036, Life Technologies)	Fig. S1A
Mouse monoclonal anti-MSH2 (NA27, Oncogene) Rabbit polyclonal anti-cyclin A (sc-751, Santa Cruz Biotechnology) Rabbit monoclonal anti-γ-H2AX (#9718, Cell Signaling)	Texas Red-conjugated anti-mouse IgG (Jackson Immunoresearch) FITC-conjugated anti-rabbit IgG (Jackson Immunoresearch)	Fig. 1E and G Fig. S1B
Mouse monoclonal anti-γ-H2AX (05-636, Millipore) Rabbit polyclonal anti-MSH3 (provided by Dr. Giancarlo Marra) or rabbit polyclonal anti-MSH6 (sc-25835, Santa Cruz Biotechnology) Rabbit polyclonal anti-cyclin A (sc-751, Santa Cruz	Texas Red-conjugated anti-mouse IgG (Jackson Immunoresearch) FITC-conjugated anti-rabbit IgG (Jackson Immunoresearch)	Fig. S1C

Biotechnology)		
Mouse monoclonal anti-RPA2 (NA19, Calbiochem) Rabbit polyclonal anti-MSH3 (provided by Dr. Giancarlo Marra) or rabbit polyclonal anti-MSH6 (sc-25835, Santa Cruz Biotechnology)	Texas Red-conjugated anti-mouse IgG (Jackson Immunoresearch) FITC-conjugated anti-rabbit IgG (Jackson Immunoresearch)	Fig. S1D

SUPPLEMENTAL REFERENCES

Bennardo, N., Cheng, A., Huang, N., and Stark, J.M. (2008). Alternative-NHEJ is a mechanistically distinct pathway of mammalian chromosome break repair. PLoS Genet *4*, e1000110.

Carson, C.T., Schwartz, R.A., Stracker, T.H., Lilley, C.E., Lee, D.V., and Weitzman, M.D. (2003). The Mre11 complex is required for ATM activation and the G2/M checkpoint. EMBO J. *22*, 6610-6620.

Gunn, A., and Stark, J.M. (2012). I-SceI-based assays to examine distinct repair outcomes of mammalian chromosomal double strand breaks. Methods Mol. Biol. *920*, 379-391.

Haugen, A.C., Goel, A., Yamada, K., Marra, G., Nguyen, T.P., Nagasaka, T., Kanazawa, S., Koike, J., Kikuchi, Y., Zhong, X., *et al.* (2008). Genetic instability caused by loss of MutS homologue 3 in human colorectal cancer. Cancer Res. *68*, 8465-8472.

Henricksen, L.A., Umbricht, C.B., and Wold, M.S. (1994). Recombinant replication protein A: expression, complex formation, and functional characterization. J. Biol. Chem. *269*, 11121-11132.

Iaccarino, I., Marra, G., Palombo, F., and Jiricny, J. (1998). hMSH2 and hMSH6 play distinct roles in mismatch binding and contribute differently to the ATPase activity of hMutSalpha. EMBO J. *17*, 2677-2686.

Palombo, F., Iaccarino, I., Nakajima, E., Ikejima, M., Shimada, T., and Jiricny, J. (1996). hMutSbeta, a heterodimer of hMSH2 and hMSH3, binds to insertion/deletion loops in DNA. Current biology : CB *6*, 1181-1184.

Raschle, M., Dufner, P., Marra, G., and Jiricny, J. (2002). Mutations within the hMLH1 and hPMS2 subunits of the human MutLalpha mismatch repair factor affect its ATPase activity, but not its ability to interact with hMutSalpha. J. Biol. Chem. *277*, 21810-21820.

Richardson, C., Moynahan, M.E., and Jasin, M. (1998). Double-strand break repair by interchromosomal recombination: suppression of chromosomal translocations. Genes Dev. *12*, 3831-3842.

Vidal-Eychenie, S., Decaillet, C., Basbous, J., and Constantinou, A. (2013). DNA structure-specific priming of ATR activation by DNA-PKcs. J. Cell. Biol. *202*, 421-429.

4.2.3. Human RECQ5 helicase promotes repair of DNA double-strand breaks by synthesis-dependent strand annealing

Shreya Paliwal, Radhakrishnan Kanagaraj, **Andreas Sturzenegger**, Kamila Burdova and Pavel Janscak

This study was published in Nucleic Acids Research in 2013.

For this study I performed a number of SA-GFP and DR-GFP reporter experiments. To optimize the production and purification of RAD51 wt and its K133R mutant version, I constructed new expression vectors based on the pTXB3 plasmid from New England Biolabs and subsequently purified both proteins. Further, I conducted strand-annealing assays to show that wild-type RAD51 also displayed a similar effect like the RAD51-K133R mutant and to check whether WRN or FBH1 could substitute for RECQ5 in RAD51-ssDNA filament disruption. Finally, by using a RAD51-interaction deficient mutant of RECQ5, I showed that RECQ5-RAD51 interaction is required for RECQ5-mediated disruption of RAD51 filaments.

Nucleic Acids Research Advance Access published December 6, 2013

Nucleic Acids Research, 2013, ***1–11***
doi:10.1093/nar/gkt1263

Human RECQ5 helicase promotes repair of DNA double-strand breaks by synthesis-dependent strand annealing

Shreya Paliwal[1], Radhakrishnan Kanagaraj[1], Andreas Sturzenegger[1], Kamila Burdova[2] and Pavel Janscak[1,*]

[1]Institute of Molecular Cancer Research, University of Zurich, CH-8057 Zurich, Switzerland and [2]Institute of Molecular Genetics, Academy of Sciences of the Czech Republic, 14300 Prague, Czech Republic

Received August 21, 2013; Revised November 9, 2013; Accepted November 12, 2013

ABSTRACT

Most mitotic homologous recombination (HR) events proceed via a synthesis-dependent strand annealing mechanism to avoid crossing over, which may give rise to chromosomal rearrangements and loss of heterozygosity. The molecular mechanisms controlling HR sub-pathway choice are poorly understood. Here, we show that human RECQ5, a DNA helicase that can disrupt RAD51 nucleoprotein filaments, promotes formation of non-crossover products during DNA double-strand break-induced HR and counteracts the inhibitory effect of RAD51 on RAD52-mediated DNA annealing *in vitro* and *in vivo*. Moreover, we demonstrate that RECQ5 deficiency is associated with an increased occupancy of RAD51 at a double-strand break site, and it also causes an elevation of sister chromatid exchanges on inactivation of the Holliday junction dissolution pathway or on induction of a high load of DNA damage in the cell. Collectively, our findings suggest that RECQ5 acts during the post-synaptic phase of synthesis-dependent strand annealing to prevent formation of aberrant RAD51 filaments on the extended invading strand, thus limiting its channeling into potentially hazardous crossover pathway of HR.

INTRODUCTION

DNA double-strand break (DSB) is the most dangerous type of DNA damage because its inaccurate repair can lead to chromosomal rearrangements, a hallmark of tumorigenesis and tumor progression. In eukaryotic cells, two mechanistically distinct pathways are known to efficiently repair DNA DSBs: non-homologous end joining and homologous recombination (HR). HR is mainly restricted to S phase, peaking in mid-S, and requires an intact homologous sequence to be used as a repair template (1 3). It is initiated by nuclease-mediated resection of the DNA ends to generate 3′-single-stranded (ss) DNA tails that are coated by the ssDNA-binding protein RPA (4). In the next step, the RAD51 recombinase replaces RPA on these ssDNA tails with the help of mediators such as BRCA2 to form a nucleoprotein filament that catalyzes the invasion of the donor chromatid, giving rise to a three-stranded structure called the displacement (D)-loop (1). After DNA synthesis primed by the invading strand, repair can proceed *via* two main sub-pathways referred to as the canonical DSB repair (DSBR) and synthesis-dependent strand annealing (SDSA) (1,2). In DSBR pathway, the second DNA end is captured by the D-loop to form an intermediate with two Holliday junctions, referred to as double Holliday junction (dHJ). This joint DNA molecule can be either resolved by specialized endonucleases into crossover (CO) or non-crossover (NCO) products or dissolved by the BLM-TOPOIIIα-RMI1/2 (BTR) complex, which gives rise exclusively to NCO products (5 7). In the SDSA pathway, the extended D-loop is disrupted by a DNA helicase, and the newly synthesized DNA is annealed to the ssDNA tail of the other part of the broken chromosome, which is followed by gap-filling DNA synthesis and ligation. As a result, SDSA yields exclusively NCO products (8).

The HR sub-pathways are under strict regulation to select the most appropriate outcome in a given state of the cell (2,9). Although formation of COs is favored during meiosis to ensure genetic diversity and accurate chromosome segregation, it is suppressed in mitotic cells to prevent loss of heterozygosity and chromosomal translocations (10,11). Recent studies in yeast and mammalian cells suggest that HJ resolvases are active only during

---

*To whom correspondence should be addressed. Tel: +41 446353470; Fax: +41 446353484; Email: pjanscak@imcr.uzh.ch
Present address:
Radhakrishnan Kanagaraj, London Research Institute, Cancer Research UK, Clare Hall Laboratories, South Mimms, Herts EN6 3LD, UK.

mitosis, biasing the outcome of recombination toward NCO products while also ensuring the elimination of any persistent joint DNA molecules (11). Most NCOs arising during HR-mediated DSBR are produced by SDSA rather than by the canonical DSBR pathway (12). Moreover, the resolution of HJs is highly constrained to generate CO products (12). Thus, it appears that the SDSA mechanism is preferred over DSBR in mitotic cells.

In budding yeast, the Mph1 DNA helicase suppresses COs by acting in a pathway distinct from dHJ dissolution (13). Mph1 influences outcome rather than the efficiency of recombinational repair events, suggesting that it acts by shunting a DNA repair intermediate into the SDSA pathway (13). In support of this notion, biochemical evidence indicates that Mph1 is capable of disrupting Rad51-made D-loops (13). Another suppressor of COs in yeast proposed to act via promotion of SDSA is Srs2, an UvrD-type DNA helicase that has the capacity to displace Rad51 from ssDNA (14,15). The mechanism of CO suppression by Srs2 appears to differ from that of Mph1. Cells lacking Srs2 display a failure to complete ectopic gene conversion with NCO outcome, which reduces the overall repair efficiency, and therefore increases the proportion of CO products among completed recombination events (14). Although Srs2 can unwind DNA duplexes covered by Rad51, it fails to unwind Rad51-made D-loops (13,16). Instead, the anti-recombinase activity of Srs2 *in vivo* is dependent on its ability to bind RAD51, suggesting that Srs2 might promote SDSA by regulating Rad51 filament stability (17).

The closest sequence homolog of Srs2 in mammals and other vertebrates is FBH1, which is also found in fission yeast but not in budding yeast. Several lines of *in vivo* evidence suggest that this UvrD-type helicase regulates HR at the stage of RAD51 filament assembly, but its role in SDSA is yet to be assessed (18). Another potential ortholog of Srs2 in mammals is RECQ5, which belongs to RecQ family of DNA helicases (19). Biochemical studies have shown that RECQ5 binds directly to RAD51 and possesses the ability to disrupt the ATP-bound form of RAD51-ssDNA filament in a manner dependent on its ssDNA-translocase activity and interaction with RAD51 (20,21). In accordance with this finding, phenotypic analysis of chicken and mouse knockout cells have revealed that RECQ5 regulates HR to suppress the formation of COs (20,22,23). Moreover, a recent study using chicken DT40 cells has demonstrated that RECQ5 suppresses COs in a manner dependent on its interaction with RAD51 (24). Here we provide several lines of evidence suggesting that RECQ5 promotes SDSA by disrupting aberrant RAD51-ssDNA filaments formed during the post-synaptic stage of HR.

MATERIALS AND METHODS

Antibodies and siRNAs

All antibodies and siRNAs used in this study are described in Supplementary Materials and Methods.

HR and SSA reporter assays

Maintenance of reporter cell lines (HEK293/DR-GFP, U2OS/DR-GFP, HEK293/SA-GFP or U2OS/SA-GFP), culture conditions and FACS analysis were done as described previously (25,26). Cells were seeded in a poly-lysine-coated 6-well plate at a density of 0.6×10^6 cells per well and transfected 24 h later with appropriate siRNA (40 nM). After 24 h, 0.2×10^6 cells for each siRNA tested were seeded in a 12-well plate, and a day later transfected with 0.6 µg of the I-SceI-expressing plasmid pCBASce (27) or empty vector (pcDNA3.1) using JETprime (Polyplus) for HEK293 cells or Lipofectamine 2000 (Invitrogen) for U2OS cells according to the manufacturer's instructions. After 6 h, cells were again transfected with appropriate siRNA (15 nM), and 48 72 h later, GFP-positive cells were quantified by flow cytometry on a Cyan ADP (Dako) using Summit software (Beckman Coulter). For overexpression of RECQ5 in U2OS/SA-GFP cells, a pcDNA3.1/HisC-based vector expressing the wild-type or mutant forms of RECQ5 (0.6 µg) was co-transfected with pCBASce (0.6 µg) using Lipofectamine 2000 (21). Cells were subjected to FACS analysis 72 h after transfection.

Strand-annealing assays

Proteins used for strand-annealing assays were purified as described in Supplementary Materials and Methods. All reactions were carried out at 30°C in buffer R [20 mM Tris-acetate (pH 7.9), 50 mM potassium acetate, 10 mM magnesium acetate and 1 mM DTT] supplemented with ATP-regenerating system (10 U/ml creatine phosphokinase and 12 mM phosphocreatine). The 5 nM $5'$-^{32}P-labeled f9 oligonucleotide (59-mer) was pre-incubated for 3 min with or without 200 nM RAD51^{K133R} in a final volume of 20 µl (reaction A). In a separate tube, 5 nM f7 oligonucleotide (30-mer), complementary to 5′ end of f9, was mixed with 120 nM RAD52 and 40 nM RPA in a final volume of 20 µl (reaction B). Where required, the latter reaction mixture also contained 5 nM 59-bp DNA duplex prepared by annealing of unlabeled f9 and f9-C oligonucleotides. The reactions A and B were mixed together, and where required RECQ5, RECQ5^{K58R}, RECQ5$^{\Delta 652-674}$, WRN or FBH1 were added to a final concentration of either 80 or 40 nM. In all, 5 µl aliquots were removed at the indicated time points and mixed with 2.5 µl of stop solution [125 nM f9 (unlabeled), 33% (v/v) glycerol, 1% (w/v) SDS, 0.15 M EDTA, 0.5 mg/ml proteinase K and 0.1% (w/v) Bromophenol Blue] followed by a 5 min incubation at 30°C. Samples were subjected to electrophoresis in a 10% non-denaturing PAGE run at 100 V for 2 h in 1× TBE buffer. Radiolabeled DNA species were visualized by phosphorimaging and quantified using ImageQuant TL software.

Chromatin immunoprecipitation assay

Chromatin immunoprecipitation (ChIP) experiments were done with the ChIP-IT® Express kit (Active Motif) as described previously (28). Briefly, U2OS/DR-GFP cells were seeded in a 10-cm plate and transfections of siRNA and I-SceI plasmid were performed as described for DR-GFP reporter assays. Two days after I-SceI plasmid transfection, cells were cross-linked with formaldehyde [1% (v/v)] at room temperature for 10 min, followed by addition of glycine (125 mM) to quench the cross-linking reaction. Chromatin fragments used in immunoprecipitation reactions were prepared by shearing of cross-linked chromatin using a bioruptor sonication device (Diagenode). One tenth of the sonicated chromatin was stored at −70°C to be used as an input sample. For each ChIP reaction, sonicated chromatin (8 µg) was immunoprecipitated overnight at 4°C with either anti-RAD51 antibody or control IgG (4 µg each) and protein G-coated magnetic beads (Active Motif). After washing, immunocomplexes were eluted from the beads and de-cross-linked according to the manufacturer's instructions (Active Motif). ChIPed and input samples were purified with the QIAquick PCR Purification Kit (Qiagen), and DNA was eluted with 50 µl of water. At least two independent experiments were performed for each ChIP reaction. In each case, eluted DNA sample (2 3 µl) was subjected to quantitative real-time PCR (qPCR) analysis in hexaplicate on a Roche LightCycler 480 Real-time PCR system with the use of Roche LightCycler 480 DNA SYBR Green I master. Data were analyzed using the Pfaffl's method (29). Fold enrichment of RAD51 binding on each target region was calculated as a ratio of the amount of DNA estimated for the RAD51-specific antibody versus the amount of DNA estimated for the control IgG. Primers used in ChIP-qPCR assays are described in Supplementary Materials and Methods.

Sister chromatid exchange assay

Sister chromatid exchange (SCE) assay was done as described previously (30). Details are provided in Supplementary Materials and Methods.

RESULTS

RECQ5 promotes formation of non-crossover products during DSB-induced HR in human cells

To gain deeper insight into the molecular mechanism of SDSA in mammalian cells, we investigated the role of two potential human orthologs of Srs2, namely, FBH1 and RECQ5, in the formation of NCO products during repair of endonuclease-induced DSBs. To selectively detect NCO events, we used the established reporter cell lines HEK293/DR-GFP and U2OS/DR-GFP (25,26,31). The DR-GFP reporter consists of a direct repeat of two mutated GFP alleles: a full length GFP interrupted by a recognition site for the I-SceI endonuclease and an internal GFP fragment that serves as a donor for HR-mediated repair of a DSB created by I-SceI in the proximal GFP allele (Figure 1A). HR-mediated repair of this DSB *via* an NCO event gives rise to a functional GFP allele, whereas repair by crossing over yields a C-terminally truncated GFP allele that does not encode for a fluorescent protein. Thus, quantification of GFP-positive cells by flow cytometry provides a measure of NCO repair efficiency. Proteins of interest were depleted from the DR-GFP reporter cell line by transfection of small interfering RNAs (siRNAs) (Figure 1B and Supplementary Figure S1). Cells were subsequently transfected with an I-SceI expression vector to induce a DSB in the reporter cassette, and the percentage of GFP positive cells arising upon DSBR was measured 2 3 days after plasmid transfection. As expected, formation of a functional GFP allele was impaired in cells depleted for the RAD51 recombinase or its loader BRCA2 (Figure 1C and D). Repair efficiency also significantly decreased on depletion of RAD52 that mediates DNA strand annealing in a reaction stimulated by RPA and is required for SDSA in budding yeast (Figure 1C) (32,33). Interestingly, depletion of BLM, the key component of the BTR complex, led to a significant increase in repair efficiency relative to control, indicating that dHJ dissolution has no role in formation of NCO repair products in the DR-GFP system (Supplementary Figure S2). This is consistent with the proposal that limited regions of homology, as is the case during ectopic recombination, decrease the possibility of forming a dHJ structure due to impediment of strand exchange by DNA end resection beyond the homologous region (34). This would imply that SDSA accounts for the majority of NCO repair events induced by I-SceI in cells harboring the DR-GFP cassette. BLM helicase probably disrupts joint DNA molecules formed during the repair process.

As for the putative Srs2 orthologs tested, only depletion of RECQ5 led to a marked reduction of repair efficiency both in HEK293 and U2OS cells, without any significant changes in cell cycle distribution (Figure 1C and D and Supplementary Figure S3). RECQ5 depletion also dramatically reduced the elevated NCO repair efficiency in HEK293/DR-GFP cells lacking BLM (Supplementary Figure S2). On the contrary, depletion of FBH1 led to a significant elevation of repair efficiency particularly in U2OS cells (Figure 1C and D). Thus, our results suggest that RECQ5 might promote DNA DSBR by the SDSA pathway of HR, whereas FBH1 might act as an SDSA suppressor.

RECQ5 counteracts the inhibitory effect of RAD51 on DSBR by SSA in human cells

It is possible that RECQ5 promotes SDSA by catalyzing disruption of an aberrant RAD51 filament that might form on the newly synthesized DNA strand after unwinding of the extended D-loop. This filament would inhibit the ssDNA-annealing step of SDSA and could promote reformation of the D-loop, shifting the balance between the HR sub-pathways in favor of DSBR. To explore this possibility, we used a GFP-based reporter for DSBR by single-strand annealing (SSA), which mechanistically resembles the post-synaptic phase of SDSA (25,31). The reporter cassette, termed SA-GFP, contains two directly oriented GFP gene fragments, 5′GFP and Sce3′GFP, forming a 280-bp repeat (Figure 2A). SSA-mediated recombination between the repeated sequences triggered by an I-SceI-generated DSB in the distal GFP fragment results in the formation of a functional GFP gene. Using HEK293-based SA-GFP reporter system (HEK293/SA-GFP), we found that

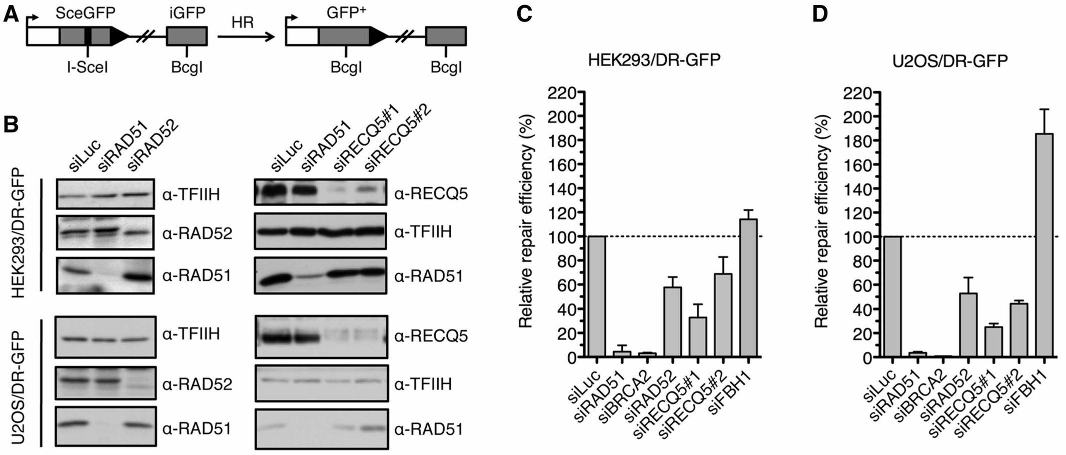

Figure 1. RECQ5 promotes homologous recombination with non-crossover outcome. (**A**) Scheme of the DR-GFP reporter cassette. The site-specific DSB in the reporter cassette is generated by I-SceI endonuclease. Only NCO events give rise to a functional GFP allele. (**B**) Western blot analysis of extracts from HEK293/DR-GFP and U2OS/DR-GFP cells transfected with indicated siRNAs. Blots were probed with indicated antibodies. (**C**) Efficiency of HR-mediated repair of I-SceI-induced DSB in HEK293/DR-GFP cells treated with indicated siRNAs. Cells were transfected with appropriate siRNA (40 nM) two days before transfection of I-SceI-expressing plasmid. Percentage of GFP-positive cells was measured by flow cytometry 2 days after DSB induction and taken as a measure of DSBR efficiency. Values plotted represent relative repair efficiency calculated as a percentage of repair efficiency measured in cells transfected with control siRNA (siLuc; 100%). All data points represent an average of at least three replicates with error bars indicating standard deviation. (**D**) Efficiency of HR-mediated repair of I-SceI-induced DSB in U2OS/DR-GFP cells treated with indicated siRNAs as compared with cells transfected with control siRNA. Experiments were performed as in (C) except that the flow cytometry analysis was performed 3 days after I-SceI transfection. HR, homologous recombination; DSB, double-strand break; NCO, non-crossover; and GFP, green fluorescent protein.

depletion of RAD51 or its loader BRCA2 resulted in a marked increase (2- to 4- fold) in SSA repair efficiency compared with control, providing evidence that formation of RAD51 filaments on resected DNA ends inhibits DSBR by SSA in human cells (Figure 2B and C and Supplementary Figure S4). On the contrary, depletion of RAD52 protein resulted in a dramatic decrease in the frequency of SSA repair events, which is consistent with the proposed role for RAD52 in promoting DNA annealing during SSA (Figure 2B and C) (31). We repeated our experiments with U2OS/SA-GFP cells, and we found that knockdown of RAD51 resulted in lethality. However, cells depleted for BRCA2 were viable and showed a dramatic increase in SSA repair efficiency compared with control cells, further supporting the aforementioned proposal (Figure 2D). As shown with the HEK293/SA-GFP cells, knockdown of RAD52 in U2OS/SA-GFP cells dramatically impaired SSA repair efficiency (Figure 2D).

Depletion of RECQ5 caused a significant reduction in SSA repair efficiency, but only if the cells contained RAD51 (HEK293/SA-GFP cells) and BRCA2 (HEK293/SA-GFP and U2OS/SA-GFP cells) (Figure 2 and Supplementary Figure S4). HEK293/SA-GFP cells depleted for both RECQ5 and RAD51 displayed a SSA repair capacity that was similar to that of cells depleted for RAD51 alone (Figure 2B and C). Similarly, the SSA defect caused by lack of RECQ5 was rescued by co-depletion of BRCA2 (Figure 2D and Supplementary Figure S4). Thus, these data suggest that RECQ5 counteracts the inhibitory effect of RAD51 on DSBR by SSA, most likely by catalyzing disruption of RAD51 filaments formed on ssDNA generated by DNA-end resection.

To verify this hypothesis, we compared the effects of overexpression of wild-type and mutant forms of RECQ5 on the efficiency of SSA-mediated repair of I-SceI-induced DSBs in U2OS/SA-GFP cells. The following RECQ5 mutants were tested: (i) mutant containing a K58R substitution in the ATP-binding site of RECQ5, which abolishes the ATPase and helicase activities of the enzyme; and (ii) mutant containing an F666A substitution in the RAD51-binding domain of RECQ5, which impairs RECQ5-RAD51 complex formation (21,35). Both mutants are defective in catalyzing RAD51 filament disruption (20,21). In line with the proposed model, we found that overexpression of wild-type RECQ5 in U2OS/SA-GFP cells resulted in a marked increase in SSA repair efficiency as compared with cells harboring control vector (Figure 2E and F). In contrast, the K58R mutant of RECQ5, which is proficient in binding to RAD51, exhibited a significant trans-dominant negative effect on the repair efficiency, possibly by preventing the access of the endogenous RECQ5 protein to RAD51 filaments formed on resected DNA ends (Figure 2E and F). For the F666A mutant of RECQ5, we found that its overexpression had no effect on SSA-mediated DSBR in U2OS/SA-GFP cells, which is consistent with the inability of this mutant to interact with RAD51 filaments (Figure 2E and F). Thus, our data strongly suggest that RECQ5 enhances the efficiency of SSA-mediated DSBR by disrupting RAD51-ssDNA filaments formed at resected DNA ends.

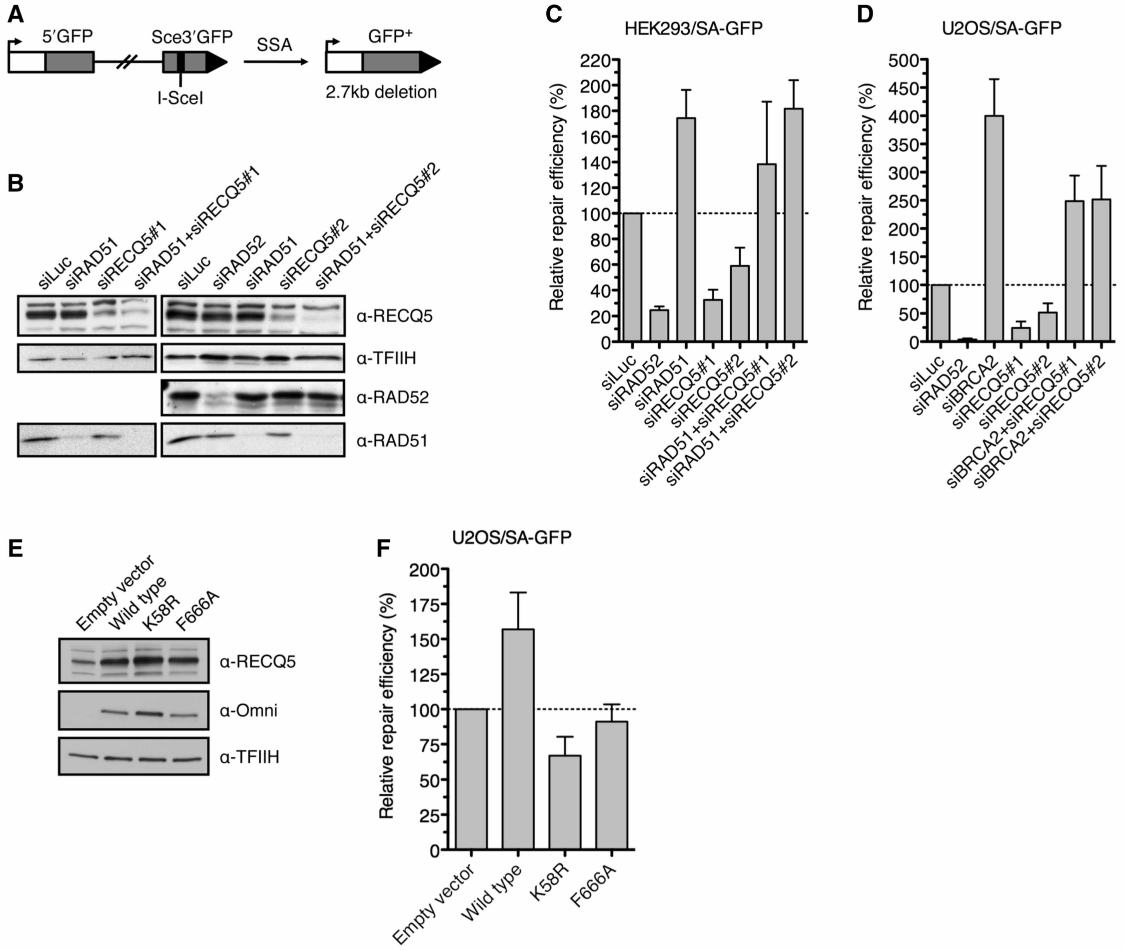

Figure 2. RECQ5 suppresses inhibitory effect of RAD51 on DNA DSBR by SSA. (**A**) Scheme of the SA-GFP reporter cassette. SSA-mediated repair of I-SceI-generated DSB results in the formation of a functional GFP allele. (**B**) Western blot analysis of extracts from HEK293/SA-GFP cells transfected with indicated siRNAs. The blots were probed with indicated antibodies. (**C**) Efficiency of SSA-mediated repair of I-SceI-induced DSB in HEK293/SA-GFP cells transfected with indicated siRNAs. Cells were transfected with appropriate siRNA (40 nM) 2 days before transfection of I-SceI-expressing plasmid. Percentage of GFP-positive cells was determined by flow cytometry 2 days after DSB induction and taken as a measure of repair efficiency. Values plotted represent relative repair efficiency calculated as a percentage of repair efficiency measured in cells transfected with control siRNA (siLuc; 100%). All data points represent an average of at least three replicates with error bars indicating standard deviation. (**D**) Efficiency of SSA-mediated repair of I-SceI-induced DSB in U2OS/SA-GFP cells transfected with indicated siRNAs. Experiments were performed as in (C) except that the percentage of GFP-positive cells was determined 3 days after DSB induction. (**E**) Western blot analysis of extracts from U2OS/SA-GFP cells transfected with pcDNA3.1/HisC-based vectors expressing wild-type RECQ5 or its mutants, K58R and F666A, respectively, as fusions with an Omni-tag. The blots were probed with indicated antibodies. (**F**) Effect of overexpression of the wild-type and mutant forms of RECQ5 on the efficiency of SSA-mediated repair of I-SceI-induced DSB in U2OS/SA-GFP**.** Cells were transfected with appropriate RECQ5 expression vector in combination with the plasmid expressing I-SceI. Percentage of GFP-positive cells was determined 3 days after plasmid transfection. Values plotted represent relative repair efficiency calculated as a percentage of repair efficiency measured in cells transfected with empty vector. All data points represent an average of at least three replicates with error bars indicating standard deviation. SSA, single-strand annealing; DSB, double-strand break; and GFP, green fluorescent protein.

RECQ5 counteracts the inhibitory effect of RAD51 on RAD52-mediated DNA annealing *in vitro*

Next, we performed biochemical experiments addressing the effect of RAD51 on RAD52-mediated annealing of two complementary oligonucleotides either in the absence or in the presence of RECQ5. In these assays, we used an ATP hydrolysis-deficient mutant of RAD51, RAD51^{K133R}, which can form a stable nucleoprotein filament in the presence of ATP, mimicking the *in vivo* ATP-bound form of the filament that is capable of catalyzing DNA strand exchange (20). Before annealing reactions, a 30-mer oligonucleotide was pre-incubated with RPA to form an ssDNA-RPA complex, whereas the other oligonucleotide (59-mer, radioactively labeled at its 5′ end) was pre-incubated either with RAD51^{K133R}

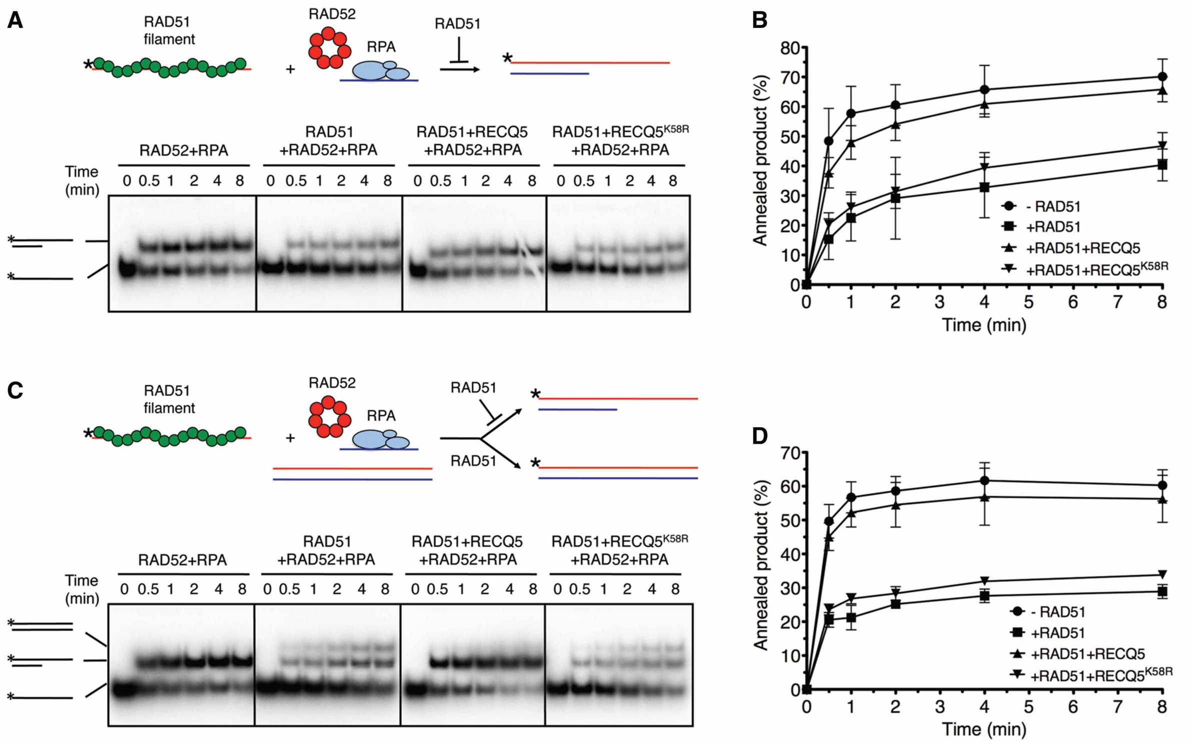

Figure 3. RECQ5 helicase counteracts the inhibitory effect of RAD51 on RAD52-mediated ssDNA annealing *in vitro*. (**A**) Upper panel: reaction scheme depicting the effect of RAD51 (green circles) on annealing of two complementary oligonucleotides (59-mer and 30-mer represented by red and blue lines, respectively) in presence of RAD52 and RPA. RAD52 is depicted as a heptameric ring structure (red circles). The 30-mer oligonucleotide can accommodate binding of one RPA heterotrimer (light blue ovals). Lower panel: all reactions were carried out at 30°C in buffer R supplemented with ATP-regenerating system. Reactions contained 5′ end radiolabeled 59-mer oligonucleotide (2.5 nM), either free or pre-coated with RAD51^{K133R} (100 nM), a 30-mer oligonucleotide (2.5 nM) complementary to the 5′-half of the 59-mer, RAD52 (60 nM) and RPA (30 nM). Where indicated, RECQ5 or RECQ5^{K58R} were present at a concentration of 80 nM. Reaction aliquots at indicated time points were subjected to PAGE followed by phosphorimaging as described in 'Materials and Methods'. (**B**) Quantification of data shown in (A). Each data point represents the mean of three independent experiments. Error bars represent standard deviation. (**C**) Upper panel: reaction scheme depicting the effect of RAD51 on annealing of two complementary oligonucleotides in presence of a homologous duplex, RAD52 and RPA. RAD51 filament formed on the radiolabeled oligonucleotide (red line with asterisk) inhibits RAD52/RPA-mediated annealing and promotes strand exchange with the homologous duplex. Lower panel: reactions were carried out and analyzed as in (B). Homologous 59-mer duplex was present at a concentration of 2.5 nM. Schemes of radiolabeled DNA species are shown on left. Radioactive label at the 5′ end is depicted by asterisks. (**D**) Quantification of data shown in (C). Each data point represents the mean of three independent experiments. Error bars represent standard deviation.

to form a nucleoprotein filament or with the reaction buffer alone. We found that addition of RPA-coated 30-mer oligonucleotide to free 59-mer oligonucleotide in presence of RAD52 resulted in rapid formation of partial DNA duplex structure with a 3′-tail (Figure 3A, *first panel from the left*, and Supplementary Figure S5). However, this RAD52-mediated ssDNA annealing was impaired if the 59-mer oligonucleotide was pre-coated with RAD51^{K133R} before its addition to the annealing reaction, demonstrating that formation of RAD51-ssDNA filaments inhibits ssDNA annealing by RAD52 (Figure 3A and B). Similar results were obtained with wild-type RAD51, although the observed inhibitory effect was less pronounced than that of RAD51^{K133R} (Supplementary Figure S6). Remarkably, the inhibitory effect of RAD51^{K133R} on RAD52-mediated ssDNA annealing was almost completely lost on addition of RECQ5 to the reaction (Figure 3A and B). On the contrary, the helicase-deficient mutant of RECQ5 (RECQ5^{K58R}) or a RECQ5 mutant lacking the RAD51-interacting domain (RECQ5$^{\Delta652-674}$) did not alleviate this inhibitory effect, suggesting that RECQ5 stimulated the ssDNA-annealing reaction by disrupting RAD51^{K133R}-ssDNA filaments (Figure 3A and B and Supplementary Figure S7). In addition, we found that the inhibition of RAD52-mediated ssDNA annealing by RAD51^{K133R} was not relieved if RECQ5 was substituted by WRN RecQ helicase or by FBH1, indicating that this reaction is specific for RECQ5 (Supplementary Figure S7).

To substantiate the aforementioned findings, ssDNA annealing reactions were also carried out in presence of a homologous DNA duplex (59-mer), conditions resembling the post-synaptic phase of SDSA. We found that this DNA duplex had no effect on RAD52-mediated annealing of the two complementary oligonucleotides (Figure 3C and D). However, if the 59-mer oligonucleotide was pre-coated with RAD51^{K133R}, we again observed a strong inhibition of RAD52-mediated ssDNA annealing with concomitant appearance of radioactively labeled 59-mer oligoduplex, an indicative of strand exchange reaction (Figure 3C and D). On addition of RECQ5, RAD51^{K133R}-catalyzed strand exchange was inhibited, and RAD52-mediated ssDNA annealing was restored to a level detected in absence of RAD51^{K133R} (Figure 3C and D). Again this effect was not seen with the K58R mutant of RECQ5 (Figure 3C and D). These data suggest that RAD51 can promote reformation of D-loop during the post-synaptic phase of SDSA and that RECQ5 can counteract this reverse reaction by removing RAD51 from the invading strand.

RECQ5 deficiency is associated with increased occupancy of RAD51 on DNA sequences flanking a DSB

To prove that the lack of RECQ5 is associated with persistence of RAD51 filaments on resected DNA ends during HR, we used ChIP to evaluate the effect of RECQ5 knockdown on RAD51 occupancy at chromatin flanking the I-SceI site in U2OS/DR-GFP cells two days after I-SceI plasmid transfection. Immunoprecipitated DNA fragments were subjected to quantitative real-time PCR analysis using primers amplifying the regions located downstream of I-SceI recognition sequence: P1, +181 to +325 and P2, +1037 to +1172 (Figure 4A). We found that RECQ5 knockdown in U2OS/DR-GFP cells was accompanied by a marked increase in the abundance of RAD51 localized near the I-SceI cutting site as compared with mock-depleted cells (Figure 4B). No significant binding of RAD51 to chromatin flanking the I-SceI site was detected in absence of I-SceI expression with both RECQ5-proficient and RECQ5-deficient cells. Thus, these data provide direct evidence that RECQ5 regulates RAD51 filament formation at DNA DSB sites.

RECQ5 acts as CO suppressor in human cells

To assess the role of RECQ5 in suppression of mitotic COs, we investigated the effect of siRNA-mediated depletion of RECQ5 and BLM on the frequency of SCEs in U2OS cells before and after induction of DNA DSBs by camptothecin (CPT). We observed that RECQ5 depletion in untreated cells had no significant effect on the SCE frequency, whereas depletion of BLM increased the SCE frequency by almost 3-fold compared with control cells (Figure 5A and C). Cells depleted for RECQ5 and BLM showed a much higher SCE frequency than cells depleted for BLM alone (Figure 5A and C), which is consistent with the studies in chicken and mouse cells (22,23). Importantly, on CPT treatment, a marked elevation of SCE frequency was observed not only in BLM-deficient cells but also in RECQ5-deficient cells, suggesting that RECQ5 has a role in CO suppression even in the presence of BLM if the load of DNA damage exceeds a certain threshold (Figure 5B). Again cells depleted for both RECQ5 and BLM exhibited a much higher frequency of CPT-induced SCEs than cells depleted for either of these proteins (Figure 5B). Thus, these data indicate that RECQ5 and BLM act in two different pathways to suppress CO formation during HR and support our hypothesis that RECQ5 promotes SDSA. It is conceivable that at low levels of DSBs in the cell, all dHJs formed as a consequence of SDSA failure (e.g. due to RECQ5 deficiency) are dissolved by the BTR complex to yield NCO products. However, at high load of DSBs, the level of dHJs formed in SDSA-deficient cells is likely to exceed the repair capacity of the BTR complex, favoring resolution to CO products. This is consistent with our finding that RECQ5-deficient cells exhibited a marked increase in SCE frequency only on exposure to CPT (Figure 5B).

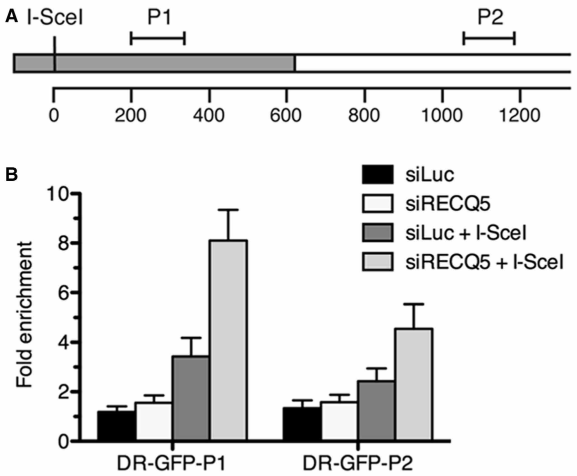

Figure 4. Effect of RECQ5 deficiency on RAD51 occupancy at chromatin flanking the I-SceI-induced DSB in U2OS/DR-GFP cells. (**A**) A schematic diagram of a part of the DR-GFP reporter cassette showing the locations of the regions amplified in ChIP-qPCR assays (P1 and P2). The GFP open reading frame with a single I-SceI recognition site is shown as gray box. The numbers correspond to base pairs. (**B**) Plot of ChIP-qPCR data. Mock-depleted (siLuc) and RECQ5-depleted (siRECQ5#1) cells were transfected with either I-SceI expression vector (+I-SceI) or empty vector, respectively. Chromatin for ChIP analysis was prepared 2 days after I-SceI transfection. Fold enrichment was calculated as a ratio of RAD51 antibody signal versus control IgG. ChIP, chromatin immunoprecipitation; and qPCR, quantitative real-time PCR.

DISCUSSION

Here we provide several lines of evidence suggesting that the human RECQ5 helicase promotes DNA DSBR by the SDSA pathway of HR. We show that (i) RECQ5 promotes the formation of NCO products during DSB-induced HR and counteracts the inhibitory effect of RAD51 filaments on DSBR by SSA; (ii) RECQ5 helicase alleviates the inhibitory effect of RAD51-ssDNA filament on RAD52-mediated DNA annealing *in vitro*; (iii) RECQ5 depletion in human cells leads to increased occupancy of RAD51 at chromatin flanking a DSB; and (iv) RECQ5 depletion is associated with increased frequency of SCEs in cells lacking the dHJ dissolvasome or in normal cells on induction of a high load of DNA damage. These data suggest that RECQ5

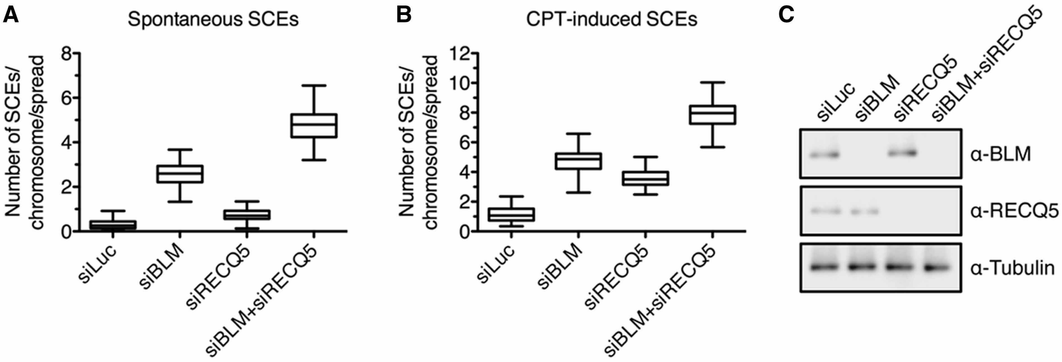

Figure 5. RECQ5 and BLM act in different pathways to suppress crossovers in human cells. (**A**) Frequency of spontaneous SCEs in U2OS cells transfected with indicated siRNAs. (**B**) Frequency of CPT-induced SCEs in U2OS cells transfected with indicated siRNA. Cells were treated with 40-nM CPT for 20 h where indicated. SCE assay and analysis was conducted as described in 'Materials and Methods'. Each data point represents number of SCEs per chromosome in a single metaphase spread. The 50 metaphase spreads were analyzed from each condition. (**C**) Western blot analysis of extracts from U2OS cells transfected with indicated siRNAs. Blots were probed with indicated antibodies. SCE, sister chromatid exchange; and CPT, camptothecin.

might act as a RAD51 filament disruptase during the post-synaptic phase of SDSA to prevent reformation of the D-loop, which would favor the classical DSBR pathway and hence increase the risk of COs (Figure 6). Futile cycles of D-loop disruption and reformation could also lead to cell death due to persistence of recombination intermediates. Consistent with our hypothesis, it has been shown that genetic ablation of RECQ5 in mouse cells is associated with persistence of RAD51 foci and increased lethality after exposure of cells to CPT, which induces DSBs during replication (20,36). Moreover, ablation of the interaction between RECQ5 and RAD51 leads to an elevation of SCEs in chicken DT40 cells lacking BLM (24). Our hypothesis is also supported by the finding that overexpression of human RAD51 has a dominant negative effect on DSB-induced gene conversion in CHO and human cells (37). RAD51 overexpression can also stimulate SCEs and the formation of interchromosomal COs (38,39). Thus, our study establishes RECQ5 as a factor that controls HR sub-pathway choice.

Counteracting Rad51 filament formation during post-synaptic phase of SDSA could as well be the underlying mechanism for the anti-recombinase function of Srs2 in budding yeast. Consistent with this proposal, it has been shown that overexpression of Rad51 in Δ*srs2* mutant cells reduces cell survival on DSB induction and nearly eliminates the NCO pathway without affecting the formation of COs, providing evidence that Rad51 inhibits the post-synaptic stage of SDSA (14,40). In addition, like RECQ5, Srs2 counteracts the inhibitory effect of Rad51 on DSBR by SSA (14,41–43). Moreover, it has been shown that overexpression of Srs2 suppresses the high level of COs in Δ*sgs1* cells, suggesting that Srs2 can shift the balance between DSBR and SDSA pathways in favor of the latter (14). This is further supported by the observation that Δ*srs2* cells show increased frequency of CO events during allelic recombination (14). Finally, yeast Rad51 was shown to inhibit Rad52-mediated DNA annealing *in vitro* (44).

It remains to be determined as to how the anti-recombinase activity of RECQ5 is regulated to prevent disassembly of the legitimate RAD51 filaments. One possibility that deserves further investigation is that the action of this helicase on RAD51 filaments might be counteracted by RAD51 mediators such as BRCA2, which facilitates filament assembly by stabilizing RAD51 binding to ssDNA (45,46). In support of this notion, it has been demonstrated that the inhibitory effect of Srs2 on Rad51 focus formation in yeast cells is antagonized by Rad52, which promotes Rad51 filament assembly by a mechanism similar to that of BRCA2 (47). Moreover, yeast Rad52 has been shown to inhibit Srs2-catalyzed Rad51-ssDNA filament disruption *in vitro* (47). It is also interesting to note that it has recently been shown that RECQ5 and BRCA2 interact with the same region on RAD51, suggesting that they exert their effect on RAD51 in a mutually competitive manner (24). In addition, overexpression of RECQ5 has been shown to impair HR-mediated repair of I-SceI-induced DSB in the HEK293/DR-GFP cells, suggesting that high levels of RECQ5 inhibit HR at the step of presynaptic RAD51 filament assembly by outcompeting the action of RAD51 mediators (21).

A previous study has shown that deletion of the mouse RECQ5 gene results in an increased frequency of I-SceI-induced HR events in cells carrying an *SCneo* reporter cassette (20). However, it has been reported that in addition to NCO-associated gene conversion, a functional *Neo* gene in this reporter system is generated by a CO recombination event, which might increase in frequency in absence of RECQ5 (48). Similarly, the frequency of I-SceI-induced HR repair within an integrated *SCneo* substrate was significantly elevate on depletion of RTEL1, which is proposed to promote SDSA by catalyzing D-loop disruption (49,50).

Disruption of the RECQ5 gene in mice leads to elevated levels of chromosomal rearrangements and cancer susceptibility (20). Moreover, a recent study has shown that

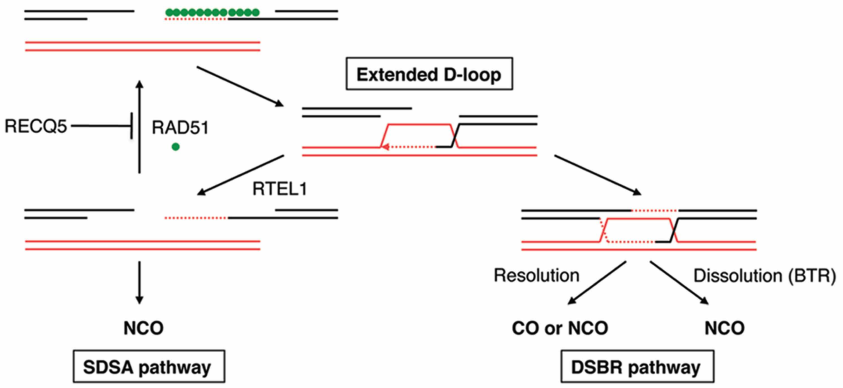

Figure 6. Model for the roles of RECQ5 and BLM in suppression of COs during DSBR by HR. RECQ5 promotes SDSA by disrupting aberrant RAD51-filaments formed after unwinding of the extended D-loop. BLM acts as a part of the BTR (BLM-TOPOIIIα-RMI1/2) complex to mediate dissolution of dHJs. RAD51 filaments formed during the post-synaptic phase of SDSA can promote re-invasion of the homologous duplex followed by formation of a dHJ structutre, increasing the risk of COs. RTEL1 promotes SDSA by catalyzing D-loop disruption. SDSA, synthesis-dependent strand annealing; dHJ, double Holliday junction; and DSBR, double-strand break repair.

RECQ5 expression levels are significantly reduced in primary colorectal cancer cells (51). Our findings suggest that these phenotypes may be a consequence of deregulation of RAD51 filament assembly, which may alter recombination pathways, leading to genomic instability. Interestingly, increased expression of the RAD51 protein has been reported in immortalized and tumor cells and its link to the genomic instability observed in these cells has been established (39,52). Thus, our study provides further insight into the molecular mechanisms underlying the build up of genomic instability associated with tumor progression.

SUPPLEMENTARY DATA

Supplementary Data are available at NAR Online, including [21,30,35,51–59].

ACKNOWLEDGEMENTS

The authors thank Jeremy Stark for DR-GFP and SA-GFP reporter cell lines, Stephen West for providing the BL21 pLysS strain overexpressing human RAD52 protein and Kasper Fugger for performing western blot analysis of FBH1 expression levels.

FUNDING

Swiss National Science Foundation [31003A-129747 and 31003A_146206], Promedica Stiftung, Czech Science Foundation [GAP305/10/0281], Stiftung zur Krebsbekämpfung and Theodor und Ida Herzog-Egli Stiftung. Postdoctoral fellowship from UBS AG (to R.K.). Funding for open access charge: Promedica Stiftung.

Conflict of interest statement. None declared.

REFERENCES

1. San Filippo,J., Sung,P. and Klein,H. (2008) Mechanism of eukaryotic homologous recombination. *Annu. Rev. Biochem.*, **77**, 229–257.
2. Heyer,W.D., Ehmsen,K.T. and Liu,J. (2010) Regulation of homologous recombination in eukaryotes. *Annu. Rev. Genet.*, **44**, 113–139.
3. Karanam,K., Kafri,R., Loewer,A. and Lahav,G. (2012) Quantitative live cell imaging reveals a gradual shift between DNA repair mechanisms and a maximal use of HR in Mid S Phase. *Mol. Cell*, **47**, 320–329.
4. Symington,L.S. and Gautier,J. (2011) Double-strand break end resection and repair pathway choice. *Annu. Rev. Genet.*, **45**, 247–271.
5. Wechsler,T., Newman,S. and West,S.C. (2011) Aberrant chromosome morphology in human cells defective for Holliday junction resolution. *Nature*, **471**, 642–646.
6. Wu,L. and Hickson,I.D. (2003) The Bloom's syndrome helicase suppresses crossing over during homologous recombination. *Nature*, **426**, 870–874.
7. Xu,D., Guo,R., Sobeck,A., Bachrati,C.Z., Yang,J., Enomoto,T., Brown,G.W., Hoatlin,M.E., Hickson,I.D. and Wang,W. (2008) RMI, a new OB-fold complex essential for Bloom syndrome protein to maintain genome stability. *Genes Dev.*, **22**, 2843–2855.
8. Nassif,N., Penney,J., Pal,S., Engels,W.R. and Gloor,G.B. (1994) Efficient copying of nonhomologous sequences from ectopic sites via P-element-induced gap repair. *Mol. Cell. Biol.*, **14**, 1613–1625.
9. Chapman,J.R., Taylor,M.R. and Boulton,S.J. (2012) Playing the end game: DNA double-strand break repair pathway choice. *Mol. Cell*, **47**, 497–510.
10. Youds,J.L. and Boulton,S.J. (2011) The choice in meiosis—defining the factors that influence crossover or non-crossover formation. *J. Cell Sci.*, **124**, 501–513.
11. Matos,J., Blanco,M.G., Maslen,S., Skehel,J.M. and West,S.C. (2011) Regulatory control of the resolution of DNA recombination intermediates during meiosis and mitosis. *Cell*, **147**, 158–172.
12. Mitchel,K., Zhang,H., Welz-Voegele,C. and Jinks-Robertson,S. (2010) Molecular structures of crossover and noncrossover intermediates during gap repair in yeast: implications for recombination. *Mol. Cell*, **38**, 211–222.
13. Prakash,R., Satory,D., Dray,E., Papusha,A., Scheller,J., Kramer,W., Krejci,L., Klein,H., Haber,J.E., Sung,P. *et al.* (2009) Yeast Mph1 helicase dissociates Rad51-made D-loops: implications for crossover control in mitotic recombination. *Genes Dev.*, **23**, 67–79.

14. Ira,G., Malkova,A., Liberi,G., Foiani,M. and Haber,J.E. (2003) Srs2 and Sgs1-Top3 suppress crossovers during double-strand break repair in yeast. *Cell*, **115**, 401–411.
15. Krejci,L., Van Komen,S., Li,Y., Villemain,J., Reddy,M.S., Klein,H., Ellenberger,T. and Sung,P. (2003) DNA helicase Srs2 disrupts the Rad51 presynaptic filament. *Nature*, **423**, 305–309.
16. Dupaigne,P., Le Breton,C., Fabre,F., Gangloff,S., Le Cam,E. and Veaute,X. (2008) The Srs2 helicase activity is stimulated by Rad51 filaments on dsDNA: implications for crossover incidence during mitotic recombination. *Mol. Cell*, **29**, 243–254.
17. Colavito,S., Macris-Kiss,M., Seong,C., Gleeson,O., Greene,E.C., Klein,H.L., Krejci,L. and Sung,P. (2009) Functional significance of the Rad51-Srs2 complex in Rad51 presynaptic filament disruption. *Nucleic Acids Res.*, **37**, 6754–6764.
18. Fugger,K., Mistrik,M., Danielsen,J.R., Dinant,C., Falck,J., Bartek,J., Lukas,J. and Mailand,N. (2009) Human Fbh1 helicase contributes to genome maintenance via pro- and anti-recombinase activities. *J. Cell Biol.*, **186**, 655–663.
19. Bernstein,K.A., Gangloff,S. and Rothstein,R. (2010) The RecQ DNA helicases in DNA repair. *Annu. Rev. Genet.*, **44**, 393–417.
20. Hu,Y., Raynard,S., Sehorn,M.G., Lu,X., Bussen,W., Zheng,L., Stark,J.M., Barnes,E.L., Chi,P., Janscak,P. *et al.* (2007) RECQL5/Recql5 helicase regulates homologous recombination and suppresses tumor formation via disruption of Rad51 presynaptic filaments. *Genes Dev.*, **21**, 3073–3084.
21. Schwendener,S., Raynard,S., Paliwal,S., Cheng,A., Kanagaraj,R., Shevelev,I., Stark,J.M., Sung,P. and Janscak,P. (2010) Physical interaction of RECQ5 helicase with RAD51 facilitates its anti-recombinase activity. *J. Biol. Chem.*, **285**, 15739–15745.
22. Wang,W., Seki,M., Narita,Y., Nakagawa,T., Yoshimura,A., Otsuki,M., Kawabe,Y., Tada,S., Yagi,H., Ishii,Y. *et al.* (2003) Functional relation among RecQ family helicases RecQL1, RecQL5, and BLM in cell growth and sister chromatid exchange formation. *Mol. Cell. Biol.*, **23**, 3527–3535.
23. Hu,Y., Lu,X., Barnes,E., Yan,M., Lou,H. and Luo,G. (2005) Recql5 and Blm RecQ DNA helicases have nonredundant roles in suppressing crossovers. *Mol. Cell. Biol.*, **25**, 3431–3442.
24. Islam,M.N., Paquet,N., Fox,D. III, Dray,E., Zheng,X.F., Klein,H., Sung,P. and Wang,W. (2012) A variant of the breast cancer type 2 susceptibility protein (BRC) repeat is essential for the RECQL5 helicase to interact with RAD51 recombinase for genome stabilization. *J. Biol. Chem.*, **287**, 23808–23818.
25. Bennardo,N., Cheng,A., Huang,N. and Stark,J.M. (2008) Alternative-NHEJ is a mechanistically distinct pathway of mammalian chromosome break repair. *PLoS Genet.*, **4**, e1000110.
26. Gunn,A. and Stark,J.M. (2012) I-SceI-based assays to examine distinct repair outcomes of mammalian chromosomal double strand breaks. *Methods Mol. Biol.*, **920**, 379–391.
27. Richardson,C., Moynahan,M.E. and Jasin,M. (1998) Double-strand break repair by interchromosomal recombination: suppression of chromosomal translocations. *Genes Dev.*, **12**, 3831–3842.
28. Kanagaraj,R., Huehn,D., MacKellar,A., Menigatti,M., Zheng,L., Urban,V., Shevelev,I., Greenleaf,A.L. and Janscak,P. (2010) RECQ5 helicase associates with the C-terminal repeat domain of RNA polymerase II during productive elongation phase of transcription. *Nucleic Acids Res.*, **38**, 8131–8140.
29. Pfaffl,M.W. (2001) A new mathematical model for relative quantification in real-time RT-PCR. *Nucleic Acids Res.*, **29**, e45.
30. Bayani,J. and Squire,J.A. (2005) Sister chromatid exchange. *Curr. Protoc. Cell Biol.*, Chapter 22, Unit 22.27.
31. Stark,J.M., Pierce,A.J., Oh,J., Pastink,A. and Jasin,M. (2004) Genetic steps of mammalian homologous repair with distinct mutagenic consequences. *Mol. Cell. Biol.*, **24**, 9305–9316.
32. Sugiyama,T., New,J.H. and Kowalczykowski,S.C. (1998) DNA annealing by RAD52 protein is stimulated by specific interaction with the complex of replication protein A and single-stranded DNA. *Proc. Natl Acad. Sci. USA*, **95**, 6049–6054.
33. Paques,F. and Haber,J.E. (1999) Multiple pathways of recombination induced by double-strand breaks in Saccharomyces cerevisiae. *Microbiol. Mol. Biol. Rev.*, **63**, 349–404.
34. Prado,F. and Aguilera,A. (2003) Control of cross-over by single-strand DNA resection. *Trends Genet.*, **19**, 428–431.
35. Garcia,P.L., Liu,Y., Jiricny,J., West,S.C. and Janscak,P. (2004) Human RECQ5beta, a protein with DNA helicase and strand-annealing activities in a single polypeptide. *EMBO J.*, **23**, 2882–2891.
36. Hu,Y., Lu,X., Zhou,G., Barnes,E.L. and Luo,G. (2009) Recql5 plays an important role in DNA replication and cell survival after camptothecin treatment. *Mol. Biol. Cell*, **20**, 114–123.
37. Kim,P.M., Allen,C., Wagener,B.M., Shen,Z. and Nickoloff,J.A. (2001) Overexpression of human RAD51 and RAD52 reduces double-strand break-induced homologous recombination in mammalian cells. *Nucleic Acids Res.*, **29**, 4352–4360.
38. Arnaudeau,C., Helleday,T. and Jenssen,D. (1999) The RAD51 protein supports homologous recombination by an exchange mechanism in mammalian cells. *J. Mol. Biol.*, **289**, 1231–1238.
39. Richardson,C., Stark,J.M., Ommundsen,M. and Jasin,M. (2004) Rad51 overexpression promotes alternative double-strand break repair pathways and genome instability. *Oncogene*, **23**, 546–553.
40. Paffett,K.S., Clikeman,J.A., Palmer,S. and Nickoloff,J.A. (2005) Overexpression of Rad51 inhibits double-strand break-induced homologous recombination but does not affect gene conversion tract lengths. *DNA Repair (Amst)*, **4**, 687–698.
41. Sugawara,N., Ira,G. and Haber,J.E. (2000) DNA length dependence of the single-strand annealing pathway and the role of Saccharomyces cerevisiae RAD59 in double-strand break repair. *Mol. Cell. Biol.*, **20**, 5300–5309.
42. Vaze,M.B., Pellicioli,A., Lee,S.E., Ira,G., Liberi,G., Arbel-Eden,A., Foiani,M. and Haber,J.E. (2002) Recovery from checkpoint-mediated arrest after repair of a double-strand break requires Srs2 helicase. *Mol. Cell*, **10**, 373–385.
43. Carter,S.D., Vigasova,D., Chen,J., Chovanec,M. and Astrom,S.U. (2009) Nej1 recruits the Srs2 helicase to DNA double-strand breaks and supports repair by a single-strand annealing-like mechanism. *Proc. Natl Acad. Sci. USA*, **106**, 12037–12042.
44. Wu,Y., Kantake,N., Sugiyama,T. and Kowalczykowski,S.C. (2008) Rad51 protein controls Rad52-mediated DNA annealing. *J. Biol. Chem.*, **283**, 14883–14892.
45. Thorslund,T., McIlwraith,M.J., Compton,S.A., Lekomtsev,S., Petronczki,M., Griffith,J.D. and West,S.C. (2010) The breast cancer tumor suppressor BRCA2 promotes the specific targeting of RAD51 to single-stranded DNA. *Nat. Struct. Mol. Biol.*, **17**, 1263–1265.
46. Jensen,R.B., Carreira,A. and Kowalczykowski,S.C. (2010) Purified human BRCA2 stimulates RAD51-mediated recombination. *Nature*, **467**, 678–683.
47. Burgess,R.C., Lisby,M., Altmannova,V., Krejci,L., Sung,P. and Rothstein,R. (2009) Localization of recombination proteins and Srs2 reveals anti-recombinase function in vivo. *J. Cell Biol.*, **185**, 969–981.
48. Johnson,R.D., Liu,N. and Jasin,M. (1999) Mammalian XRCC2 promotes the repair of DNA double-strand breaks by homologous recombination. *Nature*, **401**, 397–399.
49. Barber,L.J., Youds,J.L., Ward,J.D., McIlwraith,M.J., O'Neil,N.J., Petalcorin,M.I., Martin,J.S., Collis,S.J., Cantor,S.B., Auclair,M. *et al.* (2008) RTEL1 maintains genomic stability by suppressing homologous recombination. *Cell*, **135**, 261–271.
50. Uringa,E.J., Youds,J.L., Lisaingo,K., Lansdorp,P.M. and Boulton,S.J. (2011) RTEL1: an essential helicase for telomere maintenance and the regulation of homologous recombination. *Nucleic Acids Res.*, **39**, 1647–1655.
51. Lao,V.V., Welcsh,P., Luo,Y., Carter,K.T., Dzieciatkowski,S., Dintzis,S., Meza,J., Sarvetnick,N.E., Monnat,R.J. Jr, Loeb,L.A. *et al.* (2013) Altered RECQ helicase expression in sporadic primary colorectal cancers. *Transl Oncol.*, **6**, 458–469.
52. Klein,H.L. (2008) The consequences of Rad51 overexpression for normal and tumor cells. *DNA Repair (Amst)*, **7**, 686–693.
53. Sigurdsson,S., Van Komen,S., Petukhova,G. and Sung,P. (2002) Homologous DNA pairing by human recombination factors Rad51 and Rad54. *J. Biol. Chem.*, **277**, 42790–42794.
54. Henricksen,L.A., Umbricht,C.B. and Wold,M.S. (1994) Recombinant replication protein A: expression, complex formation, and functional characterization. *J. Biol. Chem.*, **269**, 11121–11132.

55. Benson,F.E., Baumann,P. and West,S.C. (1998) Synergistic actions of Rad51 and Rad52 in recombination and DNA repair. *Nature*, **391**, 401–404.
56. Orren,D.K., Brosh,R.M. Jr, Nehlin,J.O., Machwe,A., Gray,M.D. and Bohr,V.A. (1999) Enzymatic and DNA binding properties of purified WRN protein: high affinity binding to single-stranded DNA but not to DNA damage induced by 4NQO. *Nucleic Acids Res.*, **27**, 3557–3566.
57. Simandlova,J., Zagelbaum,J., Payne,M.J., Chu,W.K., Shevelev,I., Hanada,K., Chatterjee,S., Reid,D.A., Liu,Y., Janscak,P. *et al.* (2013) FBH1 disrupts RAD51 filaments *in vitro* and modulates homologous recombination in mammalian cells. *J. Biol. Chem.* (doi:10.1074/jbc.M113.484493; epub ahead of print).
58. Fugger,K., Chu,W.K., Haahr,P., Nedergaard Kousholt,A., Beck,H., Payne,M.J., Hanada,K., Hickson,I.D. and Storgaard Sorensen,C. (2013) FBH1 co-operates with MUS81 in inducing DNA double-strand breaks and cell death following replication stress. *Nat. Commun.*, **4**, 1423.
59. Kanagaraj,R., Saydam,N., Garcia,P.L., Zheng,L. and Janscak,P. (2006) Human RECQ5beta helicase promotes strand exchange on synthetic DNA structures resembling a stalled replication fork. *Nucleic Acids Res.*, **34**, 5217–5231.

Supplementary Information

Supplementary Materials and Methods

Antibodies and chemicals

Rabbit polyclonal anti-RECQ5 and anti-RAD51 antibodies used for Western blotting were made in the laboratory. Control IgG used for ChIP was purified from a rabbit preimmune serum. The following commercial antibodies were used in this study: rabbit polyclonal anti-BLM antibody was purchased from Abcam; rabbit polyclonal anti-TFIIH, anti-RAD51 (used for ChIP) and anti-RAD52 antibodies, goat polyclonal Omni-probe antibody and mouse monoclonal anti-β-tubulin were purchased from Santa Cruz. Chemicals used were purchased either from Sigma-Aldrich or Roche.

DNA oligonucleotides

DNA oligonucleotides used for strand-annealing assays were purchased PAGE-purified from Microsynth. The sequences of oligonucleotides used were the following:
f9 (59-mer):
5′ACTATCATTCAGTCATGTAACCTAGTCAATCTGCGAGCTCGAATTCACTGGAGTGACCT-3′
f7 (30-mer, complementary to the 5′-half of f9):
5′-ATTGACTAGGTTACATGACTGAATGATAGT-3′
f9-C (59-mer, fully complementary to f9):
5′-AGGTCACTCCAGTGAATTCGAGCTCGCAGATTGACTAGGTTACATGACTGAATGATAG-3′.
Primers used in ChIP-qPCR assays were the following:
DR-GFP-P1
Forward: 5′-TCTTCTTCAAGGACGACGGCAACT-3′
Reverse: 5′-TTGTAGTTGTACTCCAGCTTGTGC-3′
DR-GFP-P2
Forward: 5′-ACGAGAGATCTATAGATCTATAGATCATGA-3′
Reverse: 5′-CTCTTTACTGAAGGCTCTTTA-3′

Protein purification

Human RECQ5, RECQ5K58R, RECQ5$^{\Delta 652\text{-}674}$, RAD51, RAD51$^{\mathrm{K133R}}$ and RPA were over-produced in bacteria and purified as described previously (1-4). Human RAD52 was over-produced in *E. coli* BL21 (DE3) pLysS as a fusion with a hexahistidine (6xHis) tag, and purified to homogeneity as described previously with minor modifications (5). Briefly, harvested cells were resuspended in 40 ml of buffer N [20 mM Tris-HCl (pH 8.0), 0.5 M NaCl, 10% (v/v) glycerol, 0.02% (v/v) Triton X-100] containing 5 mM imidazole and lysed by sonication. After high-speed centrifugation, the lysate was loaded on a 5-ml Ni^{2+}-charged HiTrap Chelating HP column (GE Healthcare) equilibrated with buffer N containing 10mM imidazole. After washing with 50 mM imidazole in buffer N, 6xHis-RAD52 was eluted with a 50-500 mM imidazole gradient in buffer N. Peak fractions were pooled, diluted five times with buffer H [20 mM Tris-HCl (pH 8.0), 1 mM EDTA, 0.5 mM DTT, 10% (v/v) glycerol) and loaded onto a 5-ml HiTrap Heparin HP column (GE Healthcare) equilibrated with buffer H containing 100 mM KCl. After washing with equilibration buffer, 6xHis-RAD52 was eluted with a 0.1-1.0 M KCl gradient in buffer H. Peak fractions were diluted twice with buffer H and aliquots were stored at -70 °C. WRN-6xHis and GST-FBH1-6xHis were produced in Sf9 insect cells and purified as previously described (6,7).

Cell culture

All cells lines used in this study were cultured in Dulbecco's modified Eagle medium (DMEM, Gibco) supplemented with 10% fetal calf serum (FCS, Gibco) and 100 U/ml penicillin/streptomycin.

Cell Cycle Analysis

For cell cycle analysis, cells were collected, washed with PBS and fixed with 70% ethanol. Next, cells were washed with PBS, treated with 0.5 mg/ml RNaseA for 30 min at RT and stained with 50 μg/ml propidium iodide. The distribution of cell cycle phases with different DNA content was determined using LSRII (BD Biosciences) and FlowJo software.

siRNA transfection

Unless indicated otherwise, all the siRNAs used in the study were purchased from Microsynth. Transfection of siRNA was carried out using Lipofectamine RNAimax (Invitrogen) according to manufacturer's instructions. The sense strand sequences of all siRNAs used are indicated below:
siLuc: 5′-CGU ACG CGG AAU ACU UCG A dTdT-3′
siRAD51: 5′-AAG GGA AUU AGU GAA GCC AAA dTdT-3′
siBRCA2: 5′-CAGGACACAAUUACAACUAAAdTdT-3′
siRAD52: 5′-AAG GAU GGU UCA UAU CAU GAA dTdT-3′
siRECQ5#1: 5′-CAG GAG GCU GAU AAA GGG UUA dTdT-3′
siRECQ5#2: 5′-GGA GAG UGC GAC CAU GGC U dTdT-3′
siFBH1: 5′-GGG AUG UUC UUU UGA UAA AdTdT-3′ (8)
siBLM#1: 5′-CCG AAU CUC AAU GUA CAU AGA dTdT-3′
siBLM#2: a smartpool siRNA from Dharmacon (a kind gift from Dr. Pietro Pichierri).

Western blotting

Whole-cell extracts were prepared as described previously with minor modifications (9). Briefly, cells were extracted using buffer W [50 mM Tris-HCl (pH 7.5), 120 mM NaCl, 0.5% (v/v) NP-40, 20 mM NaF, 15 mM sodium pyrophosphate, 1 mM EDTA, 6 mM EGTA] supplemented with 0.1 mM PMSF and protease inhibitor cocktail (cOmplete, EDTA-free; Roche). After incubation on ice for 10 min, the lysate was sonicated and clarified by centrifugation. Total protein concentration was estimated by Bradford method. For Western blotting, whole cell extracts (50 μg) were separated on either 8% or 12% SDS-polyacrylamide gel. Proteins were transferred to PVDF membrane (Hybond, GE Healthcare), probed with appropriate antibodies and immune complexes were visualized using ECL system (Pierce).

Sister chromatid exchange assay

SCE assay was done as described previously with minor modifications (10). Briefly, cells were seeded in a 6-cm plate, and two rounds of transfection with appropriate siRNAs were performed at 24 h and 48 h post seeding. Cells were then grown for 40 h in the presence of 100 μM 5-bromo-2'-deoxyuridine (BrdU), and further incubated for 2 h with 0.2 μg/ml colcemid. Camptothecin (CPT; 40 nM) was added 20 h prior to cell harvest where indicated. Metaphase cells were harvested by mitotic shake-off, swollen in 75 mM KCl for 15 min, fixed with Carnoy's buffer (3:1 methanol and glacial acetic acid), spread on a clean glass slide and air-dried. The slides were then stained with Hoechst 33258 (50 μg/ml) for 30 min, rinsed with PBS, UV (254 nm, Stratalinker) exposed for 10 min and incubated in 2x SSC for 60 min. The slides were finally stained with 7% Giemsa solution for 15 min, washed twice with water and examined under light microscope. All quantifications were carried out blind and 50 metaphases were analyzed from each condition. Data were plotted using Prism 6 software as mean with SD.

Supplementary References

1. Garcia, P.L., Liu, Y., Jiricny, J., West, S.C. and Janscak, P. (2004) Human RECQ5beta, a protein with DNA helicase and strand-annealing activities in a single polypeptide. *EMBO J*, 23, 2882-2891.
2. Schwendener, S., Raynard, S., Paliwal, S., Cheng, A., Kanagaraj, R., Shevelev, I., Stark, J.M., Sung, P. and Janscak, P. (2010) Physical interaction of RECQ5 helicase with RAD51 facilitates its anti-recombinase activity. *J Biol Chem*, 285, 15739-15745.
3. Sigurdsson, S., Van Komen, S., Petukhova, G. and Sung, P. (2002) Homologous DNA pairing by human recombination factors Rad51 and Rad54. *J Biol Chem*, 277, 42790-42794.
4. Henricksen, L.A., Umbricht, C.B. and Wold, M.S. (1994) Recombinant replication protein A: expression, complex formation, and functional characterization. *J Biol Chem*, 269, 11121-11132.
5. Benson, F.E., Baumann, P. and West, S.C. (1998) Synergistic actions of Rad51 and Rad52 in recombination and DNA repair. *Nature*, 391, 401-404.
6. Orren, D.K., Brosh, R.M., Jr., Nehlin, J.O., Machwe, A., Gray, M.D. and Bohr, V.A. (1999) Enzymatic and DNA binding properties of purified WRN protein: high affinity binding to single-stranded DNA but not to DNA damage induced by 4NQO. *Nucleic Acids Res*, 27, 3557-3566.
7. Simandlova, J., Zagelbaum, J., Payne, M.J., Chu, W.K., Shevelev, I., Hanada, K., Chatterjee, S., Reid, D.A., Liu, Y., Janscak, P. *et al.* (2013) FBH1 disrupts RAD51 filaments in vitro and modulates homologous recombination in mammalian cells. *J Biol Chem, in press.*
8. Fugger, K., Chu, W.K., Haahr, P., Nedergaard Kousholt, A., Beck, H., Payne, M.J., Hanada, K., Hickson, I.D. and Storgaard Sorensen, C. (2013) FBH1 co-operates with MUS81 in inducing DNA double-strand breaks and cell death following replication stress. *Nat Commun*, 4, 1423.
9. Kanagaraj, R., Saydam, N., Garcia, P.L., Zheng, L. and Janscak, P. (2006) Human RECQ5beta helicase promotes strand exchange on synthetic DNA structures resembling a stalled replication fork. *Nucleic Acids Res*, 34, 5217-5231.
10. Bayani, J. and Squire, J.A. (2005) Sister chromatid exchange. *Curr Protoc Cell Biol*, Chapter 22, Unit 22 27.

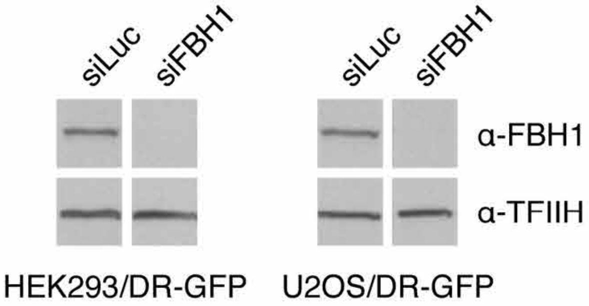

Figure S1. Confirmation of FBH1 knockdown. HEK293/DR-GFP and U2OS/DR-GFP cells were treated with indicated siRNAs. Cell extracts were subjected to Western blot analysis. Blots were probed with indicated antibodies.

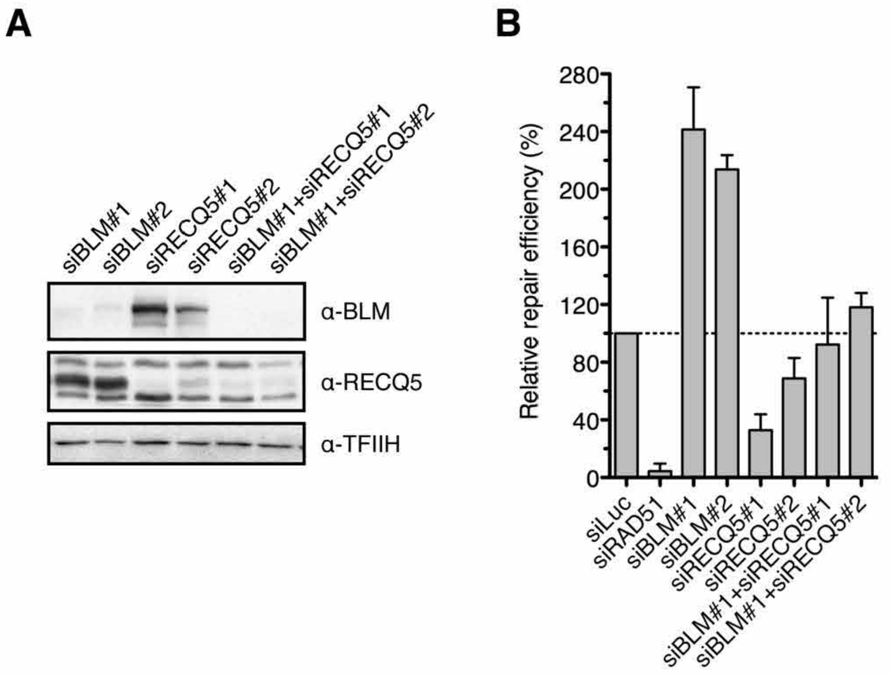

Figure S2. **(A)** Western blot analysis of extracts from HEK293/DR-GFP transfected with indicated siRNAs. Blots were probed with indicated antibodies. **(B)** Efficiency of HR-mediated repair of I-SceI-induced DSB in HEK293/DR-GFP cells treated with indicated siRNAs. Cells were transfected with appropriate siRNA (40 nM) two days prior to transfection of I-SceI-expressing plasmid. Percentage of GFP positive cells was measured by flow cytometry two days after DSB induction and taken as a measure of DSB repair efficiency. Values plotted represent relative repair efficiency calculated as a percentage of repair efficiency measured in cells transfected with control siRNA (siLuc; 100%). All data points represent an average of at least three replicates with error bars indicating standard deviation.

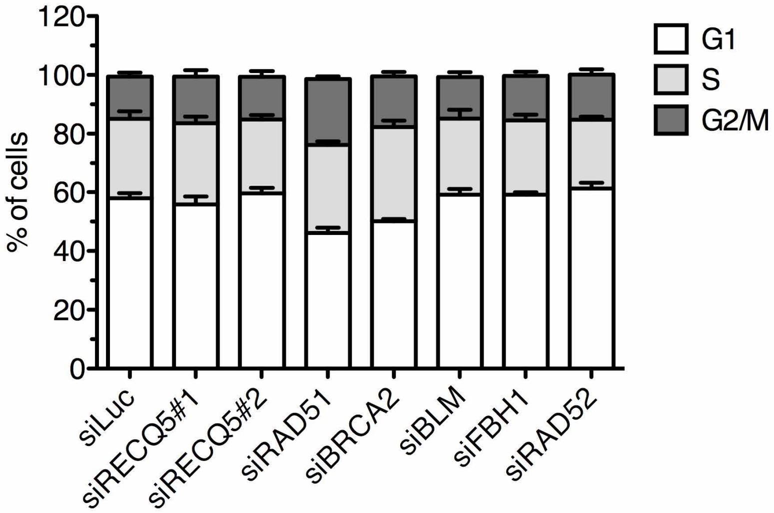

Figure S3. Cell cycle distribution of HEK293/DR-GFP cells transfected with indicated siRNAs. siRNA transfections and flow cytometry analysis were carried out as described under Materials and Methods. All data points represent an average of three replicates with error bars indicating standard deviation.

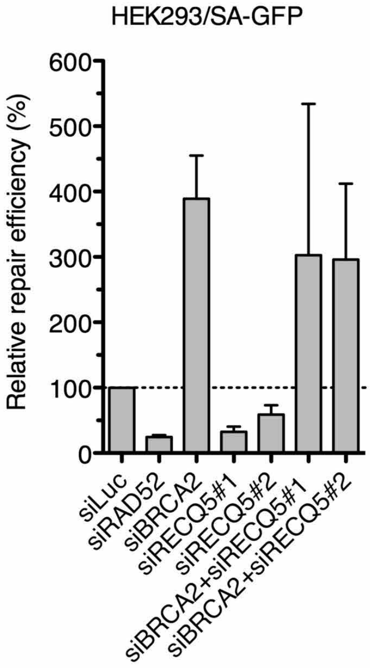

Figure S4. SSA defect of RECQ5-deficient cells is rescued by BRCA2 depletion. **(A)** Efficiency of SSA-mediated repair of I-SceI-induced DSB in HEK293/SA-GFP cells transfected with indicated siRNAs. SSA reporter assays were performed as described under Materials and Methods.

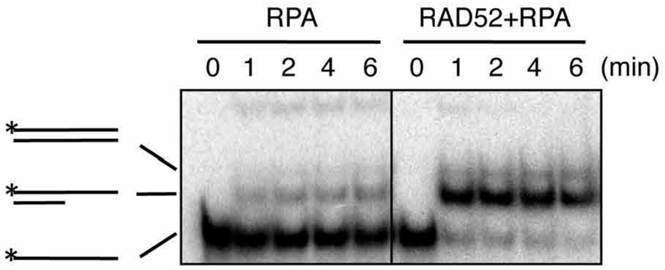

Figure S5. RAD52-mediated DNA annealing. Two complementary oligonucleotides, 5′-end radiolabeled 59mer (f9) and 30mer (f7), at a concentration of 2.5 nM, were incubated for 5 minutes in presence of RPA (30 nM) and a homologous 59mer duplex (2.5 nM). This was followed by addition of RAD52 (60 nM) where indicated. Reaction aliquots were collected at indicated time points and analyzed as in Figure 3.

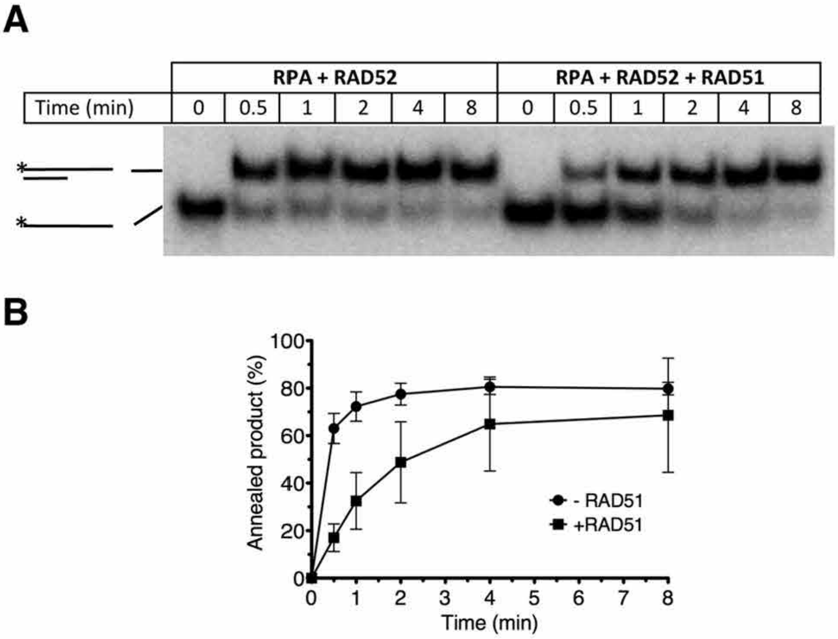

Figure S6. RAD51 inhibits RAD52-mediated ssDNA annealing *in vitro*. **(A)** Annealing reactions were carried out at 30°C in buffer R supplemented with ATP-regenerating system. Reactions contained 5′-end radiolabeled 59-mer oligonucleotide (2.5 nM), either free or pre-coated with wild-type RAD51 (300 nM), a 30-mer oligonucleotide (2.5 nM) complementary to the 5′-half of the 59-mer, RAD52 (60 nM) and RPA (30 nM). Reaction aliquots at indicated time points were subjected to PAGE followed by phosphorimaging as described in Materials and Methods. (**B**) Quantification of data shown in (A). Each data point represents the mean of three independent experiments. Error bars represent standard deviation.

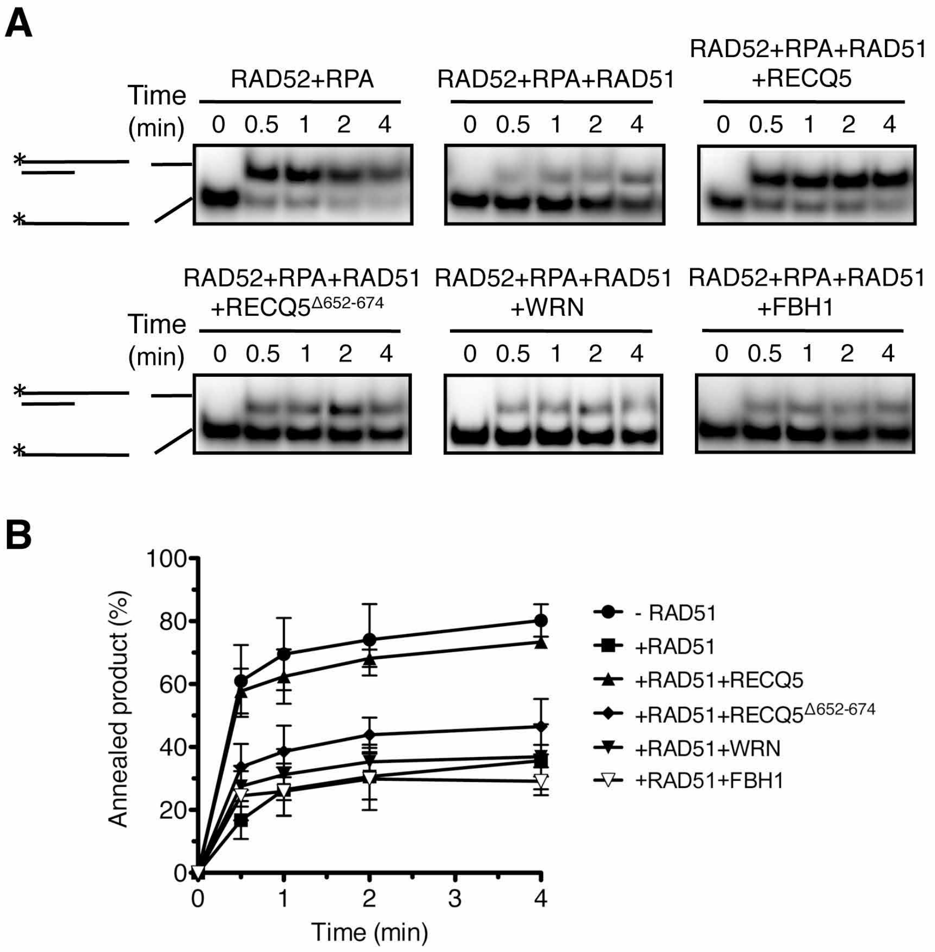

Figure S7. RECQ5, but not WRN or FBH1, alleviates the inhibitory effect of RAD51^{K133R} on RAD52-mediated ssDNA annealing. (**A**) Reactions were carried out at 30°C in buffer R supplemented with ATP-regenerating system. Reactions contained 5′-end radiolabeled 59-mer oligonucleotide (2.5 nM), either free or pre-coated with RAD51^{K133R} (100 nM), a 30-mer oligonucleotide (2.5 nM) complementary to the 5′-half of the 59-mer, RAD52 (60 nM) and RPA (30 nM). Where indicated, RECQ5, RECQ5$^{\Delta652\text{-}674}$, WRN and FBH1 were present at a concentration of 40 nM. Reaction aliquots at indicated time points were subjected to PAGE followed by phosphorimaging as described in Materials and Methods. (**B**) Quantification of data shown in (A). Each data point represents the mean of two independent experiments. Error bars represent standard deviation.

4.3. Results from collaborative work

4.3.1. Mechanistic insight into the interaction of BLM helicase with intra-strand G-quadruplex structures

Sujoy Chatterjee, Jennifer Zagelbaum, Pavel Savitsky, **Andreas Sturzenegger**, Diana Huttner, Pavel Janscak, Ian D. Hickson, Opher Gileadi and Eli Rothenberg

This Study was published in Nature communications in 2014.

For this work, I produced in E. coli and purified wild-type and helicase-dead BLM core fragments (amino acids 636-1298).

nature COMMUNICATIONS

ARTICLE

Received 12 Mar 2014 | Accepted 14 Oct 2014 | Published 24 Nov 2014

DOI: 10.1038/ncomms6556

Mechanistic insight into the interaction of BLM helicase with intra-strand G-quadruplex structures

Sujoy Chatterjee[1,*], Jennifer Zagelbaum[1,*], Pavel Savitsky[2], Andreas Sturzenegger[3], Diana Huttner[4,5], Pavel Janscak[3], Ian D. Hickson[5], Opher Gileadi[2] & Eli Rothenberg[1]

Bloom syndrome is an autosomal recessive disorder caused by mutations in the RecQ family helicase BLM that is associated with growth retardation and predisposition to cancer. BLM helicase has a high specificity for non-canonical G-quadruplex (G4) DNA structures, which are formed by G-rich DNA strands and play an important role in the maintenance of genomic integrity. Here we used single-molecule FRET to define the mechanism of interaction of BLM helicase with intra-stranded G4 structures. We show that the activity of BLM is substrate dependent, and highly regulated by a short-strand DNA (ssDNA) segment that separates the G4 motif from double-stranded DNA. We demonstrate cooperativity between the RQC and HRDC domains of BLM during binding and unfolding of the G4 structure, where the RQC domain interaction with G4 is stabilized by HRDC binding to ssDNA. We present a model that proposes a unique role for G4 structures in modulating the activity of DNA processing enzymes.

---

[1] Department of Biochemistry and Molecular Pharmacology, New York University School of Medicine, MSB 394, 550 First Avenue, New York, New York 10016, USA. [2] Genome Integrity group, Structural Genomics Consortium, University of Oxford, Oxford OX3 7DQ, UK. [3] Institute of Molecular Cancer Research, University of Zurich, CH-8057 Zurich, Switzerland. [4] NovoNordisk Foundation Center for Protein Research, University of Copenhagen, 2200 Copenhagen, Denmark. [5] Department of Cellular and Molecular Medicine, University of Copenhagen, 2200 Copenhagen, Denmark. * These authors contributed equally to this work. Correspondence and requests for materials should be addressed to E.R. (email: eli.rothenberg@nyumc.org).

G-quadruplexes (G4) are non-canonical structures formed by Hoogsteen base-pairing in guanine-rich DNA sequences[1,2]. There are >375,000 predicted G4 motifs in the human genome and >1,400 G4 motifs have been predicted in *S. cerevisiae*[3,4]. G4-forming sequences are found in telomeres and regulatory regions of the genome such as gene promoter regions, and can spontaneously form when single-stranded DNA (ssDNA) is generated during DNA metabolic processes[5,6]. The formation of G4 structures poses challenges to progression through replication, transcription and repair, and various ssDNA binding proteins and helicases are utilized for removal of G4 structures during these processes[7–13]. Specifically, it was previously shown that WRN, BLM, Pif1 and FANCJ helicases unwind G4 structures preferentially over duplex DNA *in vitro*[7–9,12,14–16]. Mutations in these helicases result in genomic instability, suggesting that their role in processing of G4 structures is central for maintaining genome integrity[17,18].

BLM and WRN belong to a highly conserved RecQ 3′-5′ helicase family implicated in DNA damage repair and the maintenance of genomic integrity[19]. A characteristic feature of RecQ helicases is their ability to recognize and unwind a wide variety of DNA structures. The diverse functionalities and often weak unwinding activity of RecQ family member proteins in a standard DNA helicase unwinding assay, together with their intrinsic strand-annealing activity, suggest a complex role for these enzymes that goes beyond a simple double-stranded DNA (dsDNA) unwinding function[9]. In particular, BLM and WRN have been suggested to play a role in the metabolism of G4 structures during chromosomal and telomeric replication, as well as in transcription[20–29]. Previous studies of the interaction of BLM with DNA substrates containing G4 structures have shown that BLM binds G4 structures with high specificity, but at the same time G4 structures can hinder BLM ssDNA translocation activity and decrease its dsDNA unwinding efficiency[30,31].

Here we define the interaction of BLM with G4 DNA through the use of single-molecule fluorescence resonance energy transfer (smFRET) analysis[32,33]. Single-molecule methods are powerful approaches capable of resolving the conformational states and dynamics of DNA and proteins in real-time that are otherwise masked by ensemble averaging. Recent single-molecule studies have provided important insights into the mechanisms of RecQ helicases with their DNA substrates and interaction of ssDNA binding proteins with G4 structures[34–37]. We used smFRET assays to monitor the conformational states of a human intramolecular G4 structure in the presence of BLM, and to analyze BLM unwinding of dsDNA located downstream of G4. Our data reveal that in substrates where a G4 motif is immediately adjacent to duplex DNA, BLM does not unfold the G4 motif, and is consequently unable to unwind the duplex DNA. On the other hand, introduction of a short ssDNA between the G4 motif and the duplex region restores BLM's activity, enabling ATP-independent unfolding of the G4 structure and permitting helicase-mediated unwinding of the downstream duplex. Analysis of G4 unfolding using BLM truncation fragments suggests a specific binding configuration where unfolding of the G4 motif by the RQC domain of BLM is facilitated by binding of the HRDC domain of BLM to the ssDNA between a G4 and a duplex region. Our experiments also reveal the existence of a different BLM-mediated and ATP-dependent G4 unfolding pathway in which unfolding is assisted by external ssDNA that is homologous to the G4 sequence. These findings define a novel mechanism of interaction between BLM and G4 structures whereby the association between BLM and the G4 structure is DNA substrate selective, and results in regulation of BLM unwinding activity via the G4 folding conformation. Based on our data, we propose that intramolecular G4 sequences confer an additional level of regulation through DNA substrate selectivity and modulation of the activity of DNA metabolic enzymes (for example, helicases) in their vicinity. These sequences consequently play a pivotal role in key biological processes such as DNA replication, transcription and repair.

Results

DNA substrate specificity of BLM in G4 unfolding. To probe the binding of BLM to G4 structures, we used a partial DNA duplex FRET substrate having a 3′-tail containing G4-forming human telomere or c-kit2 sequences ($G_3(T_2AG_3)_3$ and $(CG_3)_2CGCG(AG_3)_2G$, respectively, Supplementary Table 1, sequences 2–4 and 12–15). In these FRET substrates (illustrated in Fig. 1a–c and Supplementary Fig. 1a), the donor and acceptor dyes are placed at either end of the G4-forming sequence such that a folded G4 structure results in high FRET, while G4 unfolding would yield a low FRET signal. This arrangement enabled us to directly monitor G4 conformational changes. Previous studies have shown that monovalent cations have a pronounced effect on the stability of G4 structures; among these, K^+ has the highest stabilizing effect[38]. To establish a baseline for K^+-dependent G4 folding in our DNA substrates, we carried out a titration of our surface-tethered FRET probe with K^+ and derived the population percentage of folded G4 structures from the resulting FRET histograms (Supplementary Fig. 1b). At low K^+ ion concentration, the G4 structure is predominantly unfolded (Supplementary Fig. 1c), whereas at 50 mM K^+ the G4 structure is predominantly in a folded conformation[38].

To investigate the interaction of BLM with G4 DNA, surface-tethered G4 FRET substrates were incubated with 50 nM BLM in the presence of 50 mM K^+. We used three different partial

Figure 1 | Substrate-specific interaction of BLM with G4-forming human telomeric sequence. (a–c) BLM-mediated unfolding of G4 substrates. The illustration of each G4 DNA substrate is shown above their histograms: **(a)** G4 substrate, with G4 motif immediately adjacent to duplex region. No change in FRET distribution was observed following addition of 50 nM of BLM. **(b)** G4 (5 nt) substrate with a 5 nt ssDNA between the G4 motif and duplex region. Some change is evident upon addition of 50 nM BLM. **(c)** G4 (10 nt) substrate with a 10 nt ssDNA between the G4 motif and duplex region. A substantial change in the FRET distribution was detected upon addition of 50 nM BLM. Histograms were generated after subtracting the zero FRET values and truncating the photo bleached part from FRET trajectory. A minimum of 100 smFRET trajectories were used to generate the histograms. The concentration of K^+ was kept at 50 mM. **(d)** A representative single-molecule trajectory of the G4 substrate in the presence of 50 nM BLM showing persistent high FRET. Top panel: donor (green)–acceptor (red) intensities, bottom panel: corresponding FRET trajectory. **(e)** Representative smFRET trajectory of the G4 (10 nt) substrate in the presence of 50 nM BLM showing dynamic fluctuations in FRET signal (blue). HMM fit is in Cyan. **(f)** Quantification of observed transient trajectories in population percentage for each G4 substrate in the presence of 50 nM BLM. (Error bars = s.e.m.; $n = 5$). **(g–i)** Generated TDP matrix for each G4 substrate in the presence of 50 nM BLM, where the colour intensity corresponds to transition probability. The *y*-axis is the initial FRET prior to transition, and the *x*-axis is the final FRET after transition. **(g)** TDP for the G4 substrate with 50 nM BLM showing only the parallel and anti-parallel folded conformations of G4. **(h,i)** TDP for the G4 (5 nt) and G4 (10 nt) substrates (respectively), showing peaks corresponding to unfolding (above diagonal) and refolding (below diagonal) transitions of the G4 motif. **(j)** The calculated mean unfolding and refolding rates for the G4 (5 nt) and G4 (10 nt) substrates. (Error bars = s.e.m.; $n > 20$ for all measurements). **(k)** Illustration of the BLM-mediated sequential unfolding–refolding transitions of the G4 substrate.

duplex DNA substrates, as illustrated in Fig. 1a–c and Supplementary Table 1, with the G4 motif either immediately adjacent to the duplex region or separated by either 5 or 10 nt (substrates termed G4, G4 (5 nt) and G4 (10 nt), respectively). The histograms for these substrates before and after addition of 50 nM BLM are shown in Fig. 1a–c for telomeric G4 (upper and lower panels, respectively) and in Supplementary Fig. 2a–d for c-kit G4. Substrate G4 showed very little change in G4 folding in

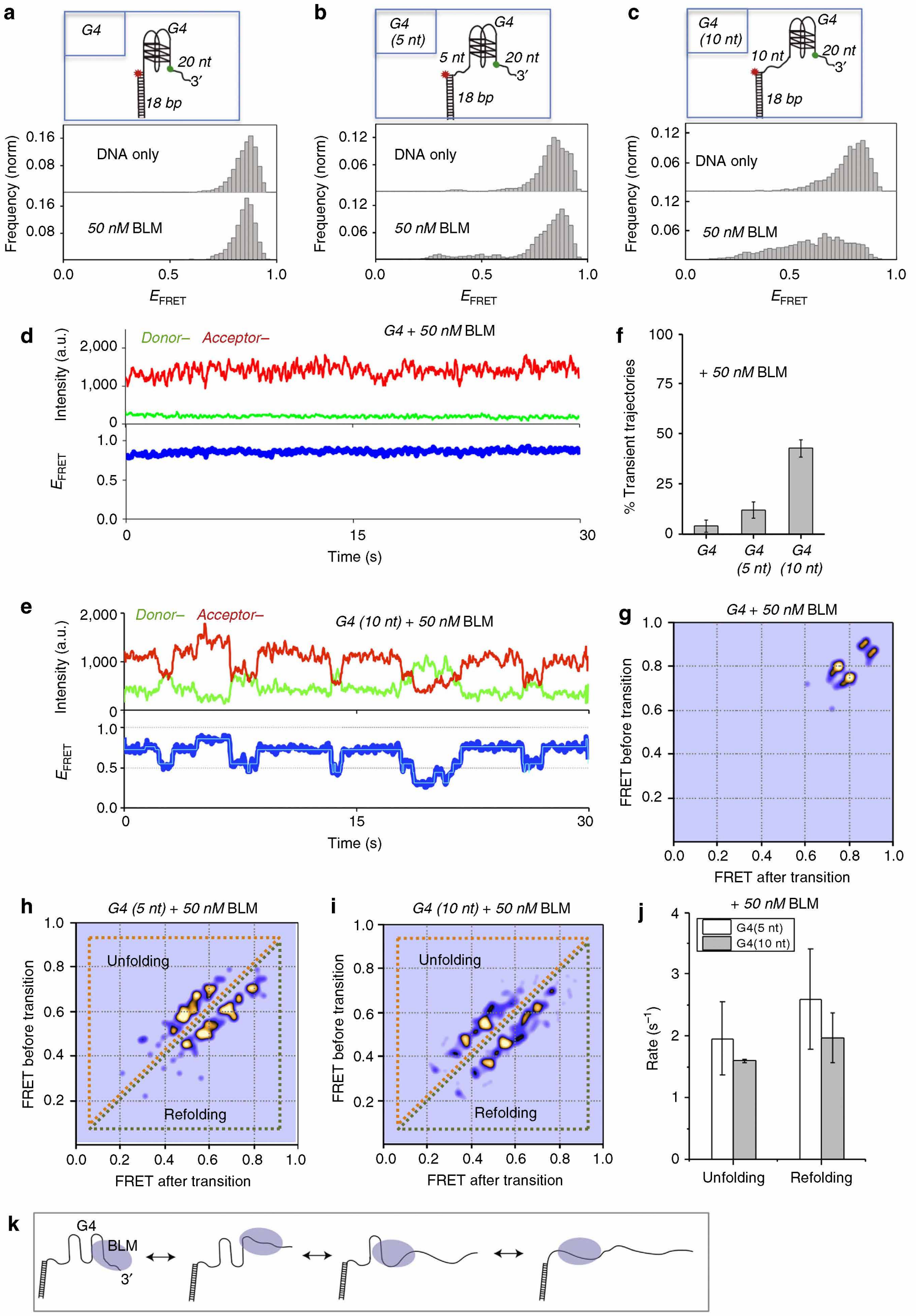

the presence of 50 nM BLM (Fig. 1a and Supplementary Fig. 2a), while substrate G4 (5 nt) displayed a change in FRET population upon addition of BLM (Fig. 1b). Substrate G4 (10 nt) showed a substantial change in FRET distribution upon addition of BLM, consistent with an efficient and ATP-independent unfolding of the G4 structure by BLM (Fig. 1c and Supplementary Fig. 2b). The unfolding of G4 structures in these substrates was found to be independent of the sequence of the ssDNA spacer used, displaying comparable unfolding for poly-dT and a mixed ssDNA spacer (Supplementary Table 1 and Supplementary Fig. 3a,b). To further establish that the observed unfolding of G4 structures by BLM is ATP independent, we tested the G4 unfolding activity of the helicase-dead BLM mutant (K695M; ref. 39). Similar to BLM, the helicase-dead BLM mutant showed no unfolding activity for the G4 substrate, but robust unfolding of the G4 (10 nt) substrate (Supplementary Fig. 4a,b). These findings demonstrate a unique and ATP-independent BLM–G4 substrate interaction, where BLM can efficiently unfold the G4 structure only when a ssDNA segment is present between the G4 motif and the duplex region.

To determine the effect of BLM binding in these substrates, we examined the temporal behaviour of individual trajectories for each DNA substrate. Figure 1d,e displays representative smFRET trajectories from the G4 and G4 (10 nt) substrates, obtained in the presence of 50 nM BLM, where the top panels show the donor (green) and acceptor (red) intensities and the bottom panel the resulting FRET efficiencies. Trajectories from the G4 substrate (Fig. 1d) showed a persistent signal indicative of a stable G4 folded conformation, whereas trajectories from both the G4 (5 nt) and G4 (10 nt) substrates (Fig. 1e and Supplementary Fig. 5) showed rapid fluctuations, indicative of G4 transitioning between folded and unfolded conformations. These repetitive unfolding–refolding transitions suggest that G4 unfolding by BLM is metastable such that G4 is capable of returning to its folded conformation. To determine the effect of BLM on the different substrates, we quantified the population percentage of trajectories showing fluctuations, evaluating a minimum of 300 molecules used for each substrate (Fig. 1f). This quantification demonstrated a clear trend, in which the percentage of trajectories exhibiting fluctuations increased with increasing distance of the G4 motif from the duplex region.

A more detailed analysis of the fluctuating trajectories revealed that G4 unfolding and refolding does not switch directly from the folded to unfolded conformations (high FRET to low FRET), but occurs via intermediate states in a step-wise manner. To map the specific BLM–G4 unfolding–refolding pathways, we conducted Hidden Markov Model (HMM) analysis on the smFRET trajectories we obtained. HMM analysis is a powerful tool for analysis of single-event trajectories, and provides important characteristics of the specific states and corresponding transition probabilities[40]. The resulting HMM fit to the G4 (10 nt) trajectory was superimposed on the smFRET trajectory, and showed both a good fit and well-defined states (Fig. 1e bottom, Cyan trace). This analysis enabled us to extract the frequency and transition rates for each FRET state and to construct a two-dimensional transition density plot (TDP). Figure 1g–i shows the TDP plots for the G4, G4 (5 nt) and G4 (10 nt) substrates, respectively, where the y-axis represents the initial FRET value before the transition and the x-axis is the final FRET value after the transition. As expected, the TDP for the G4 substrate (Fig. 1g) shows only two states, both at high FRET values, corresponding to the anti-parallel and parallel conformations of the G4 structures, which are the two main folded conformations of G4. The TDP for the G4 (5 nt) and G4 (10 nt) substrates shows a number of transitions starting from high FRET values down to intermediate and low FRET states, which correspond to transitions between G4 folded and unfolded states and *vice-versa*. Here the transitions residing below the diagonal of the TDP represent G4 refolding transitions (from lower FRET to higher FRET), whereas the transitions above the diagonal represent unfolding of the G4 structure (from higher FRET to lower FRET). The observed transition and spacing between the FRET states indicates that the G4 unfolding and refolding pathway occurs via small sequential sub-steps. This is consistent with a model in which unfolding and refolding of the four strands that participate in the G4 structure occur one strand at a time, as illustrated in the cartoon in Fig. 1k. We note that a similar observation of sequential step-wise unfolding of G4 has recently been reported for POT1-TPP1 (ref. 41).

A comparison of the mean unfolding and refolding rates for the G4 (5 nt) and G4 (10 nt) substrates revealed that refolding rates for both substrates are higher than their unfolding rates (see Supplementary Methods for rate calculation). However, the refolding rates for the G4 (5 nt) substrate were higher than the G4 (10 nt) substrate ($2.59 \pm 0.57\,\mathrm{s}^{-1}$ and $1.96 \pm 0.3\,\mathrm{s}^{-1}$, respectively). We interpret this result to mean that BLM's interaction and unfolding of the G4 motif in the G4 (10 nt) substrate is more stable than in the case of the G4 (5 nt) motif. This conclusion is in agreement with the overall increase in G4 unfolding efficiency in the case of the G4 (10 nt) substrate, as seen in the FRET histograms (Fig. 1b,c) and in the corresponding population percentage of trajectories exhibiting fluctuations (Fig. 1f). We ascribe the improved stability of BLM–G4 binding and unfolding efficiency in the G4 (10 nt) substrate to the placement of a longer ssDNA segment between the G4 motif and dsDNA.

G4 unfolding is mediated by BLM's RQC and HRDC domains. We sought to define the specific domains of BLM that participate in G4 unfolding. The full-length BLM is a 1,417 amino acids (aa) protein, whose functional core (core BLM) is located between aa 640 and 1298, and consists of three distinct domains: the helicase core, the RecQ C-terminal (RQC) domain, and the helicase and RNaseD C-terminal (HRDC) domain[42]. While the helicase domain contains the catalytic ATP and DNA binding activities, the RQC domain and HRDC domains have been identified as being important for binding non-canonical DNA substrates including G4 (refs 39,42–44). We used truncated protein fragments containing the RQC and HRDC domains (RQC–HRDC: 858–1298 aa) or HRDC domain only (HRDC: 1069–1298 aa) and compared their effect on the conformations of the G4 structure in the G4 (10 nt) substrate (Fig. 2a). Figure 2b shows the resulting smFRET histograms for the G4 (10 nt) substrate in the presence of 50 nM HRDC or 50 nM RQC–HRDC (mid and bottom panels, respectively). Both fragments resulted in altered smFRET histograms, as compared with the G4 (10 nt) DNA only histogram (top panel). However, while the HRDC fragment resulted in a change in FRET populations within the G4 folded conformation, the RQC–HRDC fragment resulted in a broader distribution corresponding to unfolded conformations of G4. Analysis of individual smFRET trajectories for each of the fragments revealed that the RQC–HRDC fragment resulted in trajectories undergoing rapid fluctuations (Fig. 2c) similar to the dynamics observed for BLM, indicative of unfolding and refolding dynamics, whereas the HRDC fragment displayed a uniform and stable signal corresponding to a folded G4 conformation. Figure 2d shows a quantification of the population percentage of fluctuating trajectories for each fragment, where both BLM and RQC–HRDC showed a considerable number of fluctuating trajectories, while HRDC did not (Supplementary Fig. 6a,b). The characteristic behaviour observed for trajectories with the RQC–HRDC fragment revealed transitions between

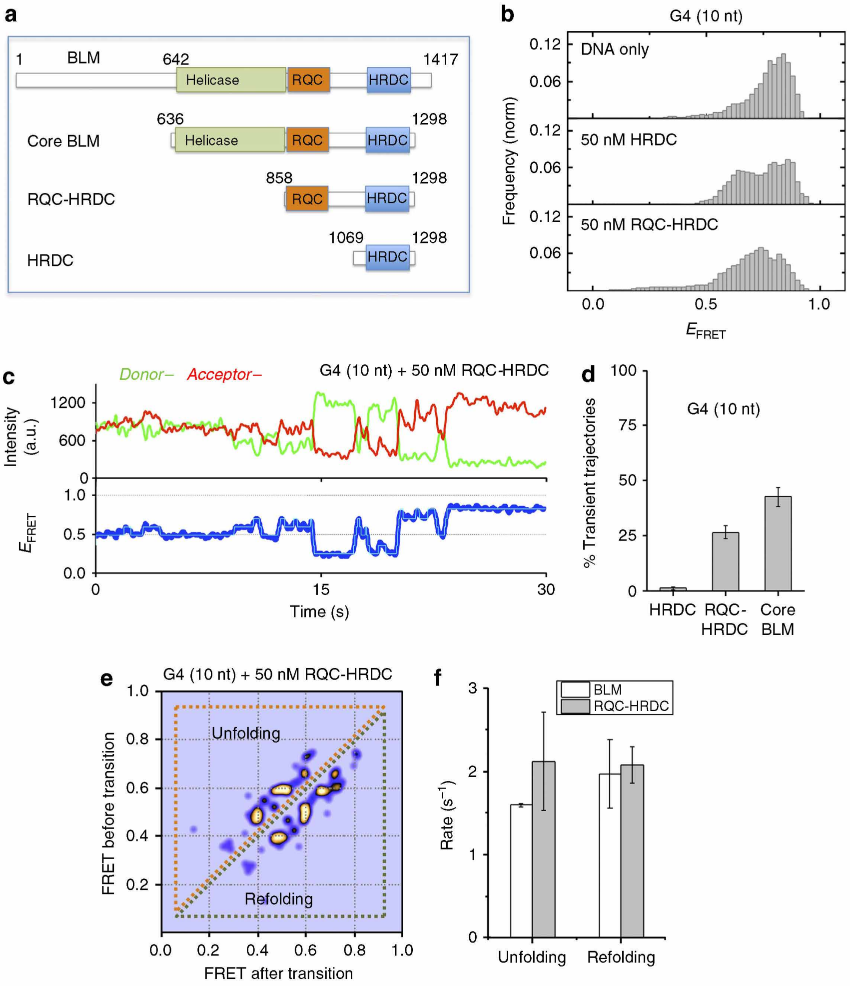

Figure 2 | Domain analysis of BLM-G4 unfolding activity. (**a**) BLM protein functional domains and truncation fragments used in this study: full-length BLM, core BLM, RQC–HRDC fragment and HRDC. (**b**) FRET histogram of the G4 (10 nt) substrate showing DNA only substrate (top panel), and in the presence of 50 nM HRDC fragment (mid panel) and RQC–HRDC fragment (bottom panel). (**c**) A representative smFRET trajectory of the G4 (10 nt) substrate in the presence of 50 nM RQC–HRDC fragment, showing rapid FRET fluctuations (blue curve). HMM fit is in cyan. (**d**) Quantification of population percentage of transient trajectories for the G4 (10 nt) substrate in the presence of 50 nM of HRDC and RQC–HRDC fragments and core BLM. (Error bar = s.e.m.; *n* = 4). (**e**) TDP for the G4 (10 nt) substrate in the presence of 50 nM RQC–HRDC fragment. (**f**) Quantification of the mean unfolding and refolding rates for the G4 motif of the G4 (10 nt) substrate, in the presence of 50 nM RQC–HRDC fragment or core BLM. (Error bar = s.e.m.; *n* > 24 for all measurements).

discrete steps, similar to those seen with BLM. We applied HMM analysis to obtain the states and corresponding rates for the observed transitions, and determined how these compared with the metrics obtained for BLM. The resulting TDP for the G4 (10 nt) substrate in the presence of 50 nM RQC–HRDC shows discrete transitions corresponding to sequential sub-steps of unfolding and refolding of G4 (Fig. 2e). We note that these transitions are comparable to the transitions observed for the same substrate in the presence of BLM. We next quantified the G4 unfolding and refolding rates for RQC–HRDC, and compared them with the rates obtained for BLM (Fig. 2f). While the G4 refolding rates for both BLM and RQC–HRDC were found to be similar ($1.96 \pm 0.3\,s^{-1}$ and $2.08 \pm 0.1\,s^{-1}$, respectively), the unfolding rate of RQC–HRDC was higher than the unfolding rate of BLM ($2.12 \pm 0.4\,s^{-1}$ and $1.5 \pm 0.01\,s^{-1}$, respectively), possibly due to an enhanced overall stability of BLM binding to DNA, as compared with RQC–HRDC[42]. We infer from the observation that both HRDC and RQC–HRDC bind the G4 substrate, while only RQC–HRDC can efficiently unfold it, that the HRDC domain assists in stabilizing the RQC domain interaction with G4, possibly by binding to the ssDNA segment downstream of G4.

To further test the hypothesis that the observed ATP-independent unfolding of G4 is unique and mediated by RQC–HRDC domains, we tested whether G4 disruption in these substrates can be carried out by other DNA helicases. We used two RecQ family helicases, WRN and RecQL5: WRN has RQC and HRDC domains similar to BLM, while RecQL5 has an RQC domain but no HRDC domain[27]. As with BLM, WRN was able to unfold the G4 structure in the G4 (10 nt) substrate, but not in the

G4 substrate alone (Supplementary Fig. 7a,b); on the other hand, RecQL5 did not display any G4 unfolding activity with either of these substrates (Supplementary Fig. 7c). We also tested the Pif1 5′–3′ helicase, previously shown to have robust G4 unwinding activity and to be implicated in the metabolism of G4 structures[10,17,45,46]. In a recent smFRET study, Pif1 was shown to bind at the 3′-tailed DNA junction, reeling in the 3′-ssDNA tail to unfold intramolecular G4 structures in an ATP-dependent manner[46]. In agreement with that study, we found that the binding of Pif1 did not result in unfolding of the G4 structure in either substrate (Supplementary Fig. 7d). These results indicate that ATP-independent G4 unfolding is carried by HRDC–RQC domains and that this is a function that is unique to RecQ helicases.

G4 structure regulates activity of BLM at proximal dsDNA. We sought to determine whether BLM's substrate selectivity in unfolding the G4 motif also affects its unwinding activity of a duplex located downstream of the G4 motif. Recent studies have shown that G4 inhibits the ssDNA translocation activity of BLM and reduces the overall efficiency of BLM-mediated duplex unwinding[31]. We first tested the regular G4 substrate (that is, having no ssDNA between the G4 and duplex region); this showed no G4 unfolding upon addition of BLM. Full unwinding of the duplex part in these FRET substrates will result in a complete loss of the donor (Cy3) labelled DNA strand and consequently loss of the fluorescence signal[32]. For our unwinding assay, BLM and ATP were added to the perfusion chamber containing surface-tethered DNA FRET substrates and incubated for 2 min, followed by a wash with high salt (500 mM NaCl) buffer to terminate the reaction. To quantify the unwinding yield, surface-tethered FRET molecules were counted before and after the unwinding reaction. Figure 3a,b shows images of individual FRET molecules obtained before and after the unwinding reaction with G4 DNA substrate (Fig. 3a) and regular partial duplex DNA substrate (Fig. 3b), where both substrates contain a duplex region of the same length and sequence (see Supplementary Table 1). These images clearly show that BLM is unable to unwind the G4 substrates, which persist after the unwinding reaction, whereas the majority of partial duplex DNA molecules were unwound and removed from the surface even in the presence of 50 nM BLM and 100 μM ATP.

To establish that the observed low yield of unwinding is indeed due to formation of G4 structures, we carried out two additional unwinding experiments with the G4 substrate, but under buffer conditions where a G4 structure cannot readily form. Instead of 50 mM KCl, we used either 2 mM KCl, where the G4 structure is

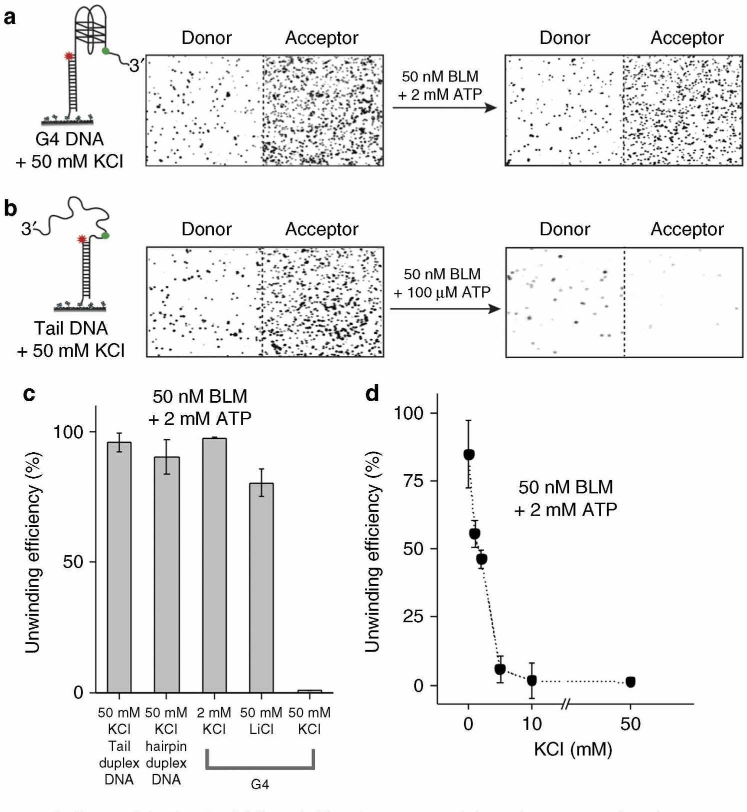

Figure 3 | Regulation of BLM unwinding activity by G4 folding. (**a**,**b**) Left—cartoon of the substrates used. Right—images of individual DNA substrate molecules before and after the unwinding reaction, where donor molecules are shown at the left and corresponding acceptor molecules are at the right. Unwinding was not seen for the G4 substrate (**a**), whereas complete unwinding was seen for the regular tailed duplex substrate (**b**). (**c**) Quantification of BLM unwinding efficiency at 50 nM BLM and 2 mM ATP for the G4 substrate at various buffer conditions. (i) Regular tailed duplex (**b**) in the presence of 50 mM KCl. (ii) hairpin substrate (Supplementary Fig. 1A) in the presence of 50 mM KCl. (iii–v) G4 substrate in the presence of: (iii) 2 mM KCl; (iv) 50 mM LiCl and (v) 50 mM KCl. (Error bar = s.e.m.; *n* = 4). (**d**) BLM unwinding activity of the G4 substrate as a function of KCl concentration (Error bar = s.e.m.; *n* = 5).

predominantly in its unfolded state, or 50 mM LiCl, as Li^+ does not stabilize G4 structures[47]. Under these conditions, BLM showed a comparable unwinding efficiency to that observed on the regular partial duplex DNA substrate (Fig. 3c), confirming that G4 structure formation indeed inhibits BLM-mediated unwinding of dsDNA when it is positioned downstream. To confirm that inhibition of unwinding is specific for the G4 containing substrate, rather than universal for substrates containing secondary structures, we used a hairpin substrate having a high GC base content ($T_m \sim 50\,°C$) with approximately the same length of G4 region (Supplementary Table 1 and Supplementary Fig. 1a). We found that unwinding of the hairpin substrate by BLM under the same buffer conditions used for the G4 substrate was highly efficient (Fig. 3c), confirming that the G4 structure specifically inhibits BLM unwinding. To further establish the effect of G4 folding on BLM unwinding activity in the G4 substrate, we quantified BLM's unwinding yield as a function of KCl concentration (Fig. 3d). This experiment showed that the unwinding yield steeply decreased with increasing KCl concentration and is fully inhibited at ~10 mM KCl and higher. The KCl-dependent reduction in unwinding yield correlates well with the increase in G4 folding stability at those concentrations (Supplementary Fig. 1b).

Next, we characterized BLM's unwinding activity for the G4 (5 nt) and G4 (10 nt) substrates, which showed elevated unfolding of G4 structures by BLM as compared with regular G4 substrate containing no ssDNA spacer (Fig. 1). Quantification of the BLM unwinding yield for these substrates and a regular G4 substrate is plotted in Fig. 4a and Supplementary Fig. 8a,b; the data show that BLM can efficiently unwind these substrates compared with the G4 substrate. Substrate G4 (10 nt) had a higher unwinding efficiency than G4 (5 nt), suggesting that initial unfolding of the G4 structure determines BLM's ability to unwind the downstream duplex. To rule out the possibility that BLM initiates unwinding of the downstream duplex directly from the 10 nt ssDNA, we used a gapped-tailed substrate (Supplementary Fig. 9 and Supplementary Table 1), which showed low unwinding efficiency compared with the G4 (10 nt) substrate. This observation confirms that unwinding is not initiated from the 10 nt ssDNA segment, but occurs after BLM unfolds and passes the G4 motif. We note that the reduced unwinding efficiency we observe for the gapped substrate is consistent with previous reports, and stem from BLM's substrate affinity rather than its binding footprint[48]. To further establish the correlation between substrate-dependent G4 unfolding and the unwinding of downstream duplex, we tested the unwinding activity of WRN and RECQL5 in these substrates. Consistent with the ATP-independent G4 unfolding observed for these helicases (Supplementary Fig. 7a,b), WRN was able to unwind the G4 (10) but not the G4 substrate, whereas REQCL5 was unable to unwind either substrate (Supplementary Fig. 10). We conclude that the RQC–HRDC-mediated unfolding of the G4 structure in these substrates governs the ability of the helicase to unwind downstream dsDNA.

To determine how ATP affects BLM's G4 unfolding activity in these substrates, we added BLM together with ATP, and then monitored G4 FRET efficiency as a function of ATP concentration. We used ATP concentrations of 1, 10 and 100 μM because at these concentrations unwinding of the downstream duplex does not dominate the observed dynamics; thus the G4 refolding–unfolding transition can be extracted and analyzed (Fig. 4b,c). While both substrates displayed a change in the FRET distribution upon addition of ATP, the G4 (10 nt) substrate showed the most substantial redistribution of the FRET populations with ATP. Analysis of individual trajectories for the two substrates showed rapid unfolding–refolding transitions for the G4 (5 nt) and G4 (10 nt) substrates, respectively (Fig. 4d,e). These fluctuations are more dynamic than the fluctuations observed for BLM unfolding–refolding transitions in the absence of ATP; this may be due to BLM's ATP-dependent translocation dynamics away from the G4 region. To obtain the specific transition states and the refolding and unfolding rates as a function of ATP, we carried out HMM analysis on individual trajectories from each substrate and generated TDP images. Figure 4f,g shows the TDP for G4 (5 nt) and G4 (10 nt) substrates in the presence of 50 nM BLM and 10 μM ATP. The TDP for the G4 (10 nt) substrate showed broadening of the transition peaks, whereas transitions for the G4 (5 nt) substrate formed defined peaks (see also Supplementary Fig. 11a–d). To determine whether the TDP reflects a specific ATP-induced G4 folding response, we plotted the unfolding and refolding rates for each substrate as a function of [ATP] for both G4 (5 nt) and G4 (10 nt) substrates (Fig. 4h,i, respectively). While the unfolding and refolding rates for the G4 (5 nt) substrate were largely unchanged as a function of [ATP], the rates for the G4 (10 nt) substrates followed a clear trend of increase with increasing ATP concentration. The increase in both unfolding and refolding rates with ATP is indicative of BLM translocating through the G4 region following G4 unfolding, which would result in an increase in both unfolding (into the G4 structure) and refolding (away from G4 towards the duplex region). The fact that this dependence is not observed for the G4 (5 nt) substrate are consistent with the dependence of this behaviour on the availability of the longer ssDNA segment between G4 and the duplex. Specifically, the length of the ssDNA spacer will govern both G4 unfolding efficiency and consequently initiation of helicase activity, so that unwinding is observed on G4 substrates where the G4 is efficiently unfolded by BLM and enough ssDNA is produced. In this event, the observed inhibition of unwinding can be ascribed to steric occlusion induced by G4 folding.

G4 complementary strand assists downstream duplex unwinding. We next sought to determine whether BLM's unwinding activity in the G4 substrate could be restored via external disruption of G4 folding. To do this, we used either replication protein A (RPA) or a short ssDNA complementary to the G4 sequence; these were added at various concentrations along with BLM (50 nM) and ATP (2 mM). Contrary to our expectations, RPA (1 or 10 nM) did not assist core BLM unwinding of the G4 substrate either when added together with BLM and ATP, or when pre-incubated with the DNA substrate prior to addition of BLM and ATP. Since core BLM lacks the RPA interaction domain[49], we also carried out these experiments with full-length BLM, which, in a similar manner to core BLM, did not show enhanced unwinding in the presence of RPA (Supplementary Fig. 12a). In contrast, addition of the complementary strand (CS) along with BLM and ATP resulted in efficient unwinding of the downstream duplex. Figure 5a shows the unwinding yield of the G4 substrate by 50 nM BLM and 2 mM ATP either added alone or in the presence of 1 or 10 nM CS, where the addition of CS enabled BLM to unwind the downstream duplex, and the unwinding efficiency increased with increasing CS concentration. To determine whether the external ssDNA-assisted G4 disruption and unwinding is homology dependent, we measured the unwinding of G4 substrate in the presence of ssDNA of similar length to CS, but with a sequence that was not complementary to G4. This resulted in a considerably lower unwinding efficiency (Fig. 5a), demonstrating that the external ssDNA-assisted unwinding of the G4 substrate is homology dependent. Figure 5b shows the resulting smFRET histograms for each concentration of CS compared with no CS, where a substantial shift and redistribution

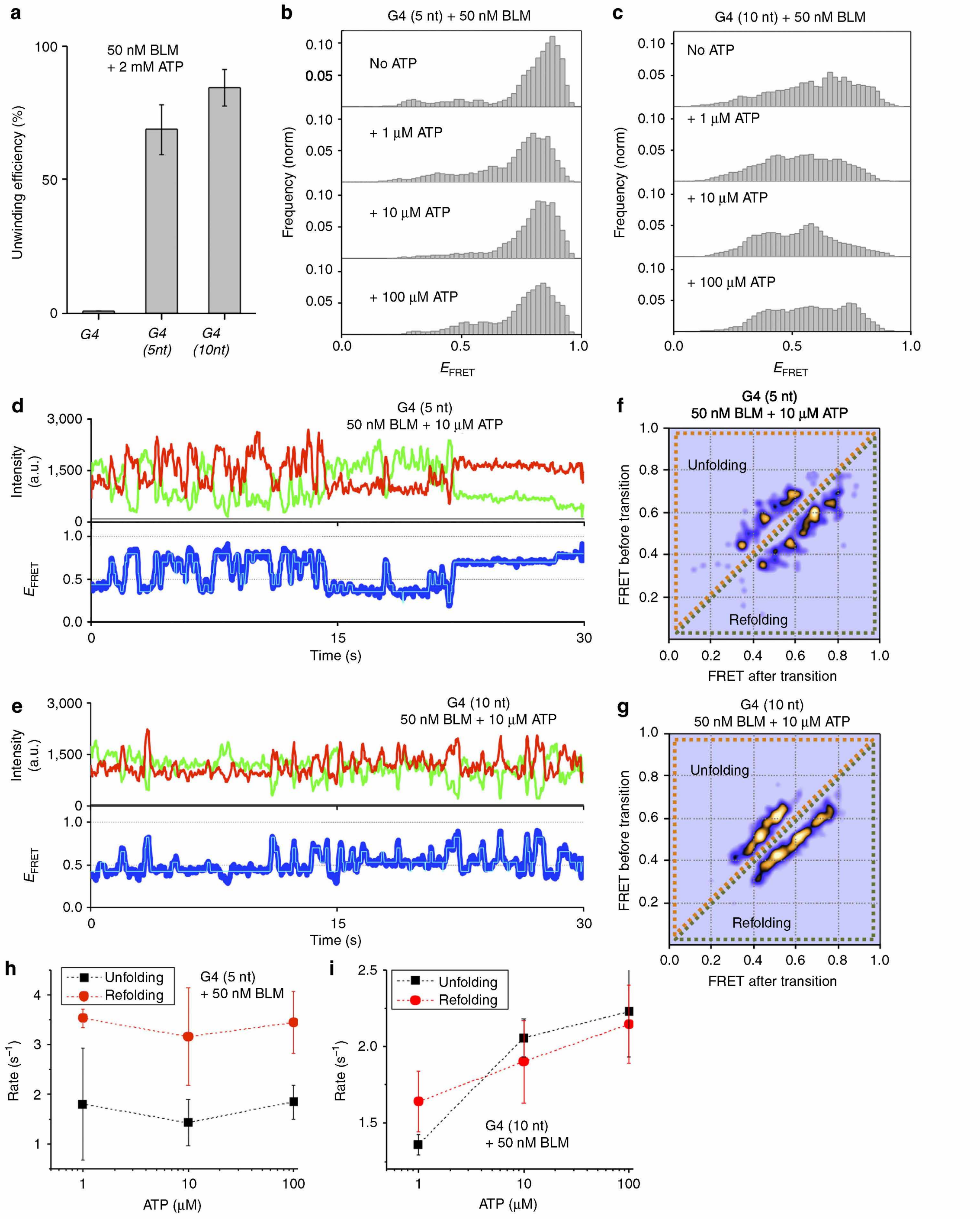

Figure 4 | BLM-dependent unwinding activity on a G4 substrate. (**a**) Quantification of BLM unwinding efficiency at 50 nM BLM and 2 mM ATP for the G4, G4 (5 nt) and G4 (10 nt) substrates (Error bar = s.e.m.; *n* = 5). (**b**,**c**) FRET histograms of the G4 (5 nt) and G4 (10 nt) substrates (**b**,**c**, respectively) in the presence of 50 nM BLM and at different ATP concentrations. (**d**,**e**) Representative single-molecule trajectories of the G4 (5 nt) and G4 (10 nt) substrates (**d**,**e**, respectively) in the presence of 50 nM BLM and 10 μM ATP. FRET trajectories were fitted with HMM (Cyan). (**f**,**g**) Generated TDP matrix of the G4 (5 nt) and G4 (10 nt) substrates (**f**,**g**, respectively) in the presence of 50 nM BLM and 10 μM ATP. (**h**,**i**) The calculated mean unfolding and refolding rates for the G4 (5 nt) and G4 (10 nt) substrates (**h**,**i**, respectively) in the presence of 50 nM BLM and at different ATP concentrations. (Error bars = s.e.m.; *n* > 15 for all measurements).

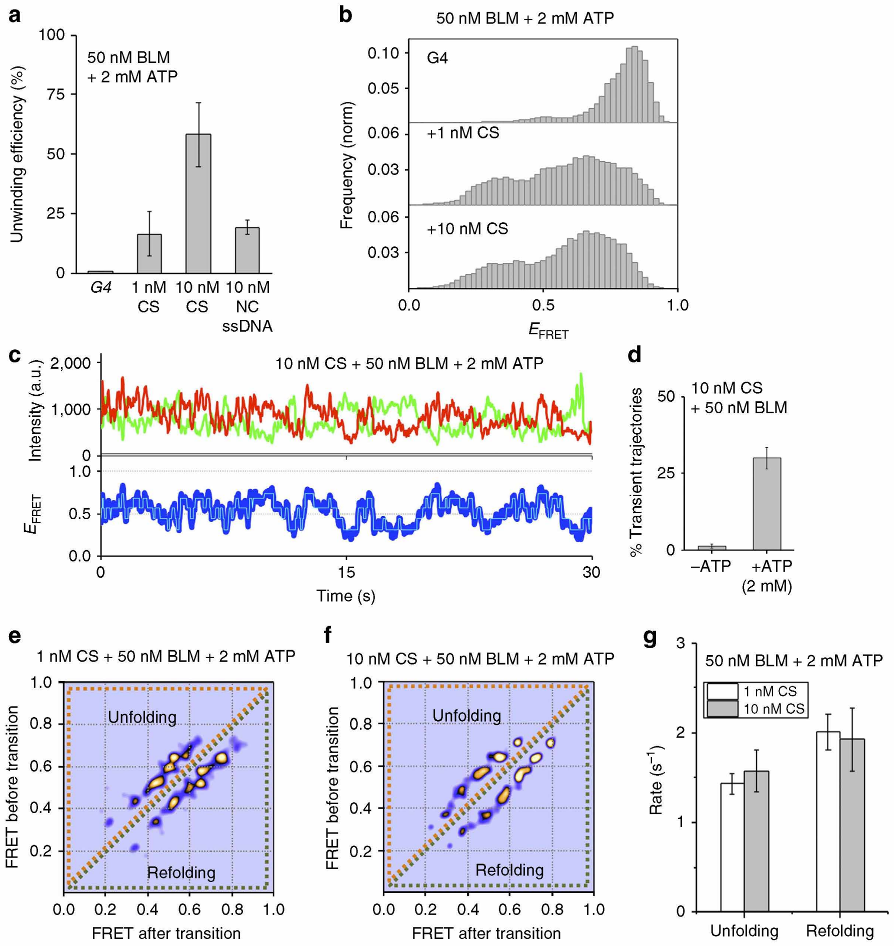

Figure 5 | G4 complementary strand-assisted unwinding of the G4 substrate. (**a**) Quantification of BLM unwinding efficiency at 50 nM BLM and 2 mM ATP for the G4 substrate in the presence of no CS, 1 nM CS or 10 nM CS, or 10 nM not complementary (NC) ssDNA (Error bar = s.e.m.; $n = 5$). (**b**) FRET histograms of the G4 substrate in the presence of 50 nM BLM and 2 mM ATP with either no CS (top panel), 1 nM CS (mid panel) or 10 nM CS (bottom panel). (**c**) Representative single-molecule trajectories of the G4 substrate in the presence of 50 nM BLM, 2 mM ATP and 10 nM CS. FRET trajectories were fitted with HMM (Cyan). (**d**) Quantification of population percentage of transient trajectories for the G4 substrate in the presence of 50 nM BLM and 10 nM CS and with our without 2 mM ATP. (Error bar = s.e.m.; $n = 4$). (**e**,**f**) Generated TDP matrix of the G4 substrate in the presence of 50 nM BLM and 2 mM ATP as well as either 1 nM CS or 10 nM CS (**d**,**e**, respectively). (**g**) The calculated mean unfolding and refolding rates for the G4 substrate in the presence of 50 nM BLM, 2 mM ATP and at 1 nM or 10 nM CS concentration. (Error bars = s.e.m.; $n > 34$ for all measurements).

of FRET values is seen for both 1 and 10 nM CS. Figure 5c shows a representative smFRET trajectory of the G4 substrate in the presence of 10 nM CS, 50 nM BLM and 2 mM ATP: here the data reveal a display of dynamic fluctuations, representing rapid unfolding and refolding transitions. These dynamics are in contrast to the stable FRET trajectory obtained for the G4 substrate in the presence of 50 nM BLM and 2 mM ATP, when no CS was added (Supplementary Fig. 12b). To determine the role of ATP in G4 unfolding, we quantified the number of trajectories showing fluctuations in the presence and absence of ATP (Fig. 5d). In contrast to the ATP-independent unfolding in the G4 (5 nt) and G4 (10 nt) substrates, unfolding–refolding transitions were not observed in the absence of ATP, confirming that CS-assisted G4 unfolding is ATP dependent. To characterize the observed transitions, we carried out HMM analysis of trajectories at two concentrations of CS, and generated their TDP (Fig. 5e,f). The resulting TDP for both CS concentrations showed similar transition probabilities. This verifies that the occurrence of G4 unfolding, but not the unfolding pathway itself, depends upon CS concentration. Moreover, this finding suggests that CS-assisted unwinding is mediated by a single CS per G4 substrate. This conclusion is further supported by the unfolding–refolding rates (Fig. 5g), which remained unchanged with increased concentration of CS.

We note that when CS was added to the G4 substrate alone no change was observed in the G4 conformation, confirming that the CS interaction with G4 is not random and is facilitated by BLM (Supplementary Fig. 12c). While BLM has strand-annealing activity, this interaction is not carried out via its annealing activity, as the core BLM lacks the domain for this activity[50]. This was also verified by testing CS-assisted unwinding of the G4 substrate using full-length BLM, which did not result in an increase in unwinding yield as compared with the core BLM (Supplementary Fig. 12d). We conclude that the HRDC domain

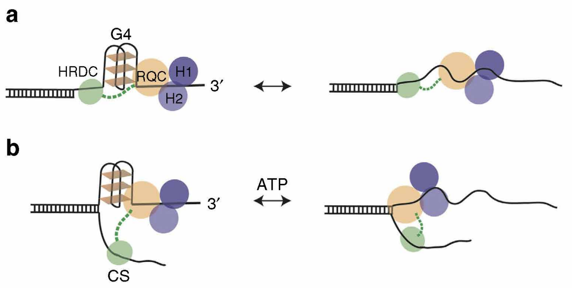

Figure 6 | Proposed model for BLM–G4 substrate selectivity, unfolding of a G4 motif and regulation of BLM activity via binding cooperativity of RQC–HRDC domains. (**a**) In binding to substrates containing ssDNA between G4 and duplex DNA, the HRDC domain, via its flexible linker, binds the ssDNA between G4 and the duplex region thus anchoring and stabilizing RQC interaction with G4, facilitating its unfolding. (**b**) ATP-dependent complementary strand-assisted unfolding of G4, the HRDC binds CS assisting to destabilize G4 structure.

may play a role here as well, in which the helicase core and the RQC domain are in contact with the G4 substrate, while the HRDC domain captures the CS and facilitates the destabilization of G4 and unwinding of the downstream duplex.

Discussion

Using smFRET we show that BLM requires a ssDNA segment between the G4 motif and duplex region to efficiently unfold intramolecular G4 DNA structures. The unfolding of G4 is ATP independent, is mediated by the RQC and HRDC domains, and occurs in a sequential manner, where G4 does not transition directly to the unfolded conformation, but proceeds via sub-steps. Moreover, BLM unfolding of G4 is metastable, which allows for repetitive refolding and unfolding transitions to occur. The length of ssDNA segment determines the magnitude of G4 destabilization and consequently unwinding of a downstream duplex. Taken together, our observations demonstrate that the BLM–G4 interaction constitutes a unique substrate-dependent activity.

Based on our findings, we propose an integrated model for the cooperative binding and interaction of BLM with an intramolecular G4 structure (Fig. 6). Unfolding of G4 by BLM is mediated via cooperative binding of the RQC and HRDC domains, where the RQC interaction with G4 is stabilized by HRDC binding to the ssDNA segment between G4 and the duplex (Fig. 6a). In addition, the ssDNA binding activity of the HRDC domain may also play a role in capturing the CS to promote BLM's CS-assisted unwinding of the regular G4 substrate, as illustrated in Fig. 6b. Previous studies have identified the RQC domain as having a high affinity for G4 structures, whereas the HRDC domain was shown to play a regulatory role in HJ dissolution and binding to ssDNA[39,43,44,51]. Recent structure-based studies have suggested a model for BLM HJ interaction, in which HRDC binds ssDNA at the junctions and operates at a distance from the RQC and helicase core[52,53]. This distant interaction is afforded by a long flexible linker (13 aa ~ 10 nm) between the RQC and HRDC, which is sufficient for binding ssDNA over the folded G4 structure (~5 nm)[52]. Cooperative binding at a distance may explain helicase selectivity in unfolding and processing specific G4 substrates.

There is a growing body of evidence that G4 structures and G4-associated proteins play a central role in chromosome metabolism. Several hundred thousand DNA sequences with the potential to form intra-stranded G4 structures are present in the human genome[5,6,54,55]. These sequences will spontaneously form intra-stranded G4 structures when ssDNA is generated during DNA replication, transcription and repair, and if not removed will obstruct these processes[18,56]. Several human helicases have been implicated in the removal of G4 structures, including FANCJ, RTEL1 and Pif1 (having a 5′–3′ directionality), and two RecQ family helicases, BLM and WRN (each with a 3′–5′ directionality)[57]. Importantly, among the five human RecQ family helicases, only BLM and WRN have both RQC and HRDC domains[27]. With respect to their function in the removal of G4 structures, BLM and WRN have been found to associate with the replication machinery in both chromosomal and telomere replication[20,22–26,35,58]. During replication, intramolecular G4 structures can form after dsDNA unwinding by the replicative helicase and impede leading or lagging strand synthesis, resulting in an accumulation of ssDNA and the collapse of the replication fork. Based on our findings and proposed model, BLM and WRN may assist in the removal of characteristic replication fork G4 structures, as previously suggested[19]. In addition, the substrate selectivity and removal of G4 structures by BLM and WRN may play an important role during transcription. Recent studies have identified a novel correlation between the presence of G4-forming sequences in the regulatory regions of genes and the regulation of gene expression by BLM and WRN helicases[28,59]. The regulation of gene expression by BLM and WRN may thus be mediated by removal of G4 structures formed on ssDNA within the transcription R-loop, which would otherwise impede gene expression.

In a recent smFRET study of Pif1 helicase it was shown that the removal of G4 structures is ATP dependent and mediated by reeling of a ssDNA tail[46]. Importantly, this study found that the binding of Pif1 and reeling of ssDNA is only permitted in substrates having a ssDNA spacer between the dsDNA and G4. While the underlining mechanisms for G4 removal by Pif1 and BLM are distinct, the striking similarity in the requirement for a ssDNA spacer suggests a unique DNA substrate selectivity among G4 specific helicases. Such selectivity may be jointly utilized in G4 metabolism. For example, BLM has been shown to interact with FANCJ, a helicase-like BLM implicated in DNA repair but with opposite directionality[60]. FANCJ has been shown to unwind G4 structures in a unique manner compared with representative Fe-S cluster helicases[61], and has been implicated with BLM in a common pathway that maintains epigenetic stability at G4 DNA[62]. We predict that G4 structural selectivity and cooperation among other DNA processing enzymes provides an additional level of functional regulation that plays a critical role in genomic metabolism.

Methods

DNA preparations. All oligonucleotides (Supplementary Table 1) were purchased from Integrated DNA Technology (IDT). For annealing, the appropriate oligonucleotides were mixed and heated for 3 min at 94 °C followed by slow cooling.

Protein purification. To investigate the interaction of BLM with G4 DNA, we used the core BLM helicase, a truncated BLM variant ($BLM^{636–1298}$) containing RQC and HRDC domains that retain the unwinding and translocation activity of the wild-type BLM[30,36,42]. In addition, we used core WRN (418–1,232) containing the RQC and HRDC domains, human Pif1 helicase domain (206–641) shown to binding G4 structures and unwind inter-stranded G4, helicase-dead core BLM (K695M) and RecQL5. Full-length BLM was used to verify our observations relating to core BLM.

Core BLM (aa 636–1,298) was expressed in *Escherichia coli* system and purified using tag affinity capture[63]. After cleavage with TEV protease, the protein retains the vector-derived sequences SM and ENLYFQ at the N- and C-termini, respectively. Truncated fragments (RQC–HRDC: aa 858–1,298 and HRDC: aa 1,069–1,298) were cloned into vector pNIC28-Bsa4 and purified on HisTrap FF and Superdex 75 columns[64]; the proteins were used without removal of the N-terminal His_6 tags. Al purified proteins maintained their native state as determined by their gel filtration absorption profile, which migrates as a single symmetrical peak (Supplementary Fig. 13 for RQC–HRDC fragment). Core WRN, Pif1 HD were expressed and purified from a Baculovirus expression vector system[65,66]. For expression and purification RecQL5 and helicase-dead core BLM we used *E. coli* expression system and purified using an affinity tag[42,67].

Expression and purification of the recombinant full-length BLM protein was performed using a three-step protocol[68]: nickel affinity, heparin affinity and gel filtration chromatography. In brief, yeast cell pellets expressing human BLM (JEL1 + pJK1_BLM) were re-suspended in an equal volume of lysis buffer, consisting of 50 mM Hepes-KOH pH 7.4, 1 M KCl, 1 mM DTT, 10% glycerol, 1 mM PMSF and supplemented with complete EDTA-free protease inhibitor (Roche). Benzonase (E1014-25kU, Sigma) was added at 25 U ml^{-1}. An equal volume of glass beads (425–600 μm, Sigma) was added to the suspension and the cells were lysed by vigorous shaking for 10 × 1 min with incubations of 30 s on ice after each burst. The lysate was clarified at 350,000*g* for 1 h at 4 °C. The supernatant was adjusted to contain 15 mM imidazole, filtered through 45 μm filter and loaded onto HisTrap column (GE Healthcare). The column was washed with lysis buffer containing 15 mM imidazole. Subsequently, the washing buffer was exchanged to the same buffer with reduced salt concentration (500 mM KCl instead of 1 M). Several step gradients of this buffer, containing different concentrations up to 80 mM imidazole, were used further to wash the column. The column was eluted using a 10-column volume gradient between 80 and 500 mM imidazole. Eluted fractions containing BLM were pooled, diluted to adjust the final pH and KCl concentration to 7.5 and 125 mM, respectively, and were loaded onto a Heparin column (GE Healthcare). The column was washed with a buffer containing 50 mM Hepes-KOH pH 6.8, 125 mM KCl, 1 mM DTT, 10% glycerol and supplemented with complete EDTA-free protease inhibitor. The BLM protein was eluted using a 20-column volume gradient between 150 mM and 1 M KCl. Eluted fractions containing the BLM protein were pooled and concentrated up to 10-fold using an Amicon Ultra-4 cetrifugal filter device (50 K cut-off, Millipore). The pooled eluate was loaded onto a gel filtration column (Superose 6 10/300 GL; GE Healthcare) using a buffer containing 50 mM Hepes-KOH pH 7.4, 10% glycerol, 500 mM KCl and 1 mM DTT. Fractions containing recombinant BLM, as determined by Coomassie-stained SDS–PAGE, were pooled and the protein was dialyzed against a buffer containing 50 mM Hepes-KOH pH 7.2, 250 mM KCl, 10% glycerol and 1 mM DTT. Finally, the protein was stored at − 80 °C in small aliquots.

Single-molecule fluorescence resonance energy transfer. Reactions were carried out at room temperature in a standard buffer composed of 50 mM Tris-HCl (pH 8.0), 2 mM MgCl$_2$ and an oxygen scavenging system (1 mg ml^{-1} glucose oxidase, 0.4% (w/v) D-glucose, 0.02 mg ml^{-1} catalase and 2 mM Trolox)[32]. The concentration of K$^+$ in the buffer was varied and is indicated accordingly in the text or in the figure legends. All experiments had 100 pM DNA immobilized on a PEG-coated quartz surface with biotin–neutravidin linkage.

Microscopy set-up and single-molecule analysis. We used a custom-built microscopy set-up based on a Leica DMI3000 microscope equipped with an HCX PL APO × 63 numerical aperture = 1.47 OIL CORR TIRF objective followed by achromatic × 2 tube lens magnification. The microscope was coupled to 532 and 640 nm solid-state lasers to excite the sample at Total-Internal-Reflection illumination mode for improved signal to noise ratio and reject out plane fluorescence.

Sample emission was collected and split into two channels through the use of proper dichroic and emission narrow-band bandpass filters (filter for green channel 580/60, filter for red channel 680/40, Semrock) in conjunction with the use of a Dual View (DV2-Photometrics) to image two colours simultaneously, side-by-side, onto a single EM-CCD camera (Andor iXon + 897) acquiring at 33 Hz. For accurate alignment and mapping of the two colour channels, we first imaged diffraction-limited fluorescent beads that have wide emission spectra spanning both channels (Invitrogen). The location of the beads was matched for both channels, and a mapping matrix was generated using an IDL (Exelis Visual Information Solutions) custom mapping routine. Briefly, this routine is based on the use of a polynomial morph-type mapping function, whereby mapping coefficients are generated by Gaussian and centroid fits to the sub-diffraction limit point-spread functions of the fluorescence beads. Another IDL code was used, along with the mapping matrix, to extract corresponding single-molecule donor and acceptor spots into single-molecule trajectories. Programmes written in MATLAB were used to view and analyze single-molecule fluorescence time trajectories. FRET efficiency, E_{FRET}, was approximated as the ratio between the acceptor intensity and the sum of acceptor and donor intensities. Each smFRET histogram was generated by a minimum of a 100 trajectories, and the contribution of each trajectory was normalized in the histogram so that the weight of the FRET states from each molecule in the histogram will be identical. For unwinding yield quantification, dual images were analyzed using a threshold and cluster counting routine, to obtain the number of molecules observed in the field of view. HMM analysis, TDP and derived statistics were done using freely available HMM and TDP software (Ha lab)[40]. The resulting TDP plots showed a number of symmetrical peaks for folding and refolding transitions, along with a low intensity singular peak for refolding into higher FRET state. We interpret this peak as possible ssDNA looping mediated by the HRDC domain occurring after unfolding of the G4 structure. To generate the mean rates for folding (unfolding) we averaged the folding (unfolding) rates obtained from each TDP peak/transition.

References

1. Gellert, M., Lipsett, M. N. & Davies, D. R. Helix formation by guanylic acid. *Proc. Natl Acad. Sci. USA* **48,** 2013–2018 (1962).
2. Sen, D. & Gilbert, W. Formation of parallel four-stranded complexes by guanine-rich motifs in DNA and its implications for meiosis. *Nature* **334,** 364–366 (1988).
3. Hershman, S. G. *et al.* Genomic distribution and functional analyses of potential G-quadruplex-forming sequences in Saccharomyces cerevisiae. *Nucleic Acids Res.* **36,** 144–156 (2008).
4. Todd, A. K., Johnston, M. & Neidle, S. Highly prevalent putative quadruplex sequence motifs in human DNA. *Nucleic Acids Res.* **33,** 2901–2907 (2005).
5. Huppert, J. L. Structure, location and interactions of G-quadruplexes. *FEBS J.* **277,** 3452–3458 (2010).
6. Qin, Y. & Hurley, L. H. Structures, folding patterns, and functions of intramolecular DNA G-quadruplexes found in eukaryotic promoter regions. *Biochimie* **90,** 1149–1171 (2008).
7. Huber, M. D., Lee, D. C. & Maizels, N. G4 DNA unwinding by BLM and Sgs1p: substrate specificity and substrate-specific inhibition. *Nucleic Acids Res.* **30,** 3954–3961 (2002).
8. London, T. B. *et al.* FANCJ is a structure-specific DNA helicase associated with the maintenance of genomic G/C tracts. *J. Biol. Chem.* **283,** 36132–36139 (2008).
9. Mohaghegh, P., Karow, J. K., Brosh, Jr R. M., Bohr, V. A. & Hickson, I. D. The Bloom's and Werner's syndrome proteins are DNA structure-specific helicases. *Nucleic Acids Res.* **29,** 2843–2849 (2001).
10. Paeschke, K., Capra, J. A. & Zakian, V. A. DNA replication through G-quadruplex motifs is promoted by the *Saccharomyces cerevisiae* Pif1 DNA helicase. *Cell* **145,** 678–691 (2011).
11. Salas, T. R. *et al.* Human replication protein A unfolds telomeric G-quadruplexes. *Nucleic Acids Res.* **34,** 4857–4865 (2006).
12. Sun, H., Karow, J. K., Hickson, I. D. & Maizels, N. The Bloom's syndrome helicase unwinds G4 DNA. *J. Biol. Chem.* **273,** 27587–27592 (1998).
13. Zaug, A. J., Podell, E. R. & Cech, T. R. Human POT1 disrupts telomeric G-quadruplexes allowing telomerase extension *in vitro*. *Proc. Natl Acad. Sci. USA* **102,** 10864–10869 (2005).
14. Fry, M. & Loeb, L. A. Human werner syndrome DNA helicase unwinds tetrahelical structures of the fragile X syndrome repeat sequence d(CGG)n. *J. Biol. Chem.* **274,** 12797–12802 (1999).
15. Sun, H., Bennett, R. J. & Maizels, N. The *Saccharomyces cerevisiae* Sgs1 helicase efficiently unwinds G-G paired DNAs. *Nucleic Acids Res.* **27,** 1978–1984 (1999).
16. Ribeyre, C. *et al.* The yeast Pif1 helicase prevents genomic instability caused by G-quadruplex--forming CEB1 sequences *in vivo*. *PLoS. Genet.* **5,** e1000475 (2009).
17. Paeschke, K. *et al.* Pif1 family helicases suppress genome instability at G-quadruplex motifs. *Nature* **497,** 458–462 (2013).
18. Tarsounas, M. & Tijsterman, M. Genomes and G-quadruplexes: for better or for worse. *J. Mol. Biol.* **425,** 4782–4789 (2013).
19. Croteau, D. L., Popuri, V., Opresko, P. L. & Bohr, V. A. Human RecQ helicases in DNA repair, recombination, and replication. *Annu. Rev. Biochem.* **83,** 519–552 (2014).
20. Edwards, D. N., Orren, D. K. & Machwe, A. Strand exchange of telomeric DNA catalyzed by the Werner syndrome protein (WRN) is specifically stimulated by TRF2. *Nucleic Acids Res.* **42,** 7748–7761 (2014).
21. Li, K. *et al.* Regulation of WRN protein cellular localization and enzymatic activities by SIRT1-mediated deacetylation. *J. Biol. Chem.* **283,** 7590–7598 (2008).
22. Lillard-Wetherell, K. *et al.* Association and regulation of the BLM helicase by the telomere proteins TRF1 and TRF2. *Hum. Mol. Genet.* **13,** 1919–1932 (2004).
23. Machwe, A., Karale, R., Xu, X., Liu, Y. & Orren, D. K. The Werner and Bloom syndrome proteins help resolve replication blockage by converting (regressed) holliday junctions to functional replication forks. *Biochemistry* **50,** 6774–6788 (2011).
24. Machwe, A., Xiao, L. & Orren, D. K. TRF2 recruits the Werner syndrome (WRN) exonuclease for processing of telomeric DNA. *Oncogene* **23,** 149–156 (2004).
25. Chan, K. L., North, P. S. & Hickson, I. D. BLM is required for faithful chromosome segregation and its localization defines a class of ultrafine anaphase bridges. *EMBO J.* **26,** 3397–3409 (2007).
26. Davies, S. L., North, P. S. & Hickson, I. D. Role for BLM in replication-fork restart and suppression of origin firing after replicative stress. *Nat. Struct. Mol. Biol.* **14,** 677–679 (2007).
27. Larsen, N. B. & Hickson, I. D. RecQ helicases: conserved guardians of genomic integrity. *Adv. Exp. Med. Biol.* **767,** 161–184 (2013).
28. Nguyen, G. H. *et al.* Regulation of gene expression by the BLM helicase correlates with the presence of G-quadruplex DNA motifs. *Proc. Natl Acad. Sci. USA* **111,** 9905–9910 (2014).

29. Selak, N. *et al.* The Bloom's syndrome helicase (BLM) interacts physically and functionally with p12, the smallest subunit of human DNA polymerase delta. *Nucleic Acids Res.* **36,** 5166–5179 (2008).
30. Liu, J. Q., Chen, C. Y., Xue, Y., Hao, Y. H. & Tan, Z. G-quadruplex hinders translocation of BLM helicase on DNA: a real-time fluorescence spectroscopic unwinding study and comparison with duplex substrates. *J. Am. Chem. Soc.* **132,** 10521–10527 (2010).
31. Wang, Q. *et al.* G-quadruplex formation at the 3' end of telomere DNA inhibits its extension by telomerase, polymerase and unwinding by helicase. *Nucleic Acids Res.* **39,** 6229–6237 (2011).
32. Rothenberg, E. & Ha, T. Single-molecule FRET analysis of helicase functions. *Methods Mol. Biol.* **587,** 29–43 (2010).
33. Yodh, J. G., Schlierf, M. & Ha, T. Insight into helicase mechanism and function revealed through single-molecule approaches. *Q. Rev. Biophys.* **43,** 185–217 (2010).
34. Ray, S., Bandaria, J. N., Qureshi, M. H., Yildiz, A. & Balci, H. G-quadruplex formation in telomeres enhances POT1/TPP1 protection against RPA binding. *Proc. Natl Acad. Sci. USA* **111,** 2990–2995 (2014).
35. Klaue, D. *et al.* Fork sensing and strand switching control antagonistic activities of RecQ helicases. *Nat. Commun.* **4,** 2024 (2013).
36. Yodh, J. G., Stevens, B. C., Kanagaraj, R., Janscak, P. & Ha, T. BLM helicase measures DNA unwound before switching strands and hRPA promotes unwinding reinitiation. *EMBO J.* **28,** 405–416 (2009).
37. Budhathoki, J. B. *et al.* RecQ-core of BLM unfolds telomeric G-quadruplex in the absence of ATP. *Nucleic Acids Res.* **42,** 11528–11545 (2014).
38. Lee, J. Y., Okumus, B., Kim, D. S. & Ha, T. Extreme conformational diversity in human telomeric DNA. *Proc. Natl Acad. Sci. USA* **102,** 18938–18943 (2005).
39. Wu, L. *et al.* The HRDC domain of BLM is required for the dissolution of double Holliday junctions. *EMBO J.* **24,** 2679–2687 (2005).
40. McKinney, S. A., Joo, C. & Ha, T. Analysis of single-molecule FRET trajectories using hidden Markov modeling. *Biophys. J.* **91,** 1941–1951 (2006).
41. Hwang, H., Buncher, N., Opresko, P. L. & Myong, S. POT1-TPP1 regulates telomeric overhang structural dynamics. *Structure* **20,** 1872–1880 (2012).
42. Janscak, P. *et al.* Characterization and mutational analysis of the RecQ core of the bloom syndrome protein. *J. Mol. Biol.* **330,** 29–42 (2003).
43. Huber, M. D., Duquette, M. L., Shiels, J. C. & Maizels, N. A conserved G4 DNA binding domain in RecQ family helicases. *J. Mol. Biol.* **358,** 1071–1080 (2006).
44. Cahoon, L. A., Manthei, K. A., Rotman, E., Keck, J. L. & Seifert, H. S. Neisseria gonorrhoeae RecQ helicase HRDC domains are essential for efficient binding and unwinding of the pilE guanine quartet structure required for pilin antigenic variation. *J. Bacteriol.* **195,** 2255–2261 (2013).
45. Bochman, M. L., Sabouri, N. & Zakian, V. A. Unwinding the functions of the Pif1 family helicases. *DNA Repair (Amst.)* **9,** 237–249 (2010).
46. Zhou, R., Zhang, J., Bochman, M. L., Zakian, V. A. & Ha, T. Periodic DNA patrolling underlies diverse functions of Pif1 on R-loops and G-rich DNA. *ELife* **3,** e02190 (2014).
47. Williamson, J. R., Raghuraman, M. K. & Cech, T. R. Monovalent cation-induced structure of telomeric DNA: the G-quartet model. *Cell* **59,** 871–880 (1989).
48. Bachrati, C. Z., Borts, R. H. & Hickson, I. D. Mobile D-loops are a preferred substrate for the Bloom's syndrome helicase. *Nucleic Acids Res.* **34,** 2269–2279 (2006).
49. Doherty, K. M. *et al.* RECQ1 helicase interacts with human mismatch repair factors that regulate genetic recombination. *J. Biol. Chem.* **280,** 28085–28094 (2005).
50. Cheok, C. F., Wu, L., Garcia, P. L., Janscak, P. & Hickson, I. D. The Bloom's syndrome helicase promotes the annealing of complementary single-stranded DNA. *Nucleic Acids Res.* **33,** 3932–3941 (2005).
51. Wu, X. & Maizels, N. Substrate-specific inhibition of RecQ helicase. *Nucleic Acids Res.* **29,** 1765–1771 (2001).
52. Kim, S. Y., Hakoshima, T. & Kitano, K. Structure of the RecQ C-terminal domain of human bloom syndrome protein. *Sci. Rep.* **3,** 3294 (2013).
53. Kim, Y. M. & Choi, B. S. Structure and function of the regulatory HRDC domain from human Bloom syndrome protein. *Nucleic Acids Res.* **38,** 7764–7777 (2010).
54. Huppert, J. L. & Balasubramanian, S. Prevalence of quadruplexes in the human genome. *Nucleic Acids Res.* **33,** 2908–2916 (2005).
55. Rodriguez, R. *et al.* Small-molecule-induced DNA damage identifies alternative DNA structures in human genes. *Nat. Chem. Biol.* **8,** 301–310 (2012).
56. Bochman, M. L., Paeschke, K. & Zakian, V. A. DNA secondary structures: stability and function of G-quadruplex structures. *Nat. Rev. Genet.* **13,** 770–780 (2012).
57. Wu, Y. & Brosh, Jr R. M. G-quadruplex nucleic acids and human disease. *FEBS J.* **277,** 3470–3488 (2010).
58. Machwe, A., Xiao, L., Lloyd, R. G., Bolt, E. & Orren, D. K. Replication fork regression *in vitro* by the Werner syndrome protein (WRN): holliday junction formation, the effect of leading arm structure and a potential role for WRN exonuclease activity. *Nucleic Acids Res.* **35,** 5729–5747 (2007).
59. Johnson, J. E., Cao, K., Ryvkin, P., Wang, L. S. & Johnson, F. B. Altered gene expression in the Werner and Bloom syndromes is associated with sequences having G-quadruplex forming potential. *Nucleic Acids Res.* **38,** 1114–1122 (2010).
60. Suhasini, A. N. *et al.* Interaction between the helicases genetically linked to Fanconi anemia group J and Bloom's syndrome. *EMBO J.* **30,** 692–705 (2011).
61. Bharti, S. K. *et al.* Specialization among iron-sulfur cluster helicases to resolve G-quadruplex DNA structures that threaten genomic stability. *J. Biol. Chem.* **288,** 28217–28229 (2013).
62. Sarkies, P. *et al.* FANCJ coordinates two pathways that maintain epigenetic stability at G-quadruplex DNA. *Nucleic Acids Res.* **40,** 1485–1498 (2012).
63. Nguyen, G. H. *et al.* A small molecule inhibitor of the BLM helicase modulates chromosome stability in human cells. *Chem. Biol.* **20,** 55–62 (2013).
64. Savitsky, P. *et al.* High-throughput production of human proteins for crystallization: the SGC experience. *J. Struct. Biol.* **172,** 3–13 (2010).
65. Gileadi, O. *et al.* High throughput production of recombinant human proteins for crystallography. *Methods Mol. Biol.* **426,** 221–246 (2008).
66. Shrestha, B., Smee, C. & Gileadi, O. Baculovirus expression vector system: an emerging host for high-throughput eukaryotic protein expression. *Methods Mol. Biol.* **439,** 269–289 (2008).
67. Garcia, P. L., Liu, Y., Jiricny, J., West, S. C. & Janscak, P. Human RECQ5beta, a protein with DNA helicase and strand-annealing activities in a single polypeptide. *EMBO J.* **23,** 2882–2891 (2004).
68. Karow, J. K., Chakraverty, R. K. & Hickson, I. D. The Bloom's syndrome gene product is a 3'-5' DNA helicase. *J. Biol. Chem.* **272,** 30611–30614 (1997).

Acknowledgements

We thank Nick Cowan and Jim Borowiec for commenting on the manuscript. Research in E.R. laboratory is supported by the NIH (GM057691/Delmar and GM110385/Rothenberg) the Arnold and Mabel Beckman Foundation and the Shifrin-Meyer Breast Cancer Discovery award. D.H. and I.D.H. were supported by The Nordea Foundation and the Danish Medical Research Council (FSS). P.J. and A.S. were supported by the Swiss National Science Foundation (31003A_146206). O.G. and P.S. were supported by the SGC, a registered charity (number 1097737) that receives funds from AbbVie, Bayer Pharma AG, Boehringer Ingelheim, the Canada Foundation for Innovation, Genome Canada, GlaxoSmithKline, Janssen, Lilly Canada, the Novartis Research Foundation, the Ontario Ministry of Economic Development and Innovation, Pfizer, Takeda and the Wellcome Trust (092809/Z/10/Z).

Author contributions

S.C., E.R. and J.Z. designed the study. P.S., D.H., A.S., P.J., I.D.H. and O.G. generated reagents. S.C., J.Z. and E.R. performed the experiments. S.C. and J.Z. analyzed the data. E.R. and S.C. wrote the manuscript, which was reviewed and approved by all co-authors.

Additional information

Supplementary Information accompanies this paper at http://www.nature.com/naturecommunications

Competing financial interests: The authors declare no competing financial interests.

Reprints and permission information is available online at http://npg.nature.com/reprintsandpermissions/

How to cite this article: Chatterjee, S. *et al.* Mechanistic insight into the interaction of BLM helicase with intra-strand G-quadruplex structures. *Nat. Commun.* 5:5556 doi: 10.1038/ncomms6556 (2014).

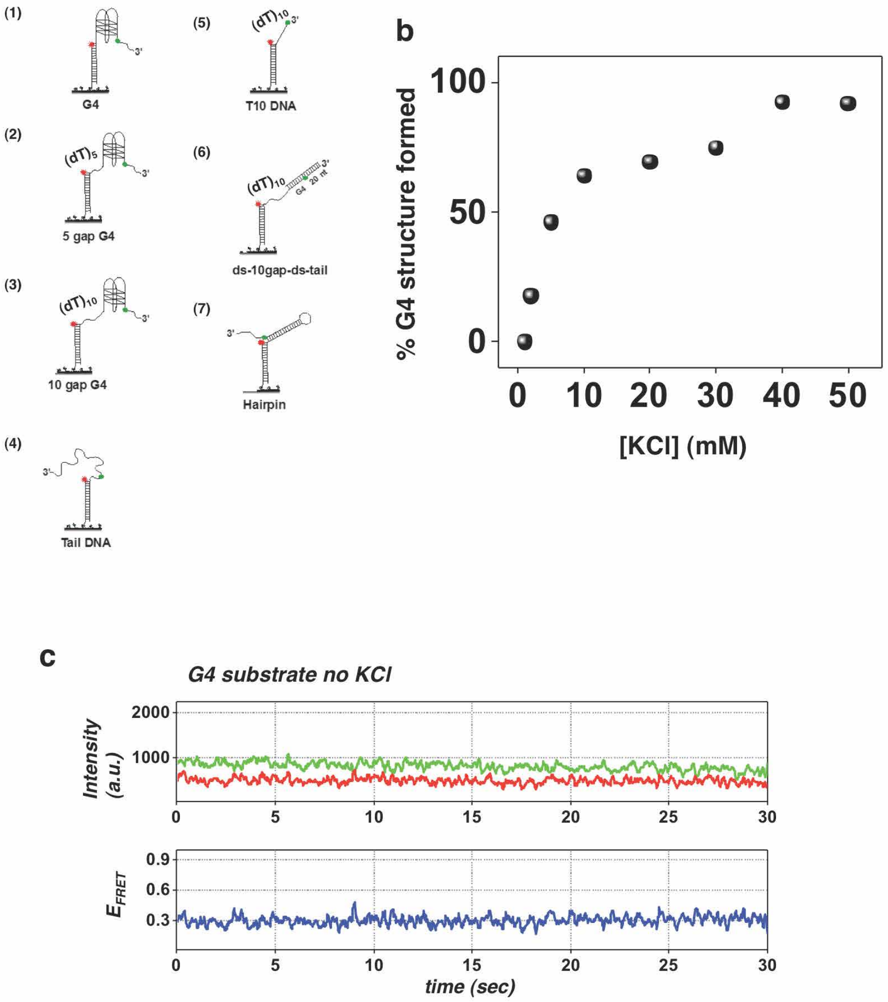

Supplementary Figure 1. Formation of G4 with titration of K, and behavior of G4 (5 nt) substrate in the presence of BLM.

(**a**) Illustrations of DNA substrates used in this study: (1) Regular G4 substrate. (2) G4 (5 nt) substrate. (3) G4 (10 nt) substrate. (4) Regular 30 nt tailed substrate. (5) Short 10 nt tailed substrate. (6) Gapped substrate with 10 nt gap. (7) Hairpin substrate. (**b**) Quantification of G4 folded population as a function of KCl. G4 folded population was calculated from the FRET histograms as the percent population at high FRET (>0.6). (**c**) Representative smFRET trajectory of the G4 substrate in the absence of salt in the buffer showing predominantly low FRET indicating that the G4 structure is unfolded

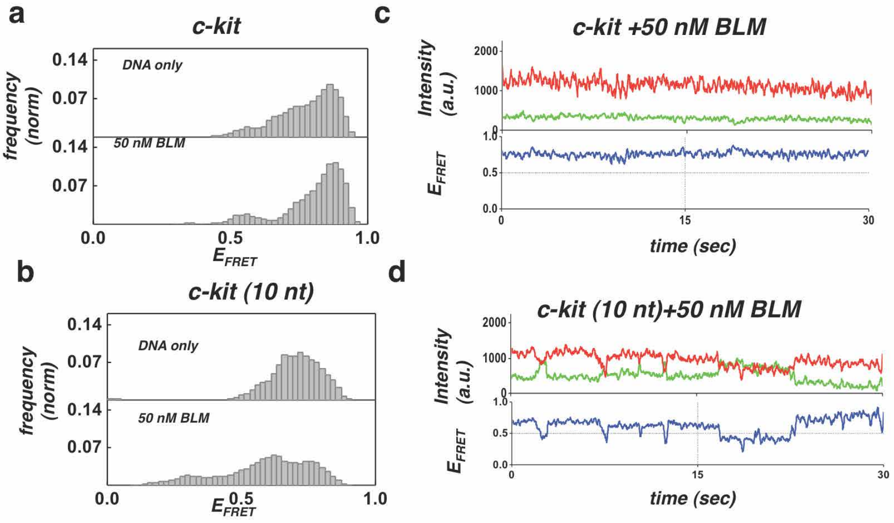

Supplementary Figure 2. Substrate specific interaction of BLM with G4-forming human c-kit2 sequence.

(**a**) FRET histograms for the c-kit2 G4 substrate, with G4 motif immediately adjacent to duplex region. No change in FRET distribution was observed following addition of 50 nM of BLM (bottom panel).

(**b**) FRET histograms for the c-kit2 G4 (10nt) substrate with a 10 nt ssDNA between the G4 motif and duplex region. A substantial change in the FRET distribution was detected upon addition of 50 nM BLM (bottom panel).

Histograms in (**a**) and (**b**) were generated after subtracting the zero FRET values and truncating the photo bleached part from FRET trajectory. A minimum of 100 smFRET trajectories was used to generate the histograms. The concentration of K^+ was kept at 50 mM

(**c**) A representative single molecule trajectory of the c-kit2 G4 substrate in the presence of 50 nM BLM showing persistent high FRET. Top panel: donor (green) - acceptor (red) intensities, bottom panel: corresponding FRET trajectory.

(**d**) Representative smFRET trajectory of the c-kit2 G4 (10nt) substrate in the presence of 50 nM BLM showing dynamic fluctuations in FRET signal (blue).

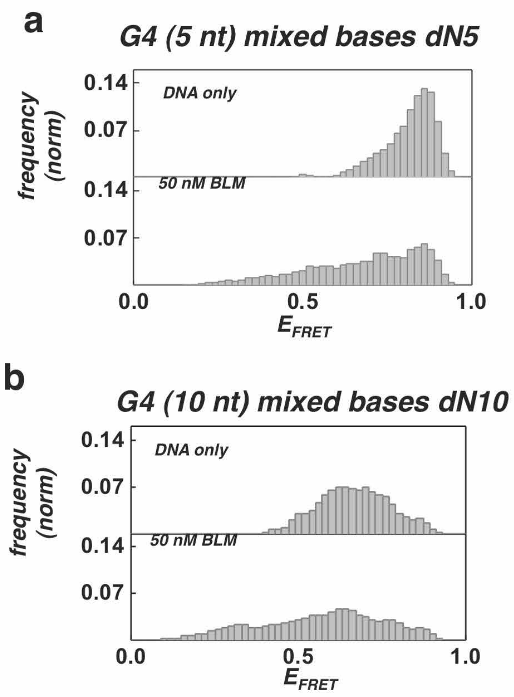

Supplementary Figure 3. Substrate specific interaction of BLM with G4-forming human telomere sequence for mixed ssDNA spacer.

(**a**) FRET histograms for the G4 (5nt) substrate with a mixed sequence of 5 nt ssDNA between the G4 motif and duplex region. A change in the FRET distribution was detected upon addition of 50 nM BLM (bottom panel).
(**b**) FRET histograms for the G4 (10nt) substrate with a mixed sequence of 10 nt ssDNA between the G4 motif and duplex region. A substantial change in the FRET distribution was detected upon addition of 50 nM BLM (bottom panel).
Histograms were generated after subtracting the zero FRET values and truncating the photo bleached part from FRET trajectory. A minimum of 100 smFRET trajectories was used to generate the histograms. The concentration of K^+ was kept at 50 mM

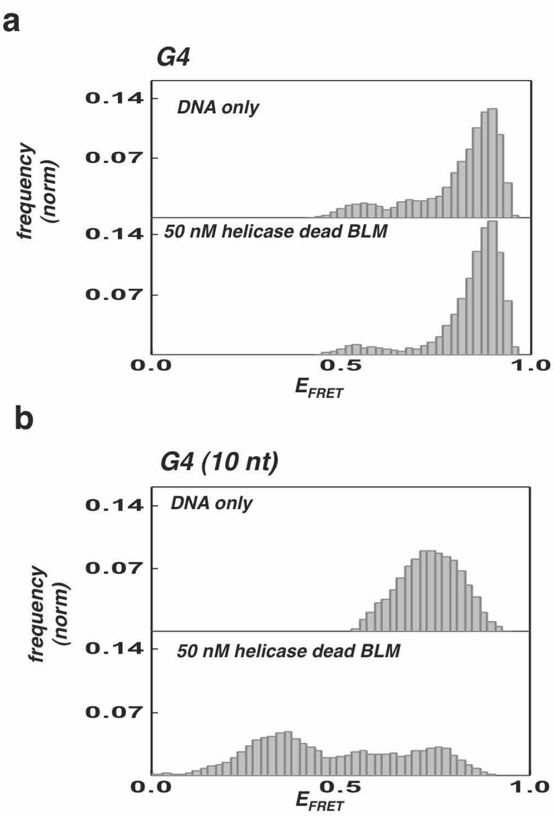

Supplementary Figure 4. Substrate specific interaction of helicase dead BLM with G4-forming human telomere sequence.

(**a**) FRET histograms for the G4 substrate, with G4 motif immediately adjacent to duplex region. No change in FRET distribution was observed following addition of 50 nM of BLM (bottom panel).
(**b**) FRET histograms for the G4 (10nt) substrate with a 10 nt ssDNA between the G4 motif and duplex region. A substantial change in the FRET distribution was detected upon addition of 50 nM BLM (bottom panel).
Histograms were generated after subtracting the zero FRET values and truncating the photobleached part from FRET trajectory. A minimum of 100 smFRET trajectories was used to generate the histograms. The concentration of K^+ was kept at 50 mM

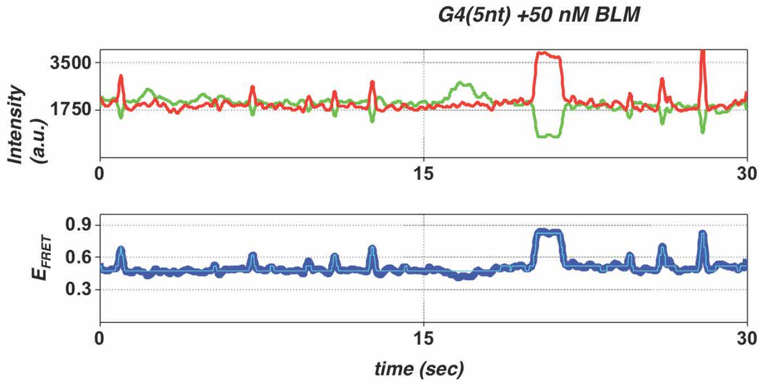

Supplementary Figure 5. smFRET trajectory of G4(5nt) substrate in the presence of BLM.

Representative smFRET trajectory of the G4 (5nt) substrate in the presence of 50 nM BLM showing dynamic fluctuations in FRET. The FRET signal in the bottom curve is in blue whereas the HMM fit is in Cyan.

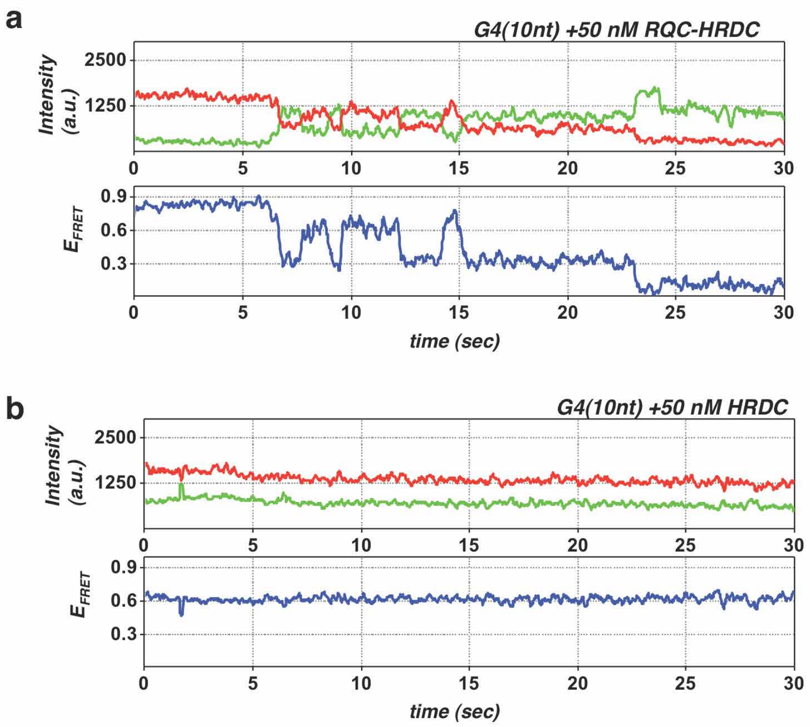

Supplementary Figure 6. smFRET trajectories of G4(10nt) substrate in the presence of RQC-HRDC and HRDC truncation mutants.

Representative smFRET trajectory of the G4 (10nt) substrate in the presence of (**a**) 50 nM RQC-HRDC showing dynamic fluctuations in FRET. (**b**) 50 nM HRDC showing persistent FRET signal.

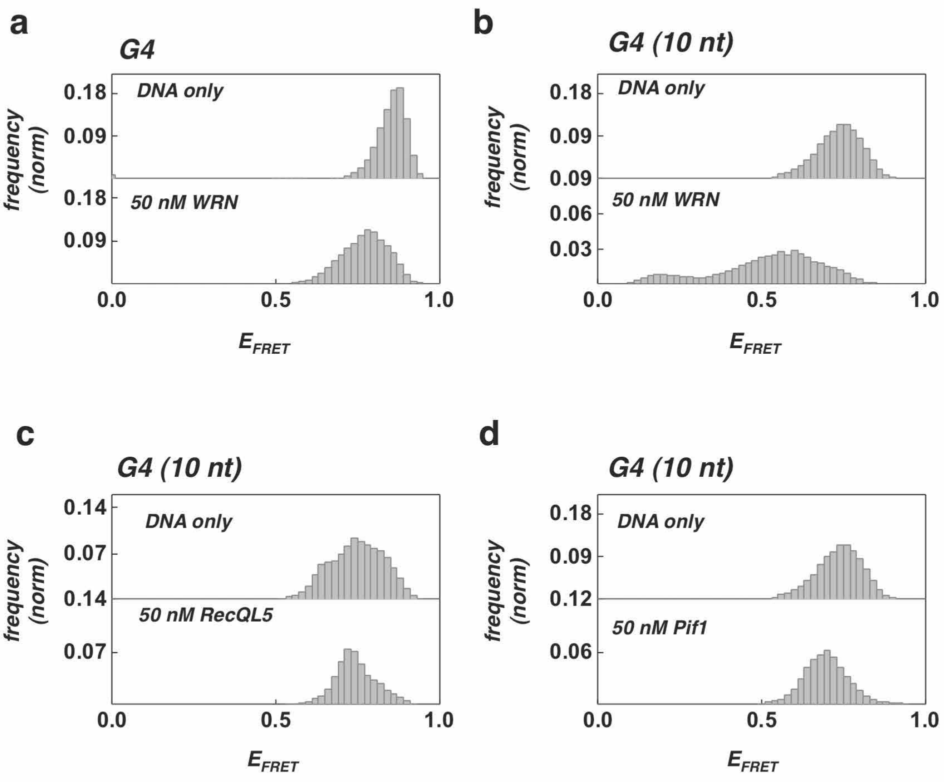

Supplementary Figure 7. Substrate specific interaction of WRN, RecQL5 and Pif1 helicases with G4-forming human telomere sequence.

(**a**) FRET histograms for the G4 substrate, with G4 motif immediately adjacent to duplex region. No change in FRET distribution was observed following addition of 50 nM of WRN (bottom panel).
(**b**) FRET histograms for the G4 (10nt) substrate with a 10 nt ssDNA between the G4 motif and duplex region. A substantial change in the FRET distribution was detected upon addition of 50 nM WRN.
(**c**) FRET histograms for the G4 (10 nt) substrate, with a 10 nt ssDNA between the G4 motif and duplex region. No change in FRET distribution was observed following addition of 50 nM of RecQL5.
(**d**) FRET histograms for the G4 (10 nt) substrate, with a 10 nt ssDNA between the G4 motif and duplex region. No change in FRET distribution was observed following addition of 50 nM of Pif1.
Histograms were generated after subtracting the zero FRET values and truncating the photobleached part from FRET trajectory. A minimum of 100 smFRET trajectories was used to generate the histograms. The concentration of K^+ was kept at 50 mM.

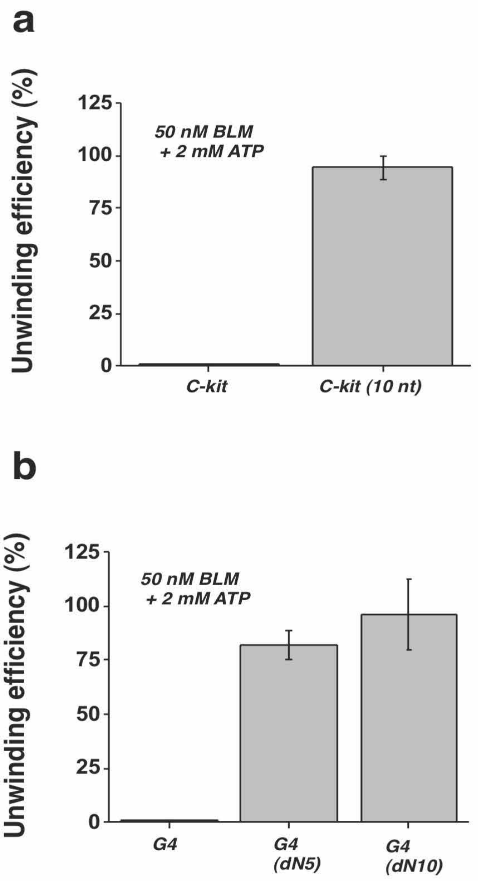

Supplementary Figure 8. Unwinding yields of BLM for c-kit substrates and G4 substrates having mixed sequence spacer.

(**a**) Quantification of BLM unwinding efficiency at 50 nM BLM and 2 mM ATP for the c-kit2 G4 substrate and c-kit2 G4 (10 nt) substrate, showing efficient unwinding in the latter.

(**b**) Quantification of BLM unwinding efficiency at 50 nM BLM and 2 mM ATP for the G4 substrate, G4 (5nt) substrate with a mixed sequence ssDNA spacer, and G4 (5 nt) substrate with a mixed sequence ssDNA spacer. Unwinding was observed only for the substrates containing the ssDNA spacers. (Error bar = S.E.M. n=5)

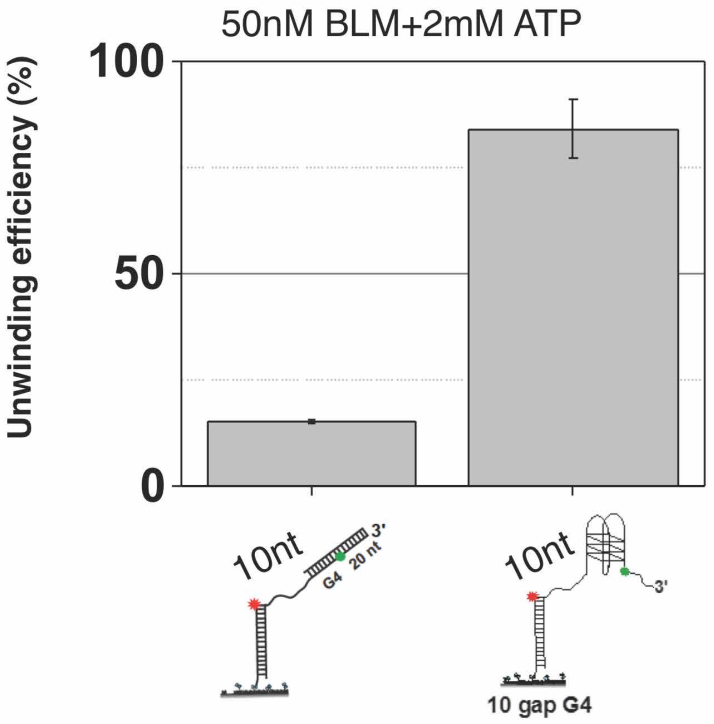

Supplementary Figure 9. Comparison of BLM's unwinding yields in the G4 (10nt) substrate and in 10 nt gapped substrate.

Quantification of BLM unwinding efficiency at 50 nM BLM and 2 mM ATP for the G4 (10 nt) substrate and a 10 nt gapped duplex substrate. (Error bar = S.E.M. n=4)

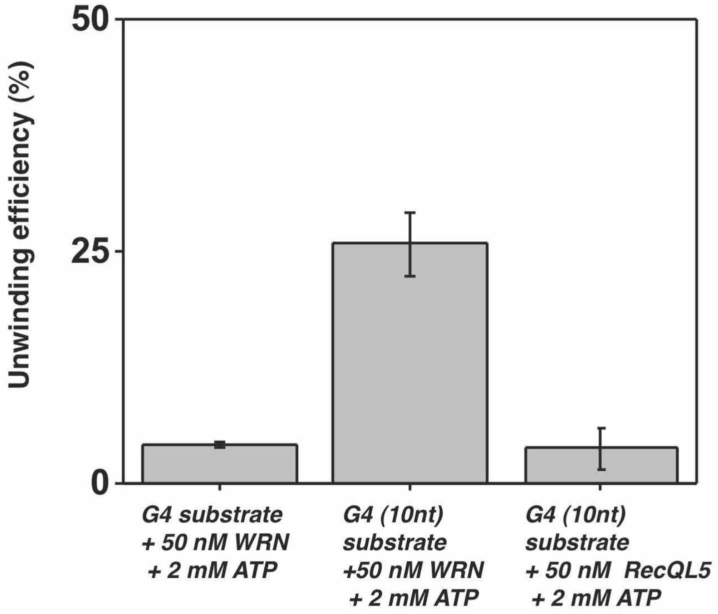

Supplementary Figure 10 | Unwinding yields of WRN and RecQL5 in a gapped substrate.

Quantification of WRN unwinding efficiency at 50 nM WRN and 2 mM ATP for the G4 and G4(10 nt) substrate are shown in the first and second columns, respectively. Unwinding by WRN was observed for the G4 (10 nt) substrate, but not for the G4 substrate. We note the WRN generally exhibit poor unwinding activity as compared with BLM even 3' tailed substrates. The last column shows that no unwinding was observed for RecQL5 (50 nM RecQL5 and 2 mM ATP) in the G4 (10 nt) substrate. (Error bar = S.E.M. n=4)

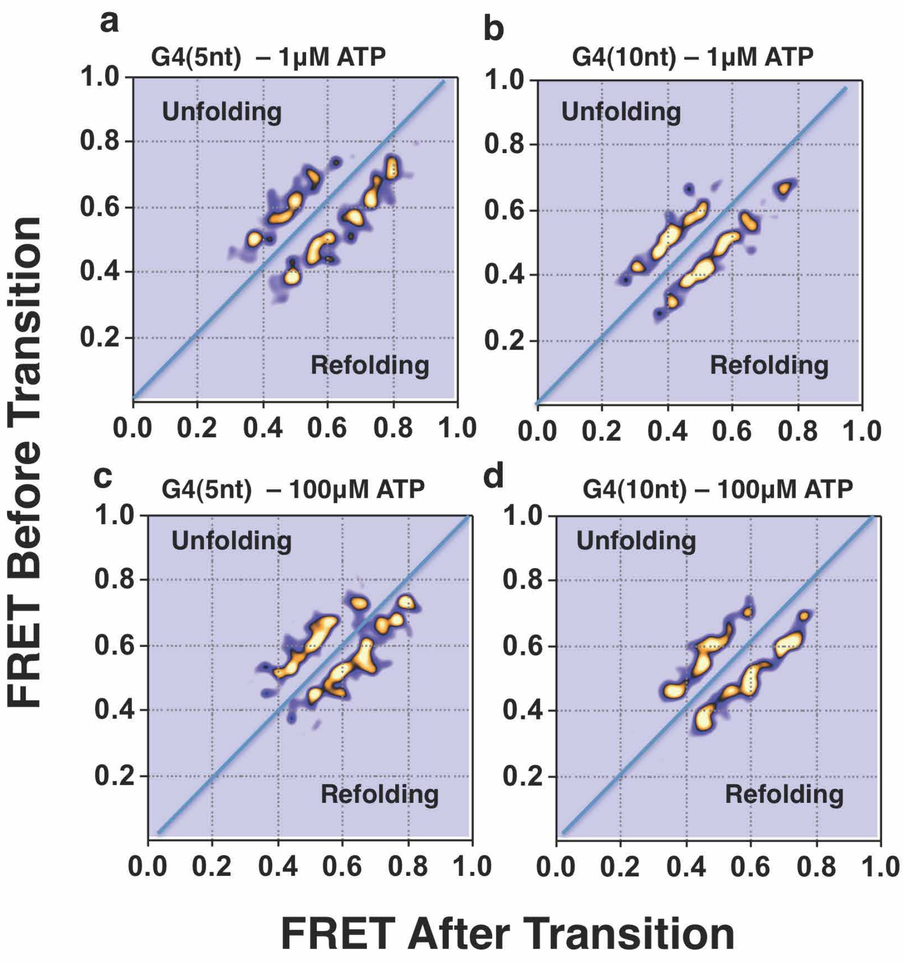

Supplementary Figure 11 | TDP for two substrates at different ATP concentrations.

(**a-d**) Generated TDP matrix for each G4 (5 nt) and G4 (10 nt) substrates in the presence of 50 nM BLM and 1 μM or 100 μM ATP. The color intensity corresponds to transition probability. The y-axis is the initial FRET prior to transition, and the x-axis is the final FRET after transition. (**a**) G4 (5nt) substrate and 1 μM ATP. (**b**) G4 (10nt) substrate and 1 μM ATP. (**c**) G4 (5nt) substrate and 100 μM ATP. (**d**) G4 (10nt) substrate and 100 μM ATP. Peaks corresponding to unfolding (above diagonal) and refolding (below diagonal) transitions of the G4 motif.

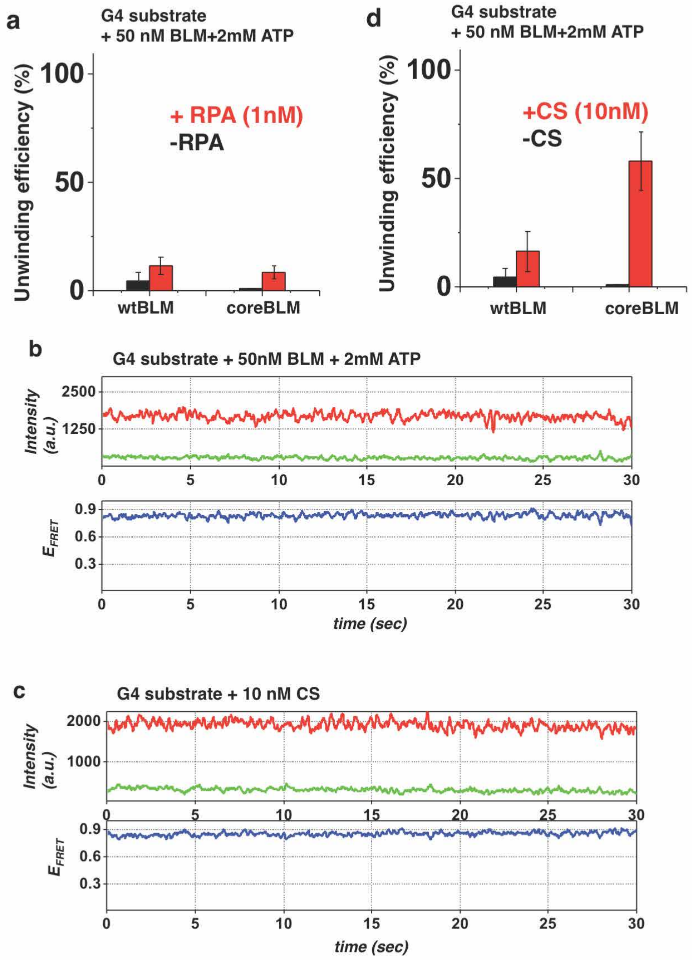

Supplementary Figure 12 | Effect of RPA and CS in the presence of coreBLM and wtBLM.

(**a**) Quantification of core BLM and wtBLM unwinding efficiency of the G4 substrate at 50 nM BLM and 2 mM ATP, either alone or with 1nM RPA. (Error bar = S.E.M. n=4)

(**b/c**) Representative smFRET trajectories of the G4 substrate in the presence of (**c**) 50 nM BLM + 2mM ATP showing persistent high FRET. (**d**) 10 nM CS showing persistent high FRET.

(**d**) Quantification of core BLM and wtBLM unwinding efficiency of the G4 substrate at 50 nM BLM and 2 mM ATP, either alone or with 10 nM CS. (Error bar = S.E.M. n=5)

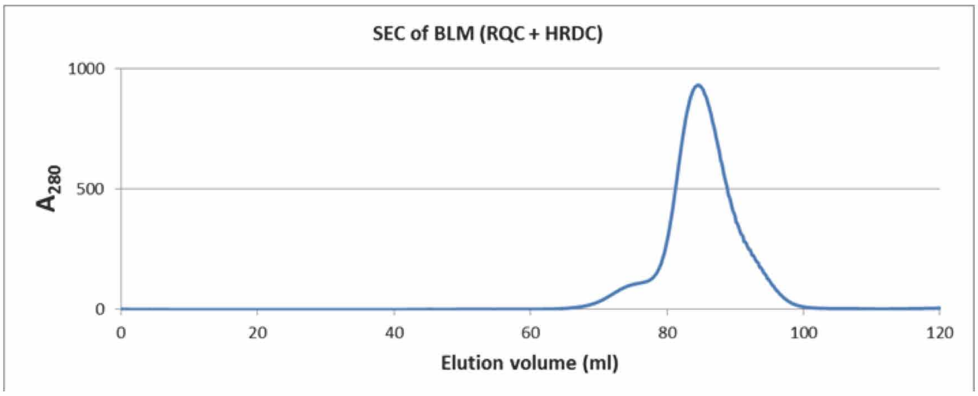

Supplementary Figure 13 | Gel filtration absorptions profile of the RQC-HRDC fragment.

The RQC-HRDC fragment migrates as a single peak in the gel filtration absorption profile.

Supplementary Table 1: DNA oligos used in this study.

No.	Name	Sequence
1	Biotin – duplex top	5'-/Cy5/GCC TCG CTG CCG TCG CCA/3BioTEG/-3'
2	Telomeric G4 substrate strand	5'-TGG CGA CGG CAG CGA GGC G GGT TAG GGT TAG GGT TAG GG/iCy3/TTT TTT TTT TTT TTT TTT TT-3'
3	Telomeric G4(5nt) substrate strand	5'-TGG CGA CGG CAG CGA GGC TTT TTG GGT TAG GGT TAG GGT TAG GG/iCy3/T TTT TTT TTT TTT TTT TTT T-3'
4	Telomeric G4(10nt) substrate strand	5'-TGG CGA CGG CAG CGA GGC TTT TTT TTT TG GGT TAG GGT TAG GGT TAG GG/iCy3/T TTT TTT TTT TTT TTT TTT T-3'
5	Telomeric G4 complementary strand (CS)	5'-CCC TAA CCC TAA CCC TAA CCC-3'
6	T10 tailed unwinding substrate strand	5'-TGG CGA CGG CAG CGA GGC TTTTTTTTTT /3Cy3Sp/3'
7	Complement strand of Telomeric G4 and T20 tail	5'-AAA AAA AAA AAA AAA AAA AAC CCT AAC CCT AAC CCT AAC CC-3'
8	T30 tailed unwinding substrate strand	5'-TGG CGA CGG CAG CGA GGC TTT TTT T/iCy3/TTT TTT TTT TTT TTT TTT TTT TT-3'
9	Non complementary strand	5’-AGG CGA CGG CAG CGA GGC-3’
10	Hairpin unwinding substrate strand	5’- TGG CGA CGG CAG CGA GGC GCG AGC GGC ATC TTT GAT GCC GCT CGC TTT /iCy3/TTT TTT TTT TTT TTT TT -3’
11	Telomeric G4 substrate strand, 7 nt tail	5'-TGG CGA CGG CAG CGA GGC G GGT TAG GGT TAG GGT TAG GG/iCy3/TTT TTT T-3'
12	c-kit2 G4 substrate	5’- TGG CGA CGG CAG CGA GGC CGG GCG GGC GCG AGG GAG GGG /iCy3/TTT TTT TTT TTT TTT TTT TT -3’
13	c-kit2 G4 substrate (10nt) spacer	5’- TGG CGA CGG CAG CGA GGC TTT TTT TTT TCG GGC GGG CGC GAG GGA GGG G/iCy3/TT TTT TTT TTT TTT TTT TTT -3’
14	Telomeric G4(5nt) mixed base spacer	5’- TGG CGA CGG CAG CGA GGC ACG GCG GGT TAG GGT TAG GGT TAG GG/iCy3/T TTT TTT TTT TTT TTT TTT T -3’
15	Telomeric G4(10nt) mixed base spacer	5’- TGG CGA CGG CAG CGA GGC ACG ATC TGG CGG GTT AGG GTT AGG GTT AGG G/iCy3/TT TTT TTT TTT TTT TTT TTT -3’

5. Discussion

In this thesis work, it is demonstrated that WRN and BLM can promote extensive DNA-end resection in conjunction with DNA2 *in vitro* and *in vivo*. We show that WRN directly interacts with DNA2 and that the resection of broken DNA ends by these proteins is dependent on the presence of RPA and ATP and occurs with a 5’ to 3’ polarity. In addition, we show that DNA-end resection by WRN/DNA2 or BLM/DNA2 can take place effectively only if the DNA substrate contains a short 3’ ssDNA tail. This observation is in line with the model where a first resection initiation step is performed by MRN/CtIP, generating the substrate for further long-range resection by WRN/BLM in conjunction with DNA2 [134, 155, 213-215].

The involvement of WRN in DNA-end resection is consistent with its fast localisation to DNA DSB sites [216]. In addition, WRN directly interacts with the MRN complex, which is one of the first proteins present at the break site and plays a crucial role in resection initiation [217]. This might imply that MRN recruits WRN to sites of DNA DSBs to start extensive resection.

Our finding that the exonuclease domain of WRN is dispensable for its function in DNA-end resection in conjunction with DNA2 is consistent with the observation that MRN stimulates WRN’s helicase but not exonuclease activity [217]. The exonuclease function of WRN seems to be rather involved in other processes like the protection of reversed forks upon replication stress or the DNA-end processing during NHEJ [218, 219]. Taken together these data demonstrate that WRN is a crucial factor in the repair of DNA DSBs and that the two functional domains of this protein mediate distinct functions in this complex process.

Further prove that WRN is a key player in preserving genome stability is provided by phenotypes of patients suffering from WS. This disorder caused by inherited mutations in the WRN gene is characterized by premature aging and cancer predisposition [220]. On the cellular level, lack of WRN is manifested in extensive chromosomal deletions and translocations [221-223]. However it should be noted that these symptoms are likely caused not only by a DNA-end resection defect but also by failure of several other processes where WRN is involved. For instance, it has been shown that WRN participates in telomere maintenance where it interacts with telomeric proteins like TRF2 and promotes strand exchange [224, 225]. Further, it seems that WRN is also engaged in DNA replication since it has been shown that WS cells have a reduced DNA synthesis rate and increased frequency of replication fork stalling [220]. These observations define WRN as a multifaceted protein that acts in various processes contributing to cell homeostasis.

In this study we found that like yeast Dna2, also the human ortholog relies on free ssDNA ends to mediate an endo/exonucleolytic flap cleavage [152, 226]. In line with this observation recent work in *Xenopus* egg extracts revealed that DNA DSB break ends with 5' adducts, which arise for instance upon treatment of cells with etoposide, are repaired by xDNA2-mediated resection mechanism but only after removal of the end-blocking obstacle [227]. In addition, our finding that the presence of RPA guides DNA2 towards degradation of the 5' terminated strand is consistent with the results that have been previously published for yeast, *Xenopus* and mouse Dna2 [135, 158-160]. These findings suggest that the nuclease activity of Dna2 is highly conserved trough evolution.

A previous study has provided evidence that BLM can mediate DNA-end processing in conjunction with DNA2 [168]. In our work, we found that although the helicase activities of WRN and BLM were similar, WRN promoted DNA resection by DNA2 more efficiently than BLM. However, the BLM/DNA2-mediated resection reaction could be stimulated by addition of the TRR complex. This is consistent with the fact that during dHJ resolution, BLM acts as a part of the BTRR complex where TOPOIIIα and RMI1 stimulate its unwinding activity that is the driving factor of the DNA-resection reaction [228]. In contrast to the *in vitro* experiments where TRR stimulated the DNA end processing activity of BLM/DNA2 only to a limited extent, depletion of RMI1 from U2OS cells lead to a marked reduction in SSA repair efficiency. These data indicate that *in vivo*, RMI1 is crucial for the DNA-end resection reaction promoted by BLM/DNA2. Consistent with this observation, it has been shown that RMI1 and RMI2 are important for the association of BLM with DNA damage sites and its stability [229, 230]. More recently, another group also demonstrated the involvement of the BTRR complex in DNA-end resection in human cells [231].

Surprisingly, depletion of BLM in HEK293 cells increased the efficiency of SSA-repair events that are dependent on extensive resection, whereas in U2OS cells a marked reduction was noticed. In addition, we found that the concentration of BLM protein in HEK293 cells was much higher than in U2OS cells (data not shown). Therefore, in HEK293 cells where BLM exceeds a certain threshold, it might counteract the repair of DNA DSB via the SSA pathway possibly by unwinding the annealed complementary repeats. A similar repair mechanism that also relies on the annealing of homologous sequences is MMEJ. BLM has been shown to be involved in regulation of this pathway to prevent its deleterious repair outcome, which supports our result [232].

Recently is has been shown that WRN/DNA2-mediated end resection is involved not only in processing DNA ends after DNA DSBs, but also in resection of reversed replication forks to allow a proper replication restart. Interestingly, BLM seems to play only a minor role in this mechanism demonstrating that the different resection machineries may also have distinct functions in human cells [233].

In addition to the investigation on how RPA-coated ssDNA is generated at sites of DNA DSBs, we also asked how this nucleoprotein structure activates simultaneously the ATR signalling cascade. We identified the mismatch-binding protein MutSβ, a heterodimer of MSH2 and MSH3, as a mediator of ATR activation. We have found that MSH2 and MSH3 associate with the ATR-ATRIP complex and are required for ATRIP foci formation and the phosphorylation of ATR targets in U2OS cells treated with CPT, which induces DNA DSBs during DNA replication. Further, we have obtained evidence for the persistence of hairpin loops in RPA-coated ssDNA *in vitro*, which are recognised by MutSβ. To demonstrate that MutSβ specifically associates with persisting hairpin loop structures in ssDNA, we mutated the amino acids in MSH3 that are responsible for mismatch binding. We found that the interaction of MutSβ mutant with hairpin loops was completely abrogated *in vitro.* Further, we demonstrated that this MutSβ mutant failed to stimulate ATR activation in nuclear extracts supplemented with ssDNA and in human cells treated with CPT. These results demonstrate that binding of MutSβ to hairpin loop structures persisting in ssDNA is essential to mediate ATR activation. Finally, we found that MutSβ dissociates from ssDNA hairpin loops upon addition of ATP and Mg^{2+}.

It has been shown previously that embryonic fibroblasts from MSH2 knockout mice displayed a reduced survival rate upon DNA damage induction by X-rays that induce DNA DSBs [196]. In addition, in these cells the checkpoint kinase CHK1 was only active for limited time and CHK2 was not phosphorylated leading to improper G2/M checkpoint function [196]. Although it has been demonstrated that also MutSα in conjunction with MutLα can activate ATR, this mechanism occurs in a resection independent manner [234, 235]. Consistent with these results, we also observed an impaired phosphorylation of ATR targets upon MSH2 and MSH3 but not MSH6 depletion in cells treated with CPT. Taken together, these results demonstrate that only MutSβ, but not MutSα, can assist in ATR activation after DNA DSB formation.

In our proposed model, MutSβ binds to hairpin loops bringing the ATR-ATRIP complex in close proximity to the RPA-coated ssDNA formed after DNA end processing. This would allow subsequent ATR activation by TOPBP1 that gets loaded on the ssDNA/dsDNA junction by the 9-1-1 complex [183, 186]. Interestingly, work done in yeast showed that the 9-1-1 checkpoint clamp is able to promote DNA-end resection by Dna2 and Exo1 [236]. If this also holds true for mammalian cells, it suggests that DNA end processing is possibly enhanced under certain circumstances to generate the substrate for MutSβ binding and thus increased ATR activation.

It has been published previously that ATR is important to prevent uncontrolled replication origin firing and protects replication forks following replication stress [237]. This mechanism is important to overcome the generation of loads of ssDNA that would exhaust the cellular RPA pool [237]. It is therefore possible that persisting hairpin loops in RPA-coated ssDNA reflect a low amount of free RPA and thus lead to MutSβ association and subsequent enhanced ATR activation. However in our DNase I footpriting assays, we found that even in the presence of an 2-fold excess of RPA over RPA binding sites in the ssDNA substrate, hairpin structures were still present. This suggests that hairpin loops are potentially also formed within RPA-coated ssDNA under normal conditions to form MutSβ binding sites.

In our experiments, we found that MutSβ disassociates from hairpin loops upon addition of ATP. This is probably required to remove the protein from the DNA so that homology-directed repair can proceed. A multi step process, including ATP binding by MSH3, ADP-ATP exchange in MSH2 and also ATP hydrolysis in MSH3, has been shown to be important for association of MutSβ with the hairpin loop substrate and potentially also for its signalling and disassociation within MMR [92, 238]. However in our study, the addition of ATP as well as its non-hydrolysable form ATPγS caused the release of MutSβ from the hairpin loop. This indicates that there might be a distinct mechanism responsible for the release of MutSβ from hairpin loops in ssDNA.

Repair of DNA DSBs *via* the HR pathway can proceed trough dHJ formation and may end up with chromosomal rearrangements due to crossover formation. However in mitotic cells, SDSA, which always results in non-crossover products, is the preferred HR mechanism to repair DNA DSBs [145]. This suggests that HR subpathway-regulating processes are active in proliferating cells that guide DNA DSB repair towards SDSA. In this thesis work, we demonstrate that lack of RECQ5 reduces the SDSA repair events in human cells. In addition, we provide mechanistic insight into how RECQ5 regulates HR by demonstrating that RECQ5 counteracts the inhibitory effect of RAD51 on RAD52-mediated ssDNA annealing *in vitro* and *in vivo*. Moreover, we provide evidence that in RECQ5-deficient cells, the loading of RAD51 at sites adjacent to DNA DSBs is increased as compared to normal cells. Finally, we show RECQ5 and BLM act is a complementary fashion to suppress sister chromatid exchange in cells. Together, our data suggest that RECQ5 promotes the use of the SDSA pathway by inhibiting the formation of RAD51-ssDNA filaments after D-loop unwinding and is therefore a crucial factor involved in HR regulation in human cells.

Our data are supported by the fact that cells from RECQ5$^{-/-}$ mice display a high level of SCEs [212]. In addition, mice lacking RECQ5 are prone to develop cancer [209]. These malignancies probably arise because of the mutagenic potential of crossover events that are not suppressed anymore by RECQ5. Consistent with this, it has been shown that in human colorectal cancer cells, the RECQ5 mRNA level is markedly reduced compared to normal cells, thereby contributing to genomic instability [239].

More recently, it has been shown that RECQ5 is involved in DNA interstrand crosslink (ICL) repair since DT40 chicken cells where RECQ5 was knocked out displayed an increased sensitivity to ICL inducing agents [240]. In addition, RAD51 foci formed after treating RECQ5$^{-/-}$ cells with MMC, which induces interstrand crosslinks, disappeared slower than in wild type cells demonstrating that RECQ5 plays a role in RAD51 filament dynamics [240].

In collaboration with Prof. Eli Rothenberg’s lab, we proposed a model for how the different BLM domains interact with the G4-quadruplex and lead to its unwinding to preserve the telomere structure. Such G4-elements can also be found adjacent to transcription start sites where they interfere with transcription [241]. A recent study has indeed demonstrated that in Bloom syndrome cells, mRNA expression levels of several genes are affected by the presence of G4-quadruplexes, indicating that BLM also plays a role in gene expression regulation by unwinding of G4-structures [242]. Interestingly, it has been shown recently that DNA2 is able to cleave DNA with G4-quadruplexes. In addition, WRN is also able to unwind G4-quadruplexes [243]. Potentially, interplay between WRN and DNA2 or BLM and DNA2 could also be observed at sites where G4-structures form, which can be telomeres but also promoter regions [244].

5.1. Future perspectives

To fight cancer and to identify new cancer therapy targets, it is absolutely necessary to understand the underlying processes and the key players that lead to cancer development. In this work, we provided mechanistic insight into DNA-end resection in mammalian cells and defined WRN as a new crucial factor participating in this process. DNA end processing mediated by EXO1 is regulated by cyclin-dependent kinase (CDK) 1 and CDK2 in human cells [245]. In addition, ATM also seems to play a role in this process since its inhibition caused slower EXO1 phosphorylation dynamics [246]. On the other hand, there is only limited knowledge about the regulation of DNA2-mediated resection. Yeast Dna2 is phosphorylated by Cdk1 at several amino acid residues located in the N-terminal region, which influences its relocalization to DNA DSBs and subsequent nucleolytic degradation of the DNA ends [247]. However, human DNA2 misses this domain and it is therefore likely that other mechanisms mediate its recruitment to broken DNA ends. A protein that is potentially involved in this process could be RPA since it has been shown that RPA is indispensable for Dna2 association with DNA damage sites in yeast [135]. In contrast, Exo1 recruitment seems to be RPA-independent [135]. These findings further indicate that Dna2 and Exo1 resection pathways are regulated differently. A very recent study identified several gene products in yeast that have an influence on Dna2 foci formation, either positively or negatively, upon DNA-damage induction by phleomycin [248]. In addition, work done in fission yeast defined Pxd1 as a protein that inhibits the association of Dna2 with RPA-coated ssDNA and therefore inhibits resection [249]. These studies suggest that there might be additional proteins that regulate DNA2 activity in human cells.

Controlling of the DNA2-mediated resection pathway in human cells could also be mediated via its interacting RecQ helicases that are crucial for the degradation of the 5’ terminated strand by DNA2, namely WRN and BLM. Consistent with this hypothesis it has been shown that acetylation and deacetylation of WRN plays a role in coordinating the activity and localization of WRN during DNA repair [250, 251]. Further, also interaction partners of WRN and BLM, for instance TRF1, could play a role in regulating mechanisms. In line with this theory, it has been demonstrated that phosphorylated TRF1 stimulates HR and its depletion diminished ATR activation after treating cells with IR [252]. Within the same study evidence is provided that DNA-end resection, which is a prerequisite for HR and also ATR activation, was abrogated upon knockdown of TRF1 [252]. Taken together, although some proteins are known to be involved in the regulating system underlying DNA-end resection in human cells, the interplay between these factors during the cell cycle are somewhat poorly understood and thus require further investigation.

BLM and WRN are not only involved in DNA-end resection but also in several other processes within the cell and are potential targets for cancer therapy. In fact, it is known that WRN protein expression is upregulated in certain leukemia cancer types [253]. Potentially, this increase in WRN expression arises because the high replicative state of cancer cells generates lesions in the DNA that have to be repaired. Evidence that targeting WRN in cancer therapy could be effective comes from a study dealing with head and neck squamous cell carcinomas where it has been demonstrated that siRNA-mediated downregulation of WRN impaired tumour cell growth [254].

Since WRN and BLM are involved in the elimination of G4-quadruplexes. It would be interesting to check whether WRN also plays a similar role like BLM in unwinding G4-structures in promoters to allow gene expression. In addition, since G4-quadruplexes can also form at telomeres, one could combine WRN or BLM inhibition with a G4-stabilizing agent like telomestatin to enhance the effect on cancer cells. Given that WRN is involved in many processes of cell homeostasis, it is an attractive target for cancer therapy and it has already been shown that inhibition of its helicase function could be used to treat certain malignancies [255].

Our study showing that the mismatch-binding factor MutSβ can mediate ATR activation brings progress in understanding the signalling mechanisms that are initiated upon DNA DSB induction. It would be interesting to define the control mechanisms in human cells that lead to association of MutSβ with hairpin loops formed in RPA-coated ssDNA. The histone deacetylase 10 has been shown to promote MMR in HeLa cells by deacetylating MSH2 [256]. It is therefore possible that acetylated MSH2 within MutSβ prevents binding to the DNA substrate. Thus, inhibiting deacetylation of MSH2, which would inhibit as well the MMR system, could be an effective approach for cancer therapy. Such an inhibitor could also be used in combined medication with a DNA damaging agent that induces DNA DSBs. Since cancer cells show a high replication rate, it is likely that RPA is limited, leading to uncovered ssDNA that would usually activate the ATR-CHK1 pathway via MutSβ and initiate a delay in cell cycle progression. If this mechanism is abolished, the checkpoint is not activated and hence DNA repair is affected which could induce lethal effects for cancer cells.

The ATP-driven dissociation of MutSβ from RPA-coated ssDNA is likely to facilitate DNA repair. However, the molecular mechanism underlying the disassociation of MutSβ from ssDNA hairpin loops is not known. To further explore this process, mutant versions of MSH2 and MSH3 in their ATPase domains, which are unable to bind or hydrolyse ATP, could be generated. These mutants could be tested for their ability to bind hairpin loops within RPA-coated ssDNA to define the exact functions of ATP binding and hydrolysis by MSH2 and MSH3 subunits in the interaction of MutSβ complex with ssDNA.

In our study, we used CPT to induce replication-associated DNA DSBs. This drug treatment caused formation of numerous DNA DSBs per cell generating artificial conditions where the amount of RPA molecules is limited due to resection-dependent repair. Under such conditions, the formation of hairpin structures within RPA-coated ssDNA could be a consequence of lack of RPA molecules leading to MutSβ-mediated ATR activation as described above. To test whether these hairpin structures do also persist under more physiological conditions, one could use cell lines carrying chromosomally-based DNA DSB repair reporters. Following induction of a single DNA DSB by expression of I-SceI endonuclease in these cells, association of MutSβ around the DNA DSB site could be studied by ChIP.

Work on RECQ5 described in this thesis has demonstrated that it is able to guide HR towards the SDSA pathway and thus is important to prevent the formation of potentially mutagenic crossovers. Although HR is limited to S and G2 phases of the cell cycle and DNA-end resection is a prerequisite for this pathway, it has been shown that resection also occurs during M phase [257]. Since the end processing mechanism within this cell cycle phase is only dependent on MRN/CtIP, it is highly likely that it is not very extensive [257]. Nevertheless, RAD51 could be loaded and perform homology search that would lead to entangled chromosomes, which would interfere with chromosome segregation. Interestingly, it has been shown that Rad51 binding to RPA-coated ssDNA in M-Phase is inhibited in a manner dependent on Cdk1 phosphorylation in *Xenopus* egg extracts [257]. This implicates that anti-recombinases such as RECQ5 act during mitosis to prevent RAD51 filament assembly in human cells. Interestingly data obtained in our lab by Jana Langhoff demonstrate that RECQ5 is phosphorylated in early mitosis at serine 727 that is located adjacent to the RAD51-interaction domain [210, 211]. As serine 727 of RECQ5 is a part of the CDK consensus site, it is possible that in M-phase, CDK1-mediated phosphorylation of RECQ5 at this residue can stimulate RECQ5’s anti-recombinase activity. Thus, it would be interesting to investigate whether RECQ5 also plays a role during mitosis to prevent initiation of HR.

6. References

1. Bianconi, E., et al., *An estimation of the number of cells in the human body.* Ann Hum Biol, 2013. **40**(6): p. 463-71.
2. Spalding, K.L., et al., *Retrospective birth dating of cells in humans.* Cell, 2005. **122**(1): p. 133-43.
3. Hanahan, D. and R.A. Weinberg, *Hallmarks of cancer: the next generation.* Cell, 2011. **144**(5): p. 646-74.
4. Kuppers, R., A. Engert, and M.L. Hansmann, *Hodgkin lymphoma.* J Clin Invest, 2012. **122**(10): p. 3439-47.
5. Gupta, G.P. and J. Massague, *Cancer metastasis: building a framework.* Cell, 2006. **127**(4): p. 679-95.
6. Steeg, P.S., *Tumor metastasis: mechanistic insights and clinical challenges.* Nat Med, 2006. **12**(8): p. 895-904.
7. Ferlay, J., et al., *Cancer incidence and mortality worldwide: sources, methods and major patterns in GLOBOCAN 2012.* Int J Cancer, 2015. **136**(5): p. E359-86.
8. Mendis, S., S. Davis, and B. Norrving, *Organizational Update The World Health Organization Global Status Report on Noncommunicable Diseases 2014; One More Landmark Step in the Combat Against Stroke and Vascular Disease.* Stroke, 2015. **46**(5): p. E121-E122.
9. Hanahan, D. and R.A. Weinberg, *The hallmarks of cancer.* Cell, 2000. **100**(1): p. 57-70.
10. Cooper, G.M., *Elements of human cancer*. 1992, Boston: Jones and Bartlett Publishers. xiv, 354 p.
11. Elenbaas, B. and R.A. Weinberg, *Heterotypic signaling between epithelial tumor cells and fibroblasts in carcinoma formation.* Experimental Cell Research, 2001. **264**(1): p. 169-184.
12. Paul, M.K. and A.K. Mukhopadhyay, *Tyrosine kinase - Role and significance in Cancer.* Int J Med Sci, 2004. **1**(2): p. 101-115.
13. Muller, P.A. and K.H. Vousden, *p53 mutations in cancer.* Nat Cell Biol, 2013. **15**(1): p. 2-8.
14. Vazquez, A., et al., *The genetics of the p53 pathway, apoptosis and cancer therapy.* Nat Rev Drug Discov, 2008. **7**(12): p. 979-87.
15. Elmore, S., *Apoptosis: a review of programmed cell death.* Toxicol Pathol, 2007. **35**(4): p. 495-516.
16. Lowe, S.W. and A.W. Lin, *Apoptosis in cancer.* Carcinogenesis, 2000. **21**(3): p. 485-95.
17. Tait, S.W. and D.R. Green, *Mitochondria and cell death: outer membrane permeabilization and beyond.* Nat Rev Mol Cell Biol, 2010. **11**(9): p. 621-32.
18. Fulda, S. and K.M. Debatin, *Extrinsic versus intrinsic apoptosis pathways in anticancer chemotherapy.* Oncogene, 2006. **25**(34): p. 4798-811.
19. Hockenbery, D., et al., *Bcl-2 is an inner mitochondrial membrane protein that blocks programmed cell death.* Nature, 1990. **348**(6299): p. 334-6.
20. Siegel, R.M., et al., *Fas preassociation required for apoptosis signaling and dominant inhibition by pathogenic mutations.* Science, 2000. **288**(5475): p. 2354-7.
21. Gilson, E. and V. Geli, *How telomeres are replicated.* Nat Rev Mol Cell Biol, 2007. **8**(10): p. 825-38.
22. Greenberg, R.A., *Telomeres, crisis and cancer.* Curr Mol Med, 2005. **5**(2): p. 213-8.
23. Campbell, P.J., *Telomeres and cancer: from crisis to stability to crisis to stability.* Cell, 2012. **148**(4): p. 633-5.

24. Shay, J.W. and W.E. Wright, *Role of telomeres and telomerase in cancer.* Semin Cancer Biol, 2011. **21**(6): p. 349-53.
25. Kim, N.W., et al., *Specific association of human telomerase activity with immortal cells and cancer.* Science, 1994. **266**(5193): p. 2011-5.
26. Carmeliet, P. and R.K. Jain, *Molecular mechanisms and clinical applications of angiogenesis.* Nature, 2011. **473**(7347): p. 298-307.
27. Folkman, J. and D. Hanahan, *Switch to the angiogenic phenotype during tumorigenesis.* Princess Takamatsu Symp, 1991. **22**: p. 339-47.
28. Weis, S.M. and D.A. Cheresh, *Tumor angiogenesis: molecular pathways and therapeutic targets.* Nat Med, 2011. **17**(11): p. 1359-70.
29. Weis, S.M. and D.A. Cheresh, *Pathophysiological consequences of VEGF-induced vascular permeability.* Nature, 2005. **437**(7058): p. 497-504.
30. Fidler, I.J., *The pathogenesis of cancer metastasis: the 'seed and soil' hypothesis revisited.* Nat Rev Cancer, 2003. **3**(6): p. 453-8.
31. Wang, S.S., et al., *Links between cancer stem cells and epithelial-mesenchymal transition.* Onco Targets Ther, 2015. **8**: p. 2973-80.
32. Hay, E.D., *An overview of epithelio-mesenchymal transformation.* Acta Anat (Basel), 1995. **154**(1): p. 8-20.
33. Pollard, J.W., *Tumour-educated macrophages promote tumour progression and metastasis.* Nat Rev Cancer, 2004. **4**(1): p. 71-8.
34. Leek, R.D. and A.L. Harris, *Tumor-associated macrophages in breast cancer.* J Mammary Gland Biol Neoplasia, 2002. **7**(2): p. 177-89.
35. Lee, E.Y.H.P. and W.J. Muller, *Oncogenes and Tumor Suppressor Genes.* Cold Spring Harbor Perspectives in Biology, 2010. **2**(10).
36. Thompson, S.L. and D.A. Compton, *Examining the link between chromosomal instability and aneuploidy in human cells.* J Cell Biol, 2008. **180**(4): p. 665-72.
37. Duijf, P.H. and R. Benezra, *The cancer biology of whole-chromosome instability.* Oncogene, 2013. **32**(40): p. 4727-36.
38. Janssen, A., et al., *Chromosome segregation errors as a cause of DNA damage and structural chromosome aberrations.* Science, 2011. **333**(6051): p. 1895-8.
39. Obe, G. and M. Durante, *DNA double strand breaks and chromosomal aberrations.* Cytogenet Genome Res, 2010. **128**(1-3): p. 8-16.
40. Lindahl, T. and D.E. Barnes, *Repair of endogenous DNA damage.* Cold Spring Harb Symp Quant Biol, 2000. **65**: p. 127-33.
41. Valko, M., et al., *Free radicals, metals and antioxidants in oxidative stress-induced cancer.* Chem Biol Interact, 2006. **160**(1): p. 1-40.
42. Valko, M., et al., *Free radicals and antioxidants in normal physiological functions and human disease.* Int J Biochem Cell Biol, 2007. **39**(1): p. 44-84.
43. Jackson, S.P. and J. Bartek, *The DNA-damage response in human biology and disease.* Nature, 2009. **461**(7267): p. 1071-8.
44. Gates, K.S., *An overview of chemical processes that damage cellular DNA: spontaneous hydrolysis, alkylation, and reactions with radicals.* Chem Res Toxicol, 2009. **22**(11): p. 1747-60.
45. Schroeder, G.K., et al., *The time required for water attack at the phosphorus atom of simple phosphodiesters and of DNA.* Proc Natl Acad Sci U S A, 2006. **103**(11): p. 4052-5.
46. Shen, J.C., W.M. Rideout, 3rd, and P.A. Jones, *The rate of hydrolytic deamination of 5-methylcytosine in double-stranded DNA.* Nucleic Acids Res, 1994. **22**(6): p. 972-6.

47. Ward, J.F., *DNA damage produced by ionizing radiation in mammalian cells: identities, mechanisms of formation, and reparability.* Prog Nucleic Acid Res Mol Biol, 1988. **35**: p. 95-125.
48. Maznik, N.A. and V.A. Vinnikov, *[The retrospective cytogenetic dosimetry using the results of conventional chromosomal analysis in Chernobyl clean-up workers].* Radiats Biol Radioecol, 2005. **45**(6): p. 700-8.
49. Chen, Y., et al., *Cytogenetic studies for a group of people living in Japan 1 year after the Fukushima nuclear accident.* Radiat Prot Dosimetry, 2014. **159**(1-4): p. 20-5.
50. Moudgil, V., et al., *A review of molecular mechanisms in the development of hepatocellular carcinoma by aflatoxin and hepatitis B and C viruses.* J Environ Pathol Toxicol Oncol, 2013. **32**(2): p. 165-75.
51. Williams, J.H., et al., *Human aflatoxicosis in developing countries: a review of toxicology, exposure, potential health consequences, and interventions.* Am J Clin Nutr, 2004. **80**(5): p. 1106-22.
52. Novi, A.M., *Liver carcinogenesis in rats after aflatoxin B1 administration. A light- and electron-microscopic study.* Curr Top Pathol, 1977. **65**: p. 115-63.
53. Butler, W.H. and G.E. Neal, *Mode of action and human health aspects of aflatoxin carcinogenesis.* Ann Nutr Aliment, 1977. **31**(4-6): p. 949-56.
54. Waring, M.J., *Complex formation between ethidium bromide and nucleic acids.* J Mol Biol, 1965. **13**(1): p. 269-82.
55. McCann, J., et al., *Detection of carcinogens as mutagens in the Salmonella/microsome test: assay of 300 chemicals.* Proc Natl Acad Sci U S A, 1975. **72**(12): p. 5135-9.
56. Ghosh, P., et al., *Increased chromosome aberration frequencies in the Bowen's patients compared to non-cancerous skin lesions individuals exposed to arsenic.* Mutat Res, 2007. **632**(1-2): p. 104-10.
57. Bhattacharjee, P., M. Banerjee, and A.K. Giri, *Role of genomic instability in arsenic-induced carcinogenicity. A review.* Environ Int, 2013. **53**: p. 29-40.
58. Krejci, L., et al., *Homologous recombination and its regulation.* Nucleic Acids Research, 2012. **40**(13): p. 5795-5818.
59. Karran, P., *DNA double strand break repair in mammalian cells.* Current Opinion in Genetics & Development, 2000. **10**(2): p. 144-150.
60. Malu, S., et al., *Role of non-homologous end joining in V(D)J recombination.* Immunol Res, 2012. **54**(1-3): p. 233-46.
61. Keeney, S., *Spo11 and the Formation of DNA Double-Strand Breaks in Meiosis.* Genome Dyn Stab, 2008. **2**: p. 81-123.
62. Harper, J.W. and S.J. Elledge, *The DNA damage response: Ten years after.* Molecular Cell, 2007. **28**(5): p. 739-745.
63. Hoeijmakers, J.H., *Genome maintenance mechanisms for preventing cancer.* Nature, 2001. **411**(6835): p. 366-74.
64. Setlow, R.B., *Repair deficient human disorders and cancer.* Nature, 1978. **271**(5647): p. 713-7.
65. Sugasawa, K., et al., *Xeroderma pigmentosum group C protein complex is the initiator of global genome nucleotide excision repair.* Mol Cell, 1998. **2**(2): p. 223-32.
66. Sugasawa, K., et al., *A multistep damage recognition mechanism for global genomic nucleotide excision repair.* Genes Dev, 2001. **15**(5): p. 507-21.

67. Reardon, J.T. and A. Sancar, *Recognition and repair of the cyclobutane thymine dimer, a major cause of skin cancers, by the human excision nuclease.* Genes Dev, 2003. **17**(20): p. 2539-51.
68. Wakasugi, M., et al., *DDB accumulates at DNA damage sites immediately after UV irradiation and directly stimulates nucleotide excision repair.* J Biol Chem, 2002. **277**(3): p. 1637-40.
69. Scrima, A., et al., *Structural basis of UV DNA-damage recognition by the DDB1-DDB2 complex.* Cell, 2008. **135**(7): p. 1213-23.
70. Osakabe, A., et al., *Structural basis of pyrimidine-pyrimidone (6-4) photoproduct recognition by UV-DDB in the nucleosome.* Sci Rep, 2015. **5**: p. 16330.
71. Yokoi, M., et al., *The xeroderma pigmentosum group C protein complex XPC-HR23B plays an important role in the recruitment of transcription factor IIH to damaged DNA.* J Biol Chem, 2000. **275**(13): p. 9870-5.
72. Compe, E. and J.M. Egly, *TFIIH: when transcription met DNA repair.* Nat Rev Mol Cell Biol, 2012. **13**(6): p. 343-54.
73. Coin, F., V. Oksenych, and J.M. Egly, *Distinct roles for the XPB/p52 and XPD/p44 subcomplexes of TFIIH in damaged DNA opening during nucleotide excision repair.* Mol Cell, 2007. **26**(2): p. 245-56.
74. Fagbemi, A.F., B. Orelli, and O.D. Scharer, *Regulation of endonuclease activity in human nucleotide excision repair.* DNA Repair (Amst), 2011. **10**(7): p. 722-9.
75. Marteijn, J.A., et al., *Understanding nucleotide excision repair and its roles in cancer and ageing.* Nat Rev Mol Cell Biol, 2014. **15**(7): p. 465-81.
76. Petruseva, I.O., A.N. Evdokimov, and O.I. Lavrik, *Molecular mechanism of global genome nucleotide excision repair.* Acta Naturae, 2014. **6**(1): p. 23-34.
77. de Laat, W.L., et al., *DNA-binding polarity of human replication protein A positions nucleases in nucleotide excision repair.* Genes Dev, 1998. **12**(16): p. 2598-609.
78. Fousteri, M., et al., *Cockayne syndrome A and B proteins differentially regulate recruitment of chromatin remodeling and repair factors to stalled RNA polymerase II in vivo.* Mol Cell, 2006. **23**(4): p. 471-82.
79. Schwertman, P., et al., *UV-sensitive syndrome protein UVSSA recruits USP7 to regulate transcription-coupled repair.* Nat Genet, 2012. **44**(5): p. 598-602.
80. Lans, H., J.A. Marteijn, and W. Vermeulen, *ATP-dependent chromatin remodeling in the DNA-damage response.* Epigenetics Chromatin, 2012. **5**: p. 4.
81. Iyer, R.R., et al., *DNA mismatch repair: functions and mechanisms.* Chem Rev, 2006. **106**(2): p. 302-23.
82. Moldovan, G.L., B. Pfander, and S. Jentsch, *PCNA, the maestro of the replication fork.* Cell, 2007. **129**(4): p. 665-79.
83. Jiricny, J., *The multifaceted mismatch-repair system.* Nat Rev Mol Cell Biol, 2006. **7**(5): p. 335-46.
84. Li, G.M., *Mechanisms and functions of DNA mismatch repair.* Cell Res, 2008. **18**(1): p. 85-98.
85. Hsieh, P. and K. Yamane, *DNA mismatch repair: molecular mechanism, cancer, and ageing.* Mech Ageing Dev, 2008. **129**(7-8): p. 391-407.
86. Genschel, J., et al., *Isolation of MutSbeta from human cells and comparison of the mismatch repair specificities of MutSbeta and MutSalpha.* J Biol Chem, 1998. **273**(31): p. 19895-901.

87. Habraken, Y., et al., *Binding of insertion/deletion DNA mismatches by the heterodimer of yeast mismatch repair proteins MSH2 and MSH3.* Curr Biol, 1996. **6**(9): p. 1185-7.
88. Palombo, F., et al., *hMutSbeta, a heterodimer of hMSH2 and hMSH3, binds to insertion/deletion loops in DNA.* Curr Biol, 1996. **6**(9): p. 1181-4.
89. Kunkel, T.A. and D.A. Erie, *Eukaryotic Mismatch Repair in Relation to DNA Replication.* Annu Rev Genet, 2015. **49**: p. 291-313.
90. Bridge, G., S. Rashid, and S.A. Martin, *DNA mismatch repair and oxidative DNA damage: implications for cancer biology and treatment.* Cancers (Basel), 2014. **6**(3): p. 1597-614.
91. Gradia, S., et al., *hMSH2-hMSH6 forms a hydrolysis-independent sliding clamp on mismatched DNA.* Mol Cell, 1999. **3**(2): p. 255-61.
92. Wilson, T., S. Guerrette, and R. Fishel, *Dissociation of mismatch recognition and ATPase activity by hMSH2-hMSH3.* J Biol Chem, 1999. **274**(31): p. 21659-64.
93. Kadyrov, F.A., et al., *Endonucleolytic function of MutLalpha in human mismatch repair.* Cell, 2006. **126**(2): p. 297-308.
94. Fishel, R., *Mismatch Repair.* J Biol Chem, 2015. **290**(44): p. 26395-403.
95. Traver, S., et al., *MCM9 Is Required for Mammalian DNA Mismatch Repair.* Mol Cell, 2015. **59**(5): p. 831-9.
96. Martin, A. and M.D. Scharff, *AID and mismatch repair in antibody diversification.* Nat Rev Immunol, 2002. **2**(8): p. 605-14.
97. Robertson, A.B., et al., *DNA repair in mammalian cells: Base excision repair: the long and short of it.* Cell Mol Life Sci, 2009. **66**(6): p. 981-93.
98. Lindahl, T., *Instability and decay of the primary structure of DNA.* Nature, 1993. **362**(6422): p. 709-15.
99. Dalhus, B., et al., *Structural insight into repair of alkylated DNA by a new superfamily of DNA glycosylases comprising HEAT-like repeats.* Nucleic Acids Res, 2007. **35**(7): p. 2451-9.
100. Sedgwick, B., et al., *Repair of alkylated DNA: recent advances.* DNA Repair (Amst), 2007. **6**(4): p. 429-42.
101. Lindahl, T. and B. Nyberg, *Rate of depurination of native deoxyribonucleic acid.* Biochemistry, 1972. **11**(19): p. 3610-8.
102. Olsen, L.C., et al., *Molecular cloning of human uracil-DNA glycosylase, a highly conserved DNA repair enzyme.* EMBO J, 1989. **8**(10): p. 3121-5.
103. Frosina, G., et al., *Two pathways for base excision repair in mammalian cells.* J Biol Chem, 1996. **271**(16): p. 9573-8.
104. Fortini, P., et al., *The base excision repair: mechanisms and its relevance for cancer susceptibility.* Biochimie, 2003. **85**(11): p. 1053-71.
105. Wilson, D.M., 3rd and D. Barsky, *The major human abasic endonuclease: formation, consequences and repair of abasic lesions in DNA.* Mutat Res, 2001. **485**(4): p. 283-307.
106. Liu, Y., et al., *Coordination of steps in single-nucleotide base excision repair mediated by apurinic/apyrimidinic endonuclease 1 and DNA polymerase beta.* J Biol Chem, 2007. **282**(18): p. 13532-41.
107. Beard, W.A. and S.H. Wilson, *Structure and mechanism of DNA polymerase beta.* Biochemistry, 2014. **53**(17): p. 2768-80.
108. Kim, K., S. Biade, and Y. Matsumoto, *Involvement of flap endonuclease 1 in base excision DNA repair.* J Biol Chem, 1998. **273**(15): p. 8842-8.

109. Klungland, A. and T. Lindahl, *Second pathway for completion of human DNA base excision-repair: reconstitution with purified proteins and requirement for DNase IV (FEN1).* EMBO J, 1997. **16**(11): p. 3341-8.
110. Caldecott, K.W., *Single-strand break repair and genetic disease.* Nat Rev Genet, 2008. **9**(8): p. 619-31.
111. Ame, J.C., C. Spenlehauer, and G. de Murcia, *The PARP superfamily.* Bioessays, 2004. **26**(8): p. 882-93.
112. Nickson, C.M. and J.L. Parsons, *Monitoring regulation of DNA repair activities of cultured cells in-gel using the comet assay.* Front Genet, 2014. **5**: p. 232.
113. Burma, S., B.P. Chen, and D.J. Chen, *Role of non-homologous end joining (NHEJ) in maintaining genomic integrity.* DNA Repair (Amst), 2006. **5**(9-10): p. 1042-8.
114. Mari, P.O., et al., *Dynamic assembly of end-joining complexes requires interaction between Ku70/80 and XRCC4.* Proc Natl Acad Sci U S A, 2006. **103**(49): p. 18597-602.
115. Davis, A.J. and D.J. Chen, *DNA double strand break repair via non-homologous end-joining.* Transl Cancer Res, 2013. **2**(3): p. 130-143.
116. Walker, J.R., R.A. Corpina, and J. Goldberg, *Structure of the Ku heterodimer bound to DNA and its implications for double-strand break repair.* Nature, 2001. **412**(6847): p. 607-14.
117. Hartley, K.O., et al., *DNA-dependent protein kinase catalytic subunit: a relative of phosphatidylinositol 3-kinase and the ataxia telangiectasia gene product.* Cell, 1995. **82**(5): p. 849-56.
118. Chiruvella, K.K., Z. Liang, and T.E. Wilson, *Repair of double-strand breaks by end joining.* Cold Spring Harb Perspect Biol, 2013. **5**(5): p. a012757.
119. Weterings, E. and D.C. van Gent, *The mechanism of non-homologous end-joining: a synopsis of synapsis.* DNA Repair (Amst), 2004. **3**(11): p. 1425-35.
120. Cary, R.B., et al., *DNA looping by Ku and the DNA-dependent protein kinase.* Proc Natl Acad Sci U S A, 1997. **94**(9): p. 4267-72.
121. Singh, D.K., et al., *RecQ helicases in DNA double strand break repair and telomere maintenance.* Mutat Res, 2012. **736**(1-2): p. 15-24.
122. Povirk, L.F., *Processing of damaged DNA ends for double-strand break repair in mammalian cells.* ISRN Mol Biol, 2012. **2012**.
123. Grawunder, U., et al., *Activity of DNA ligase IV stimulated by complex formation with XRCC4 protein in mammalian cells.* Nature, 1997. **388**(6641): p. 492-5.
124. Lu, H., et al., *Length-dependent binding of human XLF to DNA and stimulation of XRCC4.DNA ligase IV activity.* J Biol Chem, 2007. **282**(15): p. 11155-62.
125. Liu, P., et al., *Akt-mediated phosphorylation of XLF impairs non-homologous end-joining DNA repair.* Mol Cell, 2015. **57**(4): p. 648-61.
126. Moynahan, M.E. and M. Jasin, *Mitotic homologous recombination maintains genomic stability and suppresses tumorigenesis.* Nat Rev Mol Cell Biol, 2010. **11**(3): p. 196-207.
127. Mladenov, E. and G. Iliakis, *The Pathways of Double-Strand Break Repair, DNA Repair - On the Pathways to Fixing DNA Damage and Errors*. 2011: InTech.
128. McVey, M. and S.E. Lee, *MMEJ repair of double-strand breaks (director's cut): deleted sequences and alternative endings.* Trends Genet, 2008. **24**(11): p. 529-38.
129. Baudat, F. and B. de Massy, *Regulating double-stranded DNA break repair towards crossover or non-crossover during mammalian meiosis.* Chromosome Res, 2007. **15**(5): p. 565-77.
130. Heyer, W.D., K.T. Ehmsen, and J. Liu, *Regulation of homologous recombination in eukaryotes.* Annu Rev Genet, 2010. **44**: p. 113-39.

131. Krejci, L., et al., *Homologous recombination and its regulation.* Nucleic Acids Res, 2012. **40**(13): p. 5795-818.
132. San Filippo, J., P. Sung, and H. Klein, *Mechanism of eukaryotic homologous recombination.* Annu Rev Biochem, 2008. **77**: p. 229-57.
133. Mimitou, E.P. and L.S. Symington, *DNA end resection--unraveling the tail.* DNA Repair (Amst), 2011. **10**(3): p. 344-8.
134. Mimitou, E.P. and L.S. Symington, *Sae2, Exo1 and Sgs1 collaborate in DNA double-strand break processing.* Nature, 2008. **455**(7214): p. 770-4.
135. Chen, H., M. Lisby, and L.S. Symington, *RPA coordinates DNA end resection and prevents formation of DNA hairpins.* Mol Cell, 2013. **50**(4): p. 589-600.
136. Sung, P., et al., *Rad51 recombinase and recombination mediators.* J Biol Chem, 2003. **278**(44): p. 42729-32.
137. Symington, L.S., R. Rothstein, and M. Lisby, *Mechanisms and regulation of mitotic recombination in Saccharomyces cerevisiae.* Genetics, 2014. **198**(3): p. 795-835.
138. Bernstein, K.A., et al., *The Shu complex, which contains Rad51 paralogues, promotes DNA repair through inhibition of the Srs2 anti-recombinase.* Mol Biol Cell, 2011. **22**(9): p. 1599-607.
139. Taylor, M.R., et al., *Rad51 Paralogs Remodel Pre-synaptic Rad51 Filaments to Stimulate Homologous Recombination.* Cell, 2015. **162**(2): p. 271-86.
140. Roy, R., J. Chun, and S.N. Powell, *BRCA1 and BRCA2: different roles in a common pathway of genome protection.* Nat Rev Cancer, 2012. **12**(1): p. 68-78.
141. Sebesta, M., et al., *Role of PCNA and TLS polymerases in D-loop extension during homologous recombination in humans.* DNA Repair (Amst), 2013. **12**(9): p. 691-8.
142. Mazin, A.V., et al., *Rad54, the motor of homologous recombination.* DNA Repair (Amst), 2010. **9**(3): p. 286-302.
143. Llorente, B., C.E. Smith, and L.S. Symington, *Break-induced replication: what is it and what is it for?* Cell Cycle, 2008. **7**(7): p. 859-64.
144. Costantino, L., et al., *Break-induced replication repair of damaged forks induces genomic duplications in human cells.* Science, 2014. **343**(6166): p. 88-91.
145. Andersen, S.L. and J. Sekelsky, *Meiotic versus mitotic recombination: two different routes for double-strand break repair: the different functions of meiotic versus mitotic DSB repair are reflected in different pathway usage and different outcomes.* Bioessays, 2010. **32**(12): p. 1058-66.
146. Iyama, T. and D.M. Wilson, 3rd, *DNA repair mechanisms in dividing and non-dividing cells.* DNA Repair (Amst), 2013. **12**(8): p. 620-36.
147. Sarbajna, S. and S.C. West, *Holliday junction processing enzymes as guardians of genome stability.* Trends Biochem Sci, 2014. **39**(9): p. 409-19.
148. Rass, U., et al., *Mechanism of Holliday junction resolution by the human GEN1 protein.* Genes Dev, 2010. **24**(14): p. 1559-69.
149. Wyatt, H.D., et al., *Coordinated actions of SLX1-SLX4 and MUS81-EME1 for Holliday junction resolution in human cells.* Mol Cell, 2013. **52**(2): p. 234-47.
150. Szankasi, P. and G.R. Smith, *A role for exonuclease I from S. pombe in mutation avoidance and mismatch correction.* Science, 1995. **267**(5201): p. 1166-9.
151. Budd, M.E., W.C. Choe, and J.L. Campbell, *DNA2 encodes a DNA helicase essential for replication of eukaryotic chromosomes.* J Biol Chem, 1995. **270**(45): p. 26766-9.
152. Budd, M.E., W. Choe, and J.L. Campbell, *The nuclease activity of the yeast DNA2 protein, which is related to the RecB-like nucleases, is essential in vivo.* J Biol Chem, 2000. **275**(22): p. 16518-29.

153. Gravel, S., et al., *DNA helicases Sgs1 and BLM promote DNA double-strand break resection.* Genes Dev, 2008. **22**(20): p. 2767-72.

154. Gangloff, S., et al., *The yeast type I topoisomerase Top3 interacts with Sgs1, a DNA helicase homolog: a potential eukaryotic reverse gyrase.* Mol Cell Biol, 1994. **14**(12): p. 8391-8.

155. Zhu, Z., et al., *Sgs1 helicase and two nucleases Dna2 and Exo1 resect DNA double-strand break ends.* Cell, 2008. **134**(6): p. 981-94.

156. Mimitou, E.P. and L.S. Symington, *DNA end resection: many nucleases make light work.* DNA Repair (Amst), 2009. **8**(9): p. 983-95.

157. Cannavo, E. and P. Cejka, *Sae2 promotes dsDNA endonuclease activity within Mre11-Rad50-Xrs2 to resect DNA breaks.* Nature, 2014. **514**(7520): p. 122-5.

158. Cejka, P., et al., *DNA end resection by Dna2-Sgs1-RPA and its stimulation by Top3-Rmi1 and Mre11-Rad50-Xrs2.* Nature, 2010. **467**(7311): p. 112-6.

159. Zhou, C., S. Pourmal, and N.P. Pavletich, *Dna2 nuclease-helicase structure, mechanism and regulation by Rpa.* Elife, 2015. **4**.

160. Tammaro, M., et al., *The N-terminus of RPA large subunit and its spatial position are important for the 5'->3' resection of DNA double-strand breaks.* Nucleic Acids Res, 2015. **43**(18): p. 8790-800.

161. Liao, S., T. Toczylowski, and H. Yan, *Identification of the Xenopus DNA2 protein as a major nuclease for the 5'->3' strand-specific processing of DNA ends.* Nucleic Acids Res, 2008. **36**(19): p. 6091-100.

162. Yan, H., et al., *Analysis of the Xenopus Werner syndrome protein in DNA double-strand break repair.* J Cell Biol, 2005. **171**(2): p. 217-27.

163. Toczylowski, T. and H. Yan, *Mechanistic analysis of a DNA end processing pathway mediated by the Xenopus Werner syndrome protein.* J Biol Chem, 2006. **281**(44): p. 33198-205.

164. Yan, H., et al., *Replication protein A promotes 5'-->3' end processing during homology-dependent DNA double-strand break repair.* J Cell Biol, 2011. **192**(2): p. 251-61.

165. Liao, S., et al., *Analysis of MRE11's function in the 5'-->3' processing of DNA double-strand breaks.* Nucleic Acids Res, 2012. **40**(10): p. 4496-506.

166. Chu, W.K. and I.D. Hickson, *RecQ helicases: multifunctional genome caretakers.* Nat Rev Cancer, 2009. **9**(9): p. 644-54.

167. Karmakar, P., et al., *BLM is an early responder to DNA double-strand breaks.* Biochem Biophys Res Commun, 2006. **348**(1): p. 62-9.

168. Nimonkar, A.V., et al., *BLM-DNA2-RPA-MRN and EXO1-BLM-RPA-MRN constitute two DNA end resection machineries for human DNA break repair.* Genes Dev, 2011. **25**(4): p. 350-62.

169. Hottiger, M.O., et al., *Toward a unified nomenclature for mammalian ADP-ribosyltransferases.* Trends Biochem Sci, 2010. **35**(4): p. 208-19.

170. Harper, J.W. and S.J. Elledge, *The DNA damage response: ten years after.* Mol Cell, 2007. **28**(5): p. 739-45.

171. Ciccia, A. and S.J. Elledge, *The DNA damage response: making it safe to play with knives.* Mol Cell, 2010. **40**(2): p. 179-204.

172. Schreiber, V., et al., *Poly(ADP-ribose): novel functions for an old molecule.* Nat Rev Mol Cell Biol, 2006. **7**(7): p. 517-28.

173. Jazayeri, A., et al., *Mre11-Rad50-Nbs1-dependent processing of DNA breaks generates oligonucleotides that stimulate ATM activity.* EMBO J, 2008. **27**(14): p. 1953-62.
174. Kanaar, R. and C. Wyman, *DNA repair by the MRN complex: break it to make it.* Cell, 2008. **135**(1): p. 14-6.
175. Rogakou, E.P., et al., *DNA double-stranded breaks induce histone H2AX phosphorylation on serine 139.* J Biol Chem, 1998. **273**(10): p. 5858-68.
176. Doil, C., et al., *RNF168 binds and amplifies ubiquitin conjugates on damaged chromosomes to allow accumulation of repair proteins.* Cell, 2009. **136**(3): p. 435-46.
177. Yun, M.H. and K. Hiom, *CtIP-BRCA1 modulates the choice of DNA double-strand-break repair pathway throughout the cell cycle.* Nature, 2009. **459**(7245): p. 460-3.
178. Bunting, S.F., et al., *53BP1 inhibits homologous recombination in Brca1-deficient cells by blocking resection of DNA breaks.* Cell, 2010. **141**(2): p. 243-54.
179. Dimitrova, N., et al., *53BP1 promotes non-homologous end joining of telomeres by increasing chromatin mobility.* Nature, 2008. **456**(7221): p. 524-8.
180. Bartek, J. and J. Lukas, *Chk1 and Chk2 kinases in checkpoint control and cancer.* Cancer Cell, 2003. **3**(5): p. 421-9.
181. Harris, S.L. and A.J. Levine, *The p53 pathway: positive and negative feedback loops.* Oncogene, 2005. **24**(17): p. 2899-908.
182. Hollingworth, R. and R.J. Grand, *Modulation of DNA damage and repair pathways by human tumour viruses.* Viruses, 2015. **7**(5): p. 2542-91.
183. Zou, L. and S.J. Elledge, *Sensing DNA damage through ATRIP recognition of RPA-ssDNA complexes.* Science, 2003. **300**(5625): p. 1542-8.
184. Delacroix, S., et al., *The Rad9-Hus1-Rad1 (9-1-1) clamp activates checkpoint signaling via TopBP1.* Genes Dev, 2007. **21**(12): p. 1472-7.
185. Zou, L., D. Cortez, and S.J. Elledge, *Regulation of ATR substrate selection by Rad17-dependent loading of Rad9 complexes onto chromatin.* Genes Dev, 2002. **16**(2): p. 198-208.
186. Kumagai, A., et al., *TopBP1 activates the ATR-ATRIP complex.* Cell, 2006. **124**(5): p. 943-55.
187. Mordes, D.A., et al., *TopBP1 activates ATR through ATRIP and a PIKK regulatory domain.* Genes Dev, 2008. **22**(11): p. 1478-89.
188. Lee, J., A. Kumagai, and W.G. Dunphy, *The Rad9-Hus1-Rad1 checkpoint clamp regulates interaction of TopBP1 with ATR.* J Biol Chem, 2007. **282**(38): p. 28036-44.
189. Olson, E., et al., *RPA2 is a direct downstream target for ATR to regulate the S-phase checkpoint.* J Biol Chem, 2006. **281**(51): p. 39517-33.
190. Shiotani, B., et al., *Two distinct modes of ATR activation orchestrated by Rad17 and Nbs1.* Cell Rep, 2013. **3**(5): p. 1651-62.
191. Smith, J.A., B.C. Waldman, and A.S. Waldman, *A role for DNA mismatch repair protein Msh2 in error-prone double-strand-break repair in mammalian chromosomes.* Genetics, 2005. **170**(1): p. 355-63.
192. Shahi, A., et al., *Mismatch-repair protein MSH6 is associated with Ku70 and regulates DNA double-strand break repair.* Nucleic Acids Res, 2011. **39**(6): p. 2130-43.
193. Schrader, C.E., J. Vardo, and J. Stavnezer, *Role for mismatch repair proteins Msh2, Mlh1, and Pms2 in immunoglobulin class switching shown by sequence analysis of recombination junctions.* J Exp Med, 2002. **195**(3): p. 367-73.
194. Hong, Z., et al., *Recruitment of mismatch repair proteins to the site of DNA damage in human cells.* J Cell Sci, 2008. **121**(Pt 19): p. 3146-54.

195. Bennardo, N., et al., *Alternative-NHEJ is a mechanistically distinct pathway of mammalian chromosome break repair.* PLoS Genet, 2008. **4**(6): p. e1000110.
196. Franchitto, A., et al., *The mammalian mismatch repair protein MSH2 is required for correct MRE11 and RAD51 relocalization and for efficient cell cycle arrest induced by ionizing radiation in G2 phase.* Oncogene, 2003. **22**(14): p. 2110-20.
197. Pichierri, P., et al., *Hypersensitivity to camptothecin in MSH2 deficient cells is correlated with a role for MSH2 protein in recombinational repair.* Carcinogenesis, 2001. **22**(11): p. 1781-7.
198. van Oers, J.M., et al., *The MutSbeta complex is a modulator of p53-driven tumorigenesis through its functions in both DNA double-strand break repair and mismatch repair.* Oncogene, 2014. **33**(30): p. 3939-46.
199. Cimprich, K.A. and D. Cortez, *ATR: an essential regulator of genome integrity.* Nat Rev Mol Cell Biol, 2008. **9**(8): p. 616-27.
200. Mao, Z., et al., *DNA repair by nonhomologous end joining and homologous recombination during cell cycle in human cells.* Cell Cycle, 2008. **7**(18): p. 2902-6.
201. Mao, Z., et al., *Comparison of nonhomologous end joining and homologous recombination in human cells.* DNA Repair (Amst), 2008. **7**(10): p. 1765-71.
202. Frank-Vaillant, M. and S. Marcand, *Transient stability of DNA ends allows nonhomologous end joining to precede homologous recombination.* Mol Cell, 2002. **10**(5): p. 1189-99.
203. Paques, F. and J.E. Haber, *Multiple pathways of recombination induced by double-strand breaks in Saccharomyces cerevisiae.* Microbiol Mol Biol Rev, 1999. **63**(2): p. 349-404.
204. Johnson, R.D. and M. Jasin, *Sister chromatid gene conversion is a prominent double-strand break repair pathway in mammalian cells.* EMBO J, 2000. **19**(13): p. 3398-407.
205. Wu, Y., et al., *Rad51 protein controls Rad52-mediated DNA annealing.* J Biol Chem, 2008. **283**(21): p. 14883-92.
206. Prakash, R., et al., *Yeast Mph1 helicase dissociates Rad51-made D-loops: implications for crossover control in mitotic recombination.* Genes Dev, 2009. **23**(1): p. 67-79.
207. Ira, G., et al., *Srs2 and Sgs1-Top3 suppress crossovers during double-strand break repair in yeast.* Cell, 2003. **115**(4): p. 401-11.
208. Fugger, K., et al., *Human Fbh1 helicase contributes to genome maintenance via pro- and anti-recombinase activities.* J Cell Biol, 2009. **186**(5): p. 655-63.
209. Hu, Y., et al., *RECQL5/Recql5 helicase regulates homologous recombination and suppresses tumor formation via disruption of Rad51 presynaptic filaments.* Genes Dev, 2007. **21**(23): p. 3073-84.
210. Schwendener, S., et al., *Physical interaction of RECQ5 helicase with RAD51 facilitates its anti-recombinase activity.* J Biol Chem, 2010. **285**(21): p. 15739-45.
211. Islam, M.N., et al., *A Variant of the Breast Cancer Type 2 Susceptibility Protein (BRC) Repeat Is Essential for the RECQL5 Helicase to Interact with RAD51 Recombinase for Genome Stabilization.* J Biol Chem, 2012. **287**(28): p. 23808-18.
212. Hu, Y., et al., *Recql5 and Blm RecQ DNA helicases have nonredundant roles in suppressing crossovers.* Mol Cell Biol, 2005. **25**(9): p. 3431-42.
213. Nicolette, M.L., et al., *Mre11-Rad50-Xrs2 and Sae2 promote 5' strand resection of DNA double-strand breaks.* Nat Struct Mol Biol, 2010. **17**(12): p. 1478-85.
214. Shibata, A., et al., *DNA double-strand break repair pathway choice is directed by distinct MRE11 nuclease activities.* Mol Cell, 2014. **53**(1): p. 7-18.

215. Sartori, A.A., et al., *Human CtIP promotes DNA end resection.* Nature, 2007. **450**(7169): p. 509-14.
216. Lan, L., et al., *Accumulation of Werner protein at DNA double-strand breaks in human cells.* J Cell Sci, 2005. **118**(Pt 18): p. 4153-62.
217. Cheng, W.H., et al., *Linkage between Werner syndrome protein and the Mre11 complex via Nbs1.* J Biol Chem, 2004. **279**(20): p. 21169-76.
218. Iannascoli, C., et al., *The WRN exonuclease domain protects nascent strands from pathological MRE11/EXO1-dependent degradation.* Nucleic Acids Res, 2015. **43**(20): p. 9788-803.
219. Kusumoto, R., et al., *Werner protein cooperates with the XRCC4-DNA ligase IV complex in end-processing.* Biochemistry, 2008. **47**(28): p. 7548-56.
220. Martin, G.M., et al., *What Geriatricians Should Know About the Werner Syndrome.* Journal of the American Geriatrics Society, 1999. **47**(9): p. 1136-1144.
221. Hoehn, H., et al., *Variegated translocation mosaicism in human skin fibroblast cultures.* Cytogenet Cell Genet, 1975. **15**(5): p. 282-98.
222. Fukuchi, K., G.M. Martin, and R.J. Monnat, Jr., *Mutator phenotype of Werner syndrome is characterized by extensive deletions.* Proc Natl Acad Sci U S A, 1989. **86**(15): p. 5893-7.
223. Melcher, R., et al., *Spectral karyotyping of Werner syndrome fibroblast cultures.* Cytogenet Cell Genet, 2000. **91**(1-4): p. 180-5.
224. Edwards, D.N., D.K. Orren, and A. Machwe, *Strand exchange of telomeric DNA catalyzed by the Werner syndrome protein (WRN) is specifically stimulated by TRF2.* Nucleic Acids Res, 2014. **42**(12): p. 7748-61.
225. Edwards, D.N., et al., *The DNA structure and sequence preferences of WRN underlie its function in telomeric recombination events.* Nat Commun, 2015. **6**: p. 8331.
226. Bae, S.H. and Y.S. Seo, *Characterization of the enzymatic properties of the yeast dna2 Helicase/endonuclease suggests a new model for Okazaki fragment processing.* J Biol Chem, 2000. **275**(48): p. 38022-31.
227. Tammaro, M., et al., *DNA double-strand breaks with 5' adducts are efficiently channeled to the DNA2-mediated resection pathway.* Nucleic Acids Res, 2015.
228. Bussen, W., et al., *Holliday junction processing activity of the BLM-Topo IIIalpha-BLAP75 complex.* J Biol Chem, 2007. **282**(43): p. 31484-92.
229. Yin, J., et al., *BLAP75, an essential component of Bloom's syndrome protein complexes that maintain genome integrity.* EMBO J, 2005. **24**(7): p. 1465-76.
230. Xu, D., et al., *RMI, a new OB-fold complex essential for Bloom syndrome protein to maintain genome stability.* Genes Dev, 2008. **22**(20): p. 2843-55.
231. Daley, J.M., et al., *Multifaceted role of the Topo IIIalpha-RMI1-RMI2 complex and DNA2 in the BLM-dependent pathway of DNA break end resection.* Nucleic Acids Res, 2014. **42**(17): p. 11083-91.
232. Grabarz, A., et al., *A role for BLM in double-strand break repair pathway choice: prevention of CtIP/Mre11-mediated alternative nonhomologous end-joining.* Cell Rep, 2013. **5**(1): p. 21-8.
233. Thangavel, S., et al., *DNA2 drives processing and restart of reversed replication forks in human cells.* J Cell Biol, 2015. **208**(5): p. 545-62.
234. Wang, Y. and J. Qin, *MSH2 and ATR form a signaling module and regulate two branches of the damage response to DNA methylation.* Proc Natl Acad Sci U S A, 2003. **100**(26): p. 15387-92.

235. Yoshioka, K., Y. Yoshioka, and P. Hsieh, *ATR kinase activation mediated by MutSalpha and MutLalpha in response to cytotoxic O6-methylguanine adducts.* Mol Cell, 2006. **22**(4): p. 501-10.
236. Ngo, G.H., et al., *The 9-1-1 checkpoint clamp stimulates DNA resection by Dna2-Sgs1 and Exo1.* Nucleic Acids Res, 2014. **42**(16): p. 10516-28.
237. Toledo, L.I., et al., *ATR prohibits replication catastrophe by preventing global exhaustion of RPA.* Cell, 2013. **155**(5): p. 1088-103.
238. Owen, B.A., H.L. W, and C.T. McMurray, *The nucleotide binding dynamics of human MSH2-MSH3 are lesion dependent.* Nat Struct Mol Biol, 2009. **16**(5): p. 550-7.
239. Lao, V.V., et al., *Altered RECQ Helicase Expression in Sporadic Primary Colorectal Cancers.* Transl Oncol, 2013. **6**(4): p. 458-69.
240. Hosono, Y., et al., *Tumor suppressor RecQL5 controls recombination induced by DNA crosslinking agents.* Biochim Biophys Acta, 2014. **1843**(5): p. 1002-12.
241. Huppert, J.L. and S. Balasubramanian, *G-quadruplexes in promoters throughout the human genome.* Nucleic Acids Res, 2007. **35**(2): p. 406-13.
242. Nguyen, G.H., et al., *Regulation of gene expression by the BLM helicase correlates with the presence of G-quadruplex DNA motifs.* Proc Natl Acad Sci U S A, 2014. **111**(27): p. 9905-10.
243. Rhodes, D. and H.J. Lipps, *G-quadruplexes and their regulatory roles in biology.* Nucleic Acids Res, 2015. **43**(18): p. 8627-37.
244. Maizels, N., *G4 motifs in human genes.* Ann N Y Acad Sci, 2012. **1267**: p. 53-60.
245. Tomimatsu, N., et al., *Phosphorylation of EXO1 by CDKs 1 and 2 regulates DNA end resection and repair pathway choice.* Nat Commun, 2014. **5**: p. 3561.
246. Bolderson, E., et al., *Phosphorylation of Exo1 modulates homologous recombination repair of DNA double-strand breaks.* Nucleic Acids Res, 2010. **38**(6): p. 1821-31.
247. Chen, X., et al., *Cell cycle regulation of DNA double-strand break end resection by Cdk1-dependent Dna2 phosphorylation.* Nat Struct Mol Biol, 2011. **18**(9): p. 1015-9.
248. Yimit, A., M. Riffle, and G.W. Brown, *Genetic Regulation of Dna2 Localization During the DNA Damage Response.* G3 (Bethesda), 2015. **5**(9): p. 1937-44.
249. Zhang, J.M., et al., *Fission yeast Pxd1 promotes proper DNA repair by activating Rad16XPF and inhibiting Dna2.* PLoS Biol, 2014. **12**(9): p. e1001946.
250. Li, K., et al., *Regulation of WRN protein cellular localization and enzymatic activities by SIRT1-mediated deacetylation.* J Biol Chem, 2008. **283**(12): p. 7590-8.
251. Lozada, E., et al., *Acetylation of Werner syndrome protein (WRN): relationships with DNA damage, DNA replication and DNA metabolic activities.* Biogerontology, 2014. **15**(4): p. 347-66.
252. McKerlie, M., et al., *Phosphorylated (pT371)TRF1 is recruited to sites of DNA damage to facilitate homologous recombination and checkpoint activation.* Nucleic Acids Res, 2013. **41**(22): p. 10268-82.
253. Slupianek, A., et al., *BCR/ABL stimulates WRN to promote survival and genomic instability.* Cancer Res, 2011. **71**(3): p. 842-51.
254. Arai, A., et al., *RECQL1 and WRN proteins are potential therapeutic targets in head and neck squamous cell carcinoma.* Cancer Res, 2011. **71**(13): p. 4598-607.
255. Aggarwal, M., et al., *Targeting an Achilles' heel of cancer with a WRN helicase inhibitor.* Cell Cycle, 2013. **12**(20): p. 3329-35.
256. Radhakrishnan, R., et al., *Histone deacetylase 10 regulates DNA mismatch repair and may involve the deacetylation of MutS homolog 2.* J Biol Chem, 2015. **290**(37): p. 22795-804.

257. Peterson, S.E., et al., *Cdk1 uncouples CtIP-dependent resection and Rad51 filament formation during M-phase double-strand break repair.* J Cell Biol, 2011. **194**(5): p. 705-20.

7. Abbreviation Index

AP site	Apurinic or apyrimidinic site
APE1	AP endonuclease
ATM	Ataxia telangiectasia mutated
ATR	Ataxia telangiectasia mutated and rad3-related
ATRIP	ATR interacting protein
BER	Base excision repair
BTRR	BLM-TOPOIIIα-RMI1-RMI2
BLM	Bloom syndrome protein
BIR	Break-induced replication
ChIP	Chromatin immunoprecipitation
Cis-Pt	Cisplatin
CDK	Cyclin-dependent kinase
CPD	Cyclobutane pyrimidine dimer
D-loop	Displacement loop
Dam	DNA adenine methylation
DDR	DNA damage response
DSBR	DNA DSB repair
DNA2	DNA replication helicase/nuclease 2
DNA-PK	DNA-dependent protein kinase
dHJ	double Holliday junction
DSB	Double-strand break
ds	double-stranded
EJ	End joining
EXO1	Exonuclease 1
GG-NER	Global genome nucleotide excision repair
HR	Homologous recombination
IDL	Insertion-deletion loop
ICL	Interstrand crosslink
IR	Ionizing radiation
LOH	Loss-of-heterozygosity

MMEJ	microhomology-mediated end-joining
MMR	Mismatch repair
MMC	Mitomycin C
MRN	Mre11-Rad50-Nbs1
MRX	Mre11-Rad50-Xrs2
NHEJ	Non-homologous end joining
NER	Nucleotide excision repair
Nt	Nucleotides
PIKK	Phosphatidylinositol 3-kinase like protein kinase
PAR	Poly(ADP-ribose)
PARP	Poly(ADP-ribose) polymerase
ROS	Reactive oxygen species
RPA	Replication protein A
STR	Sgs1-Top3-Rmi1
SSA	Single-strand annealing
SSB	Single-strand break
ss	single-stranded
SDSA	Synthesis-dependent strand annealing
TC-NER	Transcription-coupled nucleotide excision repair
UV	ultraviolet
WS	Werner syndrome
WRN	Werner syndrome protein
9-1-1	RAD9-RAD1-HUS1
(6-4)PP	6-4 photoproduct

8. Curriculum vitae

Andreas Sturzenegger
Schaffhauserstrasse 24
CH-8400 Winterthur
(+41)79 441 73 32
andreas.sturzenegger@icloud.com

04.04.1989
Swiss
Single

Education

2012-2016	PhD in natural sciences in the group of PD Dr. Pavel Janscak at the Institute of Molecular Cancer Research, University of Zurich. Thesis title: Study of mechanisms of homologous recombination in mammalian cells
2010-2012	Master of Science at the University of Zurich in Molecular and Cellular Biology (with distinction) with master thesis work in the laboratory of PD Dr. Pavel Janscak at the Institute of Molecular Cancer Research, University of Zurich. Thesis title: Study of DNA double-strand break repair by homologous recombination
2007-2010	Bachelor of Science at the University of Applied Sciences FHNW Muttenz in Molecular Life Sciences. Thesis title: Development of a specific TaqMan real-time PCR system to detect garlic and onion in food samples
2004- 2007	Apprenticeship as a biological laboratory technician with professional maturity at Novartis Pharma AG in Basel

Fellowships/Awards

2013	Forschungskredit of the University of Zurich
2012	Legacy prize for outstanding scientific work for the Master's thesis

Languages

German:	Mother tongue
English:	Very good command in spoken and written English
French:	Basic knowledge

Additional skills

Courses in: - Statistical methods in biology
- Project management for advanced researchers
- Economics at basic level

Excellent Microsoft Office skills

Publication record

Sturzenegger, Andreas; Burdova, Kamila; Kanagaraj, Radhakrishnan; Levikova, Maryna; Pinto, Cosimo; Cejka, Petr; Janscak, Pavel (2014). DNA2 cooperates with the WRN and BLM RecQ helicases to mediate long-range DNA-end resection in human cells. Journal of Biological Chemistry, 289(39):27314-27326.

Burdova, Kamila; Mihaljevic, Boris; Sturzenegger, Andreas; Chappidi, Nagaraja; Janscak, Pavel (2015). The Mismatch-Binding Factor MutSbeta Can Mediate ATR Activation in Response to DNA Double-Strand Breaks. Molecular Cell, 59(4): 603-14

Paliwal, Shreya; Kanagaraj, Radhakrishnan; Sturzenegger, Andreas; Burdova, Kamila; Janscak, Pavel (2014). Human RECQ5 helicase promotes repair of DNA double-strand breaks by synthesis-dependent strand annealing. Nucleic Acids Research, 42(4):2380-2390.

Chatterjee, Sujoy; Zagelbaum, Jennifer; Savitsky, Pavel; Sturzenegger, Andreas; Huttner, Diana; Janscak, Pavel; Hickson, Ian D; Gileadi, Opher; Rothenberg, Eli (2014). Mechanistic insight into the interaction of BLM helicase with intra-strand G-quadruplex structures. Nature Communications, 5:5556.

Teaching experience

2015-2016	Supervising a master student in the laboratory of PD Dr. Pavel Janscak
2013-2015	Organisation and teaching of the practical block course “Genome instability and Molecular Cancer Research” in the laboratory of PD Dr. Pavel Janscak at the University of Zurich
Dec 2014	Teaching assistant in the basic biology practical block course for bachelor students at the University of Zurich
2014	Supervising a bachelor student in the laboratory of PD Dr. Pavel Janscak at the University of Zurich

9. Acknowledgements

It would not have been possible to write this PhD thesis without the help of many people. Thus, I would hereby like to thank all the people that supported me during my PhD studies.

I am greatly indebted to my thesis supervisor PD Dr. Pavel Janscak who gave me the opportunity to work in his group on different projects that enabled me to get a broad knowledge in the field of cancer research. With great enthusiasm, he explained all the concepts of various biological processes and methods associated with my projects in a clear and understandable way. He invested a lot of time in discussions about experiments, provided lots of helpful ideas and encouraged me to try different approaches if certain assays failed. Pavel made huge efforts to create an inspiring and productive work environment in the lab and while writing this thesis he supported me with very useful input.

I also wish to thank the members of my PhD committee; Prof. Dr. Petr Cejka, Prof. Dr. Alessandro Sartori and Prof. Dr. Lumir Krejci for their valuable advice.

I thank all the present and past members of the Janscak lab; Boris Mihaljevic, Shreya Paliwal, Kamila Burdova, Shruti Menon, Naga Raja Chappidi, Stefano Di Marco, Adisa Hadzic, Domino Schlegel, Amlan Chatterjee Jana Langhoff, Judith Schröder, Jana Dobrovolna and Christiane König for all the funny moments and lovely atmosphere in the lab during my Master and PhD studies.

I warmly thank all the people at the IMCR for the good times I had in the past years, especially Joe Jiricny for sustaining such a nice institute. I would also like to thank Farah M Hamedi-Baccouche and Odete Pereira Alves that were working behind the science scenes and maintained all the lab equipment.

I thank the Cancer Biology PhD Program and the Life Science Zurich Graduate School for organising many networking events and interesting courses also beyond cancer research.

Finally, I wish to thank all my colleagues and my entire family, especially my mother Verena Sturzenegger, for providing a lot of support and constantly encouraging me not only during the PhD studies but also trough all the years of my education.

Andreas Sturzenegger